Lawrence Berkeley National Laboratory
LBL Publications

Title
DECOVALEX-2023 Task F1 Final Report

Permalink
https://escholarship.org/uc/item/3sz1b7b1

Authors
Faybishenko, Boris
Mariner, Paul
Leone, Rosie
et al.

Publication Date
2024-04-12

Copyright Information

Peer reviewed

DECOVALEX-2023
Task F1 Final Report

Paul Mariner, Rosie Leone, and Emily Stein

With contributions from:

Jan Březina, Scott Briggs, Chieh-Chun Chang, Hao-Ting Chang, Jeffrey Hyman, Jung-Woo Kim, Minjeong Kim, Yong-Min Kim, Jaewon Lee, Zhenze Li, Ondrej Mikláš, Carlos Guevara Morel, Son Nguyen, Nicholas Izuchukwu Osuji, Yu-Hsiang Shen, Jan Thiedau, and Marek Vencl

February 2024

DECOVALEX 2023

Disclaimer

This document was prepared as an account of the international research project DECOVALEX-2023 comprising participants from industry, government and academia, with funding organizations--Andra, BASE, BGE, BGR, CAS, CNSC, COVRA, U.S. DOE, Enresa, ENSI, JAEA, KAERI, NWMO, NWS, SÚRAO, SSM and Taipower. The statements made in the report are, however, solely those of the authors and do not necessarily reflect those of the Funding Organizations. While this document is believed to contain correct information, neither the United States Government nor any agency thereof, nor the Regents of the University of California, nor any of their employees, makes any warranty, express or implied, or assumes any legal responsibility for the accuracy, completeness, or usefulness of any information, apparatus, product, or process disclosed, or represents that its use would not infringe privately owned rights. Reference herein to any specific commercial product, process, or service by its trade name, trademark, manufacturer, or otherwise does not necessarily constitute or imply its endorsement, recommendation, or favoring by the United States Government or any agency thereof or the Regents of the University of California. The views and opinions of the authors expressed herein do not necessarily state or reflect those of the United States Government, any agency thereof, or the Regents of the University of California.

This technical document does not consider contractual limitations or obligations under the Standard Contract for Disposal of Spent Nuclear Fuel and/or High-Level Radioactive Waste (Standard Contract) (10 CFR Part 961).

To the extent discussions or recommendations in this document conflict with the provisions of the Standard Contract, the Standard Contract governs the obligations of the parties, and this presentation in no manner supersedes, overrides, or amends the Standard Contract.

No inferences should be drawn from this document regarding future actions by DOE, which are limited by the terms of the Standard Contract and Congressional appropriations for the Department to fulfill its obligations under the Nuclear Waste Policy Act, including licensing and constructing a spent nuclear fuel repository.

Copyright

This publication has been composed under the direction of editors at Lawrence Berkeley National Laboratory under Contract No. DE-AC02-05CH11231 with the U.S. Department of Energy, Quintessa Limited, Birchwood Park, Warrington WA3 6GA, UK. The U.S. Government retains a non-exclusive, irrevocable, worldwide license to publish or reproduce this published report or allow others to do so for U.S. Government purposes.

Writers for each chapter are responsible for copyright permissions (if applicable) for graphics within their chapter.

DECOVALEX-2023

Task F1 Final Report

Main Authors :

Paul Mariner, Rosie Leone, and Emily Stein
Sandia National Laboratories (SNL)

Contributing Authors (alphabetical by organisation):

Jan Thiedau, Carlos Guevara Morel
Federal Institute for Geosciences and Natural Resources, Germany (BGR)

Zhenze Li, Son Nguyen, Canadian Nuclear Safety Commission (CNSC)

Jung-Woo Kim, Yong-Min Kim, Jaewon Lee, Minjeong Kim
Korea Atomic Energy Research Institute (KAERI)

Jeffrey Hyman, Los Alamos National Laboratory (LANL)

Chieh-Chun Chang, Yu-Hsiang Shen, Hao-Ting Chang
Taiwan National Atomic Research Institute (NARI) / Taipower Company

Scott Briggs, Nuclear Waste Management Organization (NWMO)

Ondrej Mikláš, Marek Vencl
Czech Radioactive Waste Repository Authority (SÚRAO)

Jan Březina, Technical University of Liberec (TUL)

Nicholas Izuchukwu Osuji, Uppsalla University, Sweden (UU)

Preface

The DECOVALEX Project is an ongoing international research collaboration established in 1992 to advance the understanding and modeling of coupled Thermal (T), Hydrological (H), Mechanical (M), and Chemical (C) processes in geological systems. DECOVALEX was initially motivated by recognising that predicting these coupled effects is essential to the performance and safety assessment of geologic disposal systems for radioactive waste and spent nuclear fuel. Later, it was realized that these processes also play a critical role in other subsurface engineering activities, such as subsurface CO_2 storage, enhanced geothermal systems, and unconventional oil and gas production through hydraulic fracturing. Research teams from many countries (e.g., Canada, China, Czech Republic, Finland, France, Germany, Japan, Netherlands, Republic of Korea, Spain, Sweden, Switzerland, Taiwan, United Kingdom, and the United States) various institutions have participated in the DECOVALEX Project over the years, providing a wide range of perspectives and solutions to these complex problems. These institutions represent radioactive waste management organizations, national research institutes, regulatory agencies, universities, and industry and consulting groups.

At the core of the collaborative work within DECOVALEX is the collaborative analysis and comparative modeling of state-of-the-art field and laboratory experiments. DECOVALEX engages model comparison in a broad and comprehensive sense, including the modelers' interpretation of experimental data, selection of boundary conditions, rock and fluid properties, etc., and their choice of coupling schemes and simulators. This recent phase of DECOVALEX has expanded the work scope to include the modelers being challenged to gain an understanding of the representation coupled processes in generic 'whole system' or 'performance assessment' models. In-depth and detailed discussions among the teams yield insight into the coupled THMC processes and stimulate the development of modeling capabilities and measurement methods. This would have been impossible if only one or two groups had studied the data.

Since the project initiation, DECOVALEX has been organized in several four-year phases, each featuring several modeling tasks of importance to radioactive waste disposal and other geoscience applications. Seven project phases were successfully concluded between 1992 and 2019, the results of which have been summarized in several overview publications (e.g., Tsang et al., 2009; Birkholzer et al., 2018; Birkholzer et al., 2019, Birkholzer et al., 2024). The most recent phase, DECOVALEX-2023, started in 2020 and ended in 2023. Seven tasks were conducted in DECOVALEX-2023, as follows:

- **Task A: HGFrac** – Thermal- and gas- induced fracturing of the Callovo-Oxfordian Clay, France
- **Task B: MAGIC** – Migration of gas in compacted clay
- **Task C: FE Experiment** – Thermal-hydro-mechanical (THM) modelling of the FE experiment at Mont Terri, Switzerland
- **Task D: Horonobe EBS Experiment** - THM modelling of the Horonobe EBS experiment at the Horonobe URL, Japan
- **Task E: BATS** – THM modeling for the Brine Availability Test in Salt (BATS) at the WIPP, New Mexico, USA

- **Task F: Performance Assessment** – Comparative generic performance assessment models in crystalline and salt formations
- **Task G: SAFENET** – Laboratory-scale TH and THM analyses of single fractures

The DECOVALEX Project would not have been possible without the support and engagement of the participating organizations who jointly support the coordination of the project within a given project phase, propose and coordinate modeling tasks, including the necessary experimental data, and deploy their research team (or teams) working on a selection of the tasks conducted in the project. The partner organizations in DECOVALEX-2023 were:

- Andra, National Radioactive Waste Management Agency, *France*
- BASE, Federal Office for the Safety of Nuclear Waste Management*, Germany*
- BGE, Federal Company for Radioactive Waste Disposal, *Germany*
- BGR, Federal Institute for Geosciences and Natural Resources, *Germany*
- CAS, Chinese Academy of Sciences, *China*
- CNSC, Canadian Nuclear Safety Commission, *Canada*
- COVRA, Central Organisation for Radioactive Waste, *Netherlands*
- DOE, Department of Energy, *USA*
- Enresa, National Radioactive Waste Management Agency, *Spain*
- ENSI, Swiss Federal Nuclear Safety Inspectorate, *Switzerland*
- JAEA, Japan Atomic Energy Agency, *Japan*
- KAERI, Korea Atomic Energy Research Institute, Republic of Korea
- NWMO, Nuclear Waste Management Organization, *Canada*
- NWS, Nuclear Waste Services, *United Kingdom*
- SSM, Swedish Radiation Safety Authority, *Sweden*
- SÚRAO, Radioactive Waste Repository Authority, *Czech Republic*
- Taipower, Taiwan Power Company, *Taiwan*

We are extremely grateful to these organizations for their financial and technical support of DECOVALEX-2019.

Jens Birkholzer (Chairman of the DECOVALEX project) and Alex Bond (Technical Coordinator of the DECOVALEX Project).

Berkeley, California, USA, October 2024

References:
Birkholzer, J.T., Bond, A.E., Hudson, J.A., Jing, L., Tsang, C.-F., Shao, H., Kolditz, O. (2018): DECOVALEX-2015 - An International Collaboration for Advancing the Understanding and Modeling of Coupled Thermo-Hydro-Mechanical-Chemical (THMC) Processes in Geological Systems, Environmental Earth Sciences, 77(14). https://doi.org/10.1016/j.ijrmms.2022.105097
Birkholzer, J.T., Tsang, C.-F., Bond, A.E., Hudson, J.A., Jing, L., and Stephansson, O. (2019): 25 Years of DECOVALEX - Scientific Advances and Lessons Learned from an International Research Collaboration in Coupled Subsurface Processes, Invited Review, International Journal and Rock Mechanics and Mining Sciences, 122. https://doi.org/10.1016/j.ijrmms.2019.03.015
Birkholzer, J.T., Bond, A.E. and Tsang, C.-F. (2024). The DECOVALEX international collaboration on modeling of coupled subsurface processes and its contribution to confidence building in

radioactive waste disposal. Hydrogeology Journal, https://doi.org/10.1007/s10040-024-02799-7

Tsang, C.-F., Stephansson, O., Jing, L., and Kautsky, F. (2009): DECOVALEX Project: from 1992 to 2007. Environmental Geology, 57(6). https://doi.org/10.1007/s00254-008-1625-1

Summary

DECOVALEX-2023 Task F is a comparison of models and methods for post-closure performance assessment (PA) of a deep geologic repository for radioactive waste. The general aims of Task F are to build confidence in the models, methods, and software used for PA and to stimulate additional research and development in PA methodologies. The task objectives are to motivate development of PA modelling skills and capabilities, to examine the influence of model choices on calculated repository performance, and to compare the uncertainties introduced by model choices to other sources of uncertainty.

Task F involves no actual experiment or site. It is a PA modelling exercise that requires the conceptual development of hypothetical repository designs and geologic settings. Because three of the teams were interested in salt and the rest of the teams were interested in crystalline rock, Task F was split into two branches: Task F1 for crystalline rock and Task F2 for salt.

This report is for Task F1, crystalline rock. Teams from seven countries (Canada, Czech Republic, Germany, Korea, Sweden, Taiwan, and United States) participated in Task F1. The teams worked together to define the features, events, and processes of the reference case repository and established a set of performance measures. In addition, they defined a set of benchmark problems designed to test and compare modelling capabilities for fracture flow and transport at different scales. The repository design and benchmark problems are documented in a Task Specification that evolved over time as the group honed the specifications.

The benchmark problems verified that each team can aptly model flow and transport in fractured media in 1-, 2-, and 3-dimensions. Two general approaches were used for the 3-dimensional benchmarks: discrete fracture network (DFN) and equivalent continuous porous medium (ECPM). DFN modelling involves explicit meshing of each fracture while ECPM modelling aims to capture the effective porosity and directional permeability of each cell in a space-filling mesh as affected by intersecting fractures. In some models, a combination of the two is used, i.e., DFN for large known fractures and ECPM for the rest of the domain. Transport is solved by using either the advection-dispersion equation or particle tracking. Although some variation is observed among model breakthrough curves in the benchmark problems, there is strong agreement in breakthrough behaviour up to at least the 75th percentile for all benchmarks. At the 90th percentile, breakthrough results show larger differences, suggesting several models retain substantially higher fractions of tracer in regions of slower moving water. In addition to

the flow and transport benchmarks, several teams completed the source term benchmark, verifying capabilities for modelling radionuclide decay and ingrowth, waste package breach, instant release fractions, fuel matrix degradation rates, and radionuclide solubility limitations.

The reference case is conceptualized as a generic spent fuel repository at a depth of 450 m in fractured crystalline rock. The repository has 50 parallel backfilled drifts, each with 50 deposition holes 6 m apart. Each deposition hole contains a 4-PWR waste package and bentonite buffer. The rock domain is 5 km in length, 2 km in width, and 1 km in depth. It has 6 deterministic fractured deformation zones and a multitude of stochastic fractures. Teams generally used the ECPM approach for the entire rock or a hybrid approach in which the deterministic fracture zones are modelled with a DFN and the rest of the rock is modelled by ECPM.

Of the reference case problems specified, only the results of the initial reference case problem are compared in this report. The initial problem focuses on transport from the deposition holes to the surface, i.e., it neglects waste package performance. Tracers are released at all waste package locations at time zero and tracked for their releases to the near field and ground surface.

The water fluxes calculated at the ground surface entry and exit regions of the domain are similar for all models except for two that have considerably lower fluxes. For tracer transport, large differences are observed among models in the magnitude of tracer transported. Much of the difference appears to be due to how the repository is implemented and hence the different degrees of repository simplification. Models that exclude the drifts, buffer, and backfill from the domain tend to show greater release of tracers and radionuclides from the repository.

The initial study presented here indicates that major differences in modelling important processes within the repository (e.g., diffusion through buffer and backfill) can produce broadly different release and transport results, especially when those processes are excluded. Even for the models that included all specified features, events, and processes, the results show significant differences and demonstrate the importance of examining multiple modelling approaches in performance assessment. The differences in results observed in this study are expected to motivate teams to either increase complexity in future versions of the reference case models or to improve methods to account for the effects of simplified features and processes. Either way, future improvements in these models are expected to produce results that more closely agree.

Contents

1 Introduction

1.1 Task Objectives

Task F of DECOVALEX-2023 is a comparison of the models and methods used in post-closure performance assessment of deep geologic repositories for radioactive waste. Task F has two subtasks:

- Task F1 – Performance Assessment for a Generic Repository in Crystalline Rock
- Task F2 – Performance Assessment for a Generic Repository in Domal Salt

This is the final report for Task F1 (Crystalline Rock).

Task F is intended to build confidence in the models, methods, and software used for performance assessment (PA) of deep geologic repositories and/or to bring to the fore additional research and development needed to improve PA methodologies. The objectives are:

- To motivate development of modelling and analysis software for quantitative performance assessment and to provide a platform for staff development;
- To examine the influence of modelling choices (model fidelity, omission/inclusion of processes, coupling, etc.) on performance measures (simulation outputs); and
- To compare the uncertainties introduced by modelling choices to other sources of uncertainty, such as stochastic heterogeneity, uncertain input parameters, or scenario and conceptual uncertainties.

1.2 Task Structure

The initial Task Specification (Stein et al. 2021) proposed a five-step process as indicated in Figure 1.

- Step 0: Review the DECOVALEX-2023 crystalline reference case proposal. Agree on key Features, Events, and Processes (FEPs) to form a reference case. Finalize details of conceptual model specification and parameterization for one release scenario.
- Step 1: Identify individual process models for benchmark comparisons and make the comparisons, e.g., 1-dimensional (1-D) advection and dispersion; 1-

D fracture-matrix diffusion; transport in a 4-fracture network; and transport in a single realization of a stochastic discrete fracture network (DFN). Develop additional benchmarks or modifications of these benchmarks as needed to support additional development of the reference case.

- Step 2: Deterministically simulate crystalline reference case. The only explicit uncertainty included is the uncertainty associated with the stochastic fracture network. Each team models 10 realizations.

- Step 3: Identify uncertain inputs and appropriate probability distributions for the crystalline reference case. Compare mean, median, and other quantitative metrics of uncertainty for performance measures. Calculate prescribed measure of sensitivity, such as partial correlation coefficients and standardized regression coefficients, and compare them.

- Step 4 (optional): Interested teams may apply sensitivity analysis methods of their choice to the crystalline reference case for a comparison of sensitivity analysis methods.

Steps 0 through 2 were completed by nearly all teams. Step 0 produced the Task Specification that outlined the benchmarks and reference case to implement. The Task Specification evolved over time and was finalized in early 2023 with Revision 10 (LaForce et al. 2023). Step 1 produced the benchmark problems and benchmark simulations by each team. The benchmark problems involving a stochastically generated discrete fracture network also evolved over time and were updated through 2022 and into 2023. Step 2, developing and simulating the full reference case model for 10 stochastic realizations of the fracture networks in the crystalline rock, required more time than anticipated. The group found that the reference case needed to be simpler than originally planned so that teams would have the opportunity to progressively develop simulation capability and model complexity. Step 3 was partially completed by calculating the means and confidence intervals for the performance metrics resulting from the 10 stochastic realizations, determining uncertainty distributions for many of the input parameters, and including those uncertainty distributions in the Task Specification. It is anticipated that much of the scope of Steps 3 and 4 will be included in a continuation task for DECOVALEX-2027.
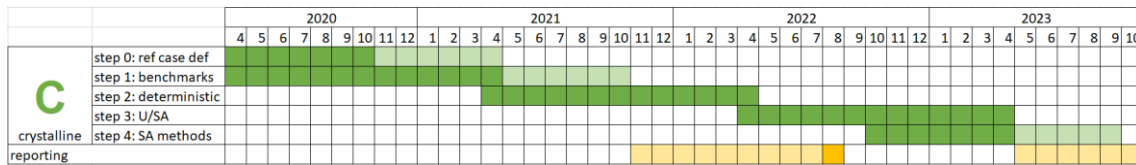
		2020									2021												2022												2023							
		4	5	6	7	8	9	10	11	12	1	2	3	4	5	6	7	8	9	10	11	12	1	2	3	4	5	6	7	8	9	10	11	12	1	2	3	4	5	6	7	8	9	10
	step 0: ref case def																																											
	step 1: benchmarks																																											
C	step 2: deterministic																																											
	step 3: U/SA																																											
crystalline	step 4: SA methods																																											
reporting																																												

Figure 1. Original schedule for Task F1.

1.3 Participating Organizations

Organizations participating in Task F1 include:

- Canadian Nuclear Safety Commission (CNSC),
- Canada's Nuclear Waste Management Organization (NWMO),
- Czech Radioactive Waste Repository Authority (SÚRAO),
- Germany's Federal Institute for Geosciences and Natural Resources (Bundesanstalt für Geowissenschaften und Rohstoffe, BGR),
- Korea Atomic Energy Research Institute (KAERI),
- Swedish Radiation Safety Authority (Strålsäkerhetsmyndigheten, SSM) and its student from Uppsalla University (UU),
- Taiwan Power Company (TPC) and its contractor National Atomic Research Institute (NARI) (formerly, the Institute of Nuclear Energy Research, INER), and
- United States (US) Department of Energy (DOE) and its contractors Sandia National Laboratories (SNL) and Los Alamos National Laboratory (LANL).

All eight participated in benchmarking exercises, and seven implemented a crystalline reference case (BGR, CNSC, KAERI, NARI, SSM-UU, SÚRAO, and SNL). Six of the eight provided brief explanations of their interests in Task F1 in the subsections below. In addition, BGR, CNSC, KAERI, NARI, SSM-UU, SÚRAO, and SNL each contributed an appendix to this report. The appendices describe the teams' methods and associated results.

1.3.1 Canada's Nuclear Waste Management Organization (NWMO)

The Nuclear Waste Management Organization (NWMO) is a not-for-profit organization whose purpose is ensuring Canada's used nuclear fuel is safely managed for generations to come – including that created using new or emerging technologies. In 2002, the Government of Canada's Nuclear Fuel Waste Act, made the NWMO responsible for the safe, long-term management of used nuclear fuel in Canada. Ever since, the NWMO has been implementing Canada's plan for used nuclear fuel. Developed through dialogue

with Canadians, Indigenous peoples, industry, regulators and technical experts, Canada's plan calls for used nuclear fuel to be stored in a deep geological repository following industry best-practice and will be subject to independent review by the Canadian Nuclear Safety Commission (CSNC). As part of on-going safety assessment validation and verification activities, the NWMO participates in DECOVALEX Task F to increase confidence in our safety assessment methodology, tools and models and to ensure consistency with international best-practice.

1.3.2 Czech Radioactive Waste Repository Authority (SÚRAO)

The Czech Radioactive Waste Repository Authority (SÚRAO) was established on 1 June 1997 by the Ministry of Industry and Trade of the Czech Republic as a state organization. On 1 January 2001, in accordance with Section 51 of Act No. 219/2000 Coll., the status of SÚRAO was changed to that of a so-called state organizational body. SÚRAO is managed by its managing director who is appointed and recalled by the Minister of Industry and Trade. The activities of SÚRAO are governed by the Atomic Act.

The state is responsible for the safe disposal of all radioactive waste in the Czech Republic. The provisions of the original Atomic Act (Act No. 18/1997 Coll.) entrusted the safe operation of waste repositories and the disposal of all radioactive waste to SÚRAO, which has been a state organizational body since 2001. SÚRAO's activities are funded by the so-called nuclear account to which, by law, all radioactive waste producers are required to contribute. The nuclear account is managed by the Ministry of Finance.

The Czech deep geological repository (DGR) project envisages the disposal of waste in a crystalline rock environment as based on the Swedish KBS-3 model. This model further assumes the disposal of spent nuclear fuel (SNF) in metal, hermetically-sealed waste packages in boreholes sealed with a bentonite buffer. In terms of PA, SÚRAO already has extensive experience with the management of its low- and intermediate-level waste repositories. However, PA activities and the creation and validation of mathematical models related to the deep geological repository project are still in the early stages of development. Hence, the main reason for SÚRAO's involvement in the crystalline reference case task is to gain more experience with concern to the preparation and application of PA modelling methods and the validation of models in the context of the Czech DGR development program.

1.3.3 Federal Institute for Geosciences and Natural Resources, Germany (BGR)

The Federal Institute for Geosciences and Natural Resources (Bundesanstalt für Geowissenschaften und Rohstoffe, BGR) is the central geoscientific authority providing advice to the German Federal Government with independent and neutral advice on all geoscientific and geotechnical issues. In cooperation with the Federal Company for Radioactive Waste Disposal, the BGR is concerned with geoscientific questions in the context of the existing repository locations in Germany and the site selection process for high-level radioactive waste. BGR's expertise comprises many geoscientific topics arising from the disposal of radioactive waste in deep geological formations. Know-how is continuously extended and consolidated through extensive research activities, often carried out in collaboration with other national and international institutions.

Working on the crystalline reference case allowed BGR to complement an investigation on German disposal options in crystalline rock carried out during the joint research project Christa-II. A methodology for the assessment of thermal-hydraulic-mechanical impacts on host rock integrity has been developed, which takes the hydraulic properties of fractured crystalline rock into account (Thiedau et al. 2021). Modelling the crystalline reference case permitted extended verification of the developed approach including a further extension to transport problems.

1.3.4 Korea Atomic Energy Research Institute (KAERI)

Korea Atomic Energy Research Institute (KAERI), which was established in 1959, is Korea's only research institute dedicated to nuclear energy. HLW disposal research at the KAERI started in 1997 with the goal of developing a deep geological disposal system for the direct disposal of spent nuclear fuel. Since then, key element technologies related to geological disposal have been developed, and KURT, which is an underground disposal research facility in KAERI, was constructed in 2006, and further expanded in 2014. The Korean disposal concept for pressurized water reactor spent nuclear fuel is the Swedish KBS-3V type whose engineered barrier system consists of a cast iron-copper dual structure disposal canister and Ca-type bentonite. Granite bedrock is considered as the host rock, as it is a representative rock type in Korea. Recently, KAERI has been developing a process-based total system performance assessment model which can reflect the complex processes occurring in each component of the repository system. Task F1 contributes to the validation of the model under development.

1.3.5 Taiwan Power Company (TPC) with National Atomic Research Institute (NARI)

Taiwan Power Company (TPC) is an electric power supplier in Taiwan who has responsibility for the final disposal of spent nuclear fuels of nuclear power plants. National Atomic Research Institute (NARI) (formerly, the Institute of Nuclear Energy Research, INER), a national research institute in Taiwan, was entrusted by Taipower Company to execute the design engineering and performance assessment for the final disposal of nuclear fuels. Based on previous work in Taiwan, the crystalline rock is considered as a potential host rock for deep geological disposal facility. The Swedish KBS-3 disposal concept has been considered as a potential disposal approach in Taiwan. Therefore, participating in the Task F1 is a good opportunity for improving the confidence of methods adopted by NARI/TPC.

1.3.6 United States Department of Energy (DOE) with Sandia National Laboratories (SNL) and Los Alamos National Laboratory (LANL)

The United States Department of Energy (DOE) is responsible for permanent disposal of commercial spent nuclear fuel. Since 2010, the DOE has engaged the national laboratories (including SNL and LANL) to pursue a generic site-independent research and development program focusing on three host rock types for deep geologic disposal of nuclear waste: argillite (also called shale or clay), salt (including bedded and domal), and crystalline rock. The strategic objectives of the program include developing a sound technical basis for multiple viable disposal options in the US, increasing confidence in the robustness of generic disposal concepts, and developing the tools needed to support disposal concept implementation.

SNL, supported by DOE, proposed DECOVALEX-2023 Task F. SNL leads and participates in the various activities of each subtask, F1 (crystalline) and F2 (domal salt). Participation in Task F benefits DOE because it motivates development of the capabilities (skills and software) needed for quantitative safety assessment of a mined repository, tests current and developing capabilities against approaches used by other participants, provides useful benchmarks that build confidence in modelling capabilities, and may help direct future development of modelling capabilities.

2 Benchmarks

2.1 1D Flow and Transport

2.1.1 Advection and Dispersion

Solutions for 1-D transient advection and dispersion of three tracers (conservative, decaying, and adsorbing) are compared to analytical solutions adapted from Vogel, Maßmann (2015), Section 2.5.2.

The model domain is a 10 m × 1 m × 1 m beam extending in the positive x direction, discretized into 200 regular hexahedral grid cells, each 0.05 m × 1 m × 1 m, where teams could modify the discretization if needed. A steady-state flow field (constant specific discharge) is applied. At the inflow face (x=0), concentrations of all three tracers are held at 1 mol/L from 0 to 15,000 s, and zero afterward. Material and fluid properties and boundary conditions are given in the Task Specification (LaForce et al. 2023, Section 5.2.2).

Teams solved this problem using the software and solution methods in Table 1. As shown in Figure 2, solutions generally plotted on top of the analytical solution, except for the solutions from SNL and SÚRAO, which were calculated with PFLOTRAN and plot slightly below the peak of the analytical solution. Teams in Task F2 discovered that the PFLOTRAN solution could be made to match the analytical solution by reducing the maximum time step size (Alex Bond, personal communication, April 26, 2022).
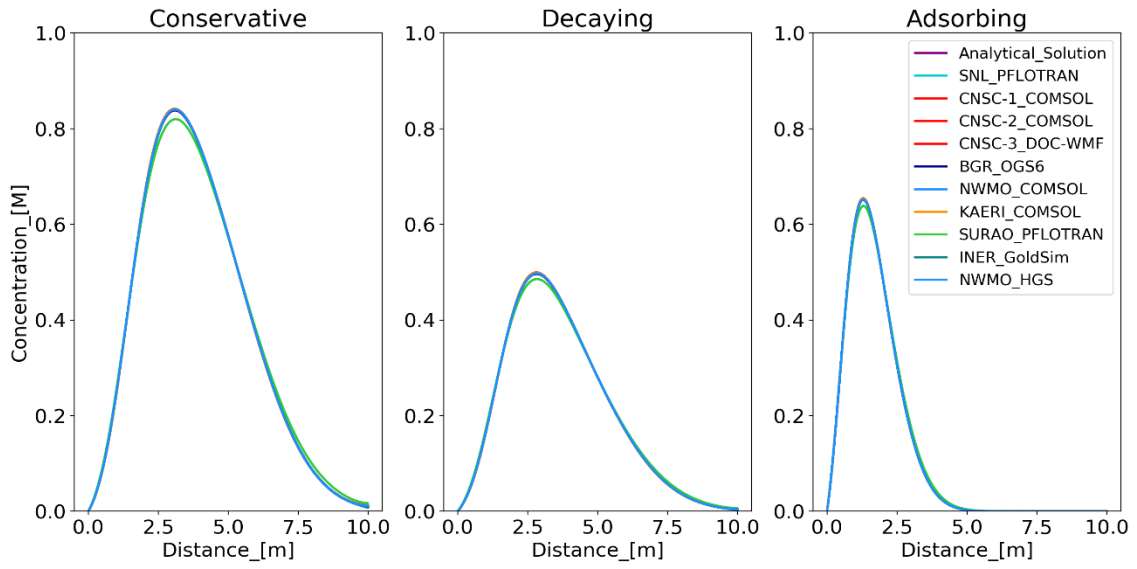
Figure 2. Team results for 1-D transient transport of conservative, decaying, and adsorbing tracers at the end of the simulation (20,000 seconds).

Table 1. Software and solution methods applied to the 1-D transport benchmark.

Team	Software	Solution Method	Boundary Conditions for Transport
BGR	OpenGeoSys Version 6	Finite element Implicit time integration	Tracers held at 1 mol/L at the inflow face (x=0) from 0-15,000 s
CNSC	COMSOL Version 5.6	Finite element with 3-D elements, quadratic shape functions	Tracers held at 1 mol/L at the inflow face (x=0) from 0-15,000 s No diffusive flux at the end (x=end)
CNSC	DOC-WMF	Pipe elements – Laplace transform to solve the transport equation	Tracers held at 1 mol/L at the inflow face (x=0) from 0-15,000 s No diffusive flux at the end (x=end)
KAERI	COMSOL Version 6.0	Finite element	Tracers held at 1 mol/L at the inflow face (x=0) from 0-15,000 s, Outflow (x=end), No flux (sides)
NARI (INER)	GoldSim Version 11.1	Pipe element Laplace transform to solve the advection-dispersion equation, decay, and sorption	Tracers held at 1 mol/L at the inflow face (x=0) from 0-15,000 s
NWMO	COMSOL Version 5.6	1-D finite element direct linear solver; using COMSOL 'Transport of Diluted Species in Porous Media' physics interface	Constant inflow from 0 s to 15,000 s and zero afterwards (change is continuous with a 10 second transition zone before and after the 15,000 second mark)
NWMO	HGS Revision 2005	1-D finite difference	Tracers held at 1 mol/L at the inflow face (x=0) from 0-15,000 s, Outflow (x=end)
SNL	PFLOTRAN	Finite volume Global implicit Euler method to solve for transport, decay, and sorption	Dirichlet boundary condition at 1 mol/L at inflow (x=0) from 0-15,000 s
SÚRAO	PFLOTRAN	Finite volume Global implicit	Tracers held at 1 mol/L at the inflow face (x=0) from 0-15,000 s

2.1.2 Single Fracture Plus Matrix Diffusion

This benchmark is based on the analytical solution by Tang et al. (1981) for the transport of a radionuclide in a single fracture with diffusion into and out of the rock matrix as specified (LaForce et al. 2023, Section 5.2.3). Calculated concentration profiles along the fracture and into the rock matrix are compared in Figure 3 to analytical solutions at 100, 1,000 and 10,000 days over 101 cells. The first set is compared with a linear velocity of 0.01 m/d along a 6 m fracture length with a domain of 2 m for the matrix. The second set is compared with a linear velocity of 0.1 m/d along a 60 m fracture length with a domain of 1 m for the matrix. Teams solved the problem using the software and solution methods in Table 2. Good agreement is achieved among all methods.
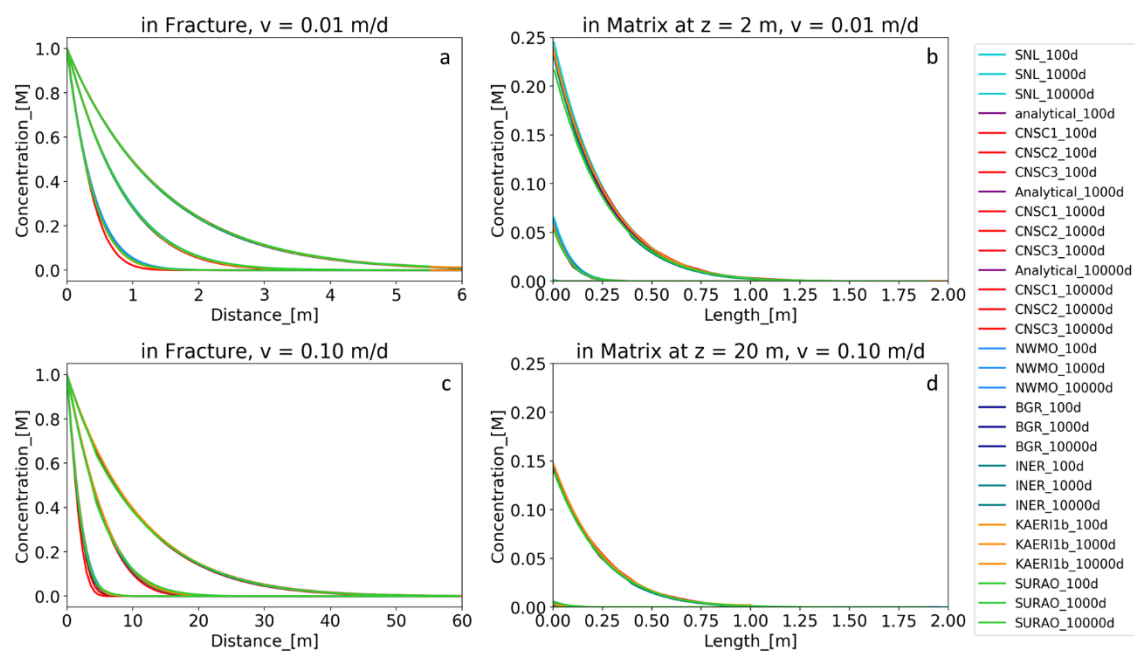
Figure 3. Tracer concentration as a function of distance along the fracture (a, c) and diffusion length into the matrix (b, d) for linear velocities of 0.01 m/d (a, b) and 0.10 m/d (c, d).

Table 2. Software and solution methods for the Single Fracture Plus Matrix Diffusion benchmark.

Team	Software	Solution Method	Boundary & Initial Conditions	Special Considerations
BGR	OpenGeoSys Version 6	Finite element for advection-dispersion equation (ADE) Implicit time integration	Fixed concentration at fracture inflow node instantaneously for times >0	Fracture represented as line elements sharing nodes with matrix elements
CNSC	COMSOL Version 5.6	3-D solid elements for rock matrix; 2-D fracture elements for the fracture	No Flux around perimeter of 3-D geometry; 0 initial concentration in whole domain Step increase in concentration from zero to 1 mol/L at inflow Zero concentration at outflow	
KAERI	COMSOL Version 6.0	Finite element Equivalent continuous porous medium (ECPM)	Constant concentration boundary condition (x=0), Outflow (x=end), No Flux (sides)	Effect of equivalent domain (or mesh) size
NARI (INER)	GoldSim Version 11.1	Cell element (compartment model) Implicit Euler method	1 mol/L at the inflow face (z=0)	The numerical dispersivity is equal to half of the length of one Cell. The dispersivity should be specified greater than half the length of one Cell in simulation. Therefore, a set of fictitious two-way flows has been established between Cells to obtain the correct dispersivity value.
NWMO	COMSOL Version 5.5	2-D finite element direct linear solver; using COMSOL 'Transport of Diluted Species in Porous Media' physics interface with a 1-D fracture sub-node	No Flux around perimeter of 2-D geometry; fixed concentration inflow; zero concentration outflow	Fracture inflow boundary condition required smooth step function increase from zero to 1 to minimize negative concentrations for t<<1 day for some cases in benchmark

SNL	PFLOTRAN Version 4	Finite volume Dual continuum (dual porosity) model	Dirichlet boundary condition: 1 mol/L at inflow (z=0)	Solutions for transport in the primary continuum (fracture) and 1-D diffusion in the secondary continuum (matrix) are sequentially coupled
SÚRAO	PFLOTRAN Version 4	Finite volume Global implicit for transport Richards mode for flow	Constant concentration boundary condition at inflow face	

2.2   Fracture Network Flow and Transport

2.2.1 4 Fractures Benchmark

The 4 Fractures benchmark (modified from an example provided with dfnWorks (Hyman et al. 2015)) simulates advection and diffusion of a conservative tracer through four fractures within a 1 km^3 cubic domain. It is assumed that flow and transport only occur in the fractures; matrix diffusion is neglected. The four fractures are illustrated in Figure 4. The full problem is defined in the Task Specification (LaForce et al. 2023, Section 5.2.4). Teams used the software and solution methods summarized in Table 3. The general methods used by the teams are indicated by the legend suffixes as defined in Table 4.

Groundwater flow is simulated by a steady state (saturated, single-phase) flow driven by a specified pressure gradient along the x-axis. Constant pressure (Dirichlet) boundary conditions are applied on the inflow and outflow faces. For simplicity, gravity is not included. No-flow boundary conditions are applied at all other faces of the domain.

Figure 5 shows the steady state water flux versus the volume of water in the fractures for the different models. The lines indicate that all models have mean fracture water residence times between 1 and 2 years. Differences between models in this figure indicate differences in implementation.
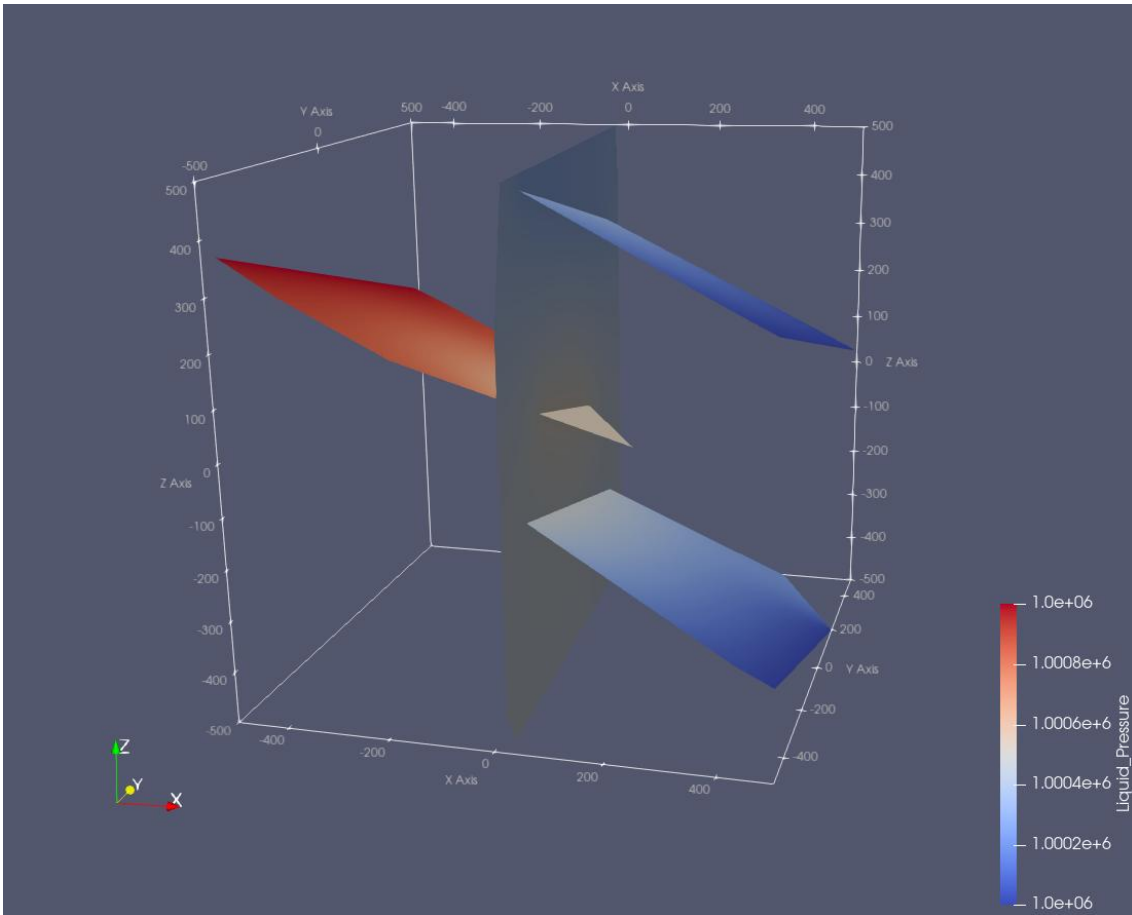
Figure 4. The 4 Fractures benchmark domain coloured by steady state liquid pressure.
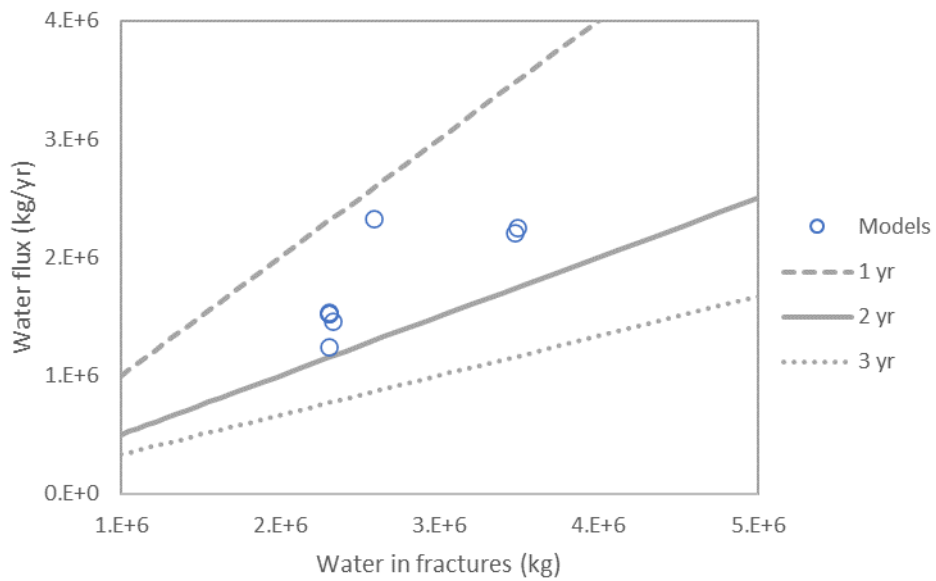
Figure 5. Water flux vs. water in fractures (circles) and mean fracture water residence times (lines) for the 4 Fractures benchmark.

Table 3. Software and solution methods for the 4 Fractures benchmark.

Simulation	Software	Solution Method	Boundary & Initial Conditions	Special Considerations
4BGR-DA	OpenGeoSys Version 6	Finite element (13,768 2D triangles) DFN ADE	Zero-concentration boundary condition for inflow/outflow Injection pulse (Gaussian 0.05a,0.015a) at west face	Inflow fracture is extended by 50 m such that injection location is away from boundary
4CNSC-DA	COMSOL Version 5.6	Finite element (20,754 2D triangles) DFN ADE	Boundary condition type (zero-gradient for tracer at inflow and outflow ends) Gaussian pulse with peak at 0.05 years and standard deviation 0.015	Darcy velocity field used for transient transport analysis
4NARI-EP	DarcyTools Version 4.1.35	Finite volume (2,555,904 hexahedrons) ECPM Particle tracking	10,000 particles uniformly distributed along the west face of the fracture at time = 0 Zero-gradient transport for inflow/outflow boundaries	To inactivate the rock matrix, the porosity and permeability of the rock matrix are set at 1E-20 and 1E-27 m^2
4KAERI-DA	COMSOL Version 6.1	Finite element (104,337 elements including 78,202 2D triangles) DFN ADE	Zero-gradient transport for inflow/outflow boundaries Tracer introduced by change in west face water source composition for one day	Boundary layer mesh is applied for the sudden change in concentration at inlet/outlet boundaries
4KAERI-EA	COMSOL Version 6.1	3-D finite element (240,950 elements including 165,630 tetrahedrons) ECPM ADE	Zero-gradient transport for inflow/outflow boundaries Tracer introduced by change in west face water source composition for one day	Boundary layer mesh is applied for the sudden change in concentration at inlet/outlet boundaries. Minimum porosity and permeability values were used for cells without fracture to minimize matrix diffusion (porosity: 10^{-14}, permeability 10^{-30} m^2)

4NWMO-DA	COMSOL Version 5.6	Finite element (61,679 2D triangles) DFN ADE	Inflow flux boundary condition (Danckwerts type); free advective outflow at east face Gaussian pulse with peak at 0.05 years and standard deviation 0.015	Darcy's Law (tangential version of 'Fracture Flow Module')
4SNL-DP	dfnWorks PFLOTRAN Version 4	Finite volume (175,920 2D triangles) DFN Particle tracking	10,000 particles injected uniformly on the inflow fracture Zero-gradient transport for inflow/outflow boundaries	Cells not intersected by a fracture are inactive
4SNL-DA	dfnWorks PFLOTRAN Version 4	Finite volume (175,920 2D triangles) DFN ADE	Zero-gradient transport for inflow/outflow boundaries Tracer introduced by change in west face water source composition for one day	Cells not intersected by a fracture are inactive
4SNL-EAS	dfnWorks PFLOTRAN Version 4	Finite volume (1,250,000 orthogonal hexahedrons, 9,704 active) ECPM ADE	Zero-gradient transport for inflow/outflow boundaries Tracer introduced by change in west face water source composition for one day	mapdfn.py is used to upscale to a uniform hexagonal mesh. A stairstep correction is applied to equivalent permeabilities. Cells not intersected by a fracture are inactive.
4SSMUU-DA	COMSOL Version 5.6	Finite element (98,345 2D triangles) DFN ADE	Zero-gradient transport for inflow/outflow boundaries Tracer introduced by change in west face water source composition for one day	
4SURAO-EA	dfnWorks PFLOTRAN Version 4	Finite volume (64,000 orthogonal hexahedrons, 5819 active) ECPM ADE	Zero-gradient transport for inflow/outflow boundaries Tracer introduced by change in west face water source composition for one day	Inactive matrix cells, zero gravity

Table 4. Key to Simulation Abbreviations for Benchmark Problems

Abbreviation	Solution Method
DA	DFN and the advection-dispersion equation (ADE)
DP	DFN and particle tracking
DEA	DFN (4 deterministic fractures) and ECPM (stochastic fractures) and ADE
EA	ECPM and ADE
EAS	ECPM and ADE with stairstep correction
EP	ECPM and particle tracking

An initial pulse of conservative tracer (Tracer 1), lasting one day, is inserted along the single fracture on the west face (x = -500) of the domain at time zero; the concentration at the west face is zero for all other times. The tracer exits the domain through the two fractures on the east face (x = 500). Output is compared by calculating the normalized mass of tracer that has crossed the outflow face as a function of time (total mass that has crossed the east face divided by the initial mass entering at the west face).

Breakthrough results as a function of time are compared in Figure 6. Figure 7 shows the same breakthrough curves plotted as a function of fracture volumes. Fracture volumes (N) are the number of times the entire void space of the fractures could theoretically be replaced by the flow of water entering the domain. It is a nondimensional unit of time calculated by dividing the mass of water in the saturated fractures by the cumulative water mass entering (or exiting) the domain. Plotting versus fracture volumes normalizes the breakthrough curves with respect to flow rate. First and second moments calculated for the first 100 years of the simulations are included in the legend in Figure 7. Moments are considered further in Section 2.2.4.
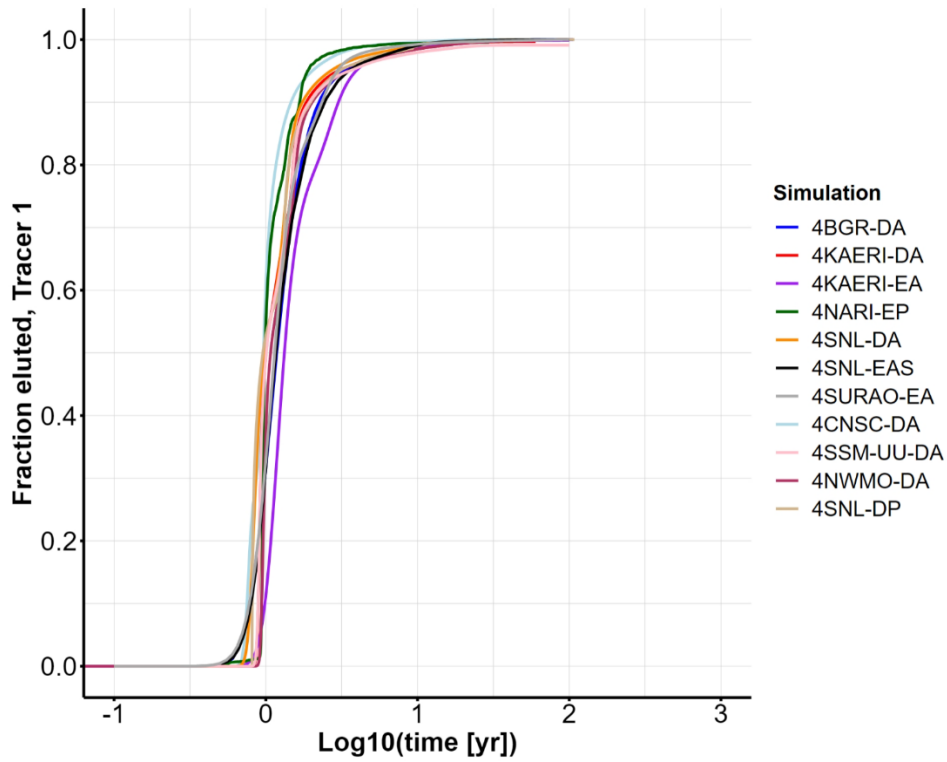
Figure 6. 4 Fractures breakthrough curves normalized by cumulative mass exiting domain vs. time.
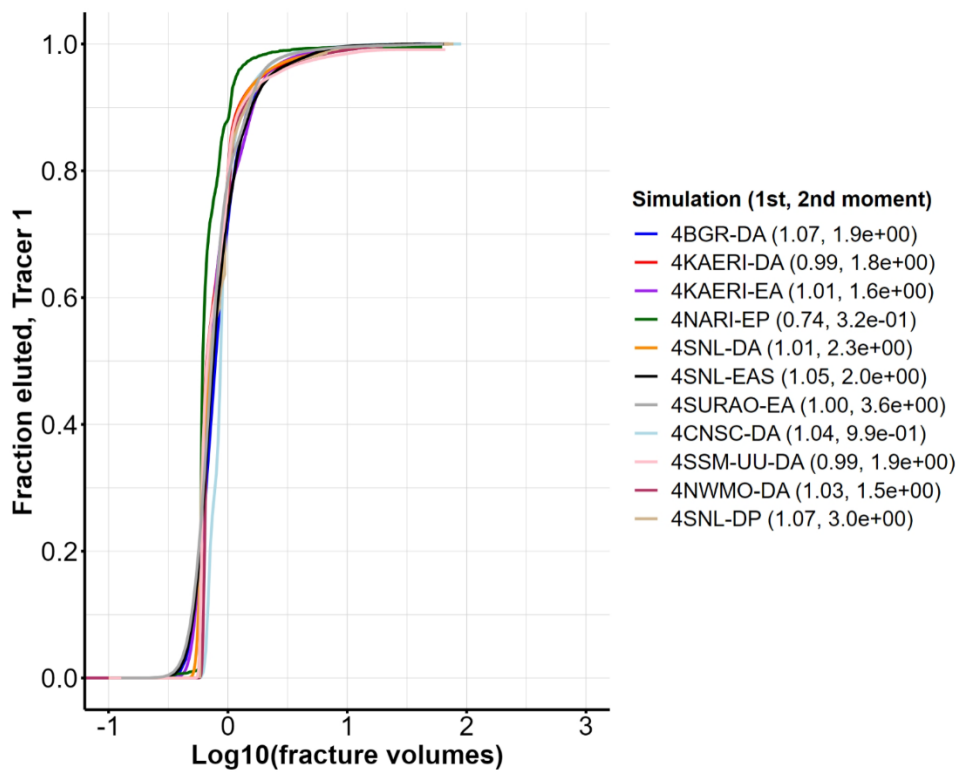
Figure 7. 4 Fractures breakthrough curves normalized by cumulative mass exiting domain vs. fracture volumes.

Breakthrough curves for the 4 Fractures benchmark are compared in terms of percentiles in Figure 8. The percentiles from the 10th to the 75th show particularly strong agreement among the 11 different models despite the broad range in mean water residence times shown in Figure 5.
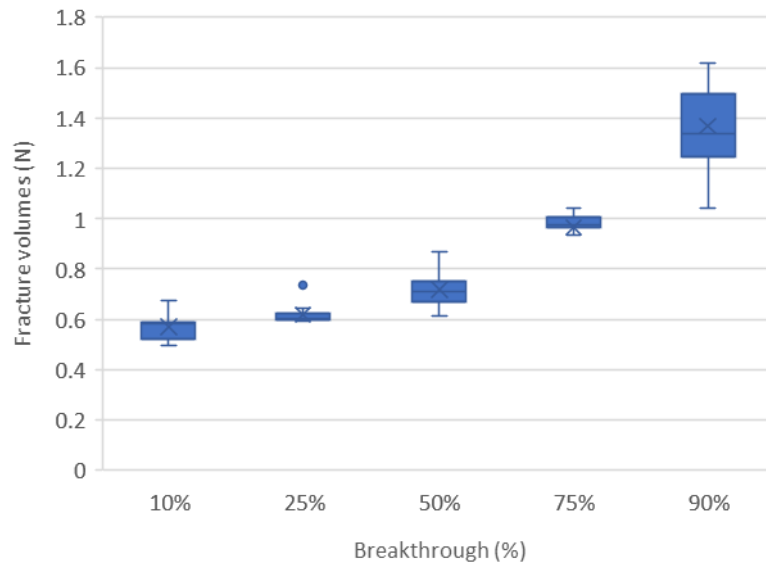
Figure 8. Box and whiskers plot of percentile breakthrough for the 4 Fractures benchmark.

2.2.2 Stochastic Fractures Benchmark

The Stochastic Fractures benchmark adds a stochastically generated fracture network to the 4 Fractures benchmark domain. The stochastic fractures are generated based on Central Hydraulic Unit West (CHUW) Case A distributions from Posiva WR 2012-42 (Hartley et al. 2012, Table D-4) corresponding to Depth Zone 4, which applies at repository depth (Hartley et al. 2016, Table 3-1). A single realization of this network, shown in Figure 9, was used by all teams (LaForce et al 2023, Section 5.2.6). For this problem three tracers were introduced over a one-day period: conservative (Tracer 1), decaying (Tracer 2), and adsorbing (Tracer 3). The decaying tracer has a half-life of 100 years, and the adsorbing tracer is specified to have a retardation factor of 5. Seven teams ran this problem using 11 different models, as summarized in Table 5.

Figure 10 shows the steady state water flux versus water volume in the fractures for the different models. With the added stochastic fractures, mean fracture water residence times increase to approximately 2 years on average.
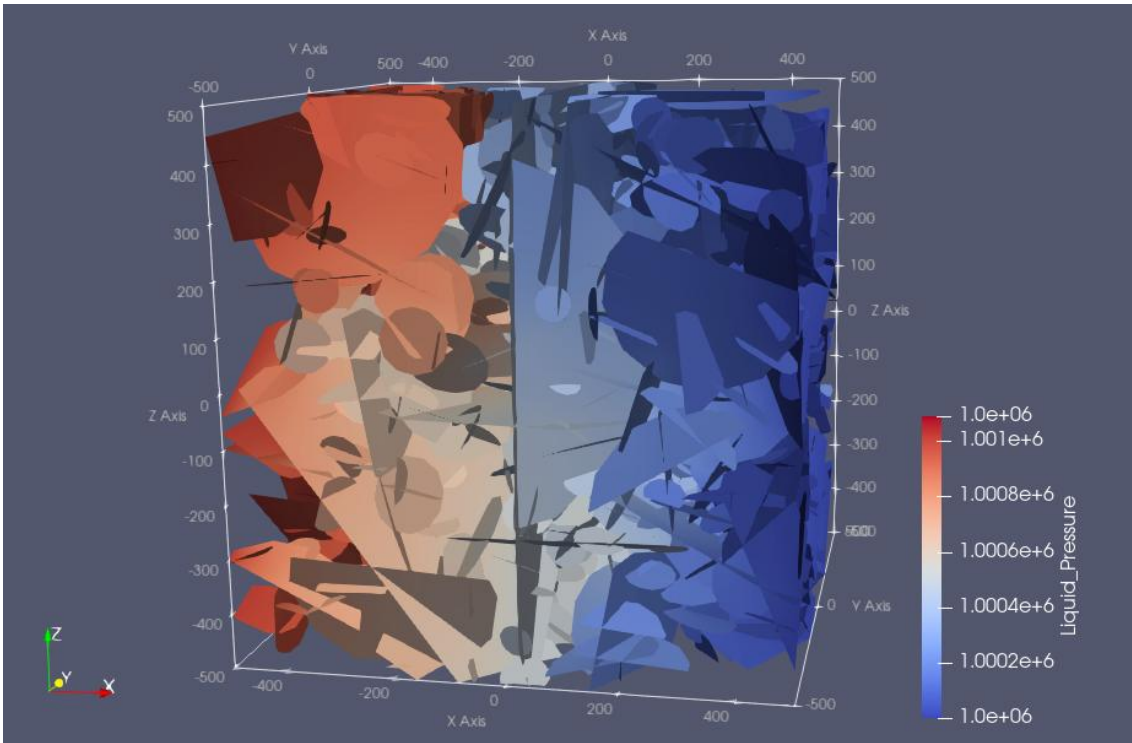
Figure 9. The Stochastic Fractures benchmark domain coloured by steady state liquid pressure.
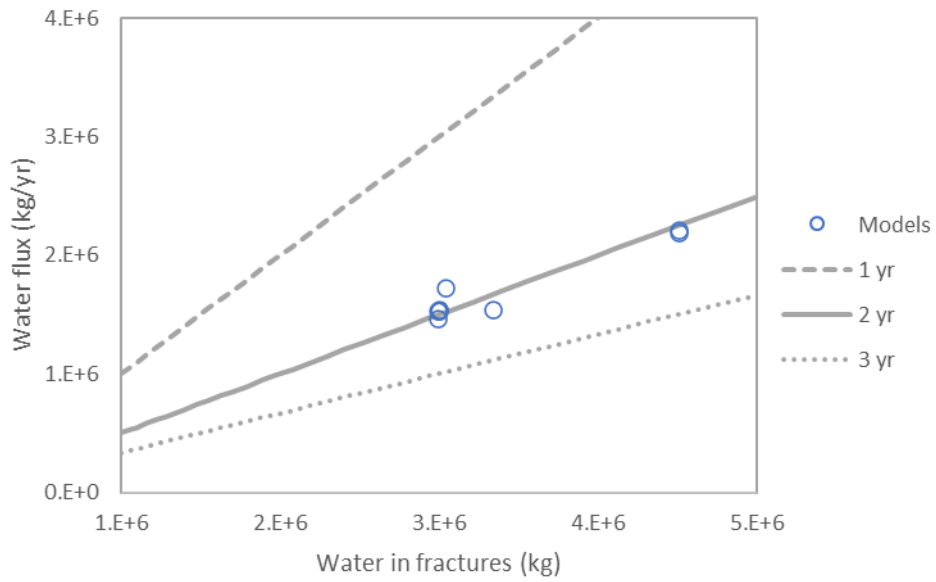
Figure 10. Water flux vs. water in fractures (circles) and mean fracture water residence times (lines) for the Stochastic Fractures benchmark.

Table 5. Software and solution methods for the Stochastic Fractures benchmark.

Simulation	Software	Solution Method	Boundary & Initial Conditions	Special Considerations
6BGR-DEA	FracMan OpenGeoSys Version 6	Finite element (13,678 triangles for fractures, 226,614 tetrahedrons for matrix) DFN: 4 fractures ECPM: matrix ADE	Zero-concentration boundary condition for inflow/outflow Injection pulse (Gaussian 0.05a,0.015a) hydraulic flow weighted at west face	Domain and fracture are extended by 50 m at inflow such that injection location is away from boundary
6NARI-EP	DarcyTools Version 4.1.35 GoldSim Version 11.1	Finite volume (4,505,600 hexahedron) ECPM: Full domain Particle tracking Laplace transform to solve ADE in Pipe pathway in GoldSim	8,875 particles injected along the trace of the inflow fractures weighted by the Darcy velocity at their respective initial positions Zero-gradient transport for inflow/outflow boundaries	Particle tracking was used to estimate flow-related transport parameters for the Pipe pathway in GoldSim
6KAERI-DA	COMSOL Version 6.1	Finite element (183,210 elements including 163,264 2D triangles) DFN: All fractures ADE	Zero-gradient transport for inflow/outflow boundaries Tracer introduced by change in west face water source composition for one day	Boundary layer mesh is applied for the sudden change in concentration at inlet/outlet boundaries
6KAERI-DEA	COMSOL Version 6.1	Finite element (187,737 elements including 135,031 tetrahedrons, 9243 2D triangles) DFN: 4 fractures ECPM: matrix ADE	Zero-gradient transport for inflow/outflow boundaries Tracer introduced by change in west face water source composition for one day	Boundary layer mesh is applied for the sudden change in concentration at inlet/outlet boundaries. Minimum porosity and permeability values were used for cells without fracture to minimize matrix diffusion (porosity: 10^{-14}, permeability 10^{-30} m^2)

6SNL-DA	dfnWorks PFLOTRAN Version 4	Finite volume (4,647,375 triangles) DFN: All fractures ADE	Zero-gradient transport for inflow/outflow boundaries Tracer introduced by change in west face water source composition for one day	
6SNL-EAS	dfnWorks mapdfn.py PFLOTRAN Version 4	Finite volume (1,250,000 orthogonal hexahedrons, 49,685 active) ECPM: Full domain ADE with stairstep correction	Zero-gradient transport for inflow/outflow boundaries Tracer introduced by change in west face water source composition for one day	Stairstep correction is applied to equivalent permeabilities. Cells not intersected by a fracture are inactive.
6SSMUU-DA	dfnWorks COMSOL Version 5.6	Finite element (329,687 2D triangles) DFN: All fractures ADE	Zero-gradient transport for inflow/outflow boundaries Tracer introduced by change in west face water source composition for one day	
6SURAO-EA	dfnWorks PFLOTRAN Version 4	Finite volume (64,000 orthogonal hexahedrons, 29,907 active) ECPM: Full domain ADE	Zero-gradient transport for inflow/outflow boundaries Tracer introduced by change in west face water source composition for one day	

Breakthrough results are compared in Figure 11 (conservative tracer), Figure 12 (decaying tracer), and Figure 13 (adsorbing tracer) as a function of fracture volumes. First and second moments calculated for the first 1000 years of these simulations are included in the legends. The added stochastic fractures introduce additional variability among results and cause the breakthrough curves to spread, as indicated by the larger second moments in Figure 11 vs. Figure 7. Results of the decaying tracer (Figure 12) are nearly the same as the conservative tracer except that the fraction eluted never makes it to 1.0 due to the 100-year half-life. Little decay is seen during the approximately 2-year mean residence time. More variability between models is apparent for the adsorbing tracer (Figure 13). Nevertheless, there is strong agreement between models.

Figure 14 compares percentile breakthroughs for the conservative and adsorbing tracers across all models. The percentiles for the conservative tracer agree well among models, especially through the 75th. There is considerable variation, however, among models for

the adsorbing tracer breakthrough curves for all percentiles. This variation motivates further study of potential causes or errors. The specified retardation factor of 5 should theoretically cause the first moment of the adsorbing tracer to be approximately 5 times that of the conservative tracer. Moments are considered further in Section 2.2.4.
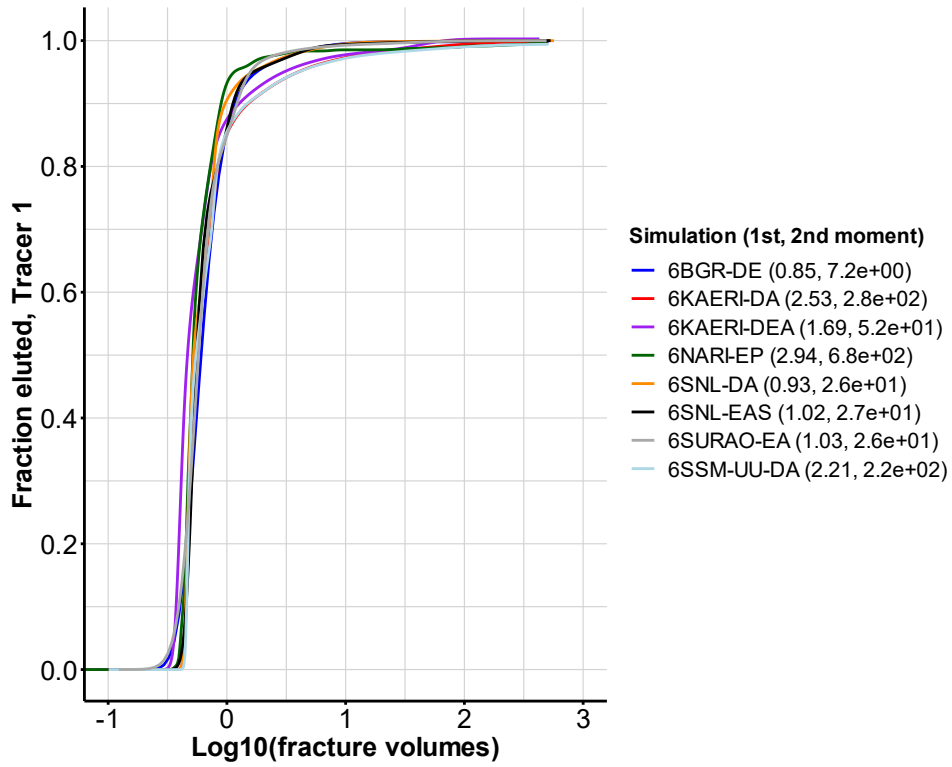
Figure 11. Stochastic Fractures conservative tracer cumulative fractions exiting domain.
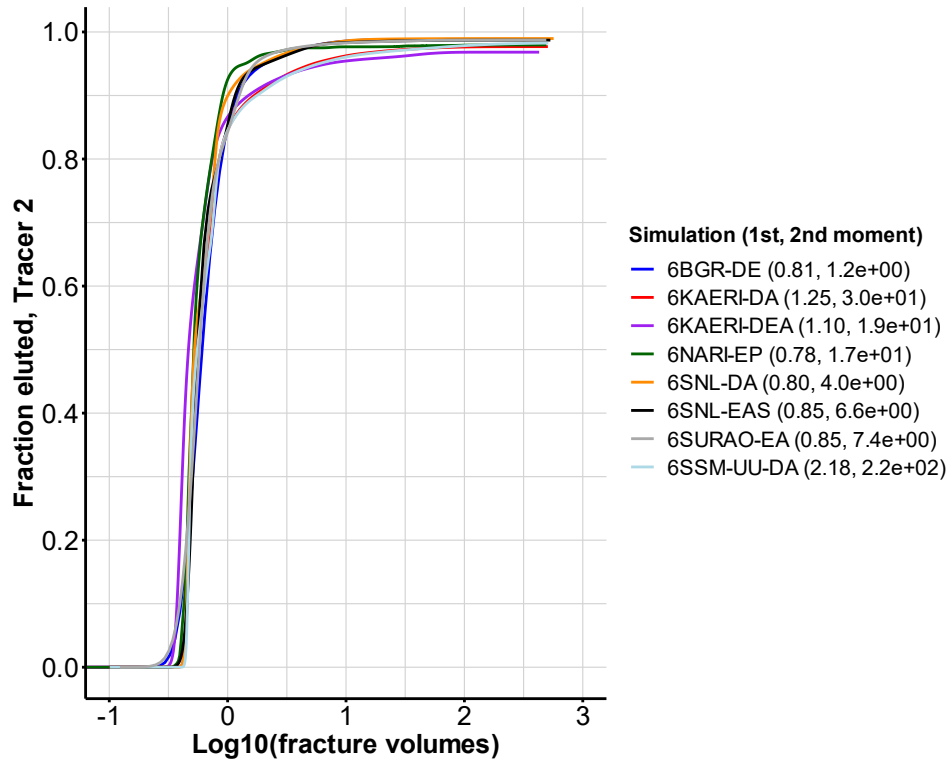
Figure 12. Stochastic Fractures decaying tracer cumulative fractions exiting domain.
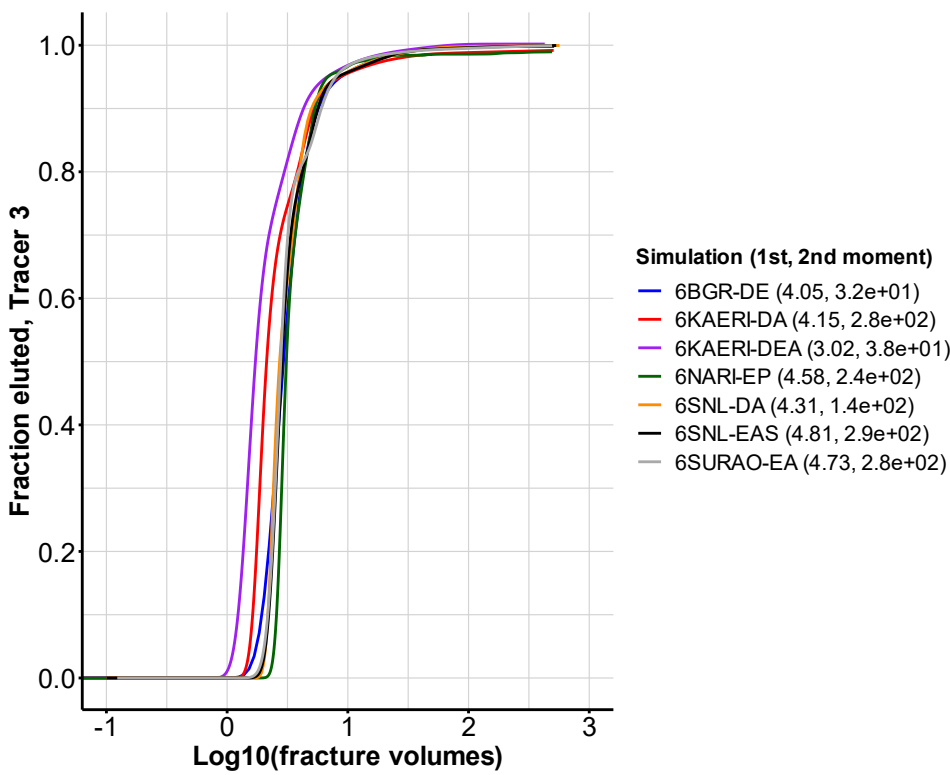
Figure 13. Stochastic Fractures adsorbing tracer cumulative fractions exiting domain.
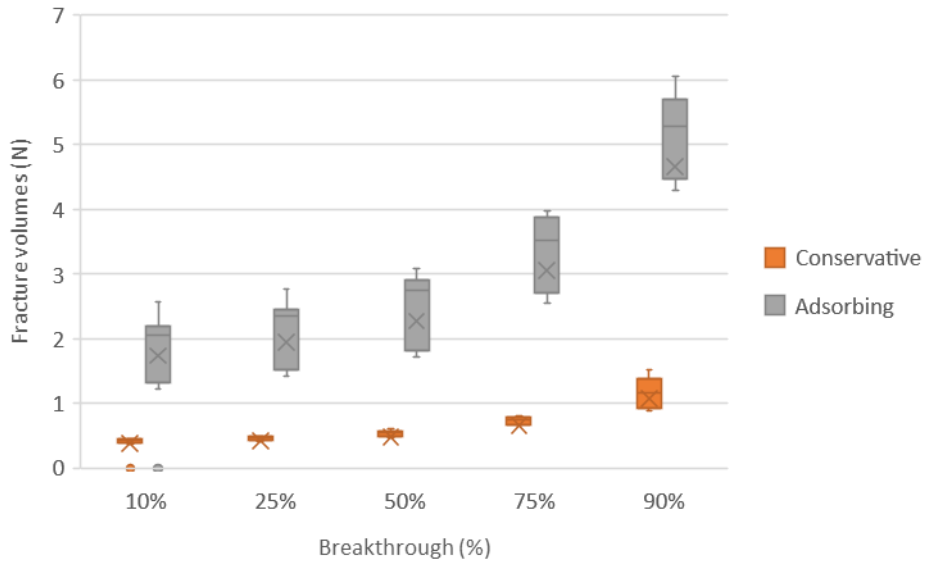
Figure 14. Box and whiskers plot of percentile breakthrough for the Stochastic Fractures benchmark.

2.2.3 Continuous Point Source Benchmark

The Continuous Point Source benchmark is a variant of the Stochastic Fractures benchmark. The difference is that the tracers are instead slowly introduced from a continuous point source as might happen for a slowly degrading waste form of a failed waste package (LaForce et al. 2023, Section 5.2.7). The point source is illustrated in Figure 15. Seven teams ran this problem using 9 different models, as summarized in Table 6.

Figure 16 shows the steady state water flux versus water volume in the fractures for the different models. Values are generally the same as the values in Figure 10. Figure 17 shows a snapshot of the conservative tracer in the deterministic fractures and in a vertical cross section of the ECPM after 0.5 year for the 7BGR-DE model.
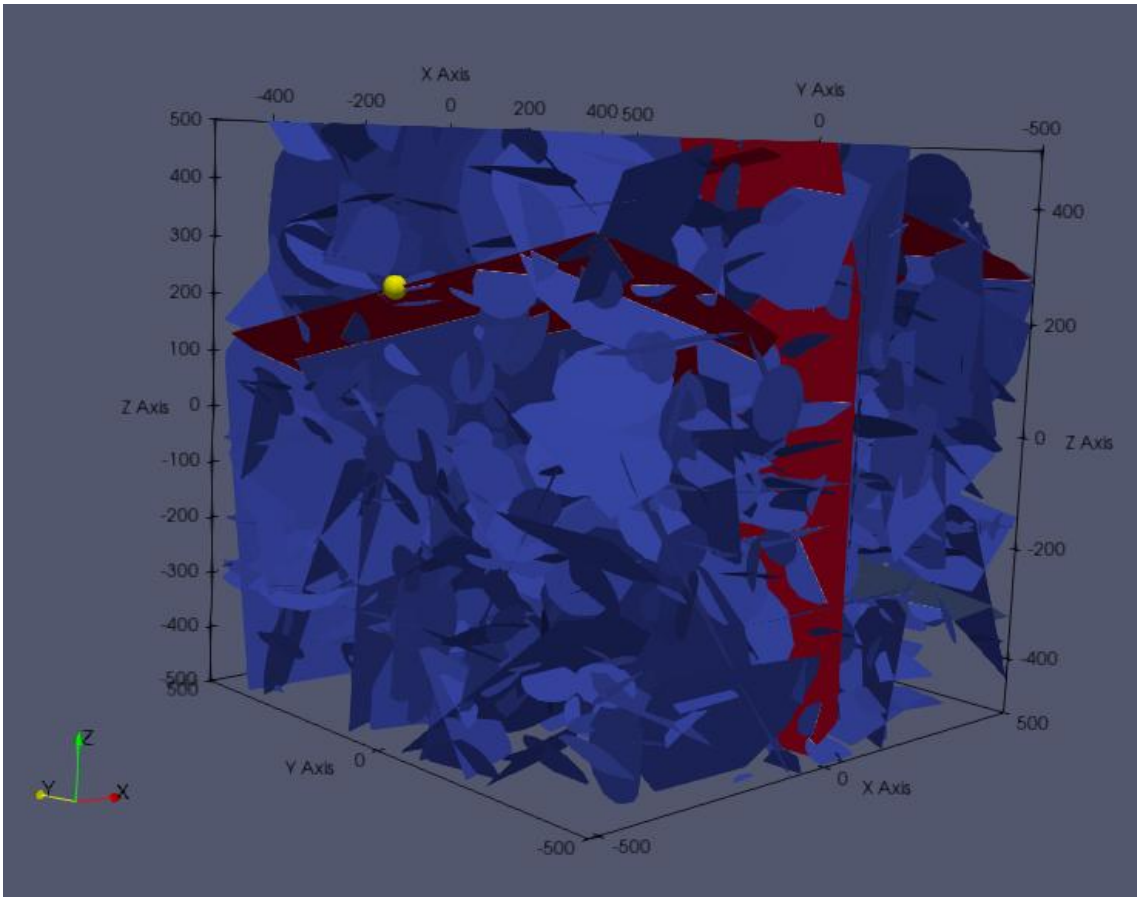
Figure 15. Continuous Point Source benchmark domain showing the point source location on the west boundary.
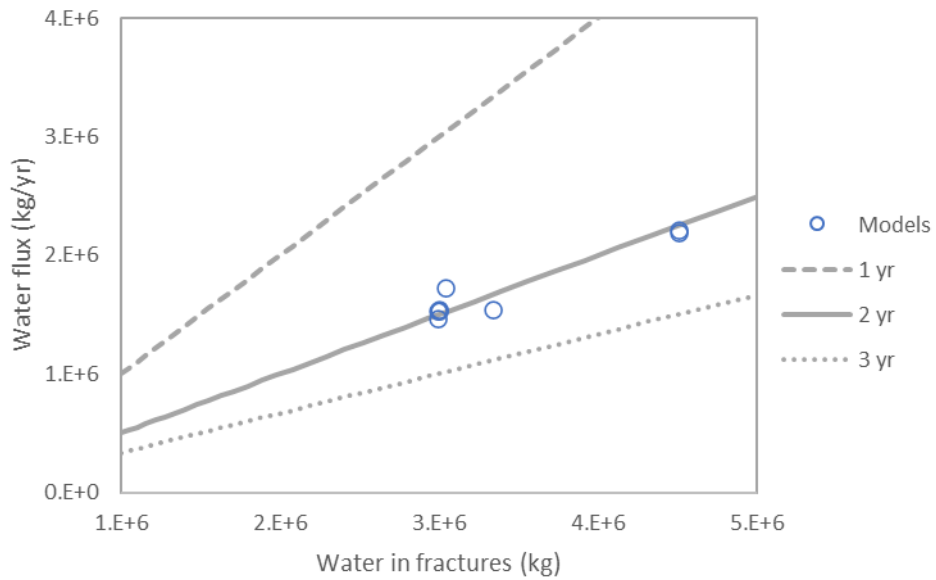
Figure 16. Water flux vs. water in fractures (circles) and mean fracture water residence times (lines) for the Continuous Point Source benchmark.
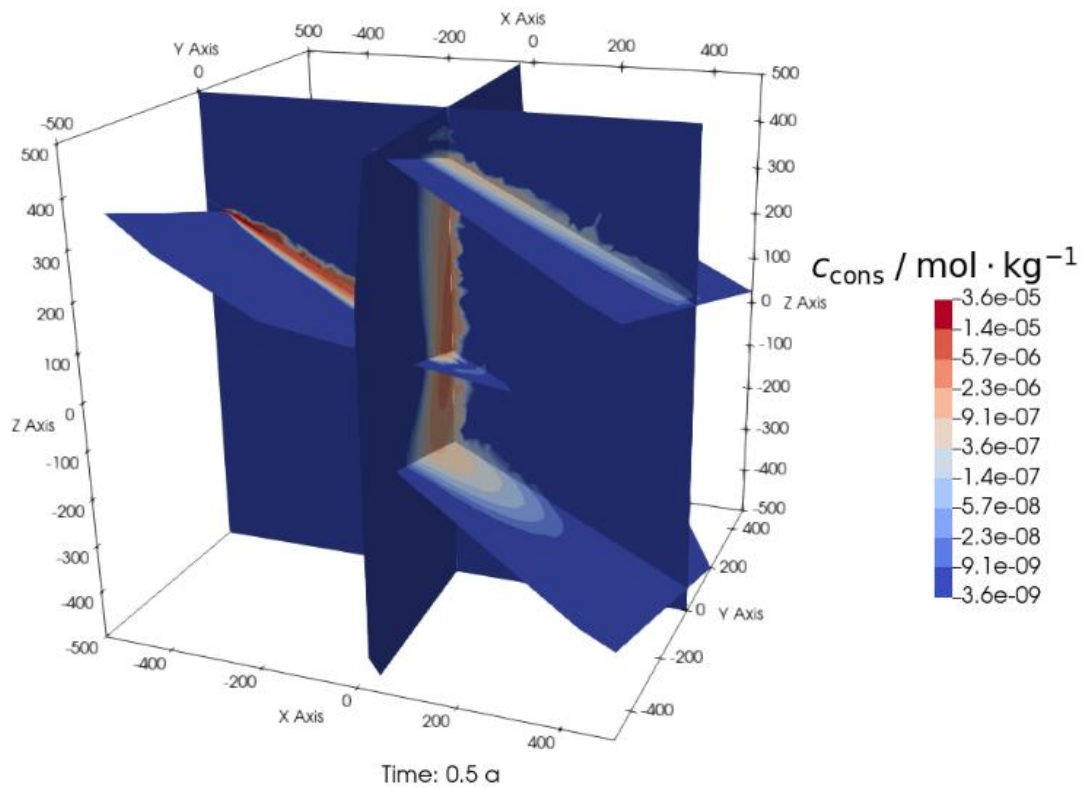
Figure 17. Calculated spatial distribution of the conservative tracer concentration for the 7BGR-DE model after 0.5 years for the Continuous Point Source benchmark.

Table 6. Software and solution methods for the Continuous Point Source benchmark.

Simulation	Software	Solution Method	Boundary & Initial Conditions	Special Considerations
7BGR-DEA	FracMan OpenGeoSys Version 6	Finite element (13,678 triangles for fractures, 226,614 tetrahedrons for matrix) DFN: 4 fractures ECPM: matrix ADE	Zero-concentration boundary condition for inflow/outflow Nodal source term with constant rate of 1 mole/year for mesh node at (-500, 4.54, 248.87)	Domain and fracture are extended by 50 m at inflow such that injection location is away from boundary
7CSNC-DEA	COMSOL Version 5.6	Finite element (20,754 2D triangles for deterministic, fractures, 386,791 tetrahedrons for matrix) DFN: 4 fractures ECPM: matrix ADE	Zero-gradient transport for inflow/outflow boundaries Gaussian pulse with peak at 0.05 years and standard deviation 0.015, along the deterministic fracture inflow boundary at Y coordinate midplane	Matrix diffusion included
7NARI-EP	DarcyTools Version 4.1.35 GoldSim Version 11.1	Finite volume (4,505,600 hexahedrons) ECPM: Full domain Particle tracking Laplace transform to solve ADE in Pipe pathway in GoldSim	9,801 particles injected on the west face of the inlet fracture at time = 0, the center of which is (-497, 7, 248.25) with side length 0.2 m Zero-gradient transport for inflow/outflow boundaries	Particle tracking was used to estimate flow-related transport parameters for the Pipe pathway in GoldSim
7KAERI-DA	COMSOL Version 6.1	Finite element (183,367 elements including 163,391 2D triangles) DFN: All fractures ADE	Boundary condition: Concentration constraint Concentration: 0.1 mol/m^3	Mass is continuously injected through edge with a length of ~0.1 m (Mass cannot be injected through a point in 3D model of COMSOL) Boundary layer mesh is applied to measure the concentration more precisely at inlet/outlet boundaries

7KAERI-DEA	COMSOL Version 6.1	Finite element (380,977 elements including 359,809 tetrahedrons, 20,970 2D triangles) DFN: 4 fractures ECPM: matrix ADE	Boundary condition: Concentration constraint Concentration: 0.1 mol/m^3	Mass is continuously injected through edge with a length of ~0.1 m Boundary layer mesh is applied to measure the concentration more precisely at inlet/outlet boundaries
7SNL-DA	dfnWorks PFLOTRAN Version 4	Finite volume (4,647,375 triangles) DFN: All fractures ADE	Zero-gradient transport for inflow/outflow boundaries Source/sink at point source location to steadily micro-titrate highly concentrated tracer solution into cell	
7SNL-EAS	dfnWorks mapdfn.py PFLOTRAN Version 4	Finite volume (1,250,000 orthogonal hexahedrons, 49,685 active) ECPM: Full domain ADE with stairstep correction	Zero-gradient transport for inflow/outflow boundaries Source/sink at point source location to steadily micro-titrate highly concentrated tracer solution into cell	Stairstep correction is applied to equivalent permeabilities. Cells not intersected by a fracture are inactive.
7SSMUU-DA	dfnWorks COMSOL Version 5.6	Finite element (439,977 triangles) DFN: All fractures ADE	Zero-gradient transport for inflow/outflow boundaries Continuous injection from a 5 m line source with the point (-500, 7.0, 248.25) located at the midpoint of the line source	
7SURAO-EA	dfnWorks PFLOTRAN Version 4	Finite volume (64,000 orthogonal hexahedrons, 29,907 active) ECPM: Full domain ADE	Zero-gradient transport for inflow/outflow boundaries Mass is continuously introduced at 1 mol/m^3 concentration in the entire cell at the point location.	

Breakthrough results of the conservative tracer and adsorbing tracer are compared in Figure 18 and Figure 19. First and second moments calculated for the first 1000 years of these simulations are included in the legends. This benchmark often produced three major increases in eluting fluxes, i.e., at around -0.4, -0.2, and 0.5 in log10 fracture volumes. This is due to the splitting of the plume into three major transport pathways that exhibit different mean residence times. The mean residence time of water in the full domain is approximately 2 years for each model, as indicated in Figure 16.

The behaviour of the narrower plume of this benchmark causes significant differences between model breakthrough curves. Small differences in the exact point source location occur due to different size meshes, but such differences do not explain some of the differences in breakthrough curves such as the strong initial breakthrough of 7NARI-EP and the smoothness in the curves and the larger first moments observed for 7CSNC-DEA and 7SSM-UU-DA. Notably, matrix diffusion is included in the 7CSNC-DEA model. The dispersion effect observed for the 7SSM-UU-DA model is under investigation; it is thought to be associated with the choice of mesh size and time stepping.

The 7NARI-EP model upscales the entire domain to an ECPM, as do the 7SNL-EAS and 7SURAO-EA models. What sets it apart is that it uses particle tracking. The higher release rate of the 7NARI-EP model at early time is thought to be a result of determining each particle's velocity inside the cells by interpolation, taking into account factors including the particle's position, the flow rate at the cell boundary, and the available cell volume. When implementing this approach (using DarcyTools), if particles are evenly distributed within a single cell, their trajectory differences are relatively small because of the similarity of their initial positions and conditions. DarcyTools provides an alternative approach to particle tracking that determines the cell wall the particles exit based on a likelihood that is directly proportional to the flux values. Adopting this alternative method may lead to improved results.

Figure 20 compares percentile breakthroughs for the conservative and adsorbing tracers across all models. As in the case of the Stochastic Fractures benchmark, the percentiles for the conservative tracer agree well among models, especially through the 75th. Also, as in the Stochastic Fractures benchmark, the percentiles for the adsorbing tracer show considerably more variation than those of the conservative tracer. Moments are considered further in Section 2.2.4.
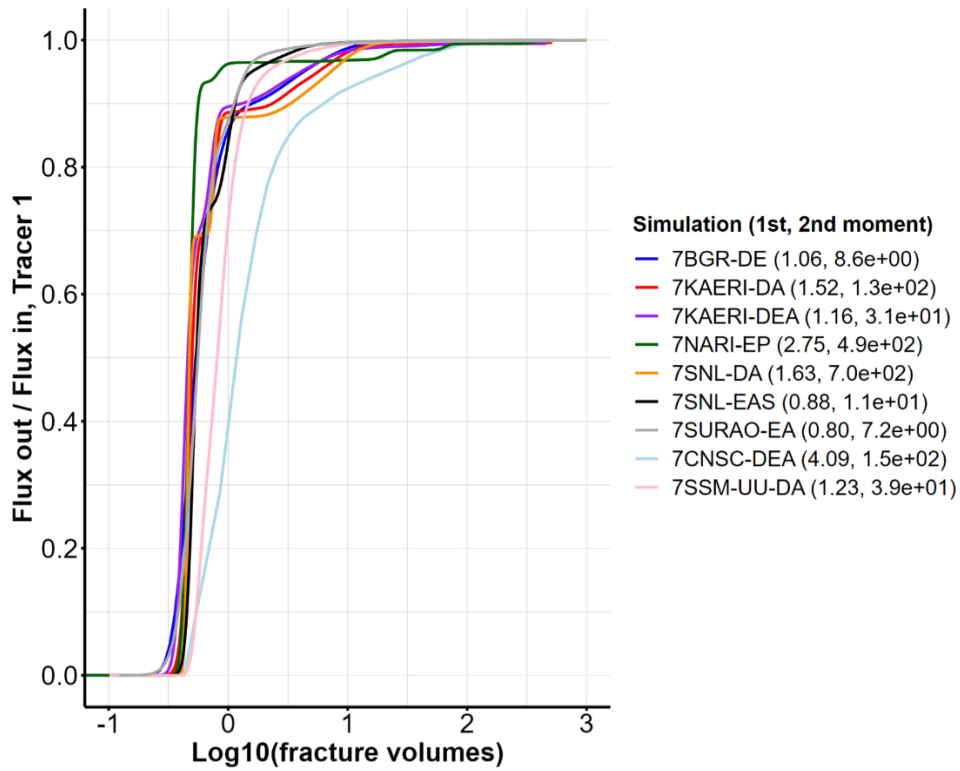
Figure 18. Continuous Point Source benchmark ratio of flux out to flux in for the conservative tracer.
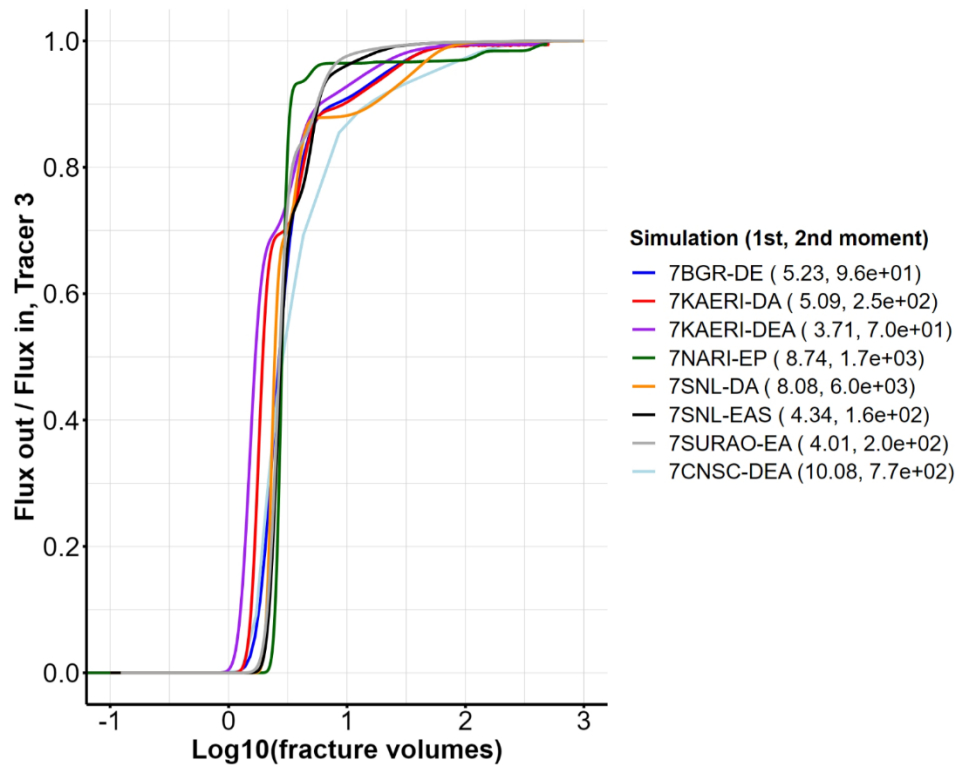
Figure 19. Continuous Point Source benchmark ratio of flux out to flux in for the adsorbing tracer.
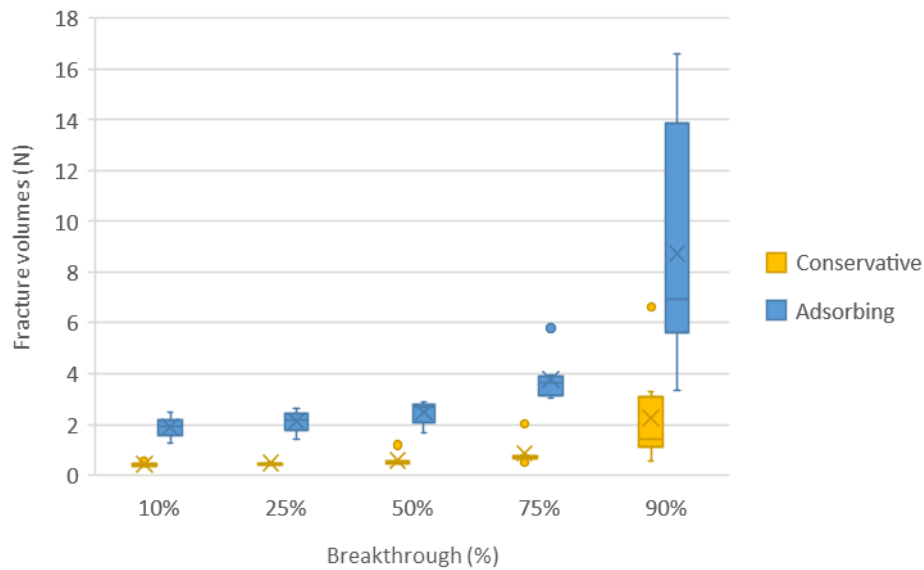
Figure 20. Box and whiskers plot of percentile breakthrough for the Continuous Point Source benchmark.

2.2.4 Moment Analysis for Fracture Network Benchmarks

Moment analysis provides quantitative comparison of breakthrough curves. Moment calculations are helpful for verification analyses, and they can help reveal important nuances of model choices and assumptions.

The first moment measures the expected or mean travel time. In this work, it is calculated by integrating the area to the left of the cumulative solute breakthrough curve. The second moment measures the observed variance from the expected travel time. It is calculated by summing the squared differences between the actual breakthrough times of solute percentiles and the first moment. The second moment is a measure of the spread of a breakthrough curve about the first moment. For the moment calculations in this report, time is represented by fracture volumes, N (Section 2.2.1). Details of moment analysis and its application to transport in porous media can be found elsewhere (e.g., Yu et al. 1999).

The first and second moments measured for the conservative tracer for each of the 4-fracture domain benchmarks are compared in Figure 21 and Figure 22. Because not all simulations reach complete breakthrough (steady state) within the simulation times and the moment calculations can be strongly affected by long tails, moments are calculated in two ways in this analysis. The first way is by simulation time; the moments shown in the legends in the breakthrough curve figures in the previous sections use cut-off times

of 100 years for the 4 Fractures benchmark and 1,000 years for the Stochastic Fractures and Continuous Point Source benchmarks. The second way is by choosing a percentile cut-off such as the 99th percentile. The moment calculations for both approaches are compared in Figure 21 and Figure 22. Median breakthrough points are plotted in Figure 23.
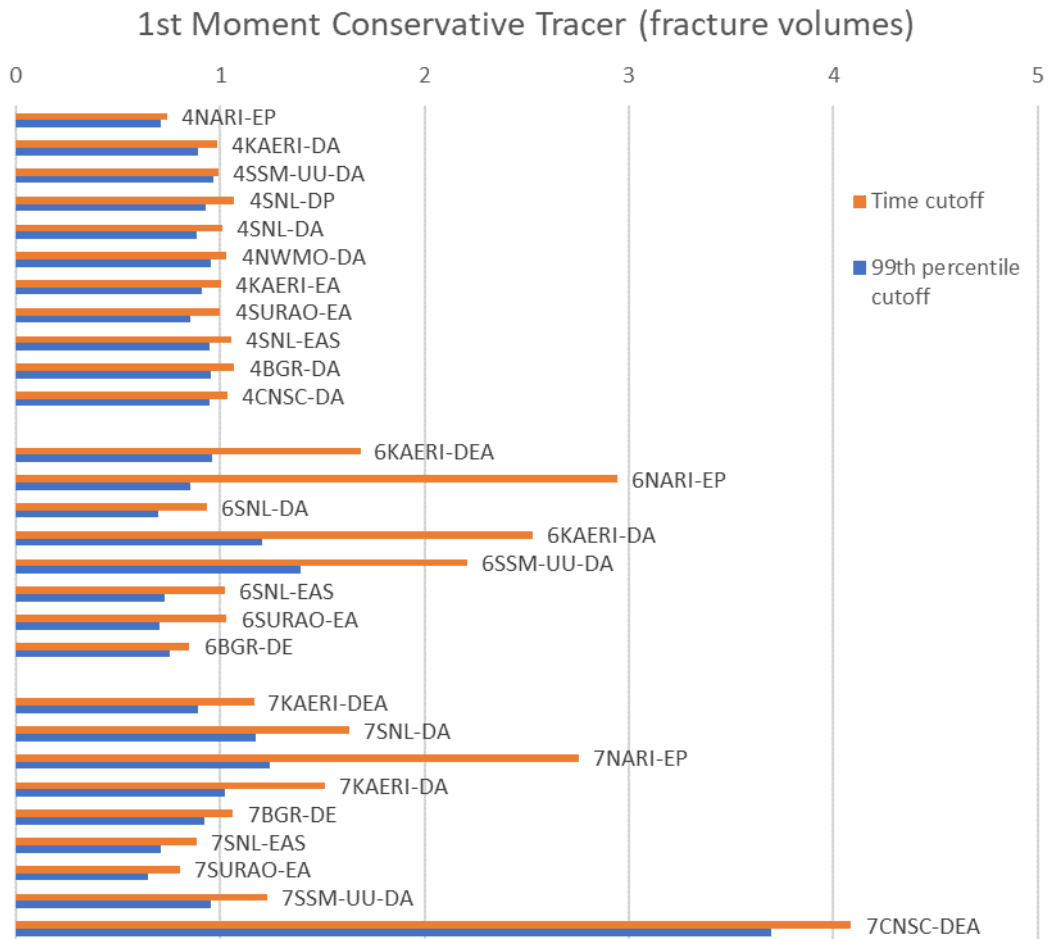
Figure 21. First moments of the conservative tracer for the 4 Fractures (top, 100 years), Stochastic Fractures (middle, 1000 years), and Continuous Point Source (bottom, 1000 years) benchmarks.
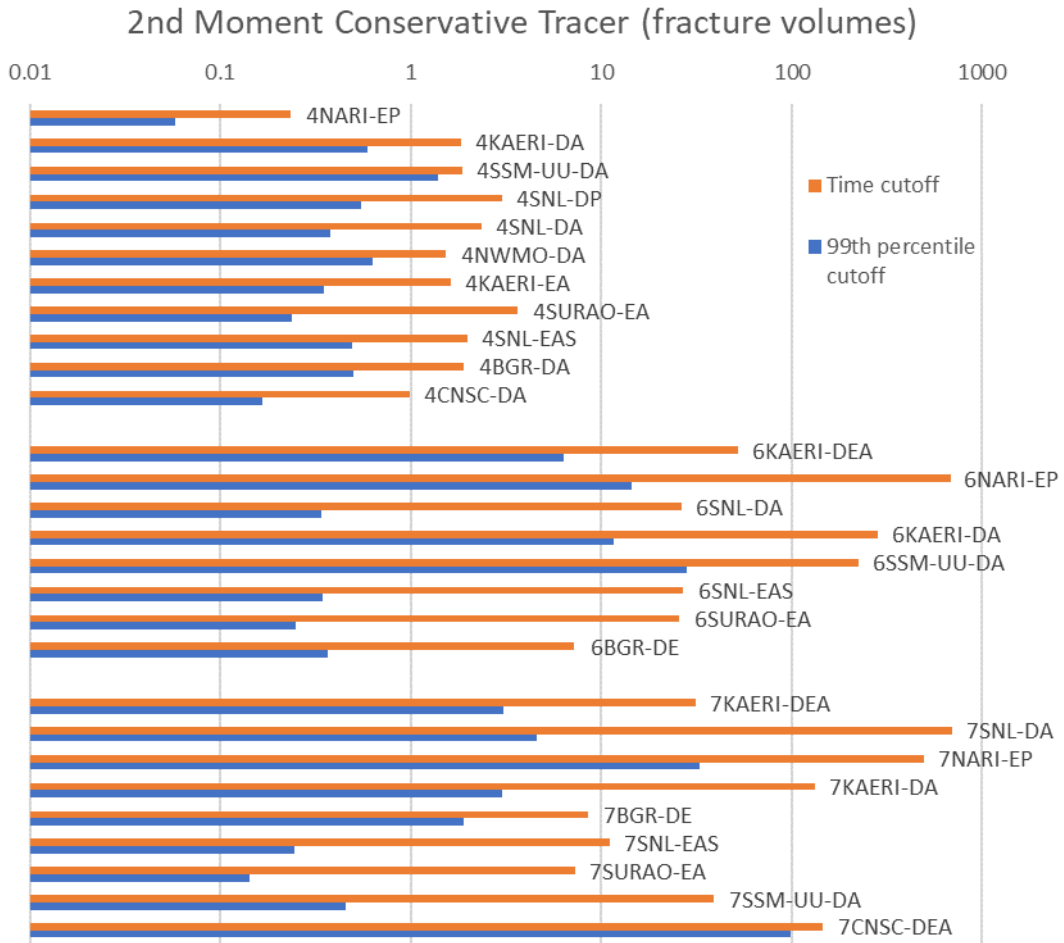
Figure 22. Second moments of the conservative tracer for the 4 Fractures (top, 100 years), Stochastic Fractures (middle, 1000 years), and Continuous Point Source (bottom, 1000 years) benchmarks.
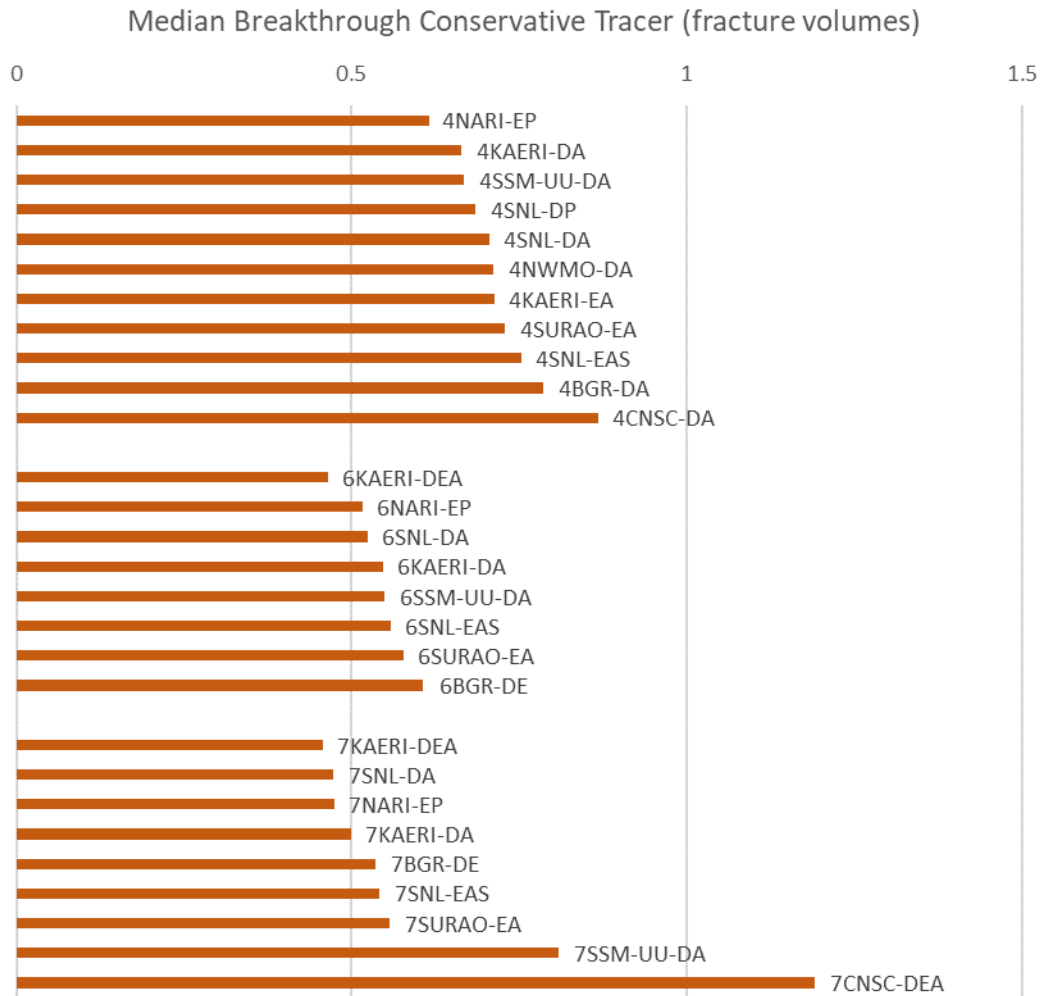
Figure 23. Median breakthrough of the conservative tracer for the 4 Fractures (top), Stochastic Fractures (middle), and Continuous Point Source (bottom) benchmarks.

The moments from the time cut-offs are larger than the 99th percentile cut-offs because the time cut-offs capture more tailing. Otherwise, both approaches indicate about the same variation among simulations. A cut-off at a higher percentile, e.g., 99.99%, might reduce variation among simulations by capturing more tailing, but not all simulations were run to such high percentile breakthroughs.

For the first moment, major departures from a value of 1 for the conservative tracer are not expected and may indicate an error in the model implementation or post-processing. Otherwise, values much larger than 1 (e.g., 7CNSC-DEA in Figure 21) suggest that a large amount of tracer is finding its way into dead-ends or slowly flowing fracture void space (or the rock matrix in this case), but how a large portion of the tracer could enter low flow areas is unclear. With flux-based injection of tracer, as specified for the 4 Fracture and Stochastic Fractures benchmarks, the vast majority of introduced tracer largely should begin in the deterministic fracture intersecting the west boundary where

the flows are relatively high. For the Continuous Point Source benchmark, the point source is in a high flow section of the deterministic fracture where the fracture intersects the west boundary.

The larger first moments for the KAERI simulations for the benchmarks with stochastic fractures originate from mesh-dependent mass transport in COMSOL Multiphysics. For 6KAERI-DA and 7KAERI-DA, KAERI explicitly models the full set of both deterministic and stochastic fractures. The injected tracer predominantly transports through deterministic fractures; however, it is observed that the transport of tracers from deterministic fractures to stochastic fractures is overestimated due to the coarse mesh at the interface between deterministic and stochastic fractures, as illustrated in Figure 24. This results in a significantly extended time required to achieve a steady state, as shown in Figure 25. The use of a finer mesh (e.g., boundary layer mesh) at the interface between deterministic and stochastic fractures would have greatly reduced mass transport into stochastic fractures, resulting in first moment values closer to 1.

The second moments in Figure 22 are plotted on a log scale. They largely indicate how much tailing (i.e., added mean residence time experienced by a small fraction of the tracer) is occurring in the breakthrough curves.

There appears to be no definitive clustering of moments based on the types of models applied. DFN vs. ECPM models and ADE vs. particle tracking models each generate breakthrough curves that exhibit relatively high and low first and second moments.

The breakthrough curves of the adsorbing tracer show greater variation among models than the conservative tracers, as indicated in Figure 14 and Figure 20. Apparent retardation factors of the adsorbing tracer can be calculated by dividing its first moment by the first moment of the conservative tracer. These ratios are plotted in Figure 26 versus water flux. Complete breakthrough curves were used for Figure 26. The plot indicates that for several of the models (i.e., those by CNSC, KAERI, and NARI) the apparent retardation factors are considerably less than the value of 5 specified in the Task Specification. Examining these ratios provides useful feedback on whether adsorption is being simulated as intended.
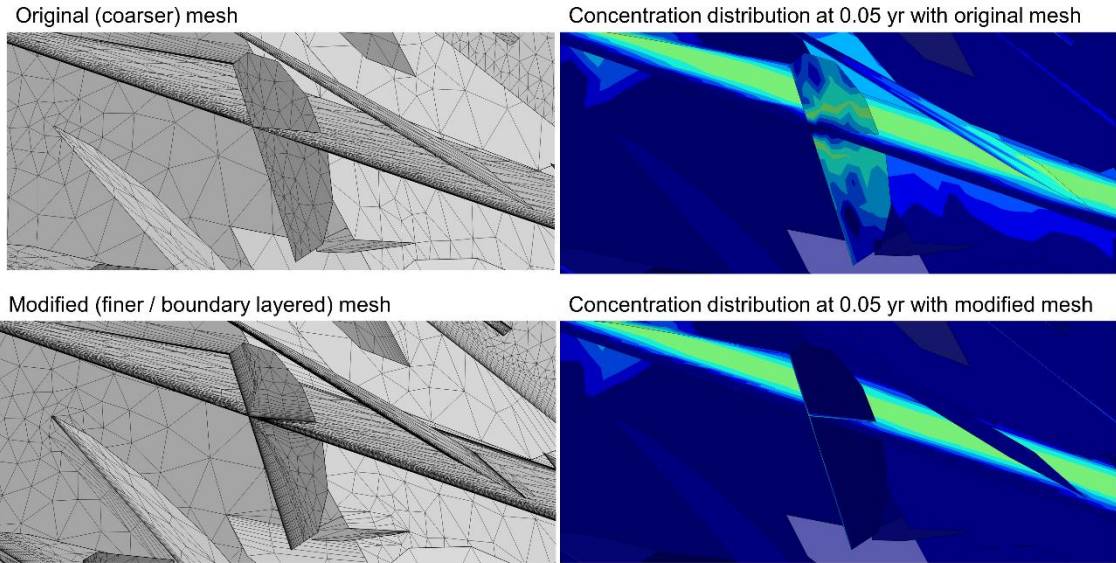
Figure 24. Meshes for 6KAERI-DA and 7KAERI-DA (left) and tracer concentrations at 0.05 yr near the intersections of one of the four deterministic fractures and multiple stochastic fractures for 6KAERI-DA (right) for the original coarser mesh (top) and the modified finer boundary-layered mesh (bottom).
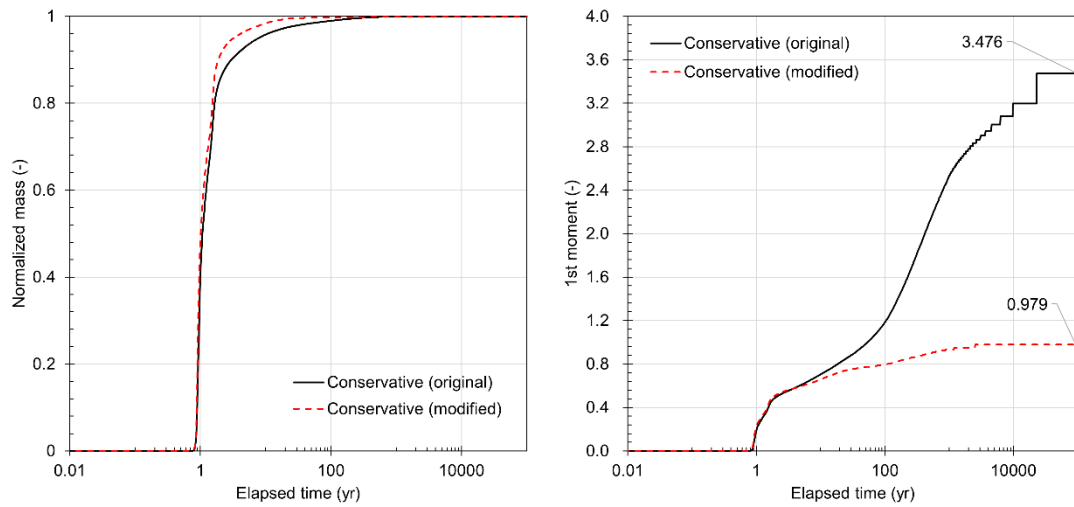
Figure 25. Comparison of 6KAERI-DA conservative tracer breakthrough curves for the original and refined meshes.
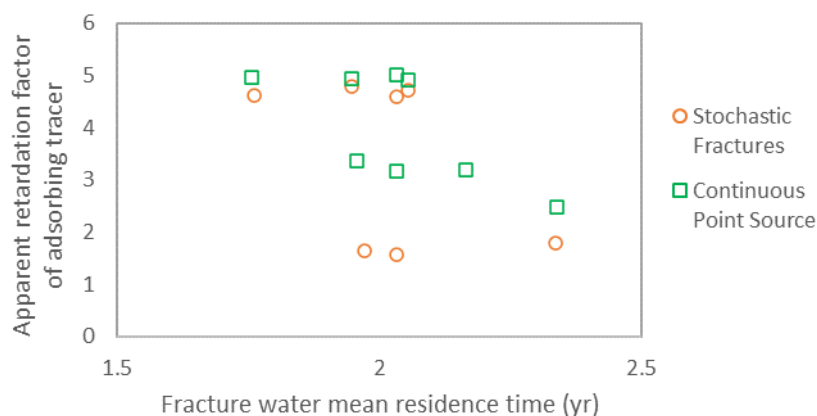
Figure 26. Apparent retardation factors of adsorbing tracers vs. fracture water mean residence time for Stochastic Fractures and Continuous Point Source benchmarks.

2.3 Radionuclide Source Term

The radionuclide source term for the reference case depends on rates of radioactive decay and ingrowth, the timing of waste package breach, and degradation properties of spent nuclear fuel (SNF). Depending on implementation, limitations on radionuclide solubility within the waste canister may be accounted for in the source term model or considered separately.

A source term benchmark problem was specified (LaForce et al. 2023, Section 5.3) to test the abilities of the models to simulate the following processes:

- Radioactive decay and ingrowth
- Waste package breach time
- Instant release fraction
- Fuel matrix degradation rate
- Solubility limitations

Three teams completed this benchmark; their methods are summarized in Table 7. Each team achieved the expected results with perfect or nearly perfect accuracy. The figures and results presented here are from the SNL team. Results of each team are included in the appendices of this report.

Table 7. Software and solution methods for the Radionuclide Source Term benchmark.

Team	Software	Numerical Method	Special Considerations
KAERI	Matlab	Matrix exponential	
NARI (INER)	GoldSim Version 11.1	Contaminant Transport Module	
SNL	PFLOTRAN Version 4	Isotope Partitioning module (UFD_DECAY)	This module currently involves sequential coupling, which requires smoothly increasing time steps for decay and ingrowth

Results of this benchmark are as follows:

- Activities of the radionuclides in the ^{245}Cm to ^{229}Th decay chain almost perfectly match the activities reported in Anttila (2005, Table 2.2.2.4) at 5, 30, 10^2, 10^3, 10^4, 10^5, and 10^6 years, as shown in Figure 27.

- Waste package breach occurs at 3,000 years causing an immediate release of 3% of the ^{99}Tc from the fuel as the waste package breaches, as indicated in Figure 28.

- The fuel matrix does not degrade before waste package breach and is calculated to be 64% degraded at one million years (Figure 28); the expected degradation is 63.1% (analytically, the fraction remaining is 36.9% calculated from $e^{-\lambda t}$ where λ is the degradation rate [10^{-6} yr^{-1}] and t is time since waste package failure). Radionuclide release from fuel degradation is confirmed to be congruent.

- Aqueous concentrations are limited by prescribed elemental solubility limits as indicated in Figure 29 by constant maximum aqueous (aq) concentrations and by the presence of precipitation (ppt).

This benchmark problem is expected to become more important as the teams develop the reference case by including more of the radionuclide inventory and more processes that affect radionuclide release and mobility.
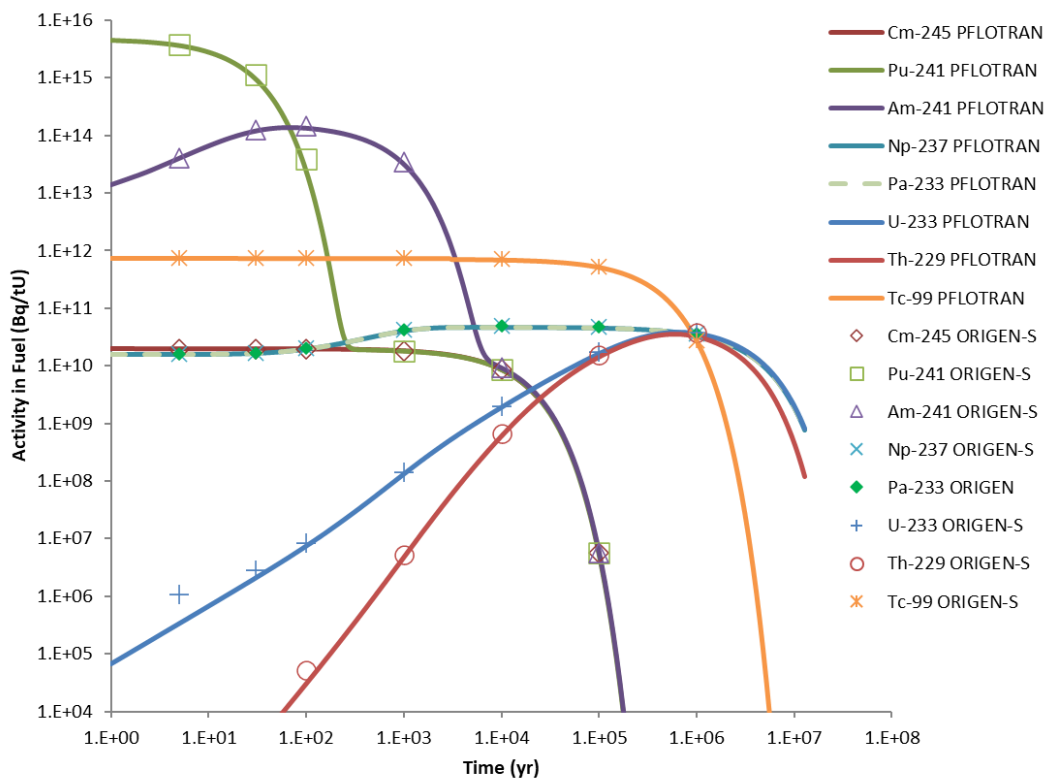
Figure 27. Calculated decay and ingrowth for the radionuclide source term benchmark (SNL) compared to ORIGEN-S calculations of Anttila (2005, Table 2.2.2.4).
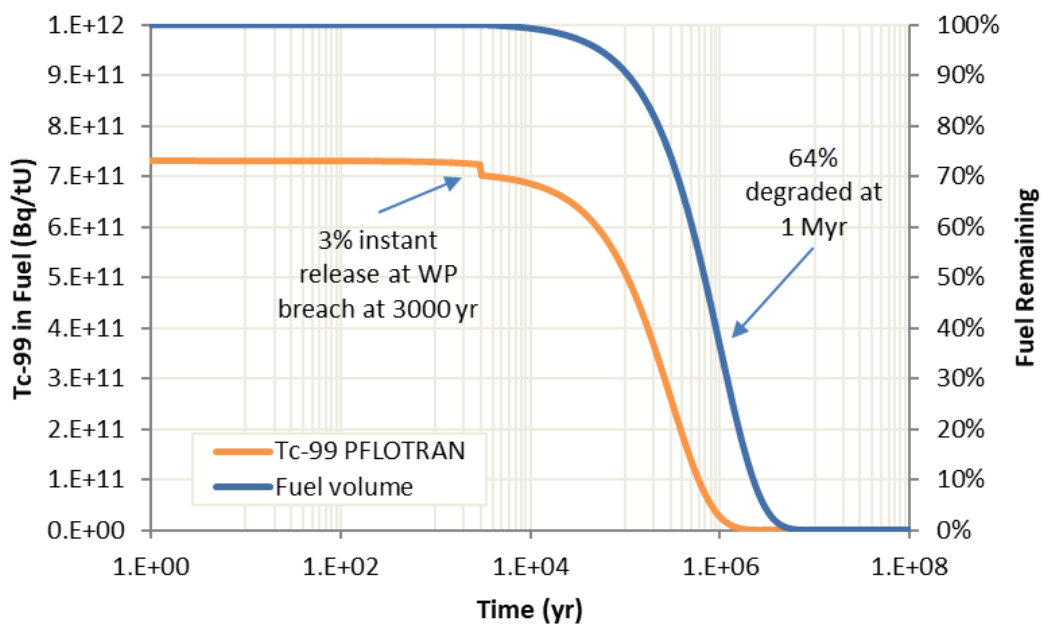
Figure 28. Calculated ^{99}Tc activity in the fuel and fuel volume remaining over time in the radionuclide source term benchmark (SNL).
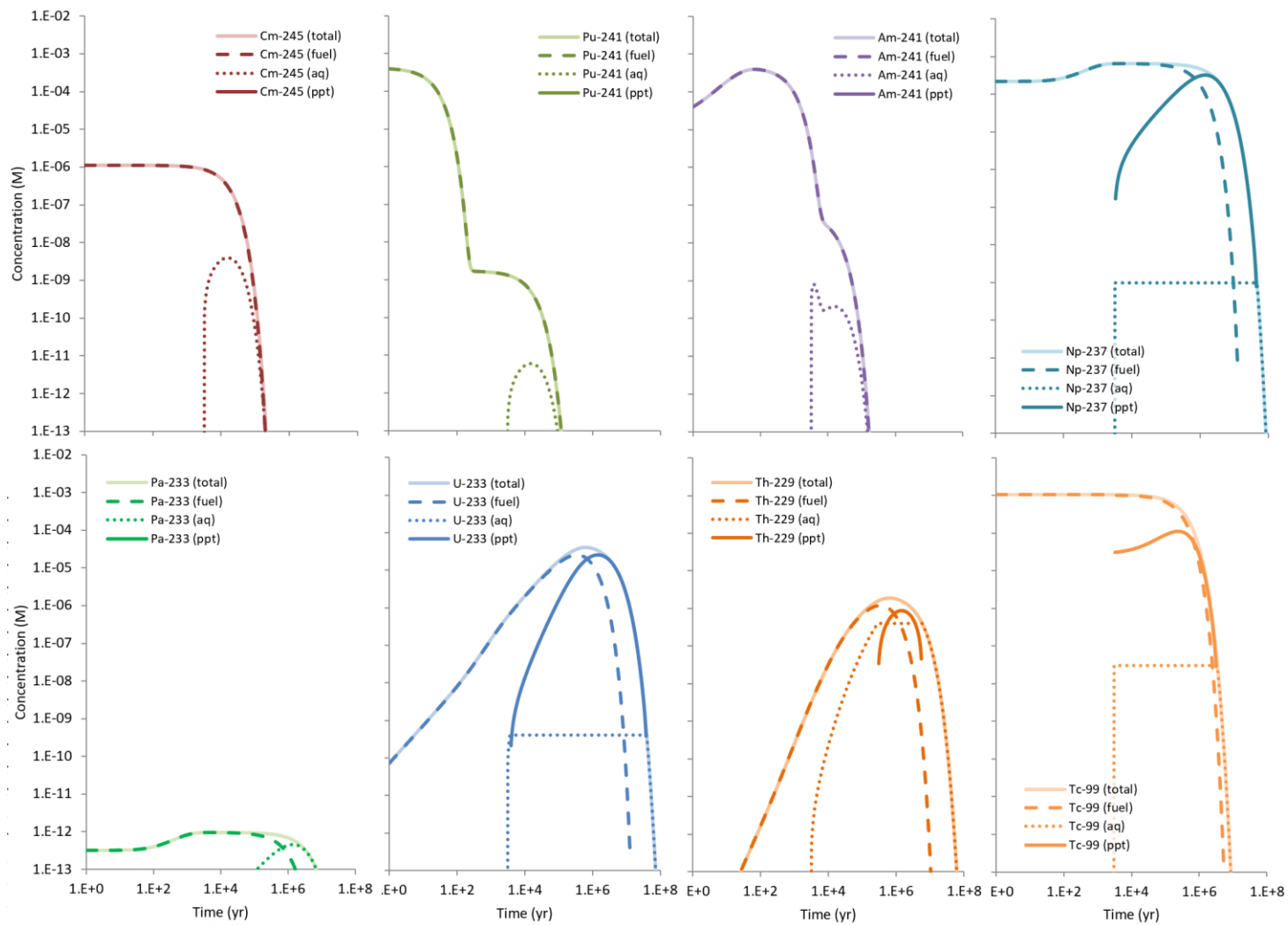
Figure 29. Calculated phase partitioning of radionuclide source term benchmark as affected by release and solubility limitations (SNL).

3 Crystalline Repository Reference Case

3.1 Crystalline Reference Case

The Task F1 reference case for a mined repository in fractured crystalline rock is defined in the Task Specification (La Force et al. 2023). An overview is given here. The reference case assumes steady state flow and transient transport of two conservative tracers upon simultaneous breach of all the canisters in the repository.

Geologic Setting: The reference case repository is located beneath a gently sloping hill in a domain 5 km in length, 2 km in width, and ~1 km in depth (Figure 30). The repository is located in the west (left) side of the domain, and the area of lowest elevation is located in the east (right) side of the domain. Surface elevation decreases 20 m over a distance of 2 km; it is assumed that the hydraulic pressure at the top surface of the domain mimics the topography. Conceptually, the area of lowest elevation represents the location where water would upwell at the surface forming a feature such as a lake or wetland; however, in this case, upward vertical flow out of the top layer is effectively swept away allowing no accumulation or dispersion of tracer in an overlying body of water with any potential feedback to the modelled domain.

Fracture intensity and fracture transmissivity decrease with depth. The decrease is implemented by assigning different parameter values to each depth zone (as given in the Task Specification, Section 3.7).
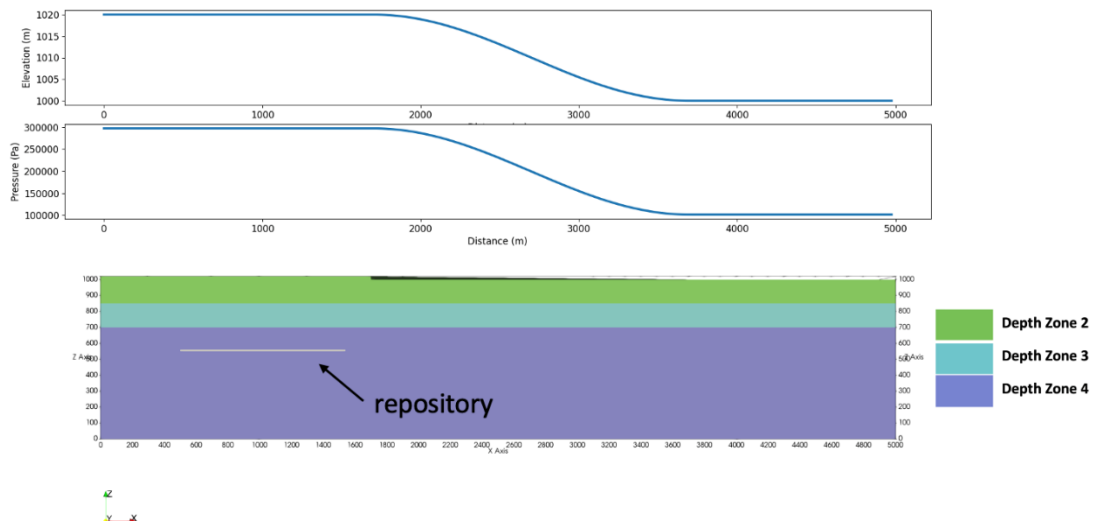
Figure 30. Elevation profile and corresponding pressure boundary condition (top) and depth zones in the domain (bottom).

Emplacement Concept and Repository Layout: The generic reference case uses the KBS-3V emplacement concept developed for the Swedish and Finnish repository programs (Pettersson and Lönnerberg 2008) and adopted by several countries as the reference design for a generic reference case or in the preliminary stages of site investigation (TPC 2017; Choi et al. 2013; NWMO 2012). The KBS-3V concept is developed for a repository mined at a depth of approximately 500 m in sparsely fractured crystalline rock. Copper canisters each containing a nominal inventory of 4 pressurized water reactor (PWR) assemblies are emplaced within rings of compacted bentonite in vertical deposition holes beneath the floor of a deposition tunnel, and tunnels are backfilled.

The waste inventory is 4,350 metric tons uranium (MTU) in the form of PWR SNF. Assuming each PWR assembly contains 0.435 MTU, 2500 4-PWR canisters are required to dispose of the inventory. The waste inventory is deliberately small to reduce the computational burden of simulations.

The repository, located at a depth of approximately 450 m, comprises 50 deposition drifts branching off two parallel access tunnels (Figure 31). The deposition drifts are spaced 40 m center-to-center; 50 deposition holes within each tunnel are spaced 6 m center-to-center. This spacing ensures that peak buffer temperatures do not exceed 100 ºC (Pettersson and Lönnerberg 2008). The deposition drifts are 306 m in length so that the deposition tunnel extends 6 m beyond the center of the last deposition hole at both ends. There are 50 individual deposition drifts which results in a total of 2,500 deposition boreholes.

Dimensions and properties of the features of the repository (i.e., the engineered barrier system) are given in the Task Specification, Section 3.5.
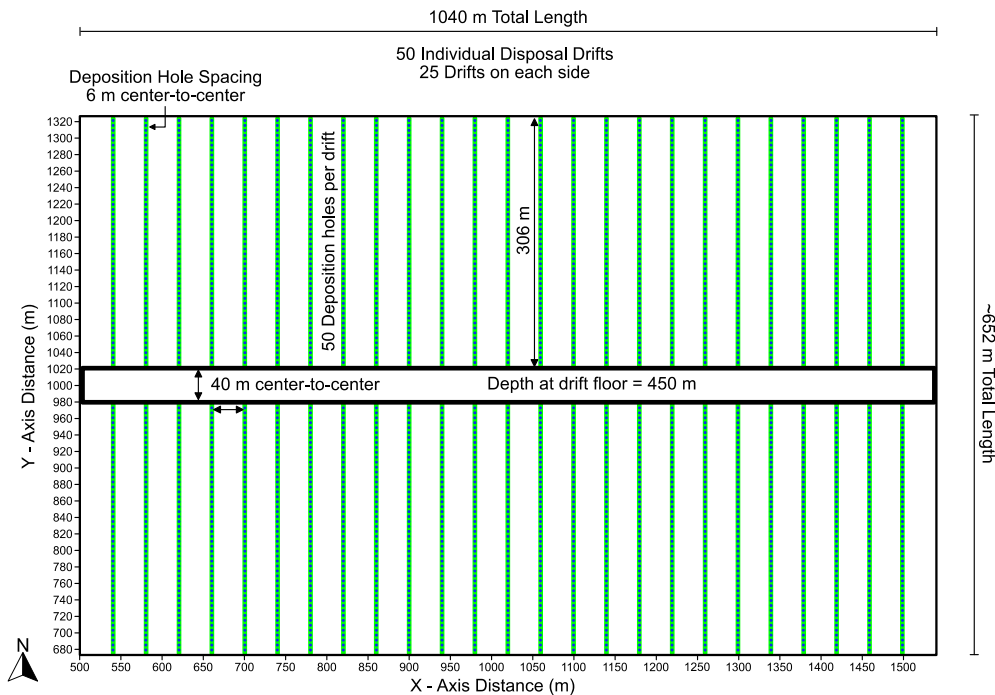
Figure 31. Repository layout for the crystalline reference case. (Black outline around the repository is not a tunnel.)

Host Rock (Natural Barrier System): The crystalline host rock is characterized by occurrence of large-scale, highly fractured brittle deformation zones and intervening masses of competent rock containing sparse networks of connected fractures. Following the example of SKB (e.g., Joyce et al. 2010), the former are named Hydraulic Conductor Domains (HCD) and the latter are named Hydraulic Rock Mass Domains (HRD).

The fractures within the HRD are subdivided into three different depth zones, representing vertical variations within the subsurface. Each depth zone contains three different fracture families, representing variations in orientation (strike and dip, or equivalently, trend and plunge) and hydraulic properties.

Conceptually, present-day properties such as transmissivity of individual fractures exhibit a dependence on the present-day stress field. As a result, there is a greater density of fractures, larger proportion of sub-horizontal fractures, and higher fracture transmissivity at shallower depths, and lower density of fractures, lower proportion of sub-horizontal fractures, and lower fracture transmissivity at greater depths.

The HCD and HRD are described in more detail in the Task Specification (LaForce et al. 2023, Section 3.7). The HCD are treated as deterministic features, i.e., their geometry and properties are the same in all realizations of reference case simulations (Figure 32). Fractures within the HRD are treated as stochastic features, i.e., multiple realizations of

the fractured rock mass are generated by sampling probability distributions for fracture radius, fracture orientation, and fracture location (Figure 33).
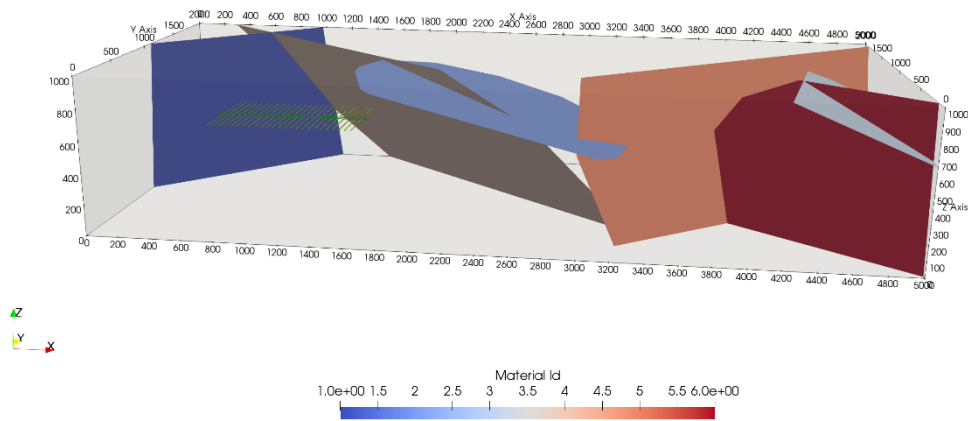
Figure 32. Deterministic fractures (representing HCD) in the model domain.
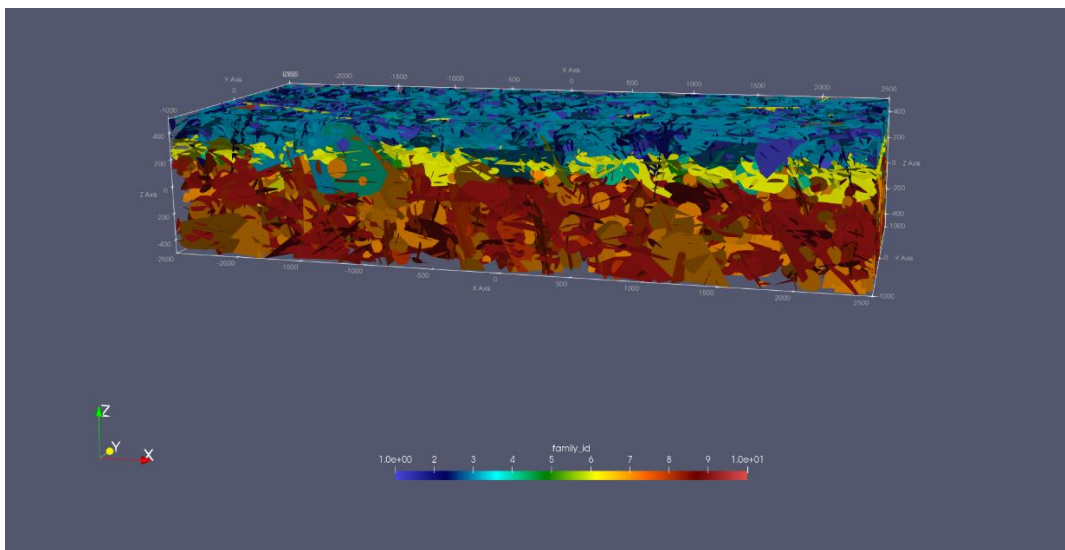
Figure 33. One realization of the stochastic fractures, coloured by fracture family. Depth zones correspond to different colours.

Conservative Tracer Transport: In the first iteration of the reference case, teams modelled steady state flow and conservative transport of two tracers. Tracer 1 and Tracer 2 are like [129]I but they do not undergo radioactive decay. Both have an atomic weight of 128.9 g/mol. The total inventory of the two tracers in each waste package is 5.45 g (0.0423 moles), equivalent to 1/100th of the expected inventory of [129]I in a waste package containing 4 PWR assemblies. The inventory of Tracer 1 is 0.545 g (0.00423 moles), or 10% of the total; it is instantly released at the start of the transport simulation.

The inventory of Tracer 2 is 4.90 g (0.038 moles), or 90% of the total; it is released at a fractional rate of 10^{-7}/y throughout the transport simulation.

Teams first established a steady state flow solution using a constant pressure (Dirichlet) boundary condition at the top surface of the domain and no flow boundary conditions at all other faces of the domain. Then, they simulated steady-state flow for 100,000 years. Initially the domain is empty of tracer everywhere except in the waste packages. Tracer is allowed to advect out of the domain at the top surface; zero gradient boundary conditions are applied to prevent diffusion out of the domain.

Output Metrics for Comparison: Teams ran 10 realizations of the preliminary reference case, varying the network of stochastic fractures. They either used fracture realizations provided by SNL or their own based on probability distributions given in the Task Specification. Output metrics for comparison focus on tracer transport across the top surface of the model domain. They include integrating tracer mass flows across specified areas (the area of the hillslope and the area of lowest elevation) and locating the greatest tracer mass flow within a specified area (both hillslope and area of lowest elevation). Additional metrics are given in Section 3.3.

3.2 Team Approaches

Seven teams implemented simulations of the reference case: CNSC, BGR, KAERI, NARI (for TPC), SNL (with LANL for DOE), SÚRAO, and SSM-UU. Their approaches are summarized in Table 8.

All 7 teams upscaled the stochastic fracture network to an ECPM. Those using finite element simulators (CNSC, BGR, KAERI, SSM-UU) embedded the deterministic features (HCD) as 2-D planes or thin volume elements in a 3-D tetrahedron mesh populated with the upscaled properties of the ECPM. Those using finite volume simulators (NARI, SNL, SÚRAO) included the deterministic features in upscaling to an ECPM that is mapped to an unstructured or structured mesh composed primarily of regular hexahedrons (cubes).

Most teams solved for tracer transport in the 3-D model domain using a Eulerian reference frame (the advection-dispersion equation). NARI first used particle tracking in the 3-D domain to identify particle paths between each deposition hole and the surface of the model domain, then used GoldSim pipe elements to simulate transport along each path.

Representation of the engineered barrier system and the tracer source term varies among teams:

- CNSC implemented a single deposition hole model to calculate tracer flux across the bentonite/rock interface. Outputs from this model provide the tracer source term for transport calculations in the larger model domain. The deposition hole model accounts for engineered barriers and their properties.

- BGR modelled the repository as a box-shaped, finely discretized interior volume within the reference case model domain. For each canister a dedicated node is defined within the mesh where the tracer is introduced as a nodal source term; engineered barriers and their properties have not yet been considered and the medium of the box is simulated as fractured rock.

- KAERI used grid refinement to represent access tunnels, emplacement drifts, and deposition holes in the reference case model domain. The near field and the far field are coupled together using the "Identity mapping" function in COMSOL.

- NARI used grid refinement to represent access tunnels, emplacement drifts, and deposition holes in the reference case model domain, allowing precise placement of a particle in each deposition hole location. For each transport calculation in GoldSim, the tracer source term is released into a cell element having the volume of a canister.

- SNL used grid refinement to represent access tunnels, emplacement drifts, and deposition holes in the reference case model domain; these features are assigned properties corresponding to the appropriate engineered materials (backfill, buffer, canister). The tracer source term is released into the grid cells corresponding to the canister.

- SÚRAO upscaled waste package material properties so there are exactly 5 waste packages included in a cell. The source term is implemented using a custom Reaction Sandbox implementation in PFLOTRAN, modelling the flux from the immobile phase into the mobile one (representing the radionuclide flux from the deposition hole into the rock). A new reactive mineral was introduced to model the fractional dissolution rate.

- SSM-UU modelled the repository as two rectangular boxes representing the tunnels and deposition holes and upscaled based on the properties specified in the task specification. The dimensions of the tunnel box are 1050 x 660 x 30 m and the dimensions of the deposition holes box are 1050 x 660 x 15 m. Tracers are released from the surface of the repository box representing the deposition holes with an area averaged to the area of all 2500 deposition holes.

More information is given in the appendices:

- Appendix A: BGR
- Appendix B: CNSC
- Appendix C: KAERI
- Appendix D: NARI
- Appendix E: SNL
- Appendix F: SÚRAO
- Appendix G: SSM-UU

Table 8. Software and solution methods applied to reference case simulations.

Team	Software	Natural Barrier System Solution Method	Engineered Barrier System Solution Method	Special Considerations
CNSC	COMSOL Version 5.6 (Finite element)	DFN+ECPM with ADE Finite element mesh that embeds 2-D discrete fractures representing the HCD into a 3-D upscaled porous medium representing the HRD.	The near field model is separated from the far field model. The mass flux of tracers across the EBS to the host rock was computed for each emplacement room and used a source term to interface with far field model.	
BGR	FracMan for fracture generation and upscaling OpenGeoSys version 6 (Finite element)	DFN+ECPM with ADE The HCD are meshed using 2-D surface elements while the stochastic fracture network (HRD) is represented via upscaling, e.g., using Oda's method for permeability.	The repository is represented as a box within the model domain which is parameterized as fractured rock. For each canister there is one dedicated mesh node where the tracers are introduced.	The upscaled properties from the regular mesh produced by FracMan are further mapped to the unstructured tetrahedral volume mesh. No repository features were modelled.

KAERI	FracMan COMSOL Version 6.0 (Finite element)	ECPM with ADE using a tetrahedral mesh Upscaling conducted by KAERI using an in-house code using Oda's method. Uniform grid size set to 50 m.	Near field and far field coupled using "Identity Mapping" function in COMSOL. Maximum mesh size set to 1 m for the waste package, 1 m for the buffer, and 5 m for the backfill.	Artificial diffusion added to solve model convergence issues in COMSOL.
NARI	Flow: DarcyTools Version 4.1.35 (Finite volume)	ECPM A discretization length of 8 m is applied around (upscaled) fractures.	Layout created using SketchUp. A discretization length of 1 x 1 x 1 m was globally applied in the repository, a discretization length of 0.25 x 0.25 x 0.50 m was applied around deposition holes.	
	Mass Transport: DarcyTools Version 4.1.35	Particle tracking	One particle is introduced in each deposition hole, resulting in 2,500 particle paths.	Obtain two near-field parameters and three far-field parameters for each particle
	Mass Transport: GoldSim Version 11.1	Pipe element Laplace transform to solve ADE	Near field models based on conditions of deposition hole; deposition holes without a fracture intersecting and deposition holes with a fracture intersecting.	2,500 GoldSim realizations are carried out, one for each particle path. Goldsim results are summed to calculate output metrics.
SNL/DOE	dfnWorks, mapdfn.py PFLOTRAN (Finite volume)	ECPM with ADE Two different grids with two different far field discretization lengths are used: 20 m and 25 m.	Disposal drifts and deposition boreholes are represented in the model through grid refinement and assignment of material properties. Dimensions approximate but do not equal nominal dimensions.	Mapdfn.py is used to upscale to a uniform hexahedron mesh. A stairstep correction is applied to equivalent permeabilities. All cells are active.

SÚRAO	dfnWorks, mapdfn.py PFLOTRAN (Finite volume)	ECPM with ADE Discretized into 20 x 30 x 25 m cells (domain is 10 m longer in the Y direction)	Upscaled where 5 waste packages included in a single cell. Tracer source and near field integrated into one system based on buffer parameters and concentrations in rock and waste package. The canister shell and backfill are not modelled.	Radionuclide source modelled via custom Reaction Sandbox module in PFLOTRAN which models flux from immobile phase into mobile one (represents the radionuclide flux from deposition hole into the rock).
SSM-UU	dfnWorks COMSOL (Finite element)	Finite element mesh that embeds 2-D discrete fractures representing the HCD into a 3-D upscaled porous medium representing an unfractured rock matrix.	Two rectangular boxes for tunnels (backfill) and deposition holes (buffer). Upscaled based on material properties in task specification to get a value of 9.79e-19 m^2 for the tunnels and 9.95e-19 m^2 for the deposition holes.	

3.3   Results

Conceptually, the reference case considers two pathways by which a person could ingest radionuclides. The first is by drinking water from a well located at the end of the highest consequence path between the repository and the surface of the hillslope (1700 m < x < 3700 m). The second is by drinking water from the hypothetical body of water resting on the area of lowest elevation (3700 m < x < 5000 m). The following outputs for comparison are designed with these two ingestion pathways in mind. Means and 95% confidence intervals of the means are calculated from the 10 realizations for each output and shown on plots.

1. Steady state flow of water (kg/year) into and out of the top surface of the domain over the area where 0 m < x < 1700 m (high point).

2. Steady state flow of water (kg/year) into and out of the top surface of the domain over the area where 1700 m < x < 3700 m (hillslope).

3. Steady state flow of water (kg/year) into and out of the top surface of the domain over the area where 3700 m < x < 5000 m (low point).

4. The inventory (moles) of each tracer in the repository region as a function of time (years). The repository region is defined as the tightest hexahedron

encompassing all drifts, access tunnels, and deposition holes; thus, it includes the host rock that falls within the hexahedron.

5. Over the surface area of the hillslope (1700 m < x < 3700 m):

    a. Mass flow (moles/year) of each tracer across the top surface of the domain as a function of time (years).

    b. Cumulative mass flow (moles) of each tracer across the top surface of the domain as a function of time (years).

6. Over the surface area of low point (3700 m < x < 5000 m):

    a. Mass flow (moles/year) of each tracer across the top surface of the domain as a function of time (years).

    b. Cumulative mass flow (moles) of each tracer across the top surface as a function of time (years).

7. At the cell location on the surface of the hillslope (1700 m < x < 3700 m) where the tracer mass flow is greatest (which may exaggerate numerical differences between approaches):

    a. Mass flow (moles/(year-m^2)) of each tracer across the top surface of the cell as a function of time (years).

    b. Cumulative mass flow (moles/m^2) of each tracer across the top surface of the cell as a function of time (years).

8. At the cell location on the surface of the low point low point (3700 m < x < 5000 m) where the tracer mass flow is greatest:

    a. Plot mass flow (moles/(year-m^2)) of each tracer across the top surface of the cell as a function of time (years). Also, provide the cross-sectional area of the cell surface.

    b. Plot cumulative mass flow (moles/m^2) of each tracer across the top surface of the cell as a function of time (years).

9. The aqueous concentrations (moles/litre) of tracers over time in the vicinities of two locations:

    a. Hillslope at (3500, 831, 1000) where a deterministic fracture zone (HCD) intersects the bottom of the hill.

    b. Low point at (4337, 609, 1000) where two HCDs intersect at the surface.

The general plume behaviour is shown in Figure 34, a representation from BGR of the streamlines from the canister positions for a DFN realization. The streamlines initially follow stochastic fractures deeper in the domain and then follow the flow field up to the top of the domain mainly through the deterministic fractures. Most of the tracer leaves the domain through the low point.
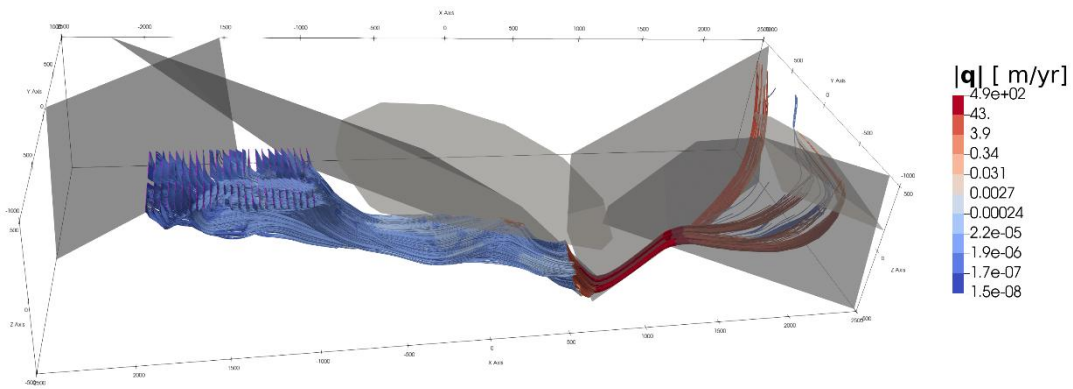
Figure 34. BGR representation of streamlines starting at canister positions for the computed stationary flow for the stochastic DFN realization 1.

3.3.1 Steady State Flow

Figure 35 shows a comparison of the steady state flow of water for the high point, hillslope, and low point reported for each team. At the high point there are variances among each team but realizations within each team tend to cluster together with the exception of NARI. Teams BGR, KAERI, SNL, and SÚRAO all have one or two realizations approximately 20000 kg/y higher than the rest of the realizations. In the hillslope there is more overlap between teams except for NARI, while the low point has more scattered results and more variance between the realizations within each team. Differences could be due to different upscaling methods, mesh sizes, or numerical methods. For example, CNSC simplified the treatment of the DFN model by using the average of the fracture parameters and hypothesize that the fracture density used should have been increased to double the quantity, SSM also simplified the model by not including stochastic fractures which results in effectively zero flow through most of the system, and NARI used stochastic fractures generated by DarcyTools.
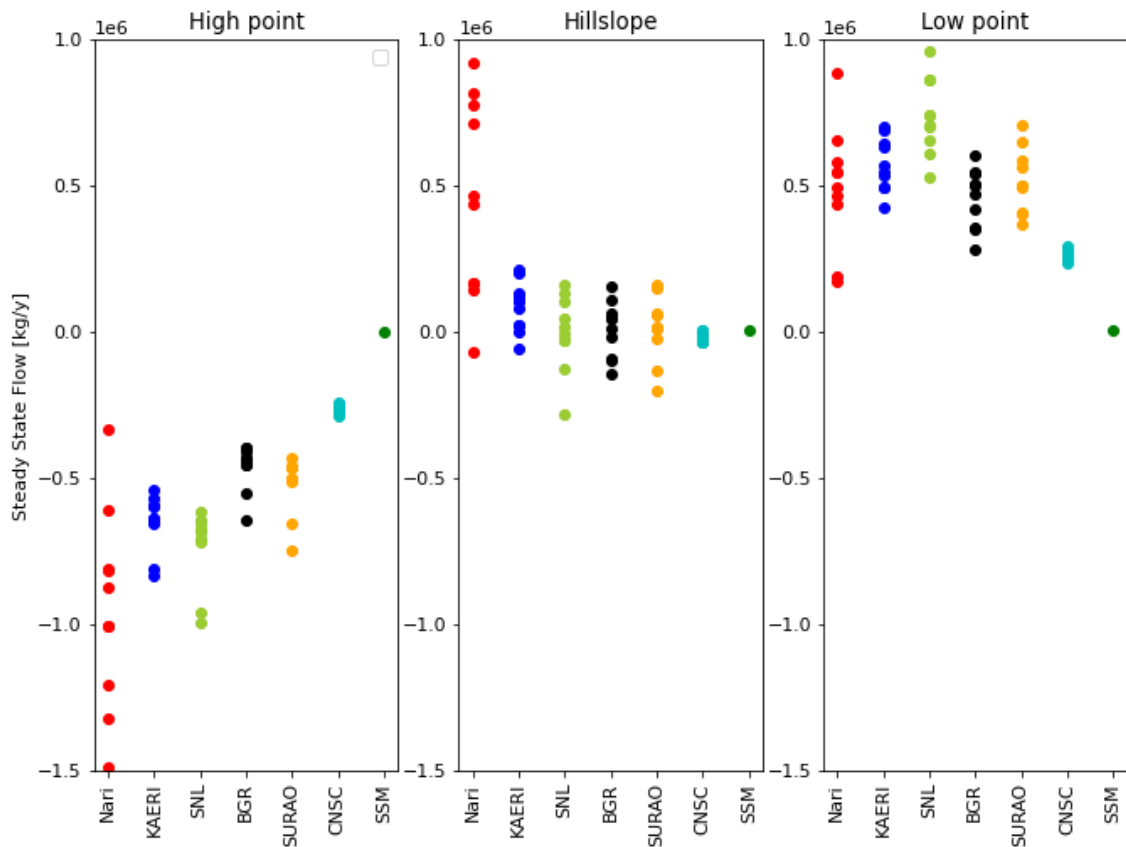
Figure 35. Steady state flow of water (kg/y) for each team and realization, integrated over the three surfaces of interest: High point (0 m < x < 1700 m), hillslope (1700 m < x < 3700 m), and low point (3700 m < x < 5000 m). SSM includes only one realization.

3.3.2 Release of Tracer from the Repository

The amount of mass remaining in the repository region is plotted in Figure 36. SNL, NARI, and CNSC show that most of the mass of Tracer 1 remains in the repository while BGR, SÚRAO, SSM, and KAERI show that a significant amount leaves the repository. There were several assumptions and simplifications made by the latter group resulting in a large amount of tracer leaving the repository region. BGR has not yet accounted for the engineered barrier system, SÚRAO does not include the backfill and does not include the surrounding rock around the deposition holes in their calculation, SSM models the repository as a simplified equivalent porous medium representing the tunnels and deposition holes and does not consider the decreasing trend in transmissivity with depth, and KAERI includes artificial isotropic diffusion. SNL had the least amount of tracer exiting the repository, this could be due to the way the repository was discretized which resulted in slightly larger dimensions of the repository region and the buffer than specified in the task specification. Similar trends are seen for Tracer 2. Differences of less than 0.2 moles in the initial amount are likely due to rounding errors.
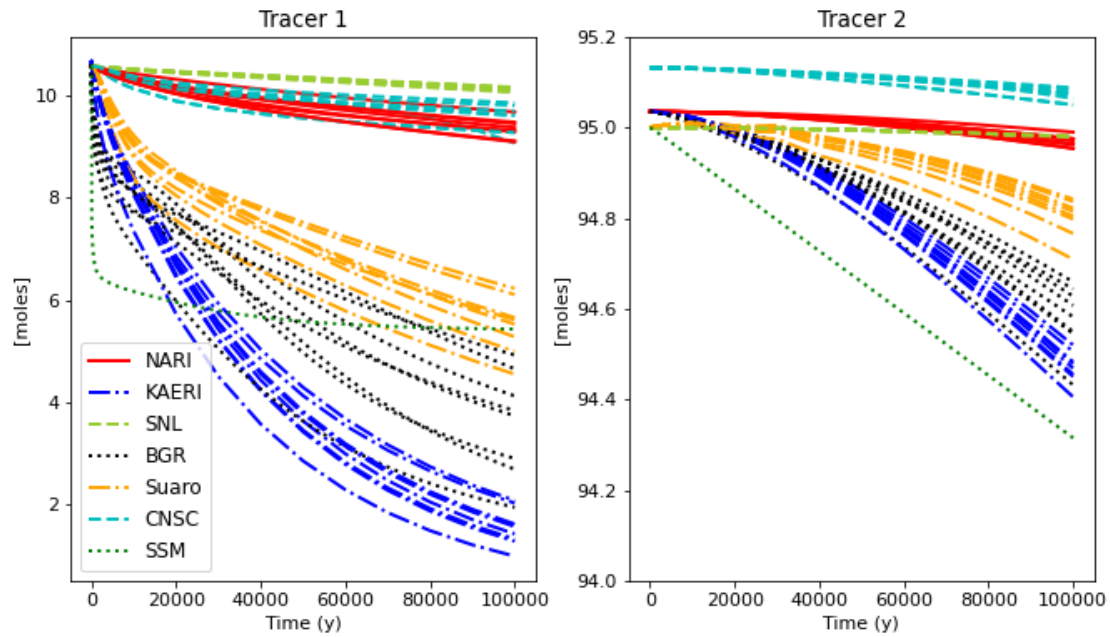
Figure 36. Mass remaining in the repository for Tracer 1 (left) and Tracer 2 (right) for each team and realization. SSM includes only one realization. The large amounts of tracer leaving the repository for BGR, KAERI, SÚRAO, and SSM are due to assumptions and simplifications made about the repository (e.g., excluding the engineered barrier system) and domain.

3.3.3 General Transport to Hillslope Surface

Figure 37 shows the tracer mass out of the hillslope for each team and realization. Figure 38 shows the means and 95% confidence interval of the mean for each team. KAERI and CNSC show little difference between realizations. Most of the means follow a similar trend, increasing over time, except for the mass flow of Tracer 1. Some teams show it decreasing over time (KAERI, SSM, NARI) and others show a general increase over time (SNL, SÚRAO). KAERI and SSM show the largest cumulative mass flow and mass flow. This is likely due to the larger amount of tracer exiting the repository in the KAERI simulation and the exclusion of depth dependent transmissivity for the SSM team. BGR and SÚRAO show similar results, where both teams excluded parts of the engineered barrier system. NARI, SNL, and CNSC show the lowest results, likely due to the inclusion of the full engineered barrier system. Several of the confidence intervals overlap between teams showing some agreement between results.
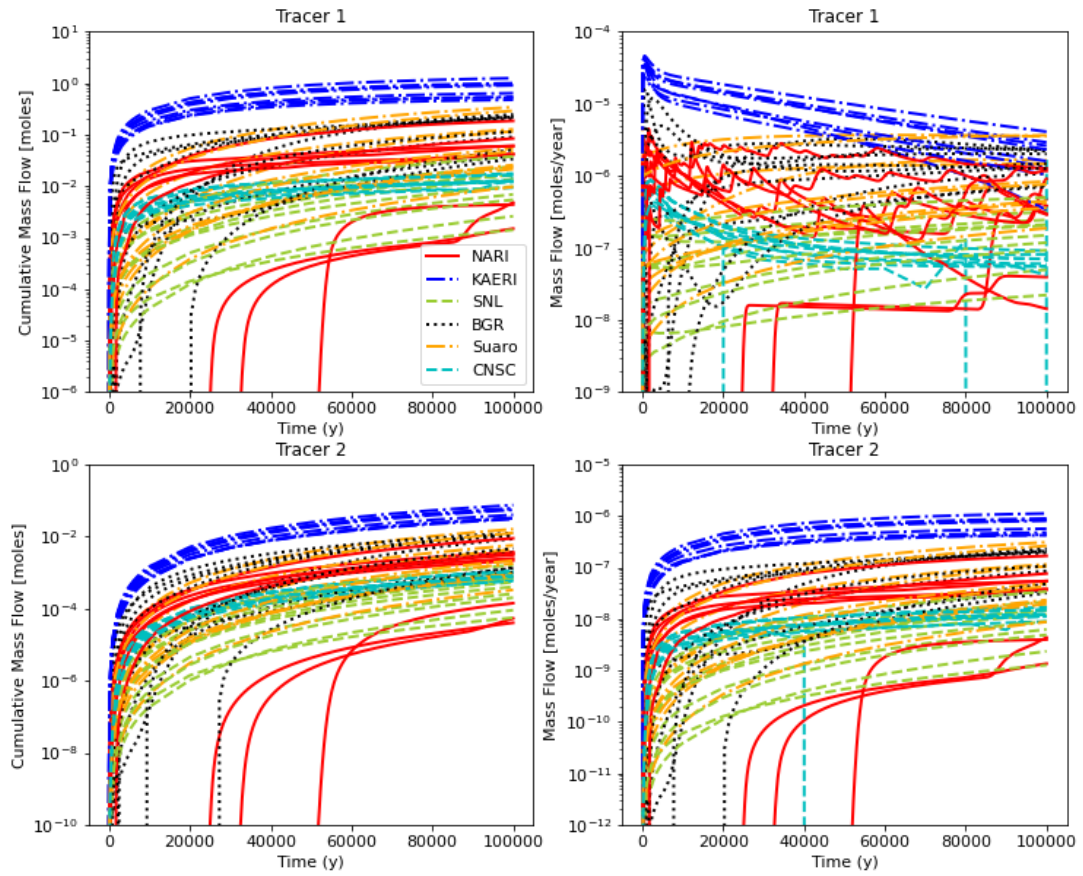
Figure 37. Cumulative mass flow (left column) and mass flow (right column) out of the hillslope (1700 m < x < 3700 m) for Tracer 1 (top row) and Tracer 2 (bottom row) for each team and realization.
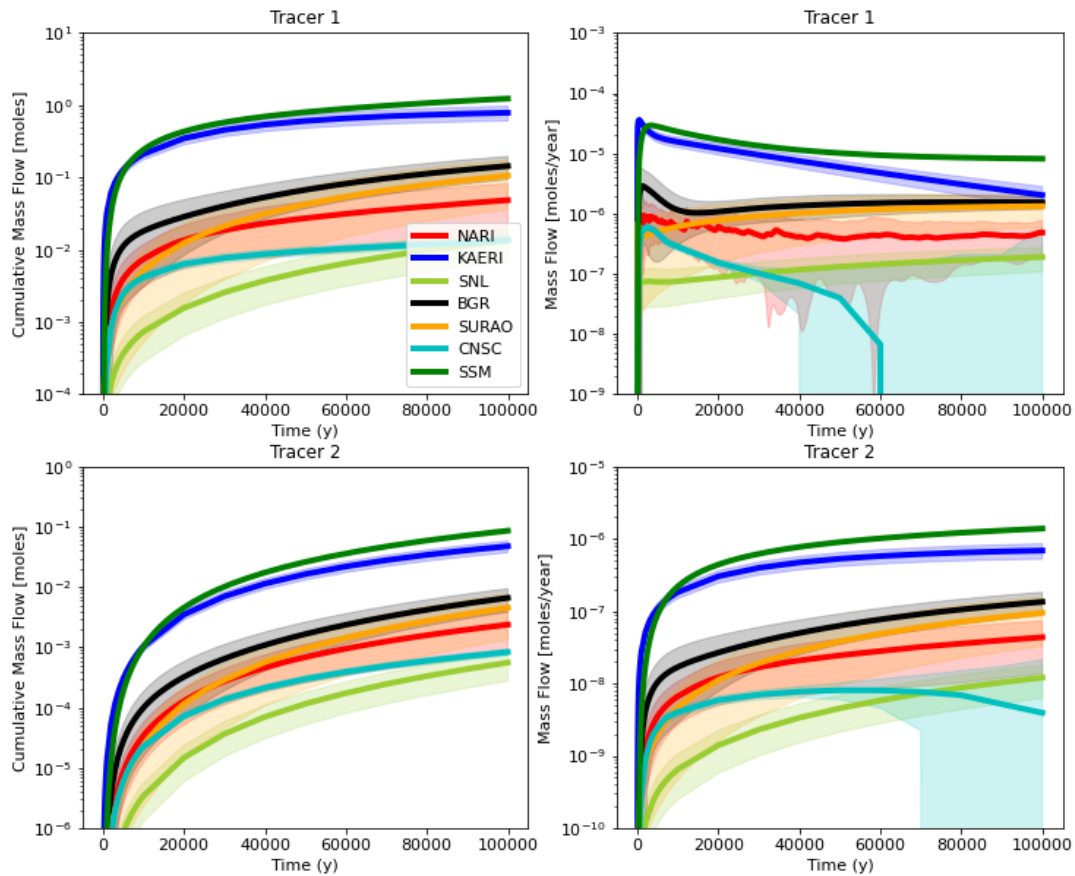
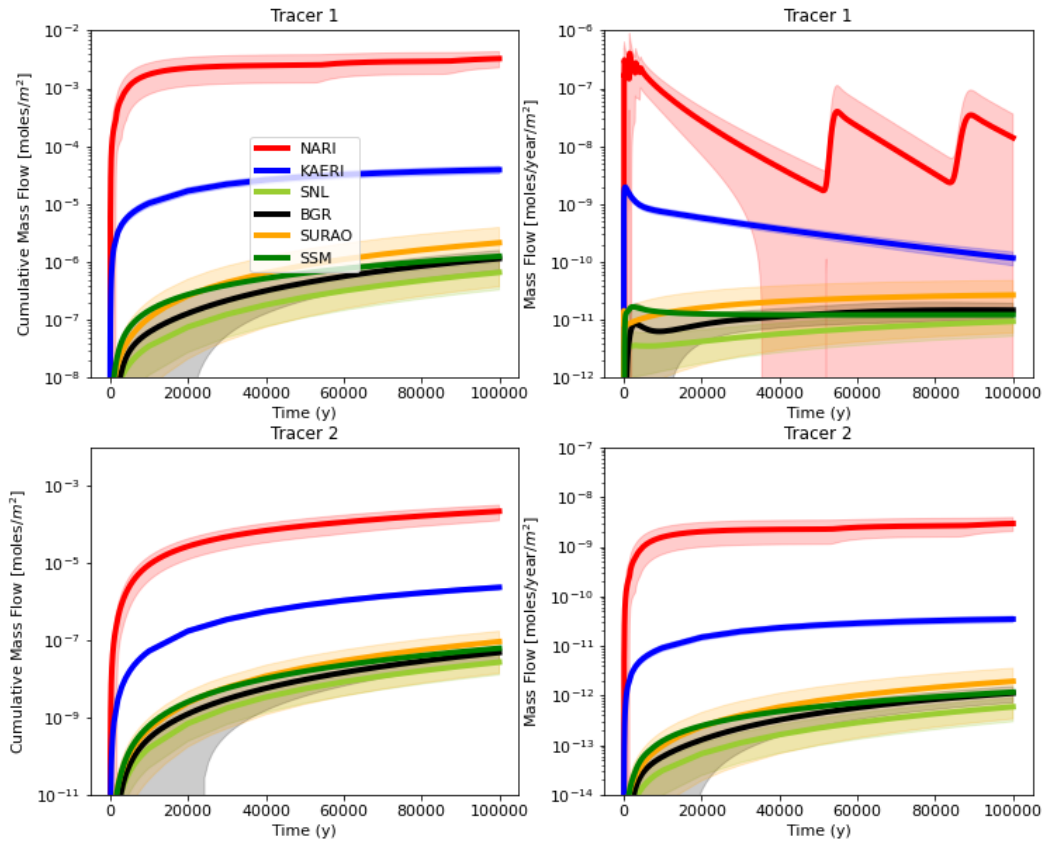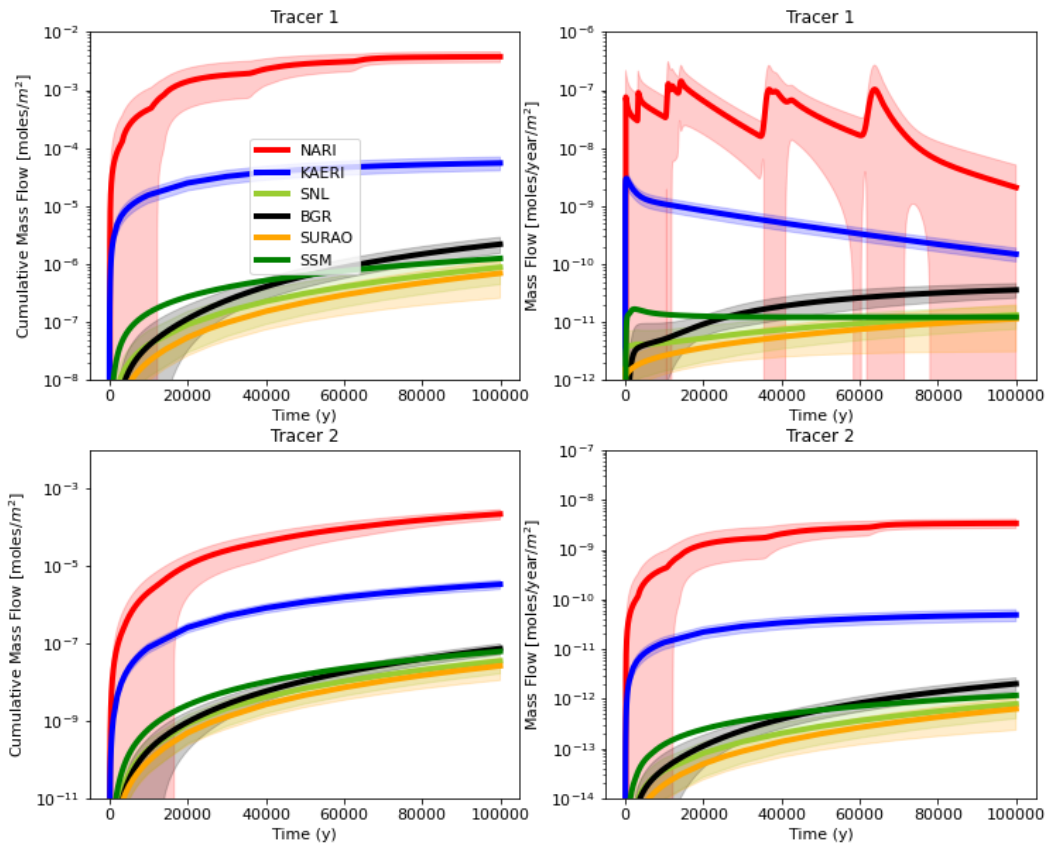**Figure 38. Means and 95% confidence intervals of the means for cumulative mass flow (left column) and mass flow (right column) out of the hillslope (1700 m < x < 3700 m) for Tracer 1 (top row) and Tracer 2 (bottom row) for each team. SSM includes only one realization.**

3.3.4 General Transport to Low Point Surface

Figure 39 shows the tracer mass out of the low point for each team and realization. Figure 40 shows the means and 95% confidence interval of the mean for each team. Similar trends are seen compared to the hillslope. SNL and NARI fall within the confidence intervals of one another for all four metrics. CNSC falls within the confidence intervals of SNL and NARI at beginning times and dips slightly below at later times. The KAERI, BGR, SÚRAO, and SSM simulations, which had more tracer leaving the repository due to assumptions made, show the greatest mass flow. BGR, SÚRAO, and SSM fall within the confidence intervals of each other while KAERI remains an outlier. The confidence intervals for each team are relatively tight showing that the variation of realizations for a given model that includes the deterministic fractures is minimal.
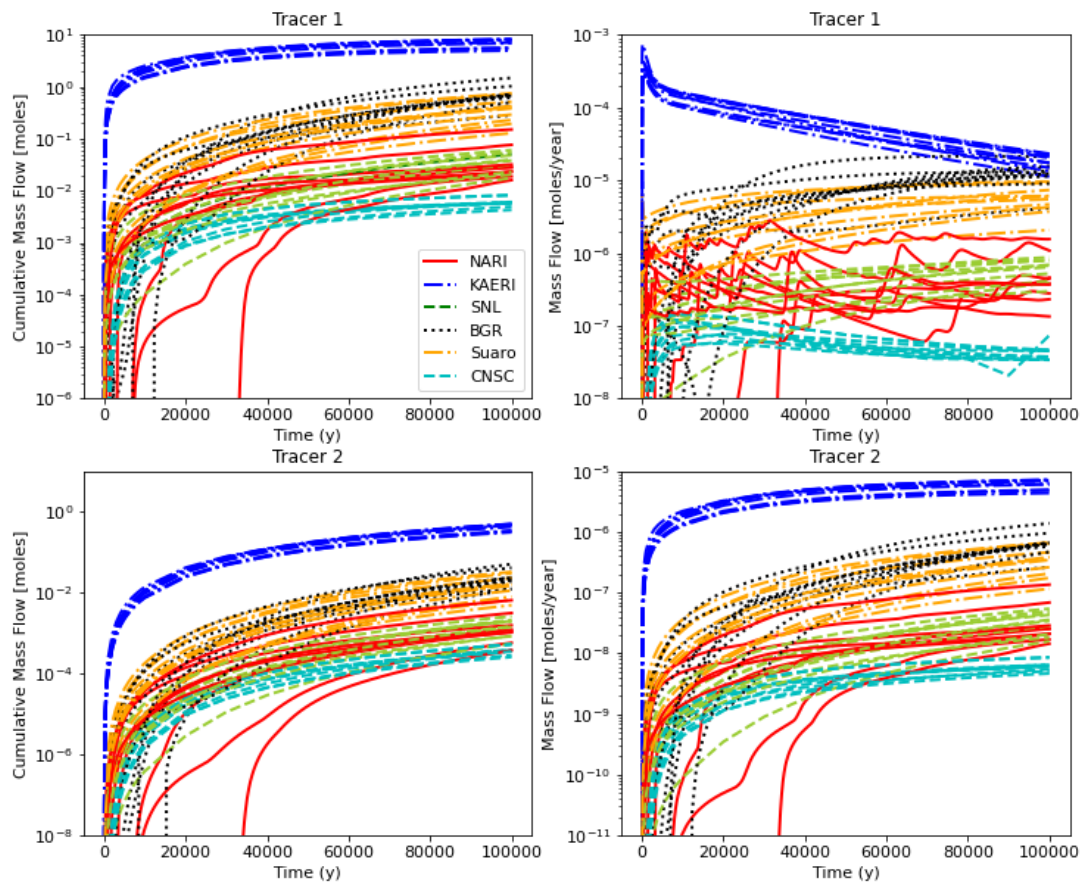
Figure 39. Cumulative mass flow (left column) and mass flow (right column) out of the low point (3700 m < x < 5000 m) for Tracer 1 (top row) and Tracer 2 (bottom row) for each team and realization.
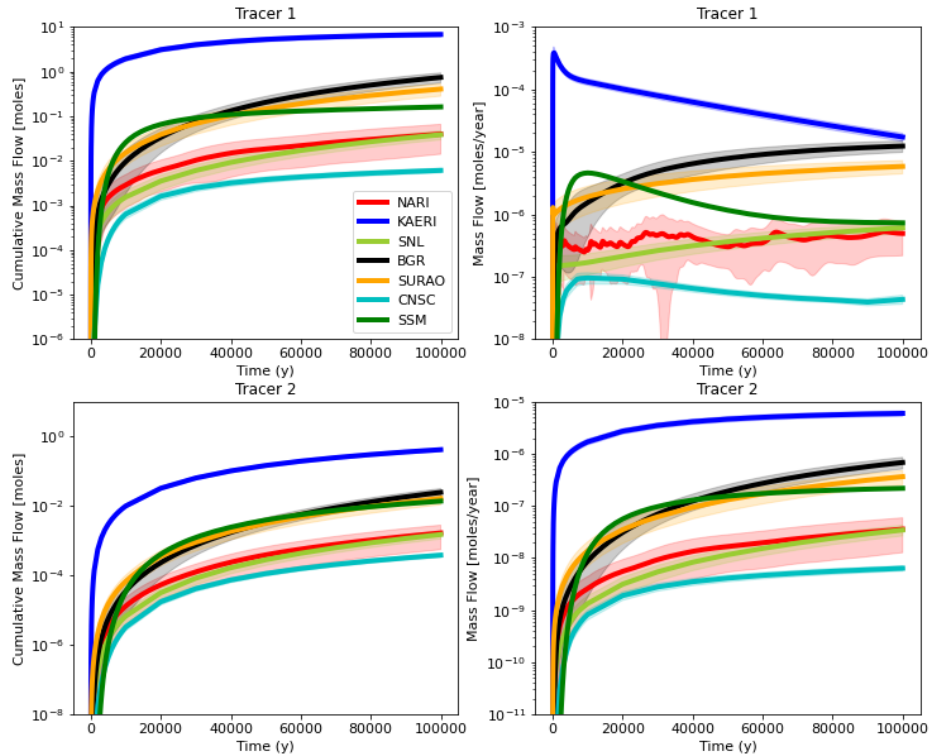
Figure 40 Means and 95% confidence intervals of the means for cumulative mass flow (left column) and mass flow (right column) out of the low point (3700 m < x < 5000 m) for Tracer 1 (top row) and Tracer 2 (bottom row) for each team. SSM includes only one realization.

3.3.5 Transport to Specific Surface Locations

The means and 95% confidence intervals of the means for the cumulative mass flow and mass flow at the location with the maximum mass flow for the hillslope and low point are shown in Figure 41 and Figure 42 respectively. In the hillslope there is good agreement between SNL, SÚRAO, SSM, and BGR where the 95% confidence intervals overlap. For the low point there is good agreement between SNL, SSM, and BGR. NARI has the largest confidence intervals between the teams. The mean for NARI on the mass flow for Tracer 1 produced a zig-zag flux due to mass transport being simulated in a one-dimensional manner where the dispersion effect is ignored, leading to a larger peak in the breakthrough curve occurring at different times for each stochastic realization. If a larger number of particles had been placed in waste package locations, a more dispersed effect would have been observed. The locations of the maximum mass flow for the hillslope and low point are shown in Figure 43 and Figure 44, respectively.

Figure 41. Means and 95% confidence intervals of the means for cumulative mass flow (left column) and mass flow (right column) at the location of the maximum mass flow on the hillslope for Tracer 1 (top row) and Tracer 2 (bottom row) for each team. Cumulative mass flow and mass flow were normalized by the cross-sectional area of the cell in each model. SSM includes only one realization.

Figure 42. Means and 95% confidence intervals of the means for cumulative mass flow (left column) and mass flow (right column) at the location of the maximum mass flow on the low point for Tracer 1 (top row) and Tracer 2 (bottom row) for each team. Cumulative mass and mass flow were normalized by the cross-sectional area of the cell in each model. SSM includes only one realization.
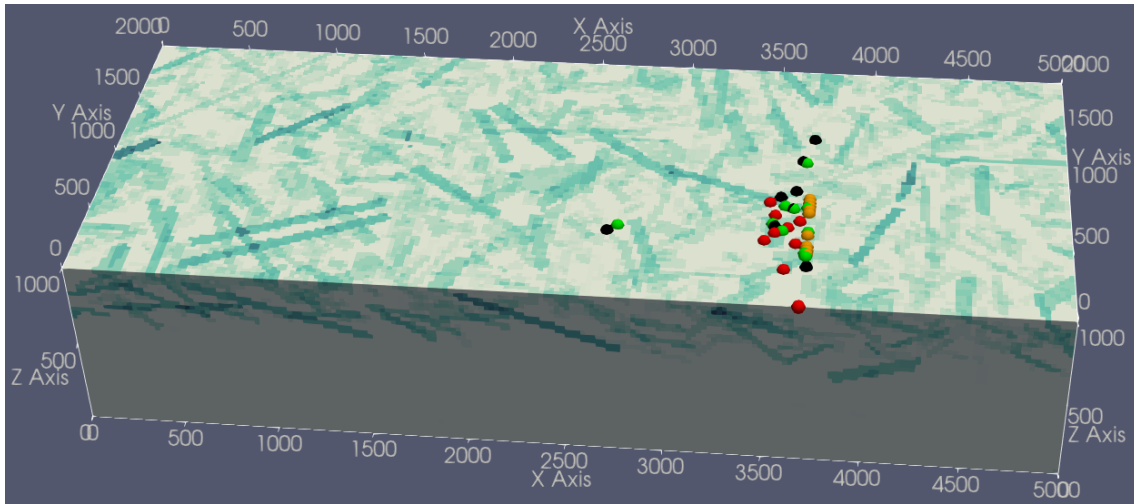
Figure 43. Locations of maximum mass flow for each team at the hillslope shown on upscaled permeability.
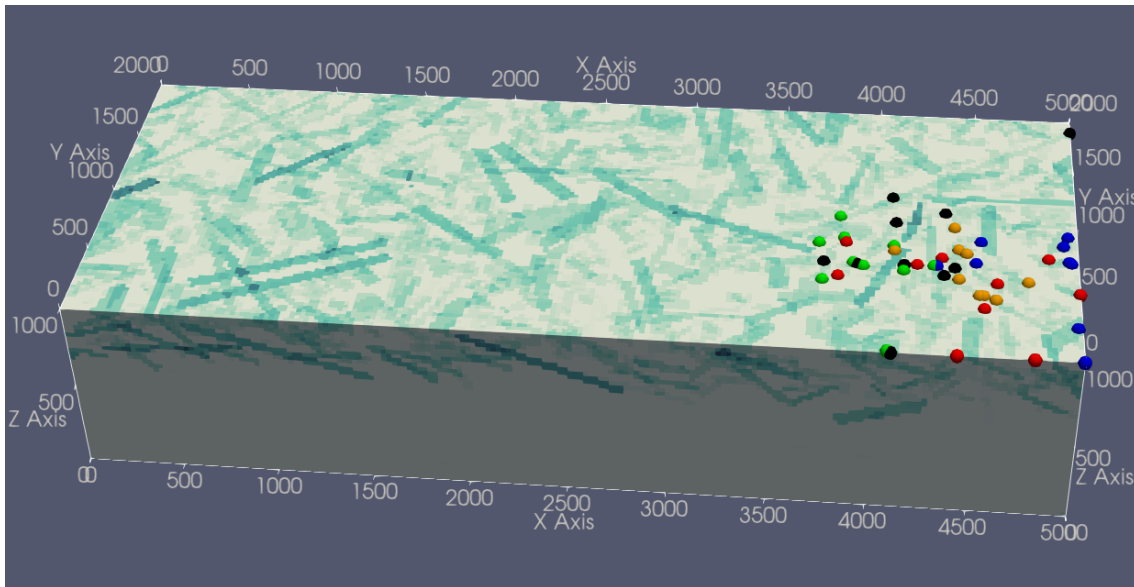
Figure 44. Locations of maximum mass flow for each team at low point shown on upscaled permeability.

Figure 45 shows the concentration of the observation points on the hillslope and low point for each team and realization. Figure 46 shows the means and 95% confidence interval of the mean for each team. Over the hillslope there are multiple orders of magnitude differences between teams and more agreement is seen on the low point between the teams that had large amounts of tracer leaving the repository (BGR, SÚRAO, KAERI, SSM) resulting in higher concentrations of the tracers at the surface. SSM has one of the highest concentrations measured at the high point and low point showing the importance of including the stochastic fracture network and modelling a more complex EBS. SNL, NARI, and CNSC reported the lowest concentrations, suggesting the

importance of the engineered barrier system in the model. NARI simulated the reference case using particle tracking and placed one particle in each deposition hole. NARI noted that the quantity of particles reaching the two observation points may not be representative; in several realizations no particles reached the observation points or the time it took for particles to reach the observation points exceeded 100000 years, resulting in an underestimation of results. SSM had some of the highest concentrations, which could be due to the lower water flux observed at the hillslope and low point compared to other teams. Higher water fluxes in sub-horizontal fractures near the surface would tend to cause the tracer to be more diluted at the surface. The large confidence intervals seen in Figure 46 show there is a large variance between realizations for some teams.
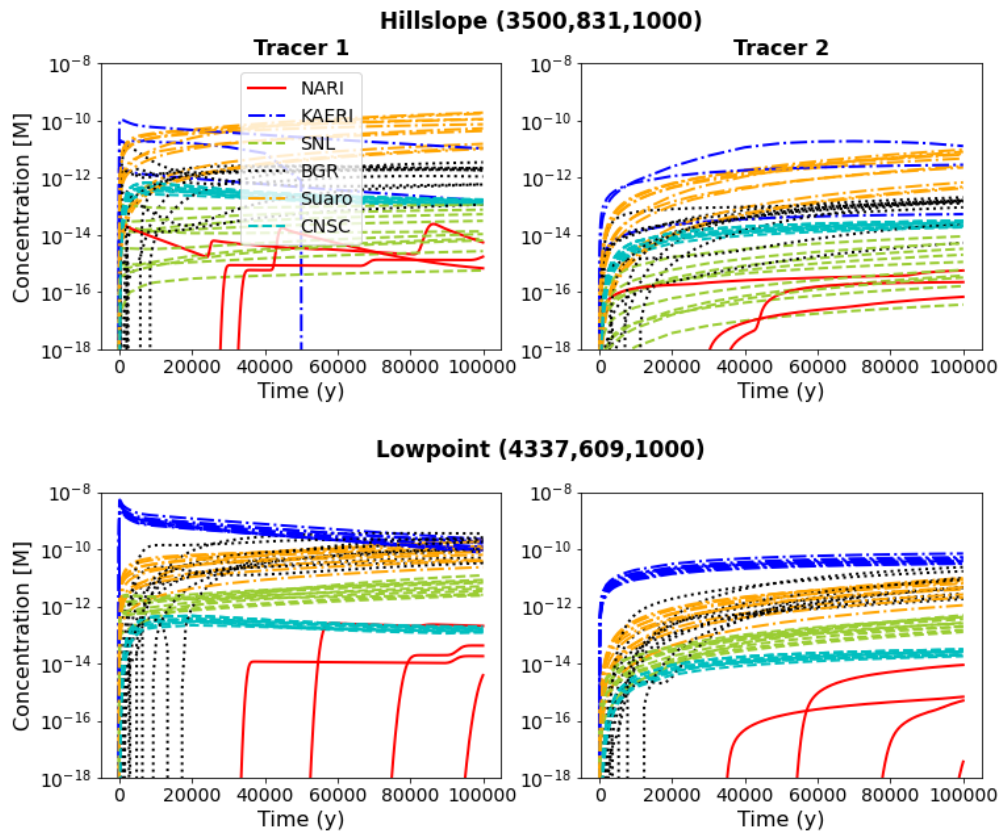
Figure 45. Concentration [M] at the observation point on the hillslope (top row) at coordinate (2500,831,1000) and the low point (bottom row) at coordinate (4337,609,1000) for Tracer 1 (left column) and Tracer 2 (right column) for each team and realization.
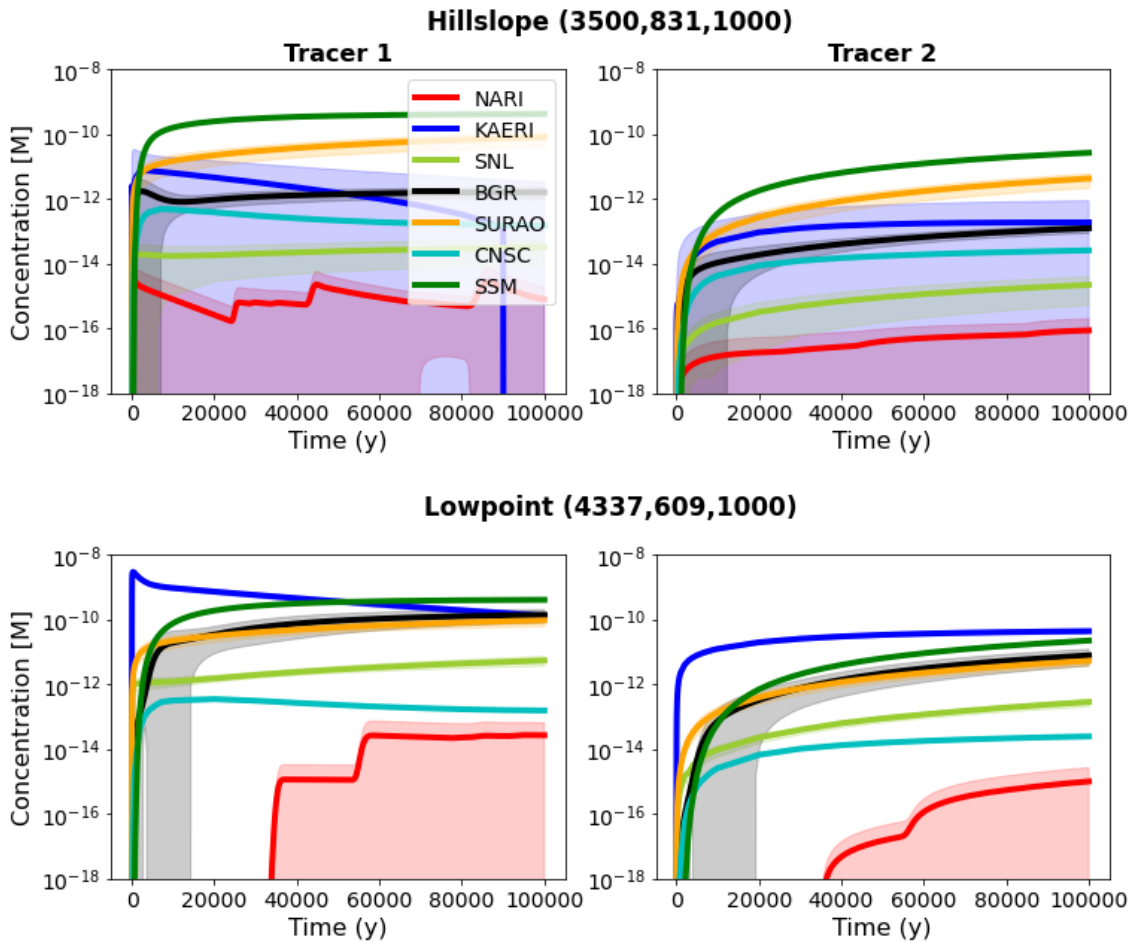
Figure 46. Means and 95% confidence intervals of the means for concentration [M] at the observation point on the hillslope (top row) at coordinate (2500,831,1000) and the low point (bottom row) at coordinate (4337,609,1000) for Tracer 1 (left column) and Tracer 2 (right column) for each team. SSM includes only one realization.

3.3.6 Reference Case Summary

The differences between the results of different teams demonstrate the importance of certain model or system parts when doing a performance assessment in crystalline rock. For example, modelling the engineered barrier system with all the components (buffer and backfill) appears to play a key role in keeping the tracers from reaching the surface. However, if the buffer and backfill are included there are multiple ways to model the repository demonstrated by CNSC's approach of implementing a single deposition hole model to calculate tracer flux across the bentonite/rock interface, SNL's approach of grid refinement with a tracer source term in the canister grid cells, and NARI's approach using grid refinement and particle tracking where mass transport in the near field is calculated based on whether a fracture intersects the deposition hole.

Another key factor appears to be domain scale heterogeneity and the inclusion of stochastic fractures in the domain. Heterogeneity and inclusion of the stochastic fracture families makes a difference when looking at the results from SSM-UU. The importance of including the accurate statistics for the stochastic fractures was also shown in the differences of the flow rates between teams which resulted in higher concentrations observed.

There was minimal variation within modelling frameworks due to fracture realizations but differences were more pronounced when using a Lagrangian framework in transport modelling. The mass flux across the hillslope and low point showed good agreement between teams that modelled the whole repository and teams that omitted all or part of the repository, as shown by overlapping confidence intervals. The maximum mass flux out of the low point and hillslope showed good agreement between most teams also demonstrated by overlapping confidence intervals, suggesting that for this measurement near field choices make less of a difference.

4 Conclusions

Since the inception of Task F in 2019, the F1 teams accomplished much. Each year, the teams worked individually and as a group to make substantial progress on each task objective.

The first objective was to motivate the development of crystalline repository performance assessment modelling capabilities and modelling skills. The group developed a task specification that included benchmark modelling and the development of a generic crystalline repository reference case. Eight teams modelled some or all benchmarks. Seven modelled most or all major features and processes of the reference case. Along the way, teams developed new modelling capabilities and skills, including upscaling discrete fracture networks (DFNs) to an equivalent continuous porous medium (ECPM), new comparison and verification methods, and new ways to model matrix diffusion.

The second objective was to examine the influence of modelling choices. Different teams developed different models to simulate the benchmarks and reference case. In some cases, individual teams developed two or three models to simulate the benchmark cases or tried different resolution meshes. When teams developed variations of model choices for their own model, it was clear to see the effects because the rest of the model was the same. For example, when a team modelled a benchmark with a DFN and upscaled the DFN to an ECPM, breakthrough tended to be smoother with the ECPM, as

expected. The effects of model choices between teams are less clear because there are often multiple differences in model choices between teams (e.g., gridding, representation of repository features, etc.). For the reference case, excluding the drifts, buffer, and backfill from the domain, generally results in faster release of tracers and radionuclides from the repository region. Teams that excluded parts of the engineered barrier system did so mainly due to technical and time constraints. Comparison of the results of all models clarify the effects of explicit inclusion of drifts, buffer, and backfill in the reference case models and motivate improved methods to account for the effects of those features.

For the models with a comparable repository inventory evolution (NARI, CNSC, and SNL), there are still considerable differences in model results. The main differences between these models are in the model choices of how to simulate the features and processes. The differences in the results indicate the sizeable effects of model form uncertainty and demonstrate the utility of a range of approaches to build confidence in a performance assessment.

The third objective was to compare uncertainties introduced by modelling choices to other sources of uncertainty such as stochastic heterogeneity, uncertain input parameters, and scenario/conceptual uncertainties. Nearly all teams that modelled the reference case produced 10 stochastic realizations of the fracture networks in the crystalline rock so that the resulting effects of stochastic spatial heterogeneity could be evaluated. While the 10 realizations each team simulated help to approximate the expected means for the models, many more realizations would likely improve these approximations and their confidence intervals. The variations observed in the resulting performance metrics, such as the concentrations of radionuclide tracers at the biosphere interface, indicate that the uncertainty introduced by stochastically generated fractures propagates to produce considerable variance in performance metrics. Additional progress toward this third objective includes the addition of uncertainty distributions for many of the input parameters to the Task Specification. Further work toward this objective, including the propagation of input value uncertainty and the application of advanced sensitivity analysis methods, is anticipated in a continuation task for DECOVALEX-2027.

5 Planned and Completed Publications

Table 9 gives the planned and completed publications under this task, correct at the time of writing.

Table 9: Planned and completed journal and conference papers for Task F1.

Author(s)	Title	Journal/ Conference	Status
Mariner PE, Leone RC, Hyman J, et al.	Discrete fracture network (DFN) benchmarking for DECOVALEX-2023	Geomechanics for Energy and the Environment (special issue)	Planned
Leone RC, Hyman J, et al.	Comparison of crystalline repository reference case approaches for DECOVALEX-2023	Geomechanics for Energy and the Environment (special issue)	Planned
Li Z, Nguyen S, et al.	Modelling of transport in fractured crystalline rock mass using porous medium equivalent and discrete fracture network approaches	Geomechanics for Energy and the Environment (special issue)	Planned
Mariner PE, Leone RC, Stein ER	Performance Factor Analysis for Performance Assessment	WM2024 Conference, March 10 – 14, 2024, Phoenix, Arizona, USA	Accepted

6 Acknowledgements

7 References

Anttila, M. 2005. Radioactive Characteristics of the Spent Fuel of the Finnish Nuclear Power Plants. Working Report 2005-71. Posiva Oy, Olkiluoto, Finland.

Choi, H. J., J. Y. Lee, and J. Choi 2013. "Development of Geological Disposal Systems for Spent Fuels and High-Level Radioactive Wastes in Korea". Nuclear Engineering and Technology, 45(1), 29-40. doi: 10.5516/net.06.2012.006

Hartley, L., J. Hoek, D. Swan, P. Appleyard, S. Baxter, D. Roberts, and T. Simpson. 2012. Hydrogeological Modelling for Assessment of Radionuclide Release Scenarios for the Repository System 2012. Working Report 2012-42. Posiva Oy, Eurajaki, Finland.

Hartley, L., S. Baxter, and T. Williams. 2016. Geomechanical Coupled Flow in Fractures during Temperate and Glacial Conditions. Working Report 2016-08. Posiva Oy, Eurajoki, Finland.

Hyman, J. D., S. Karra, N. Makedonska, C. W. Gable, S. L. Painter, and H. S. Viswanathan. 2015. DFNWORKS: A discrete fracture network framework for modeling subsurface flow and transport. Computers & Geosciences 84, 10-19. DOI: 10.1016/j.cageo.2015.08.001

Joyce, S., T. Simpson, L. Hartley, D. Applegate, J. Hoek, P. Jackson, D. Swan, N. Marsic, and S. Follin 2010. Groundwater flow modelling of periods with temperate climate conditions - Forsmark. SKB R-09-20. Svensk Kärnbränslehantering AB, Stockholm, Sweden.

LaForce, T., R.S. Jayne, R. Leone, P. Mariner, E. Stein, E., S. Nguyen, T. Frank. 2023. DECOVALEX-2023 Task F Specification Revision 10. SAND2023-04005 R. Sandia National Laboratories, Albuquerque, New Mexico.

NWMO 2012. Used Fuel Repository Conceptual Design and Postclosure Safety Assessment in Crystalline Rock. NWMO TR-2012-16. Nuclear Waste Management Organization, Toronto, Ontario.

Pettersson, S. and B. Lönnerberg 2008. 16-18 June 2008. Final Repository for Spent Nuclear Fuel in Granite - The KBS-3V Concept in Sweden and Finland. Paper presented at the International Conference Underground Disposal Unit Design & Emplacement Processes for a Deep Geological Repository, Prague.

Stein, E.R., R. Jayne, T. LaForce, R. Leone, and S. Nguyen. 2021. DECOVALEX-2023 Task F Specification, Revision 7. SAND2021-13423 O. Sandia National Laboratories, Albuquerque, New Mexico.

Tang DH, Frind, EO and Sudicky EA 1981. Contaminant transport in fracture porous media: analytical solution for a single fracture. Water Resources Research 17(3): 555-564. DOI: 10:1029/WR017i003p00555

Thiedau, J., Maßmann, J., Guevara Morel, C., Weihmann, S., Alfarra, A. 2021. CHRISTA-II - Analysen zur Integrität von geologischen Barrieren von Endlagersystemen im Kristallin. Ergebnisbericht, Bundesanstalt für Geowissenschaften und Rohstoffe, Hannover.

TPC (Taiwan Power Company) 2017. The Technical Feasibility Assessment Report on Spent Nuclear Fuel Final Disposal. Main Report. Taiwan Power Company, Taipei, Taiwan.

Vogel, P., J. Maßmann. 2015. Verification Tests. In: Kolditz, O., Shao, H., Wang, W., Bauer, S. (eds) Thermo-Hydro-Mechanical-Chemical Processes in Fractured Porous Media: Modelling and Benchmarking. Terrestrial Environmental Sciences. Springer, Cham. https://doi.org/10.1007/978-3-319-11894-9_2.

Yu, C., Warrick, A.W., and Conklin, M.H. 1999. A moment method for analysing breakthrough curves of step inputs. Water Resources Research 35(11): 3567-3572. DOI: 10.1029/1999WR900225

Appendix A. Bundesanstalt für Geowissenschaften und Rohstoffe (BGR) (Federal Institute for Geosciences and Natural Resources, Germany)

A.1 Introduction

This appendix summarizes the participation in Task F1 from the modelling team of the Federal Institute for Geosciences and Natural Resources (Bundesanstalt für Geowissenschaften und Rohstoffe, BGR). BGR is the central geoscientific authority providing advice to the German Federal Government with independent and neutral advice on all geoscientific and geotechnical issues. The BGR is concerned with geoscientific questions in the context of the existing repository locations in Germany and the site selection process for high-level radioactive waste, often in cooperation with BGE which is the German federal company for radioactive waste disposal. BGR expertise comprises many geoscientific topics arising from the disposal of radioactive waste in deep geological formations. To extend and consolidate know-how, continuously extensive research activities are carried out in collaboration with other national and international institutions.

Working on the crystalline reference case allowed BGR to complement the investigation on German disposal options in crystalline rock carried out during the joint research project Christa-II. Therein, a methodology for the assessment of thermo-hydro-mechanical impact on host rock integrity has been developed, which takes the hydraulic properties of fractured crystalline rock into account (Thiedau et al. 2021). Modelling the crystalline reference case aims for extended verification of the developed approach including a further extension to transport problems.

Section A.2 contains a description of the modelling approach applied by BGR and references to the used software and implementations. A brief summary on the simple benchmarks is given in A.3.1 and A.3.2 . The described methodology has then been applied to the different 4-Fracture benchmarks. Sections A.3.3 to A.3.5 give details on parametrization, results and findings from the benchmarks. In section A.4 the modelling work on the crystalline reference case is presented as well as first results. A short discussion of the results regarding achievements and remaining issues is added.

A.2 Methods

The BGR modelling strategy for the Task F crystalline reference case follows the specifications of the proposed reference system (LaForce et al. 2023). For a small number of large fracture zones, their locations and orientations can be characterized using observations. Such fracture zones are considered as deterministic features (HCD) in the hydrogeological model. However, for the large number of (smaller) fractures (HRD), only statistical characterizations can be obtained. Therefore, the performance assessment model is based on different realizations of these stochastic Discrete Fracture Networks.

The BGR-modelling approach to describe flow and transport in fractured crystalline rock is based on the Discrete Fracture Matrix approach, a combination of Equivalent Continuous Porous Media (ECPM) and Discrete Fracture Network (DFN) approaches. Consistent with the above described fracture categorization, the deterministic fracture zones are meshed explicitly while the characteristics of the realization of the stochastic fracture network are represented via upscaling and mapping procedures as heterogeneous and possibly anisotropic parametrization of the rock domain (Fig. A-1). This combined approach requires more effort in mesh generation and possibly computation in comparison to some other modelling approaches (Kröhn and Zielke 1991, Dietrich et al. 2005). On the other hand, it has the potential to represent a system where networks of smaller connected fractures, represented as porous matrix, as well as the large deterministic zones (i. e deterministic fractures) have a significant influence on flow and transport processes.
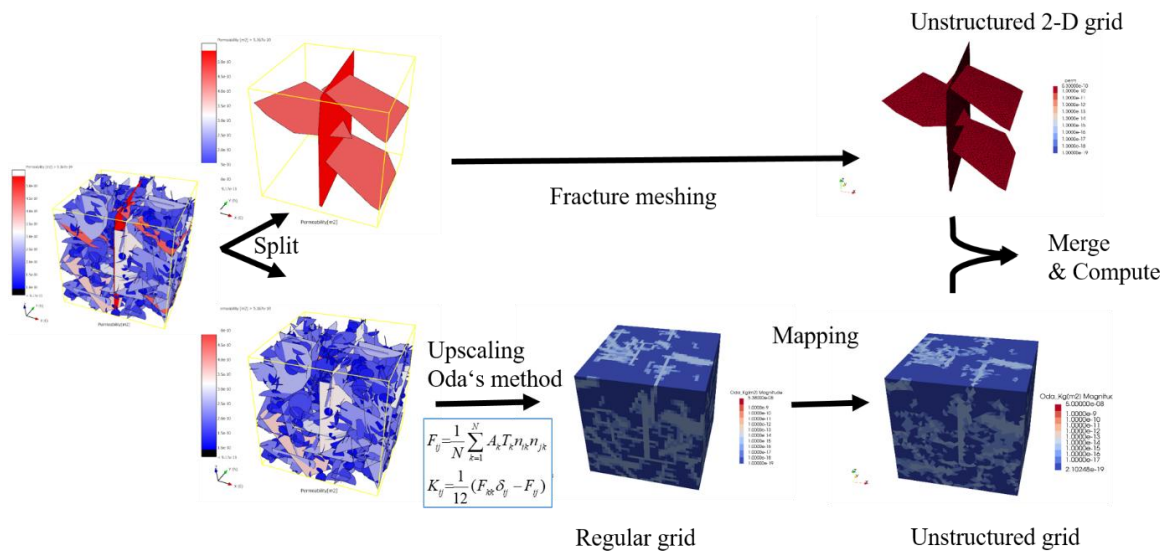
Fig. A-1. Concept for the numerical modelling of fractured media illustrated for permeability in the "4-Fracture Plus Stochastic Fractures"-Benchmark.

The whole model domain has to be discretized using volume elements. At the same time, in the deterministic fracture zones each particular fracture is discretely meshed using 2-D planar elements. A discretization with tetrahedral and triangular elements, respectively, facilitates conforming volume and fracture meshes as well as the refinement of the volume mesh in particular areas of interest within the model domain such as the repository nearfield. The conforming 2/3D-mesh for the reference case with refinement in the repository area is shown in Fig. A-2.
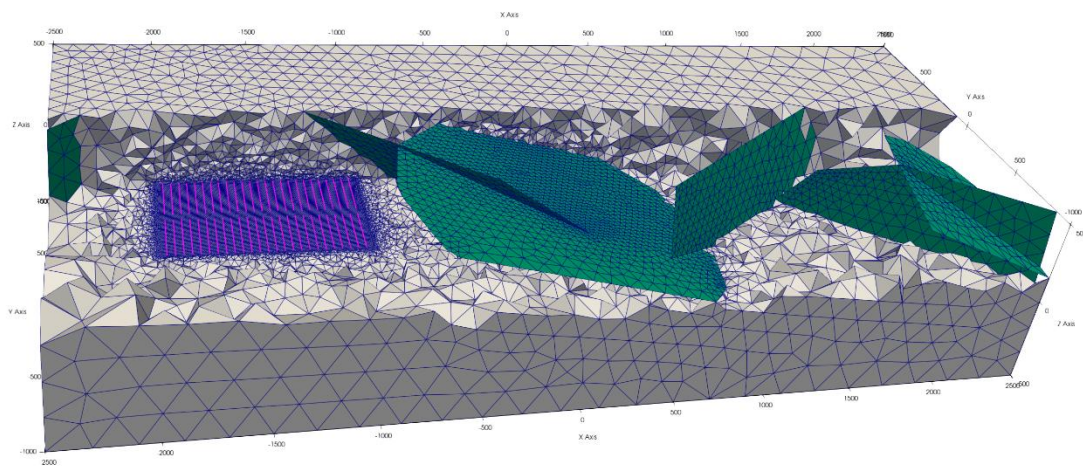
Fig. A-2. Conforming 2- and 3-D meshing of the reference case domain.

To derive the flow and transport parametrization of the volume elements from the hydraulic properties of the fractures not explicitly meshed, a two-step procedure comprising upscaling and mapping is applied (Thiedau et al. 2021). Realizations of the statistically characterized fracture sets can be created in FracMan® (Golder 2017, 2021).

FracMan® offers different options for the generation of realizations of the stochastic fracture networks given in the Task specification.

FracMan® provides an upscaling functionality for the hydraulic properties (e.g. permeability, porosity). The upscaling is then used to get properties of an ECPM on regular rectangular ("cube") grids. In case of the permeability, the upscaling is based on the Oda (1985) approach, which computes a full 3-D permeability tensor as the weighted sums of the permeability values of fractures intersecting the volumetric grid cells.

In order to transfer the upscaled properties from the regular cubical mesh to the unstructured tetrahedral volume mesh, a mapping procedure based on geometric consideration has been developed. In this procedure, illustrated in Figure 3 for the 2-D case, each tetrahedral volume element is assigned the calculated hydraulic properties. During this mapping the average of the values of those regular grid cells that either contain the midpoint of the tetrahedron or that have their midpoint within the tetrahedron is computed. This procedure allows properties to be transferred between different meshes. Nevertheless an increased blurriness in the representation of the fractures properties can be expected with different grid sizes. Although in this study the procedure is only used for permeability and porosity, it is extendable to other parameters or upscaling algorithms.
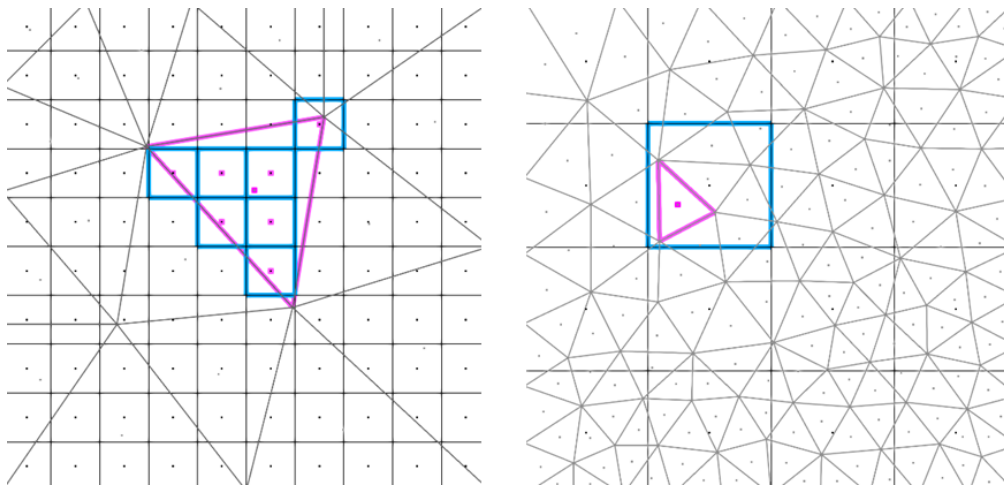
Fig. A-3. 2-D illustration of employed mapping procedure to transfer upscaled hydraulic properties from regular square mesh to unstructured triangular mesh. The parameters assigned for the triangles outlined in magenta are averaged parameters of the squares outlined in blue. The dots represent the midpoints of the squares and triangles.

The open source finite element implementation OpenGeoSys version 6 (OGS-6) is then used to solve the stationary flow problems as well as the transport process based on the advection-dispersion equation. OGS is a scientific, open-source project for the development of numerical methods for the simulation of thermo-hydro-mechanical-

chemical (THMC) processes in porous and fractured media (Bilke et al 2022, Kolditz et al. 2012). OGS is designed object-oriented and implemented in C++. It focuses on the numerical solution of coupled multi-field problems (multi-physics). Parallel versions of OGS are available relying on both MPI and OpenMP concepts. Application areas of OGS currently include water resources management, hydrology, geothermal energy, energy storage and nuclear waste disposal. The code has been successfully employed in numerous DECOVALEX tasks.

The underlying partial differential equation for the stationary case simplifies to the stationary fluid mass balance for the stationary pressure and liquid flow field given as:

$$-\nabla \cdot \rho \mathbf{q} + Q_p = 0,$$

based on the Darcy flow $\mathbf{q} = \frac{\mathbf{k}}{\mu}(\nabla p + \rho g)$, with permeability tensor $\mathbf{k}$, fluid viscosity μ, fluid density ρ, pressure p, gravitational acceleration g and fluid mass source term Q_p. Solute transport in terms of transient concentration distribution is modelled using the advection dispersion equation:

$$\phi R \rho \frac{\partial C}{\partial t} - \nabla \cdot [C\rho \mathbf{q} + \rho \mathbf{D}\nabla C] + Q_C + R\lambda\phi\rho C = 0,$$

where R denotes the retardation constant, ϕ porosity, C the concentration, Q_C the mass source, λ the decay constant and $\mathbf{D}$ the dispersion tensor combining molecular diffusion and dispersion:

$$\mathbf{D} = \phi D^* + \beta_\mathrm{T}\|\mathbf{q}\|\mathbf{I} + (\beta_\mathrm{L} - \beta_\mathrm{T})\frac{\mathbf{q}\mathbf{q}^\mathrm{T}}{\|\mathbf{q}\|},$$

where D^* is diffusion coefficient in pore space, β_T, β_L are transversal and longitudinal dispersion coefficients, respectively.

Fluid flow is assumed to be independent of time and concentration, therefore a simple staggered solution scheme can be employed. To stabilize the numerical solution of the mass transport, different stabilization schemes are implemented in OGS-6 e.g. artificial isotropic diffusion and full upwinding (Dalen 1979). Isotropic diffusion stabilization increases the diffusion tensor $\mathbf{D}$ locally by $\mathbf{D}_\alpha = \frac{1}{2}\,\alpha\,\|\mathbf{q}\|h\mathbf{I}$ with the tuning parameter $\alpha \in [0,1]$ and element size h. This leads to smaller Peclet numbers and hence stabilizes the solution. However, the transport regime is artificially changed towards a more diffusive behavior.

OGS-6 applies a standard Lagrange finite element discretization to the governing equations stated above. Primary variables, represented by spatially piecewise linear functions are the pressure and the concentration fields. Other quantities like the Darcy velocity are computed via the constitutive equations from the primary variables. For

analysis of boundary fluxes OGS offers the possibility to obtain residuum based boundary fluxes.

OGS-6 includes the functionality to solve the transport problem governed by advection-dispersion-equation on inclined 2-D-domains embedded in the 3-D-domain. This assumes that the solution is homogeneous across the fracture aperture, which is then only considered as parameter to ensure mass conservation.

The time discretization is done by a fully implicit Euler scheme, i. e. all time dependent evolutions are evaluated at the end of each time step leading to a large system of possibly nonlinear equations which is then solved iteratively by a Newton-Raphson or Picard solver. The time step size is automatically adjusted by a heuristic approach where the number of iterations of the nonlinear solver is used as an indicator for the need of refinement. The time step is, for example, decreased if in the previous time step a large number of iterations, each including the solution of the linearized system, was necessary to match the defined error tolerances. The time step is then also increased if the solution is found within only a few iterations. Alternatively, a prescribed time stepping scheme can be employed.

A.3 Benchmarks

A.3.1　1D Transport

The selected 1-D benchmarks for flow and transport are part of the standard OGS benchmark collection. Mesh and boundary elements are described in Vogel and Maßmann (2015). There were no deviations from the Task specification required. The results show good agreement with the analytical results for the three considered tracers: conservative, decaying and adsorbing tracer.
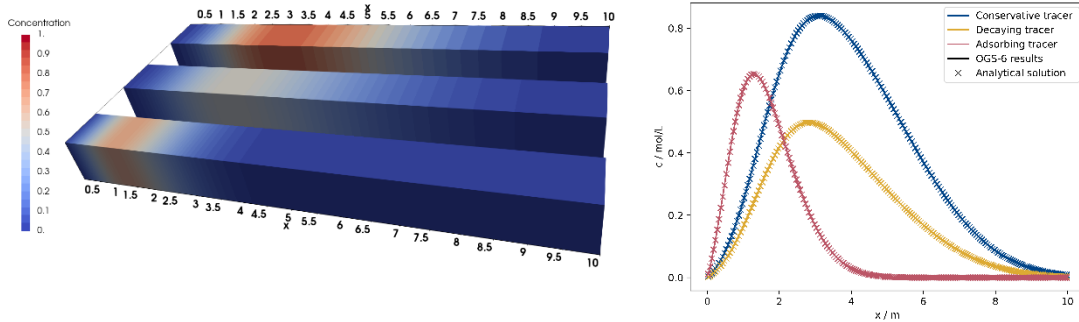
Fig. A-4 Results for 1-D-Transport Benchmarks after 20000s: Contour plots for conservative, decaying and adsorbing tracer (left from back to front); Line profiles vs. analytical solution (right).

A.3.2   1D Fracture Plus Matrix Diffusion

This benchmark is used to verify the solution on a combined one and two dimensional mesh. The fracture is modelled as 1-D line element along the x-axis which shares nodes with the connected 2-D quadrilateral mesh of the rock matrix. The mesh is graduated in both direction with smaller mesh size around the source location on the fracture where the concentration is fixed instantaneously for times >0.
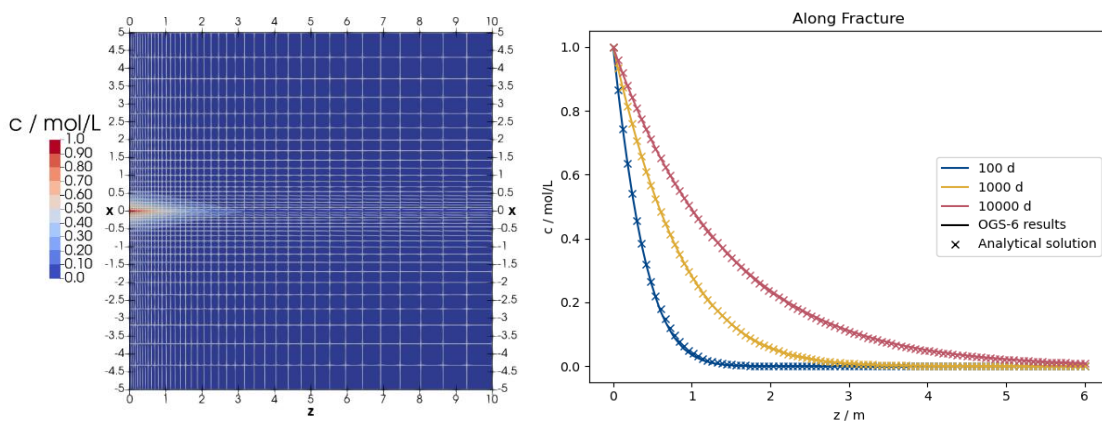
Fig. A-5. Results for the 1-D-Fracture Plus Matrix Diffusion benchmark. Left: Contour after 10 000 days; right: Tracer concentration along facture vs. analytical solution.

A.3.3   Four-Fracture Transport

The Four-Fracture Transport benchmark is used to test the DFN part of the BGR modelling approach. Hence the four fractures are directly meshed with 2-D-triangular elements using Gmsh (Geuzaine and Remacle 2009). The 13 768 elements defined by the 7030 Nodes have edge lengths between 10 and 25 m. The single core computation with OpenGeoSys on an Intel® Xeon® CPU with 2.1 GHz lasted about 2 hours for a total of 235 time steps.

Since higher pressure is prescribed at $x = -500$ m and lower pressure at $x = 500$ m liquid flow and hence all advective transport is globally directed in x-direction entering the domain through Fracture 1. Flux is then divided in the vertical Fracture 2 and exits the domain through Fracture 3(upper) and Fracture 4(lower). Because the permeability of Fracture 4 is lower, more fluid and tracer leave through the Fracture 3. The conservative tracer is injected as initial pulse at the entry end of Fracture 1. At this inflow end, the domain has been slightly extended to have the injection line in the interior of the domain which circumvents numerical problems with the boundary condition.

The tracer distribution evolves as expected over time following the flow regime. The upper exit fracture has a higher transmissivity such that the tracer reaches the downstream end first through Fracture 3. Accordingly, a significantly larger amount of tracers reach the outflow measurement of Fracture 3 (Fig. A-7). After 10 years almost all tracer has already left the domain. Hence, the decay with a half-life time of 100 years does not significantly influence the results.
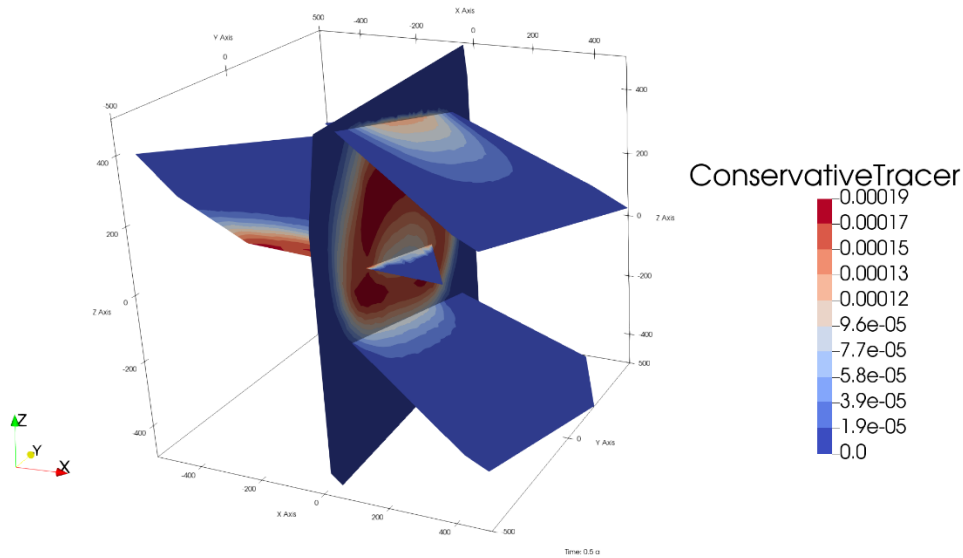
Fig. A-6. Calculated concentration distribution of the conservative tracer after 0.5 year.
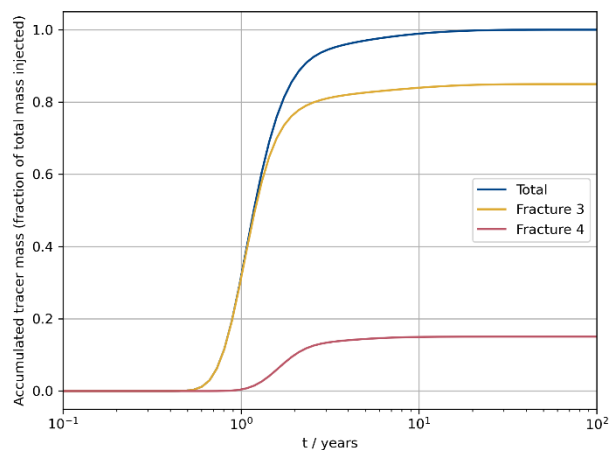
Fig. A-7. Cumulative mass breakthrough of the conservative tracer normalized by total injected mass.

A.3.4 Four-Fracture Plus Stochastic Fractures

The addition of the specified realization of the stochastic fracture network is done as a direct extension of the model for the Four-Fracture Benchmark. The discretization and parametrization of the deterministic fractures as well as flow boundary conditions are unchanged. The volume of the domain is meshed by a conforming tetrahedral mesh using Tetgen (Si 2015).

For parametrization of the volume elements, the two-step upscaling procedure is applied as described in A.2 . In the first step equivalent permeability and porosity values for a regular cubical grid of 25 m edge length are computed using Oda's approach as

implemented in FracMan®. Consequently, this values are mapped to the unstructured tetrahedral FE mesh. By this procedures, some mesh cells are assigned with zero permeability and porosity, since there are grid cubes not intersected by any of the fractures. Those tetrahedral elements are completely excluded from the computation.
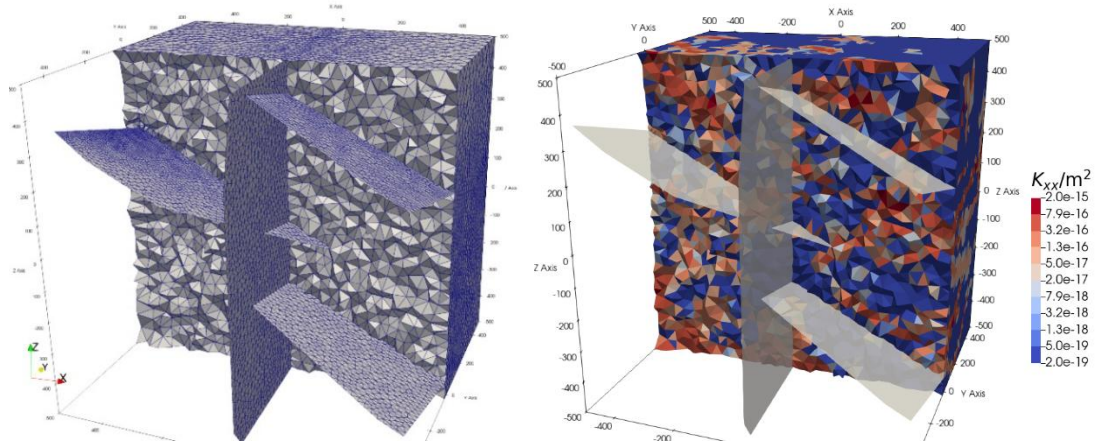
Fig. A-8. Cut through adapted volume and fracture surface mesh (left) and distribution of assigned bulk permeability value for the Four-Fracture-Plus domain.

The tracers are released on the complete inflow surface ($x = -500$ m). However, the source term is flow weighted in space, i.e. the boundary fluid mass flux is assigned as source term for all the tracers. As a consequence, almost all of the injected tracers go directly into the deterministic fracture (Fig. A-9). To smooth the pulse temporally, the injection is done as a Gaussian pulse over time. As previously done, the domain has been slightly extended in order to have the injection surface in the interior of the domain.
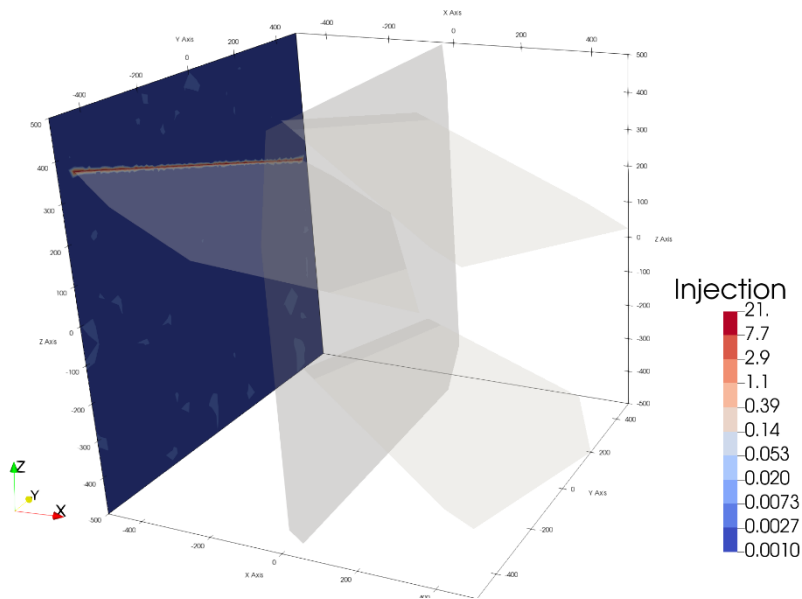
Fig. A-9. Spatial distribution of tracer injection.

In comparison to the Four-Fracture case, slower transport is computed. This does not match the expectation to obtain a similar breakthrough behaviour even though most of the tracer is released in the deterministic fracture. Since the breakthrough is substantially delayed, a high amount of decay occurs for the decaying tracer. Since hydraulic parametrization of the deterministic fractures is unchanged, different aspects of the numerical discretization have been analysed to explain the differences
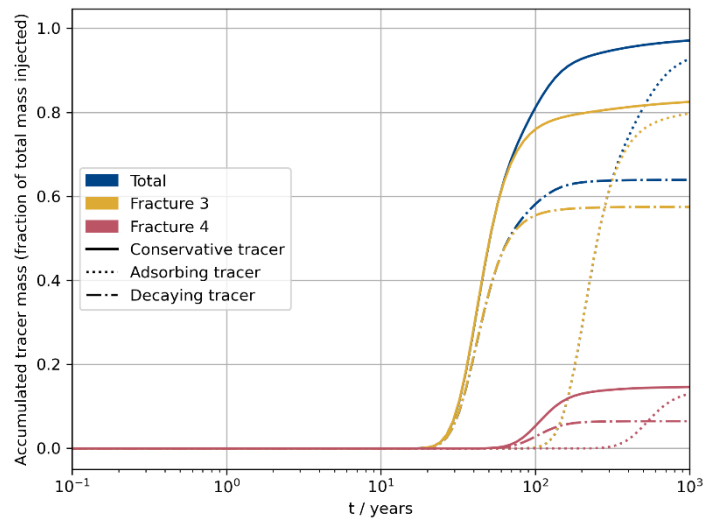
Fig. A-10. Cumulative mass breakthrough of tracers normalized by total injected mass.

It has been found that the applied finite element discretization of the problem with piecewise linear functions introduces excessively large storage and slows down the dominating advective flow within the deterministic features. This occurs because

calculating the discretized equations includes inherently an arithmetic mean over deterministic fracture elements and neighbouring volume cells. Because of the relatively coarse discretization perpendicular to the fracture, the storage term changes significantly. Using piecewise linear approximations for the concentration, which are continuous at the fracture-bulk interface, the steep concentration gradient from the deterministic fracture into the neighbouring ECPM is poorly represented (Fig. A-11). A mesh refinement perpendicular to all fractures would be required for a better gradient discretization, which is not feasible in this context.
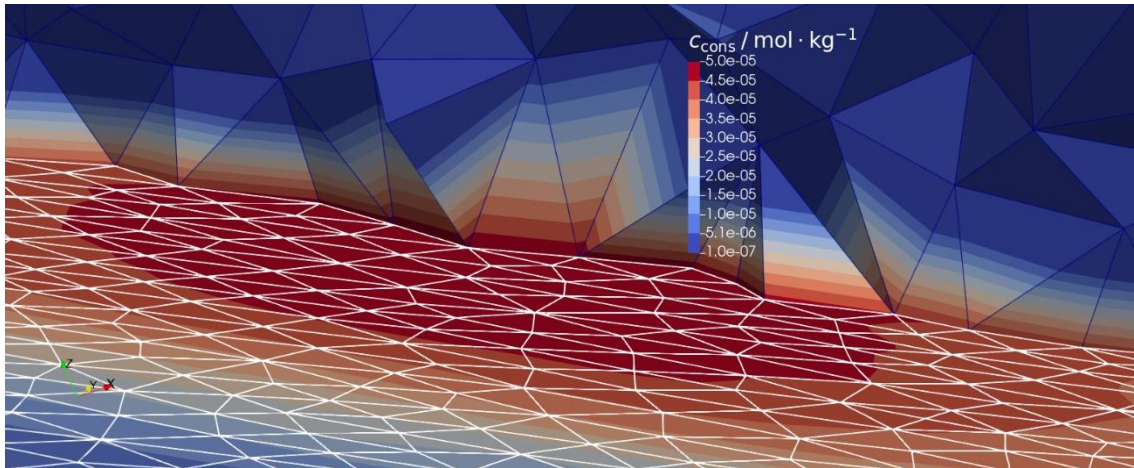
Fig. A-11. Exemplary zoom into the tracer field discretization at the interface between Fracture 3 (bottom with white edges) and attached volume cells (top with blue edges).

As a workaround, assigning small porosity values to a layer of elements around the deterministic fractures leads to smaller discretized storage coefficients and hence faster transport that matches much better with the Four-Fracture results (Fig. A-12)
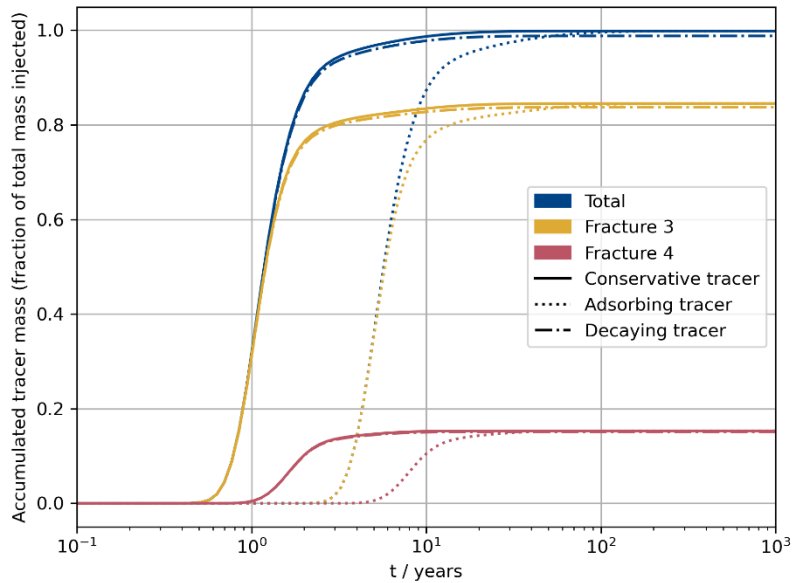
Fig. A-12. Cumulative mass breakthrough of tracers normalized by total injected mass after applying workaround.

The breakthrough curves show a very long tail. The results show that after about 12 years 99 % of the tracer has reached the downstream boundary. Nevertheless after 100 000 years, a small amount of tracer still remains in the domain such that even at late time there is still a small increase in the normalized breakthrough curves. One reason leading to this behaviour is possibly a quite large amount of numerical diffusion.

A.3.5 Continuous Point Source

In A.3.5 the source term is changed to a constant influx in point (-500, 7.0, 248.25) according to the task specification. Apart from that there is no difference in the model compared to the description in A.3.4 . Without re-parametrization of the element layer around the deterministic features, the computed relative breakthrough flow is again too slow. After re-parametrization the shape and times of breakthrough seem comparable to the Four-Fracture results (Fig. A-13, Fig. A-14). However, numerically the solution has not completely reached steady state after 100 000 years.
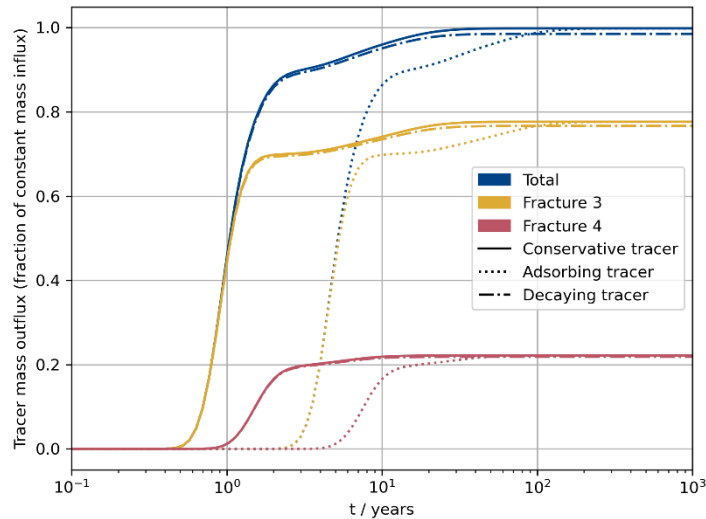
Fig. A-13. Summed tracer outflux normalized by constant point source influx using modelling workaround.
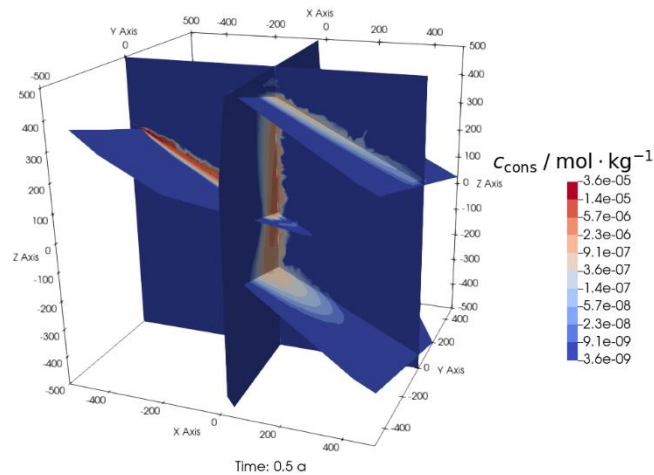
Fig. A-14. Calculated spatial distribution of the conservative tracer concentration after 0.5 years for Four-Fracture Plus Stochastic Fractures with Continuous Point Source.

A.3.6   Discussion of Benchmark Results

The transport of the tracers have been successfully computed. Hence, these results show the features but also some inherent flaws in the approach. To be able to resolve correctly the interface between the two flow and transport regimes of fracture and matrix correctly, a proper spatial resolution of the bulk mesh elements in the direction perpendicular to the fracture is required. However, this seems to be a strong restriction since a large number of bulk elements is not desired. It is expected that the flow in the deterministic fracture dominates compared to the matrix even if the local concentration

gradients are large. Here, a workaround is employed that artificially reduces the storage coefficient of the volume attached to the deterministic features.

A.4 Reference Case

The BGR work on the reference case has been concentrated on flow and transport in the fractured host rock which is assessed based on a full 3-D flow and transport simulation. Near field elements, representing the repository, have not been incorporated yet. Hydraulic flow and transport properties are taken directly from the task specification. As slight difference to the specification, the modelled domain center is located at (x=0, y=0, z=0) while in specification it is defined as (2500, 1000, 500).

A.4.1   Model Domain

The specified model domain is included explicitly for the flow and transport simulations. According to the modelling approach described above, the six deterministic fractures are represented and discretized using 2-D triangular elements with edge lengths between 25 m and up to 100 m at the edges intersecting the model bottom (Fig. A-15). This results in a total number of 6140 triangular elements.

The repository is not explicitly resolved. The representation comprises a mesh node at each of the 2500 canister positions used for tracer injection. These nodes are contained in a box with dimensions 1040 m x 652 m x 20 m that contain the originally specified extension of drifts and boreholes. Canisters, buffer inside the boreholes as well as drifts with backfill are not included in the mesh. Meshing of the deterministic fracture surfaces and the repository box is done using Gmsh (Geuzaine and Remacle 2009) and the BGR tool GINA_OGS (Kunz 2016).
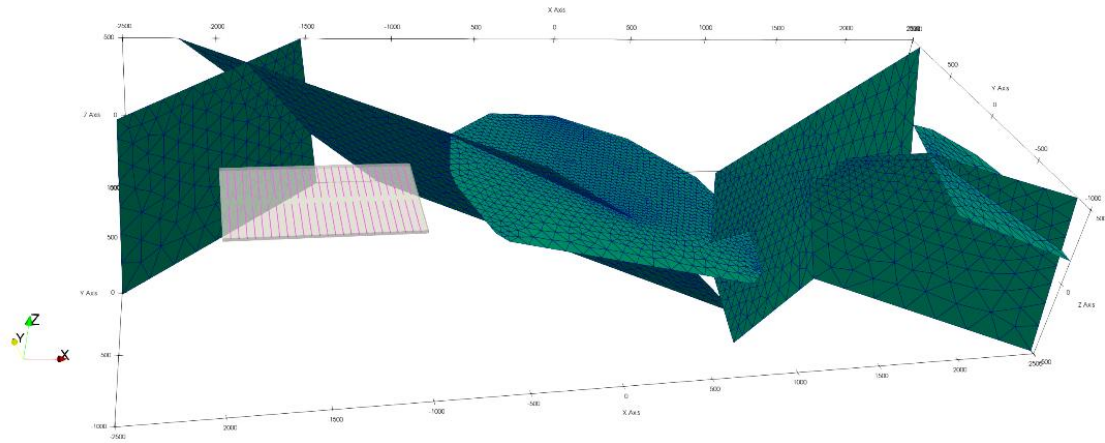
Fig. A-15. 2D mesh elements for representation of deterministic fracture zones and repository bounding box.

Using the surface meshes as fixed input, the tool Tetgen (Si 2015) is applied to obtain a conforming tetrahedral volumetric mesh (Fig. A-2). According to the smaller mesh size of the repository bounding box and the deterministic fractures around the repository the volumetric mesh is finer discretized in this area (Fig. A-16). The meshing comprises 637 029 3-D-elements and total number of 104 449 nodes.
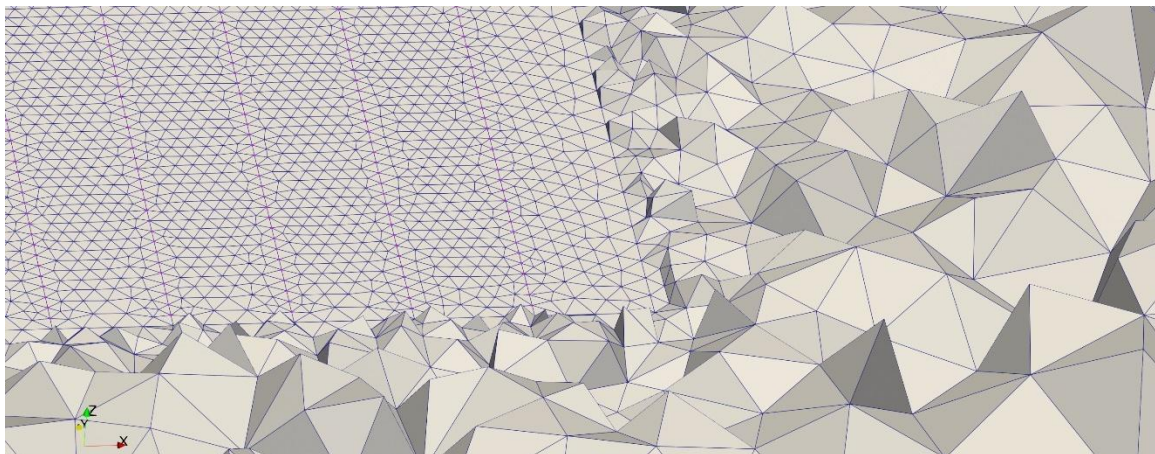
Fig. A-16. Zoom into the mesh at a corner of the repository.

A.4.2 Fracture Network

The stochastic fracture network is analyzed using the 10 realizations provided by Sandia. The provided data is then, after a technical format conversion, imported into the software FracMan® as polygonal, planar, 2-D objects. Although, FracMan® itself also offers functionality to sample fracture realizations from the statistical, priority has been set on computing stable flow and transport results. Hence, no additional realizations have been analyzed so far which also eliminates another source of possible deviations.

The hydraulic fracture properties (i. e permeability, porosity) are consequentially upscaled to parametrize the FE representation of the domain using the upscaling and mapping procedure (Fig. A-17). Mesh size for the intermediate cubical mesh is set to an edge length of 25 m. The computational grid is coarser away from the repository and fracture zones, such that the permeability provided by the fractures is smeared out additionally.

Since not all FE cells obtain non-zero permeability and porosity by this upscaling procedure these cells have to be treated differently. In contrast to the Four-Fracture benchmark, for the reference case these cells are considered in the computation avoiding isolated parts in the domain. These cells are assigned with a matrix porosity value of $\phi = 1.8 \cdot 10^{-3}$. To obtain a less heterogeneous parametrization, this value is also assigned to cells which obtained an upscaled porosity value of $\phi < 10^{-9}$. Moreover an isotropic permeability value of $k = 1.5 \cdot 10^{-18} \text{ m}^2$ is added to all cells. This is an increase by a factor of 1.5 in comparison with the value for the "fractured rock matrix" from the task specification (LaForce et al. 2023).

A.4.3   Flow Model

The OGS-6 implementation applies a direct bi-directional coupling between the hydraulic flow process and the modelled transport of solutes. This includes for example concentration dependent fluid density and permeability changes due to dissolution-precipitation. In general, this requires the solution of the fluid mass balance in each time step. Since the current state of the reference case, stationary flow using constant hydraulic properties is assumed, the flow field does not change over the assessment period. However, the numerical solver re-computes the flow field in every time step, which is done in very few linear solver iterations.
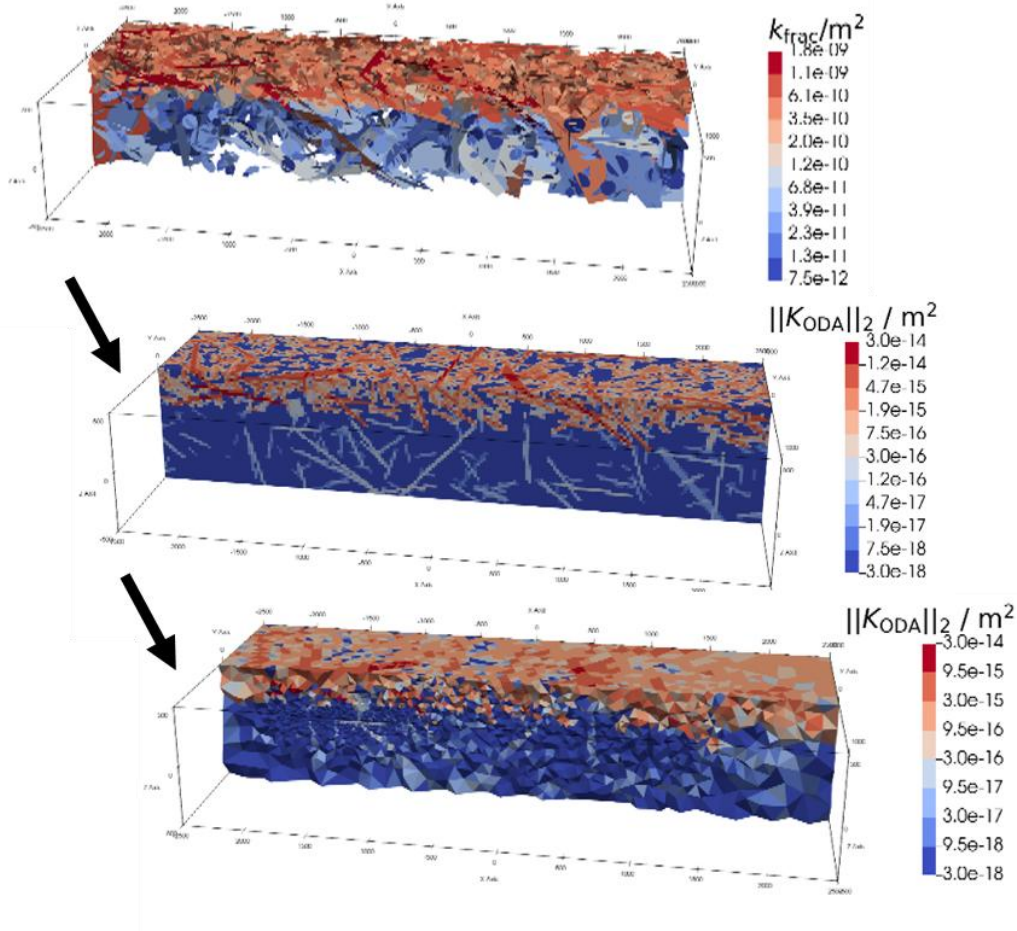
Fig. A-17. Illustration of the upscaling and meshing procedure for the permeability of the stochastic fracture network of realization 1 for flow and transport modelling in the reference case.

Since the model of the hydraulic system does not include nonlinear dependencies, the flow can be computed without gravitational body forces, i.e. the calculated pressure field has to be considered as difference to the hydrostatic pressure as it is imposed by the boundary conditions. The specified surface topology dividing the top surface in the three areas top of hill, hillslope and area of lowest elevation is modelled using Dirichlet boundary conditions. The fixed top surface pressures values provide the driving hydraulic gradient. All other boundaries are set to no-flow boundary conditions.
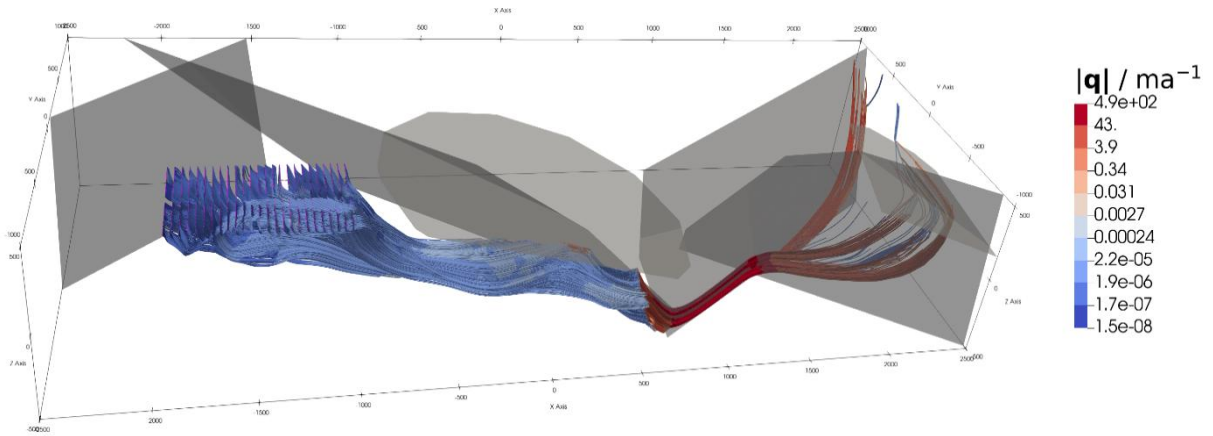
Fig. A-18. Streamlines starting at the canister positions for computed stationary flow for stochastic DFN realization 1.

The evaluation of Darcy flux at the top boundary show the strong influence of the deterministic fracture zones connected to the top surface. Main outflow region is computed along the deterministic fracture zone near (1500, 0, 500) (Fig. A-19). The summed values show the overall flow regime with inflow at the top of hill and outflow at the area of lowest elevation for all realizations. For the hill slope area some realizations yield overall influx while others show overall outflow (Tab. A-1).
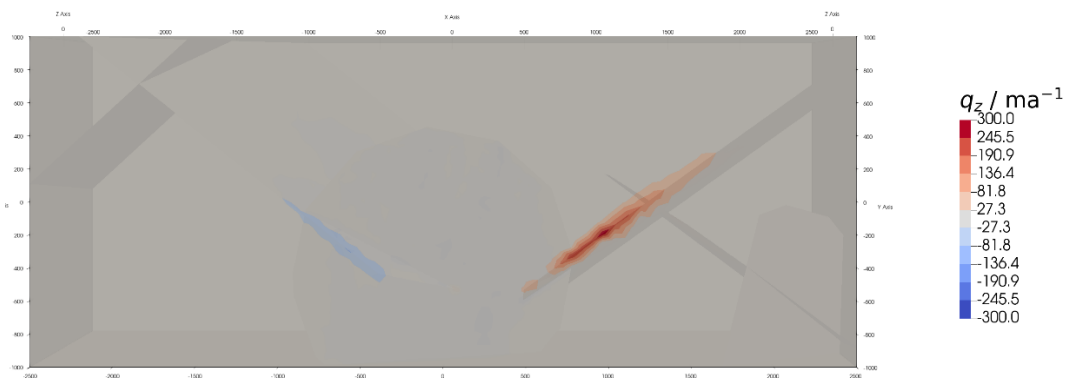
Fig. A-19. Vertical component of Darcy flow velocity on top surface.

Tab. A-1 Values for stationary summed in- and outflow of fluid mass in kg/year at top surface.

	Mean	95% CI min	95% CI max
Top of hill	463 303	418 074	508 531
Hill slope	-6413	-62 627	49 800
Area of lowest elevation	-456 889	-516 921	-396 857

A.4.4   Tracer Release and Transport

Tracer 1, representing an instant release fraction, is released into the crystalline rock domain as initial pulse. The amount of tracer corresponding to one canister is released at each of the nodes located at the canister locations. To get a slightly smoother problem the release is distributed as Gaussian pulse centered at 0.015 years.

Since fractional release results in a very slight decrease over 100 000 years, a constant yearly release of 1e-7 times the initial amount is assigned for Tracer 2. Similar to Tracer 1 the corresponding amount of one canister is released at each of the prepared injection nodes.

The parametrization of additional transport parameters does not currently include the information on underlying fractures. Inside the deterministic fractures the coefficient for free diffusion in water is assigned while for the volume elements, independent if they represent fractures or not, the effective value for the fractured rock mass is assigned for isotropic diffusion. Dispersion coefficients are not considered in this study.

In response to numerical instabilities during the solution procedure, a stabilization scheme has to be applied. For the reference case the isotropic diffusion stabilization with tuning parameter 0.25, as described above, is applied. Here, isotropic diffusion stabilization leads to sufficiently stable solutions for all realizations. However, this additional artificial diffusion even increases the diffusive transport in originally impermeable regions of the domain.

The breakthrough curves show some difference between the realizations however all cases show that a large part of the tracers is transported out of the domain during the assessed period of 100 000 years.
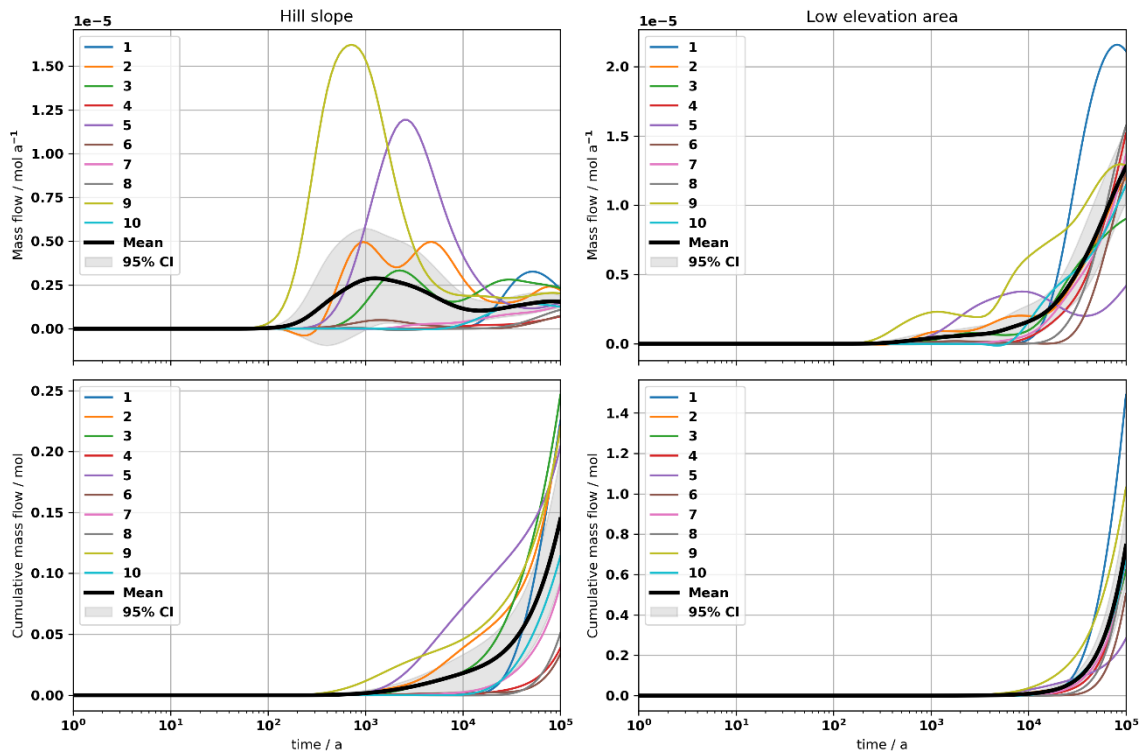
Fig. A-20. Mass flow and cumulative mass flow of Tracer 1 over top surface in hill slope and low elevation area: Results for 10 realizations, mean and 95% confidence interval for mean.
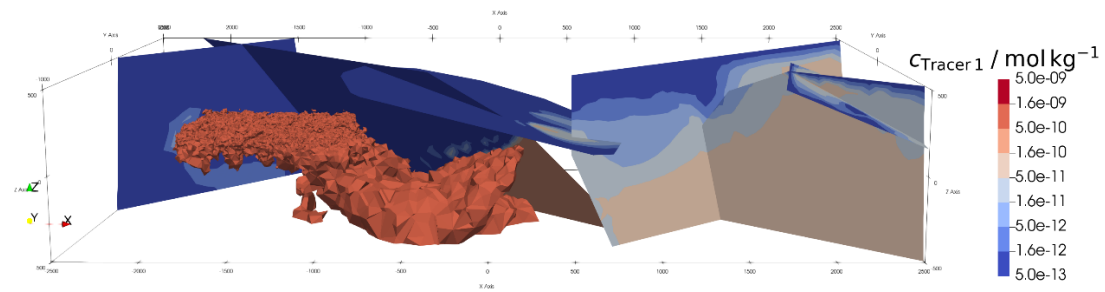
Fig. A-21. Surface plot and contour surface for Tracer 1 concentration of 1e-9 mol/kg after 15 000 years for realization 1.
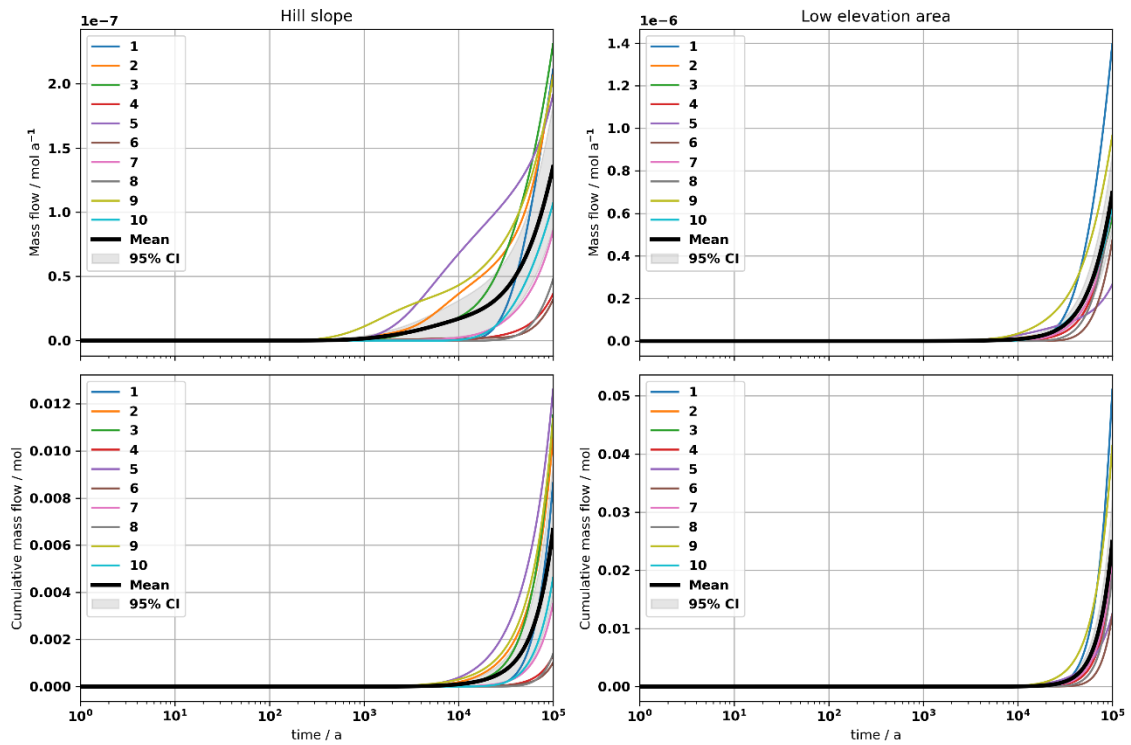
Fig. A-22. Mass flow and cumulative mass flow of Tracer 2 over top surface in hill slope and low elevation area: Results for 10 realizations, mean and 95% confidence interval for mean.

Results show that large portions of tracers are transported out of the domain. Since the tracers are directly released into the crystalline host rock and none of the near field components like a bentonite buffer is considered in this modelling study, relatively fast transport through the domain is expected. This is also reflected in the amount of tracer retained around the repository (Fig. A-23) which show that the tracers are transported away from the disposal area.
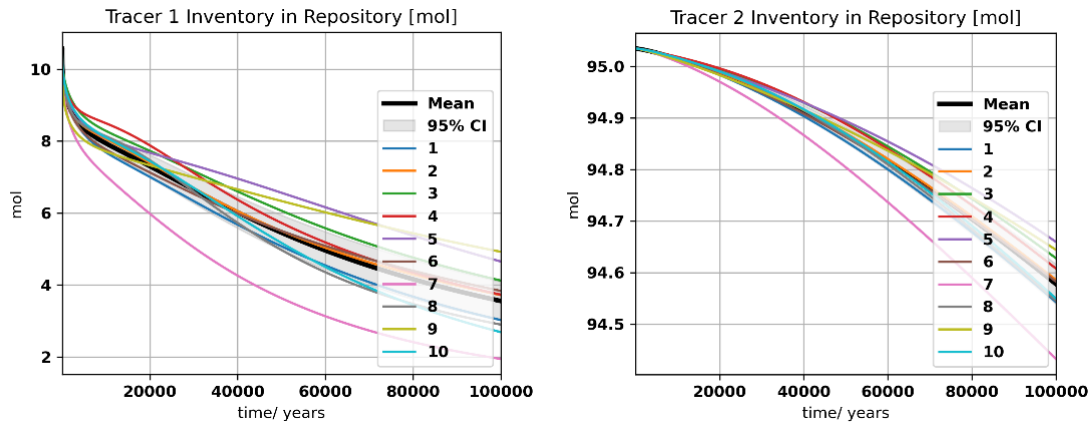
Fig. A-23. Amount of tracer retained in repository region.

A.5 Discussion

BGR contributed to the task with an approach for flow and transport through fractured rock. Features and issues (e.g. numerical instabilities) of the methodology were shown using the benchmarks as well as the reference case model. The modelling is based on the Discrete Fracture Matrix approach and an upscaling procedure aiming to represent the hydraulic characteristics of smaller fractures and their networks as properties from a porous medium. Here, permeability is upscaled using the procedure proposed by Oda (1985) which results in a full equivalent permeability tensor on a regular cube grid. Afterwards the upscaled parameters (i. e permeability, porosity) are mapped to an unstructured finite element mesh used for the numerical simulations. The procedure is extensible to other parameters and other upscaling approaches.

The flow and transport implementation as well as the developed modelling workflow have been applied to a set of Benchmarks of increasing complexity. The simple models with analytical solutions verify the correct implementation of the advection-dispersion process. The Four-Fracture benchmark provides a more realistic test for the approach. While the transport results for pure fracture transport case fit the flow results consistently, the addition of a network of smaller fractures to the rock matrix reveal a challenge for the selected approach. The interface between the fracture and the rock matrix is crucial for a correct representation of flow and transport within the fracture.

Finally the approach has been applied to the reference case repository system including the ten realizations of fracture networks generated by Sandia. A conforming finite element mesh of fractures, bulk and simplified repository design has been constructed. The computational results show that the selected approach can capture the flow and transport processes for this example.

In comparison, the computed tracer mass coming out of the domain is quite large. This is due to the missing representation of the near field elements in the model, especially the bentonite buffer. The underlying repository concept of the reference case, the Finnish/Swedish KBS-3 concept, heavily depends on the canister and, in case of canister failure (Posiva and SKB 2017), on the retention behaviour of the buffer. Hence, it is expected that in the comparison a system without bentonite buffer yields large amounts of transported tracer. Therefore without such extensions, the BGR approach is still not applicable for a repository performance assessment.

Consequently, the next step would be to add near field components to the model. Computationally efficient options include an independent near field model or a simplified representation of radionuclide mobilization and diffusion through the buffer. Although this would increase the numerical effort significantly, the Finite Element approach itself also provides the possibility to add a highly resolved near field representation directly into the 3-D-model. In essence, the selected modelling strategy has proven to be a flexible and effective basis for flow and transport simulations for the reference case.

A.6 References

Bilke, L., T. Fischer, D. Y. Naumov, C. Lehmann, W. Wang, R. Lu, B. Meng, K. Rink, N. Grunwald, J. Buchwald, C. Silbermann, R. Habel, L. Günther, M. Mollaali, J. Randow, T. Meisel, S. Einspänner, H. Shao, J. Rodriguez, K. Kurgyis, and O. Kolditz. 2022. "OpenGeoSys (6.4.3)." https://doi.org/10.5281/zenodo.7092676

V. Dalen. 1979. "Simplified Finite-Element Models for Reservoir Flow Problems." Society of Petroleum Engineers Journal 19 (05): 333-343. https://doi.org/10.2118/7196-pa

Dietrich, P., R. Helmig, M. Sauter, H. Hötzl, J. Köngeter, and G. Teutsch. 2005. Flow and Transport in Fractured Porous Media. Berlin Heidelberg, Springer-Verlag. DOI:10.1007/b138453

Geuzaine, C. and J.-F. Remacle. 2009. Gmsh: A 3-D finite element mesh generator with built-in pre- and post-processing facilities. International Journal for Numerical Methods in Engineering, 79, 11: 1309-1331. DOI:10.1002/nme.2579

Golder. 2017. FracMan® User's Manual Release 7.6. Golder Associates Inc.

Golder .2021. FracMan® 8.0 Manual. Golder Associates (UK) Ltd.

Kolditz, O., U.-J. Görke, H. Shao, and W. Wang, eds. 2012. Thermo-Hydro-Mechanical-Chemical Processes in Porous Media - Benchmarks and Examples. vol. 86, ISBN: 978-3-642-27176-2, Springer, DOI:10.1007/978-3-642-27177-9

Kolditz, O., S. Bauer, L. Bilke, N. Böttcher, J. O. Delfs, T. Fischer, U. J. Görke, T. Kalbacher, G. Kosakowski, C. I. McDermott, C. H. Park, F. Radu, K. Rink, H. Shao, H. B. Shao, F. Sun, Y. Y. Sun, A. K. Singh, J. Taron, M. Walther, W. Wang, N. Watanabe, Y. Wu, M. Xie, W. Xu, and B. Zehner. 2012. OpenGeoSys: an open-source initiative for numerical simulation of thermo-hydro-mechanical/chemical (THM/C) processes in porous media. Environmental Earth Sciences, vol. 67 (2): 589-599, DOI:10.1007/s12665-012-1546-x

Kröhn, K.-P., and W. Zielke. 1991. "FE-Simulation von Transportvorgängen im klüftigen Gestein." Deutsche Gewässerkundliche Mitteilungen 35 (3/4): 82-88.

Kunz, H. 2016. "GINA_OGS." In Thermo-Hydro-Mechanical-Chemical Processes in Fractured Porous Media: Modelling and Benchmarking, edited by O. Kolditz, U.-J. Görke, H. Shao, W. Wang and S. Bauer, In Terrestrial Environmental Sciences, 219-222. DOI:10.1007/978-3-319-29224-3

Kuzmin, D. 2009. "Explicit and implicit FEM-FCT algorithms with flux linearization." Journal of Computational Physics 228 (7): 2517-2534. https://doi.org/10.1016/j.jcp.2008.12.011.

LaForce, T., R. Jayne, R. Leone, P. Mariner, E. Stein, S. Nguyen, and T. Frank. 2023. DECOVALEX-2023 Task F Specification Revision 10. Sandia National Laboratories, Albuquerque, New Mexico, USA.

Oda, M. 1985. "Permeability tensor for discontinuous rock masses." Géotechnique 35 (4): 483-495. https://doi.org/10.1680/geot.1985.35.4.483.

Posiva, and SKB. 2017 Safety functions, performance targets and technical design requirements for a KBS-3V repository. Conclusions and recommendations from a joint SKB and Posiva working group. Posiva SKB Report 1.

Si, H. 2015. "TetGen, a Delaunay-Based Quality Tetrahedral Mesh Generator." ACM Transactions on Mathematical Software, 41 (2) 1-36. DOI:10.1145/2629697

Thiedau, J., J. Maßmann, C. Guevara Morel, S. Weihmann, and A. Alfarra. 2021. CHRISTA-II - Analysen zur Integrität von geologischen Barrieren von Endlagersystemen im Kristallin. Ergebnisbericht, Bundesanstalt für Geowissenschaften und Rohstoffe, Hannover.

Vogel, P., and J. Maßmann. 2015. "Verification Tests." In Thermo-Hydro-Mechanical-Chemical Processes in Fractured Porous Media: Modelling and Benchmarking.

Closed-Form Solutions edited by O. Kolditz, H. Shao, W. Wang and S. Bauer, In Terrestrial Environmental Sciences, 13-111. https://doi.org/10.1007/978-3-319-11894-9_2

Watanabe, N., and O. Kolditz. 2015. "Numerical stability analysis of two-dimensional solute transport along a discrete fracture in a porous rock matrix." Water Resources Research 51 (7): 5855-5868. https://doi.org/10.1002/2015wr017164.

Appendix B. Canadian Nuclear Safety Commission (CNSC)

B.1 Introduction

This study is based on the consideration of possible implementation of deep geological disposal for nuclear wastes in crystalline rocks. Many countries are actively developing their national programs for disposal of nuclear waste in underground environment. Two types of host rock appear to gain more interest lately, e.g. sedimentary rocks and crystalline rocks. There are many, including scientific, engineering, and political factors that affect the decision making on which type of host rock to be selected for waste disposal.

Crystalline rock is known to be mechanically strong. It is also known for its abundance in fractures and faults. The former provides solid foundation for the disposal facility to withstand geomechanical disturbances such as excavation damage and future glaciation impact. The latter usually raises environmental concerns regarding the potential pathways for contaminants to transport from the disposed wastes to the human accessible environment.

A few seminal review articles on flow and transport in crystalline rocks are worth mentioning in this introduction. Neumann (2005) reviewed studies on theoretical quantification of flow and transport in fractured rocks up to the time when it was published, and identified several critical challenges for a discrete fracture network (DFN) approach to overcome. Three types of modelling strategies were critically reviewed and compared therein: continuum strata, discrete fracture, and the hybrid of both (Neumann 2005). For continuum approach, a dual continuum model involves the rock matrix as one continuum and the fracture network as a separate but overlapping continuum to account for fluid and mass exchange between continua. By adjusting the parameters, it can be reduced to a single continuum if an overlapping entity dominates the flow and transport. Such models occasionally over-simplify the porous medium system, as fractures usually take up much less volume than the matrix medium. Multi-continua models lack the capacity to capture the discrete characteristics of the fractures, which are highly heterogenous, localized, and direction dependent.

On the other hand, a discrete fracture approach treats the fracture and the rest of rock mass in a non-overlapping manner, with the network of discrete fractures characterized as either deterministic or stochastic continuum with prescription of a uniform transmissivity. This requires detailed, and always challenging, mapping and delineation

of the geometry of fractures and the 3-dimensional network in the rock, as well as their characterization for transmissivity and aperture (Neumann 2005). The studies applying DFN for modelling of coupled hydraulic-mechanical processes in rocks was reviewed by Lei et al. (2017), with emphasis on geomechanical models and geomechanical effects on fluid flow in DFNs.

By joining the DECOVALEX project, CNSC staff are actively engaged in cutting-edge research activities, contribute to acquiring up-to-date knowledge about environmental risk assessment, and improve our preparedness for the future review and licensing activities for the disposal of nuclear wastes.

In this task (Laforce et al. 2023), we developed the skills and capacity to model the fractured crystalline rocks using a discrete fracture network (DFN) approach. We investigated several different approaches to the modelling of fractured flow and transport. Eventually we identified the most efficient approach and streamlined the workflow to implement the DFN in the framework of finite element model. With the developed workflow and numerical models, we assessed the advective-diffusive transport of tracers through the connected fracture networks. The numerical results are comparable to those of peer international teams (see main text).

B.2 Numerical methods and tools

The flow and transport in fractured medium are modelled with the finite element method in this study. Darcy's law is applied to the flow problem, while the advection-diffusion equation is applied to the transport problem. The numerical models were developed using COMSOL version, 6.0.

There are two types of fractures considered in this study, namely the stochastic and deterministic fractures. The deterministic fractures could be implemented as plane interface elements in COMSOL. However, the authors noted the difficulty to analyse the results in the postprocessing. Therefore, solid elements of a relatively small thickness are used to represent the deterministic fractures.

For the stochastic fractures, there are several different approaches available for modelling. The authors believe two categories of methods are available for DFN realization, i.e. the explicit and implicit methods. The explicit method involves creating fracture features in the geometric model, with specific geometric characteristics. COMSOL provides the functionality to create explicit fractures in either plane, or solid domains. For a large field model with scale of several kms, it is very computationally demanding to take the explicit approach to create DFNs. One of the reasons is that the

FE solver needs to integrate over each boundary to retain mass balance and calculate boundary fluxes, which entails more interfacial boundaries resulting in increased computing time. A DFN model usually has a substantial number of fracture planes, with complex interconnection often resulting in ill-shaped elements at the interconnection leading to numerical problems (Benedetto et al. 2016) Therefore, it proves to be challenging and nearly impractical to implement an explicit DFN model for the complex field problems in finite element codes such as COMSOL.

On the other hand, an implicit DFN approach relies on the representation of fractures with a dataset of characteristic properties, such as permeability. This is very efficient to solve by FEM since there is no redundant internal boundaries between elements. In COMSOL, the authors noticed that the spatial resolution of implicit DFN can be very well maintained, regardless of the constraint of meshing size. After careful evaluation of these available realization strategies, the implicit DFN approach was adopted in this study for the modelling.

The authors also proposed an EPM model to represent the permeability of the stochastic fractures, which was implemented successfully in COMSOL to calculate the flow parameters on the basis of a 3D matrix of random numbers. The task leaders from Sandia National Laboratory created a permeability dataset upscaled from discrete fracture network approach. The dataset was used by several participating teams for their modelling realizations.

The authors developed a similar DFN approach for permeability upscaling. Our approach was based on a stack of cross-sectional images of fractures at multiple depths, which was then transformed into pixel values and imported into COMSOL for 3-dimensional interpolation. The resulted data was further processed inside COMSOL to derive the corresponding permeabilities usable for the flow and transport model. The images of DFN were created by a self-developed Python code, with the stochastic natures precisely accounted for.

B.2.1   Equivalent permeability of fractures

The statistical characteristic of the fracture size follows a power law distribution of the following form:

$$R = R_0 \left(1 - u + u \left({R_0}/{R_u} \right)^\alpha \right)^{-1/\alpha}$$

where u is a random number range from 0 to 1, R0 and Ru are minimum and maximum radius of the fracture, respectively, and index α. Three parameters constrain the DFNs, i.e. minimum and maximum radii, and the index α. For the field model of this study,

these parameters were given as R0=15m, Ru=560m, and α is varied dependent on orientation for each hydrogeological unit, approximately ~2.5.

Transmissivity is correlated with fracture size using a power law in the form of

$$T = aR^b$$

where parameters a and b are dependent on hydrological units and are varied across depth, with a governing the order of magnitude and b about 0.8.

Hyman et al. (2016) has thoroughly investigated the relationship between transmissivity and fracture size using DFN modelling of three types of correlational models that are function of power law, log-normal law, and the mixture of both. The above equation is one of those used by Hyman et al. (2016) as perfectly correlated model, and was proven reliable and in great agreement with other correlated models with respect to characteristics of tracer transport and hydraulic flow. Therefore, it is well justified to use a power law correlation for the following investigations.

Permeability obeying the cubic law of fracture aperture is correlated to transmissivity of rock mass as follows:

$$B = \sqrt[3]{\frac{12\mu T}{\rho g}}$$

where B is aperture, T is transmissivity, µ is dynamic viscosity, ρ is density and g is specific gravity.

It is important to upscale the transmissivity of a plane fracture to the permeability of a solid domain fracture with thickness meaningful to the scale of mesh size for a FE model. The key to this upscaling is the equivalence of transmissivity between plane fracture and solid fracture. In order to overcome numerical difficulties as a result of thin abnormal element in the simulation, a minimal thickness (L) of 20 m is applied to all fracture elements in this study for the DFN realization. Therefore, the equivalent permeability of the solid domain fracture can be calculated as the geometric mean of both portions as given below,

$$K = \frac{\rho g}{12\mu}\frac{B^3}{L} + K_i\left(1 - \frac{B}{L}\right)$$

where B is fracture hydraulic aperture, L is applied solid fracture thickness, K_i is the permeability of intact rock.

It is noted that the intact rock has permeability much less than that of the fractures, but due to its dominance in volume and is thus a significant term in this system. The average aperture B of the stochastic fractures is in the range of tens of micrometers.

B.2.2   Explicit DFN realization examples

Thin disc

This example of thin disc-shaped DFN is shown in figure below. The density of fractures varies with fracture size and follows a power law of distribution. The example shows the created DFN for a field model as used in the reference case. Fractures are in solid element, 10m thick, spatially orientated and depth dependent for each layer of geological strata. For convenient implementation, a JAVA script was programmed to automate the realization of DFN.
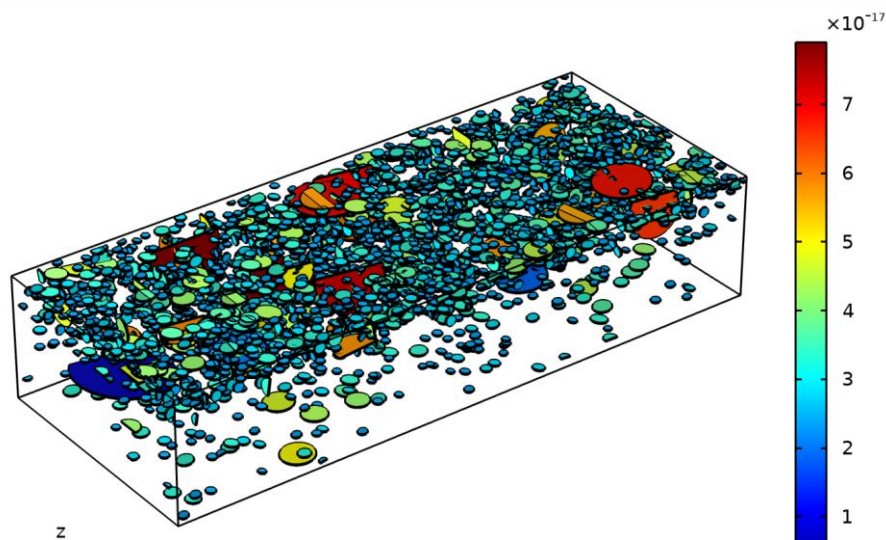
Fig. B-1. Illustrative sketch of DFN realization by thin discs.

Regularly patterned fine elements

This example involves creating an array of solid domains that are regularly patterned and is composed of interfaced fine elements. For creation of DFN, a sequence of selections was made in COMSOL to identify the spatial dimension and geometry of a single fracture, and to assign corresponding material properties to the selection. This method was found to be heavily CPU demanding, as arrayed domain has much more connected boundaries to resolve by FEM. It is also found to run through for Darcy flow problems, but hardly succeed for advective diffusion problems.
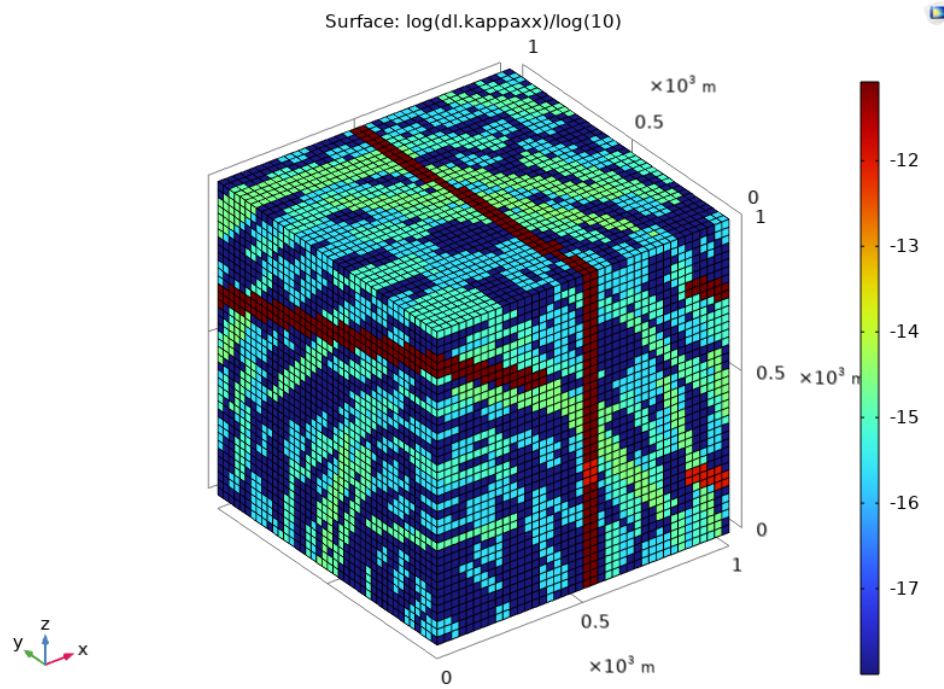
Fig. B-2. Illustrative sketch of DFN realization by array of fine elemental domains.

B.3 Benchmarks

The benchmark test case consists of a cubic domain containing 4 interconnected deterministic fractures. The properties of the fractures are shown in table below. The shape, size, and coordinates of the 4 fractures are prescribed in the task specification. This study follows the exact definition with no modification.

B.3.1 FEM model and meshing

The following graphs show the realized 4 fractures and the obtained mesh. For implicit realization of the deterministic fractures, a prerequisite model was created with the geometric feature of 4 fractures represented by thin solid domains. The prerequisite model was solved to derive a datafile containing the permeability of the fractures to be used in following studies. The prerequisite model is obviously realized by the explicit DFN approach.
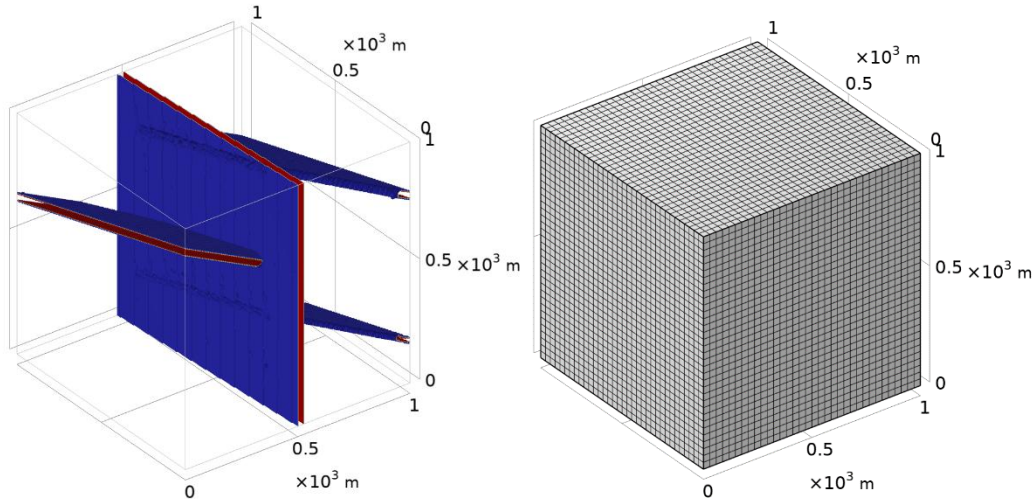
Fig. B-3. Geometry of the 4 fractures and the obtained meshing of the FEM model.

B.3.2 Four-Fracture Transport

Boundary conditions and model parameters

The following table presents the pressure boundary conditions along with the properties of each fracture. These parameters are sufficient to model the 4 fractures network. This test case omits the influence of matrix diffusion and matrix permeability, therefore only the fractures are simulated.

Tab. B-1. Boundary conditions and relevant fracture characteristics.

Parameter	Value	Units
Pressure (inlet, x=0)	1.001×10^6	Pa
Pressure (outlet, x=1000)	1×10^6	Pa
Deterministic fracture 1 aperture	1	mm
Deterministic fracture 2 aperture	1	mm
Deterministic fracture 3 aperture	1	mm
Deterministic fracture 4 aperture	0.5	mm
Deterministic fracture 1 permeability	8.333×10^{-8}	m^2
Deterministic fracture 2 permeability	8.333×10^{-8}	m^2

Deterministic fracture 3 permeability	8.333×10^{-8}	m^2
Deterministic fracture 4 permeability	2.083×10^{-8}	m^2

Results

This test case only considers 4 deterministic fractures. The fracture aperture and permeability are given in the above table. Three types of tracers are simulated, respectively. The tracers are all released continuously from the left boundary. The outlet is set on the right boundary, and tracer fluxes are monitored during the simulation. Results are shown in below.
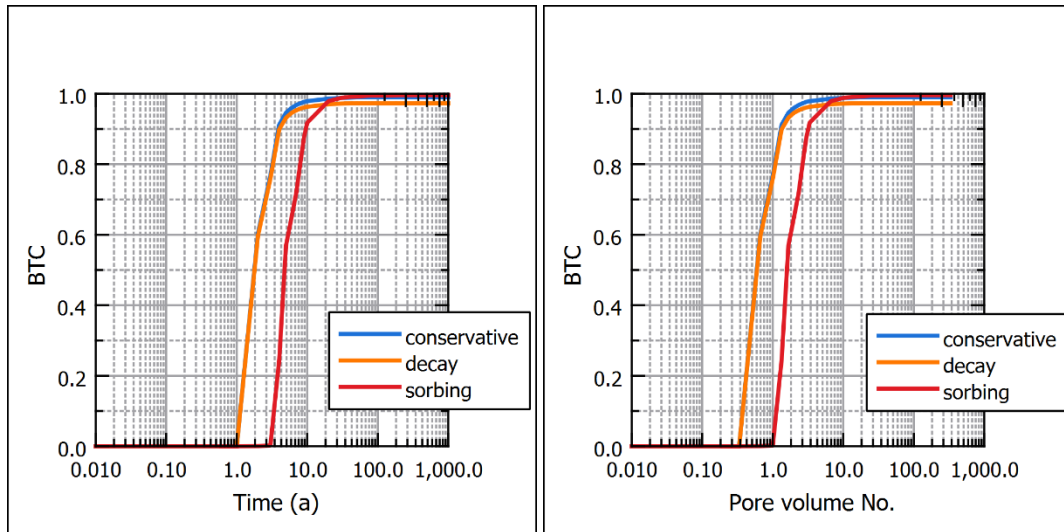
Fig. B-4. Breakthrough curves of study cases against elapsed time (left) and pore fluid volume (right).

B.3.3   Continuous Point Source

Boundary conditions and model parameters

The following table presents the pressure boundary conditions and the properties of the matrix. This test case considers the influence of matrix flow and matrix diffusion. Two additional scenarios of decay and sorption are also included in the simulation.

Tab. B-2. Boundary conditions and relevant fracture characteristics.

Parameter	Value	Units
Pressure (inlet, x=0)	1.001×10^6	Pa
Pressure (outlet, x=1000)	1×10^6	Pa
Porosity in a fracture	1.0	-
Tortuosity in a fracture	1.0	-
Matrix porosity	0.005	-
Matrix permeability	10^{-18}	m^2
Diffusion coefficient in water (D_0)	1.6×10^{-9}	m^2/s
Half-life ($t_{1/2}$)	100	year
Retardation factor in fracture (R)	5	-

Results

This test case has both deterministic and stochastic fractures in consideration. The model resulted in total pore volume of 4.97E6 m^3, and total deterministic fracture volume of 1.13E6 m^3.

Three test problems were simulated, i.e. the conservative tracer, sorbing tracer and decaying tracer, respectively. The breakthrough curves of the three test problems were plotted against the time and number of pore volumes, as shown below. It is shown that the time when tracer first breaks through to the exit boundary is increased from 1 year to 4 years when sorbing is considered. Total breakthrough can be achieved after 200 years for conservative tracers. Sorbing can delay this to over 400 years. Decaying tracer is found to result in a reduced exit concentration to 95% of the inflow.

When pore volume is accounted for, the tracer transport appears to occur preferentially in the fractures because breakthrough occurs at 0.4 pore volume for both conservative and decaying tracers, and at 1.0 pore volume for sorbing tracers. If the transport takes place in a homogeneous porous medium, an ideal scenario of breakthrough is expected to occur at a unit pore volume of flow. The presence of deterministic fractures greatly enhanced the flow and facilitated the transport by reducing 60% of pore volume. This

simulation result is consistent with the general understanding of the role of preferential flow pathway in solute transport.
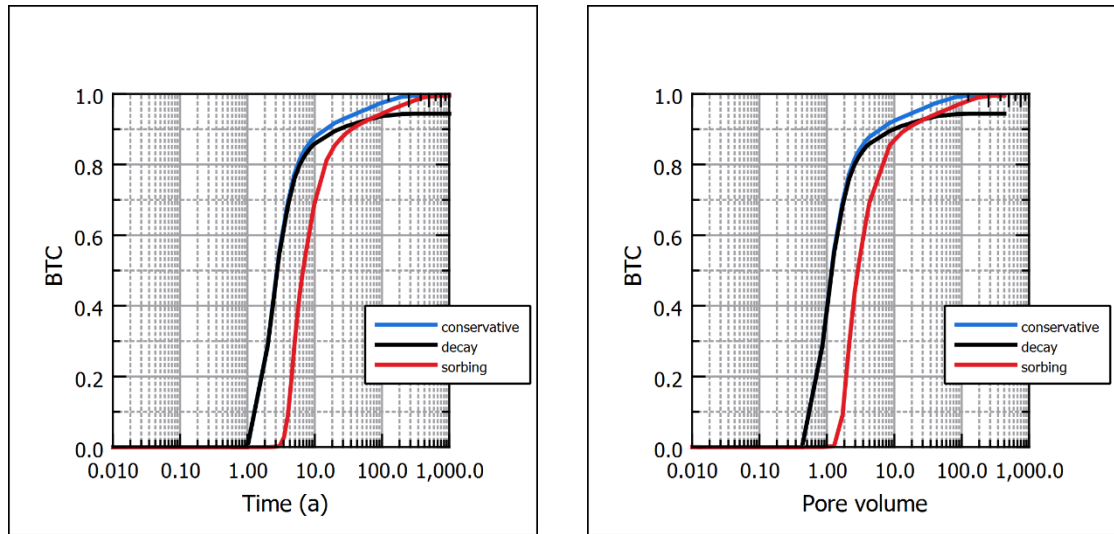
Fig. B-5. Breakthrough curves of study cases against elapsed time (left) and pore fluid volume (right).

B.4 Reference Case

The reference case studies the tracer release from waste containers into the repository environment. The engineered barrier systems of the near field system are clearly defined with fundamental parameters for hydraulic flow and solute transport. The far-field repository consists of three depth zones of substantially different hydrogeological properties. Fractures include both the deterministic and the stochastic ones as given in the task specifications.

One of the biggest challenges to this reference case is how to address the multi-scale modelling problem that encompasses elemental sizes ranging from centimeters to tens of meters. Although, it is technically possible to discretize the problem by adaptive meshing and mesh refinement in regions of finer resolutions, this will inevitably increase the degree of freedom of the obtained numerical model to a substantially high amount so that only super computers could satisfy the computational needs.

This study proposes to divide the multiscale problem into two parts, i.e. the near-field and the far-field problems. The near-field model simulates a single canister placed in the emplacement. The representative element volume was taken between the midline of neighbour emplacement rooms. Hydraulic field of the small-scale REV was taken from the large-scale field model. Solute transport from the waste package was modelled with the advective-diffusion equation. The mass flux of tracers across the EBS outwards to

the host rock was computed for each emplacement room and was used as a source term to interface with the far-field model for long-term assessment.

B.4.1   Near Field Model

Boundary conditions and parameters of the near-field model

The following Figure shows the geometry of the near-field model. The connecting tunnel and emplacement room are highlighted in blue, while the surroundings are host rock in repository. The elevation and coordinates are identical to those used in the far-field model. The cross-sectional profile of the emplacement room is also shown below. The waste canister is contained in compacted bentonite clay. In this model, the waste package is not considered, but is represented by surface reaction at its interface with the bentonite. Two types of tracers are considered, i.e. the transient release of tracer 1 and constant release of tracer 2.
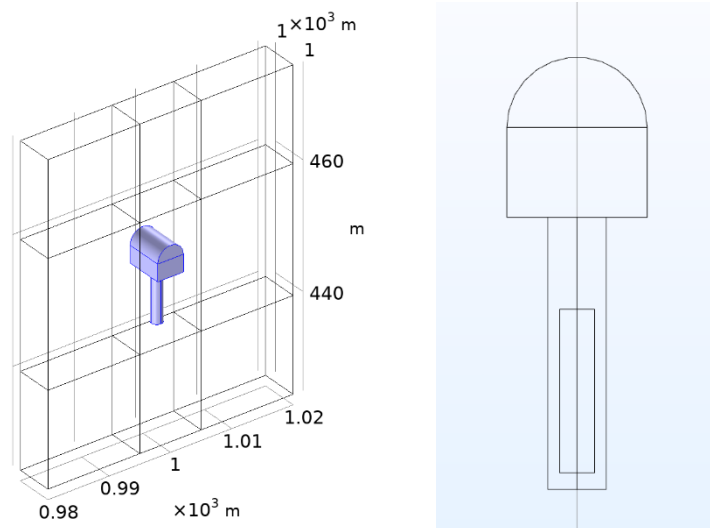
Fig. B-6. Diagram of geometric model for the near field model.

Results

The release rates of both tracers were predicted by the near-field model, and are shown in the figure below. This result is further used as the source term in the following far-field model. The concentration distribution of tracer 1 is shown at different post-closure duration of time. It is clear that solute transport follows the direction of groundwater flow. Transport in EBS is dominated by diffusion. Tracers are found to be contained inside EBS for about 100 yrs. Breakthrough of tracers into the host rock is observed after 1000 yrs. The peak concentration is found to decrease with increasing elapsed time, indicating the consistent spread of tracers in space.
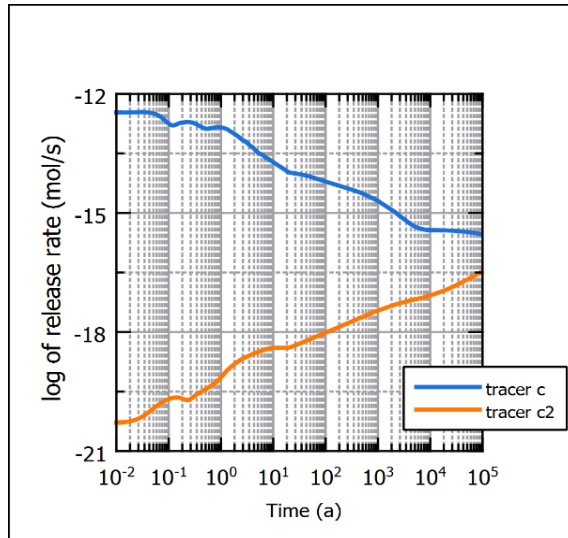
Fig. B-7. Release rates of tracers from the waste package into repository host rock.
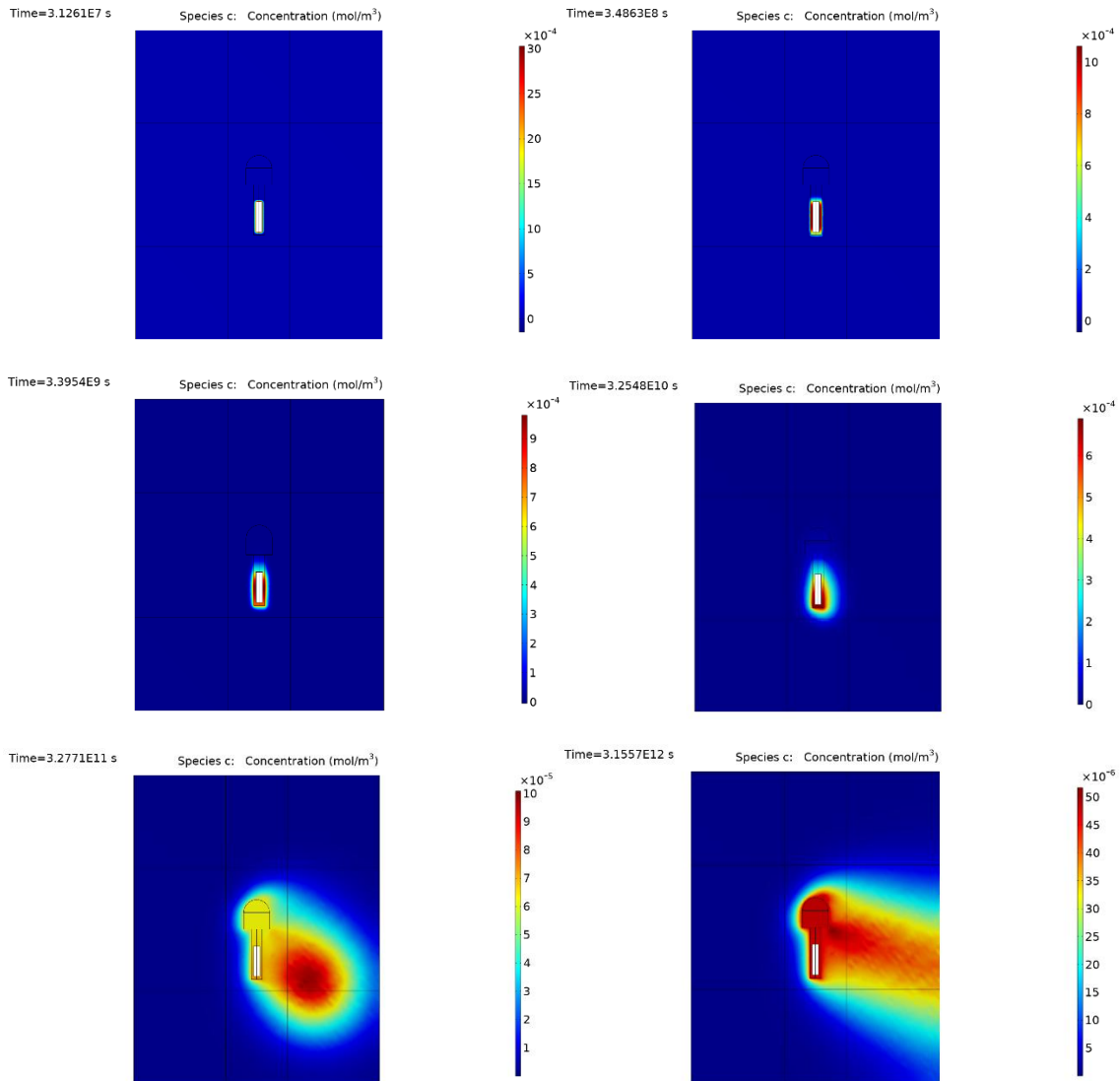
Fig. B-8. Concentration distribution of tracer 1 in different time.

B.4.2 Far-field model

Boundary conditions and parameters of the far-field model

In the reference case, the surface slope is from left to right with 20 m height difference as shown in the following figure. The surface is flat from left (x=0) to x=1700m. It gradually slopes down by 20 m from x=1700m to x=3700 m, then becomes flat again from x=3700 to x=5000 m. Pressure is defined as atmospheric pressure for both the upper and lower flat surfaces while the slope surface is impermeable.

Stochastic fractures are considered in the model. The fracture parameters are shown in the specification document. Three depth zones are defined in this test problem, with the shallow zone having the most abundant and most permeable fracture networks.

The pore pressure distribution in steady-state conditions is shown below. It is noted that a 40% of underpressure is present to the upper portion of the slope surface until x<2500 m. Meanwhile, an overpressure (40% in average, and 200% in maximum) is present to the lower portion of the slope surface. Overpressure is results from the highly permeable fracture network that connects with the deeper regions with higher static pore pressure.
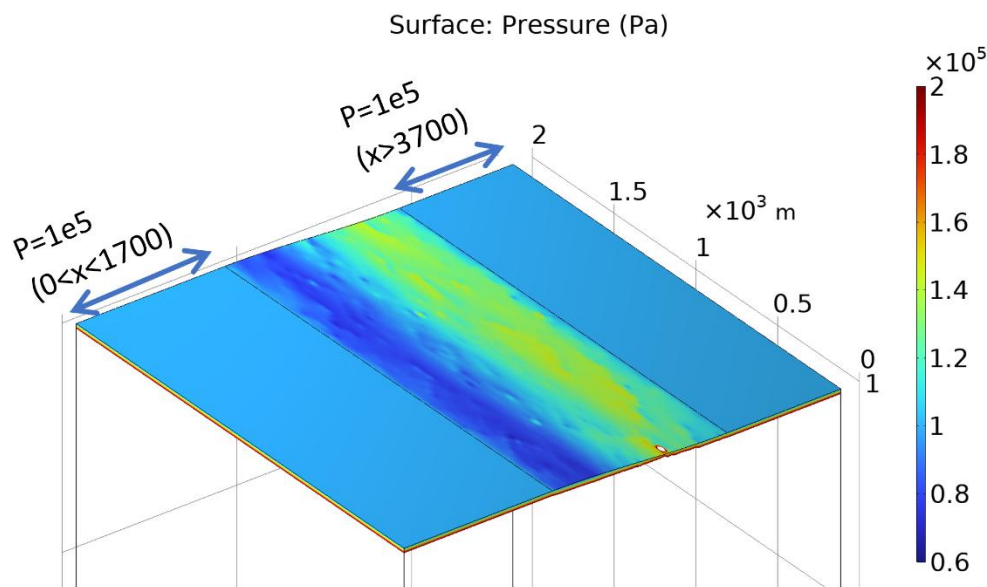
Fig. B-9. Ground surface elevation, the boundary condition of pressure and its distribution on slope.

FEM model and meshing

The FEM model and its meshing are shown in figure below. Using the implicit method described above, permeability is assigned to the Darcy's flow module by interpolation of an imported dataset as a result of permeability upscaling for the fracture networks.

The resolution of the imported dataset is much less than the mesh size of the FEM model to ensure precise representation of the DFNs (Fig 11).
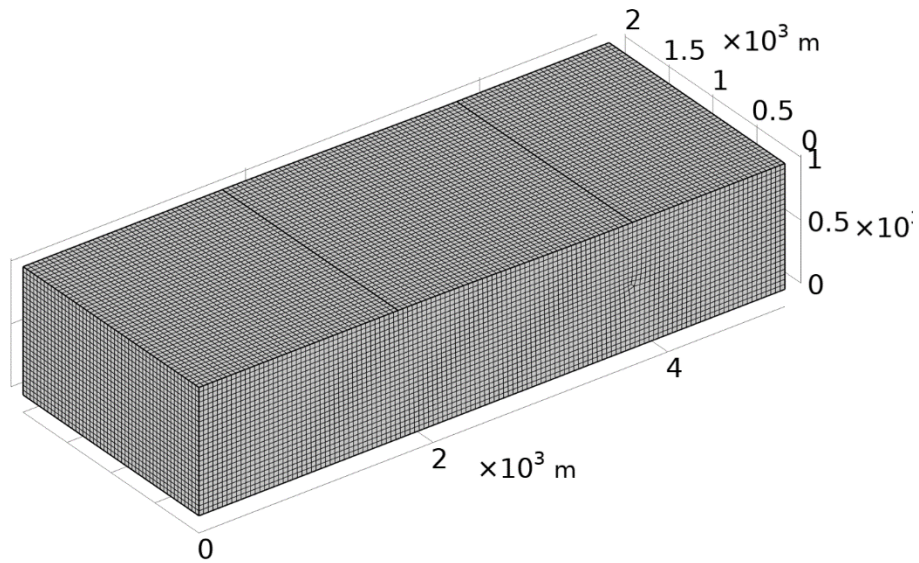
Fig. B-10. Geometric domain and the meshing of the field model.
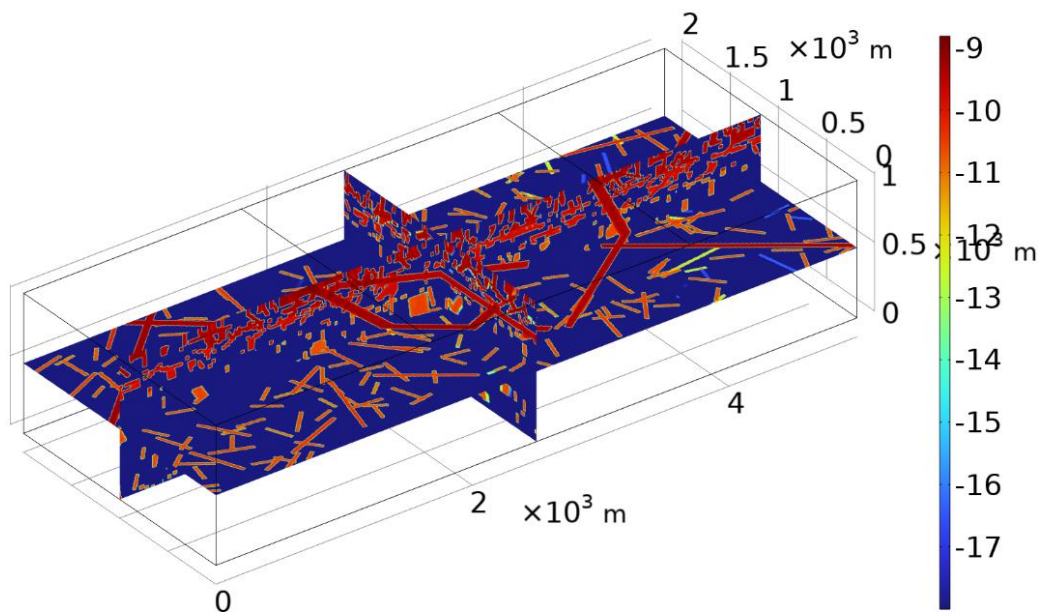
Fig. B-11. Multislice plot of permeability distribution.

Results

Retention of tracers was calculated by subtracting the integral of boundary flux from the total input. The graphs show the temporal evolution of tracer retention in the repository. Simulations were repeated for 10 reproductions of the DFN model. All the results are plotted in the graph below. It is clear that the results are closely correlated and consistent with each other. Despite the fact that discrete fractures are based on random numbers with stochastic nature, the implicit DFN model proved to successfully capture the hydraulic properties of the repository. Transport of tracers in the repository is dominated by advective diffusion in the network of fractures. In the shallow depth zone, the permeability of stochastic DFN is comparable to that of the deterministic fractures, which further enhances the migration towards the discharge zone at the toe area of the slope.
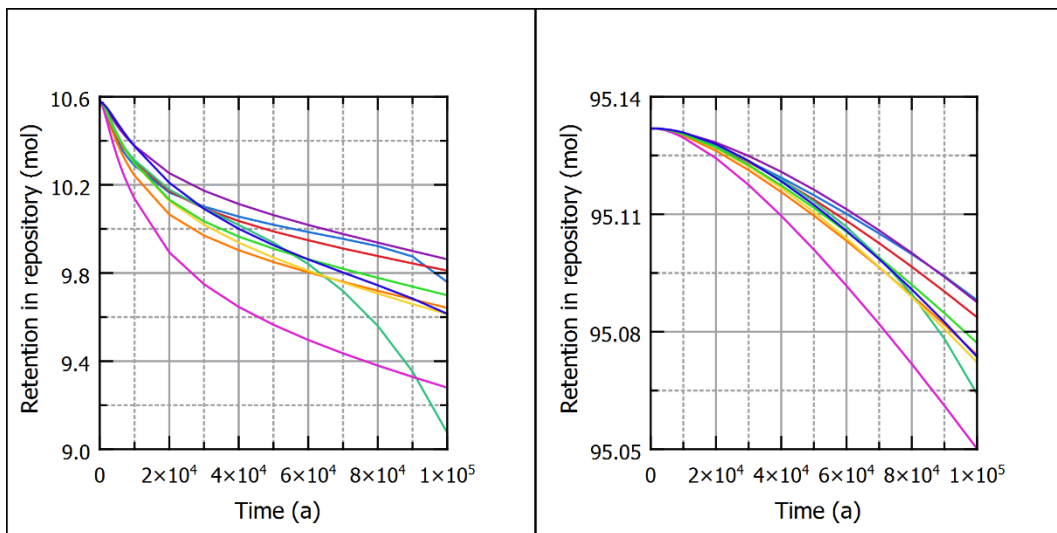
Fig. B-12. Total quantity of tracers retained in the repository versus elapsed post-closure time.
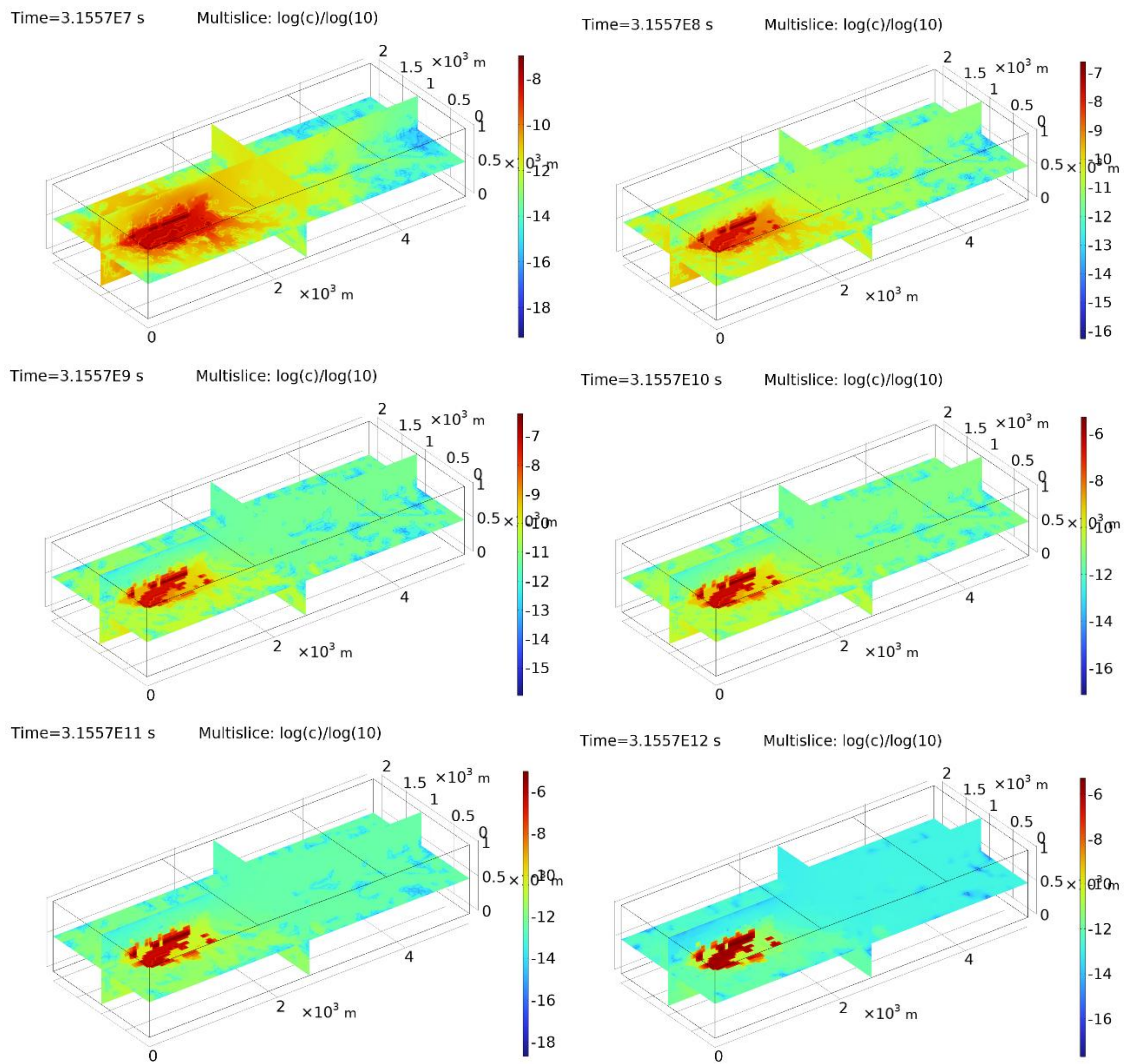
Fig. B-13. Multislice plotting of tracer concentration at various post-closure time.

B.5 Conclusions

This study tested a number of different approaches to realizing discrete fracture networks in the FEM framework for the study of flow and transport in crystalline rocks. The best practice of DFN realization was identified and optimized for the evaluation and assessment of tracer transport in two types of test cases, namely the 4FRAC benchmark and the reference case. The 4FRAC benchmark test case modelled both deterministic and stochastic fractures. The successful calibration of the models with this test case promised the extended implementation into the study of field case. The field case simulated flow and tracer transport from hypothetical waste packages emplaced in the geological formation containing 6 deterministic fractures and a number of stochastic fractures that were well characterized. Ten realizations of the field case were produced and the results are consistent and comparable to each other. It is found that the majority

of tracers are still retained in the repository, particularly in the engineered barrier systems. Through this study, the authors acquired up-to-date knowledge about discontinuities in crystalline rocks and the skill of DFN modelling, which significantly improved our preparedness for the future assessment and review of relevant waste disposal projects.

B.6 References

Benedetto, M.F., Berrone, S., Borio, A. et al. (2016) A hybrid mortar virtual element method for discrete fracture network simulations. Journal of Computational Physics. 306: p. 148-166. DOI: https://doi.org/10.1016/j.jcp.2015.11.034

Hyman, J.D., Aldrich, G., Viswanathan, H., et al. (2016) Fracture size and transmissivity correlations: Implications for transport simulations in sparse three-dimensional discrete fracture networks following a truncated power law distribution of fracture size. Water Resources Research. 52(8): p. 6472-6489. DOI: https://doi.org/10.1002/2016WR018806

Laforce, T. R.J., Leone, R., Mariner, P., Stein, E., Nguyen, S., Frank, F., (2022) DECOVALEX-2023 Task F Specification (Revision 10), US Department of Energy

Lei, Q., Latham, J.-P. and Tsang, C.-F. (2017) The use of discrete fracture networks for modelling coupled geomechanical and hydrological behaviour of fractured rocks. Computers and Geotechnics. 85: p. 151-176. DOI: https://doi.org/10.1016/j.compgeo.2016.12.024.

Neuman, S.P. (2005) Trends, prospects and challenges in quantifying flow and transport through fractured rocks. Hydrogeology Journal. 13: p. 124-147

Appendix C.   Korea Atomic Energy Research Institute (KAERI)

Acronyms

1D	1-dimensional
ADE	advection-dispersion equation
BTC	breakthrough curve
DECOVALEX	DEvelopment of COupled models and their VALidation against Experiments
DFM	discrete fracture matrix
DFN	discrete fracture network
ECPM	equivalent continuous porous medium
HCD	hydraulic conductor domain
HLW	high-level radioactive waste
HRD	hydraulic rock mass domain
IRF	instant release function
KAERI	Korea Atomic Energy Research Institute (KOREA)
NBS	natural barrier system
PWR	pressurized water reactor
SNF	spent nuclear fuel
SNL	Sandia National Laboratories (US)

C.1 Introduction

HLW disposal research at the KAERI started in 1997 with the goal of developing a deep geological disposal system for the direct disposal of spent nuclear fuel. The Korean disposal concept for PWR spent nuclear fuel is the KBS-3V type whose engineered barrier system consists of a cast iron-copper dual structure disposal canister and Ca type bentonite. And, granite bedrock, which is a representative rock type in Korea, is considered as the host rock. Recently, KAERI has been developing an adaptive process-based total system performance assessment modelling framework which can reflect the complex processes occurring in each component of the repository system. The DECOVALEX Task F contributes to the validation of the modelling framework under development.

In the Task F, KAERI has conducted various benchmarks related to radionuclide transport through the fractured rock using the modelling framework under development, and finally applied it to the reference case which is composed of an artificial geological disposal system. In this appendix, the overall methodology of the modelling framework and the specific approaches to performing benchmarks and reference case with their results will be documented.

C.2 Methods

KAERI's PA modelling tool is mainly COMSOL Multiphysics v.6.1 which uses the finite-element method. In this study, *Darcy's Law* physics and *Transport of Diluted Species in Porous Media* physics (advection-dispersion equation, ADE) are used for groundwater flow and solute transport, respectively.

In *Darcy's Law* physics, the continuity equation is as follows (COMSOL, 2019):

$$\frac{\partial}{\partial t}(\rho \epsilon_p) + \nabla \cdot (\rho u) = Q_m$$

where, ρ represents the fluid density (kg/m³), ϵ_p is the porosity, and Q_m is a mass source term (kg/m³·s). For a steady-state problem, the first term disappears. Meanwhile, velocity field u takes the form:

$$u = -\frac{\kappa}{\mu}(\nabla p)$$

where, κ denotes permeability of porous media, μ is dynamic viscosity of the fluid, and p is pressure in the porous media.

In *Transport of Diluted Species in Porous Media* physics, the governing equation for solute transport in porous media is as follows:

$$\frac{\partial(\epsilon_p c_i)}{\partial t} + \frac{\partial(\rho c_{P,i})}{\partial t} + u \cdot \nabla c_i = \nabla \cdot [(D_{D,i} + D_{e,i})\nabla c_i] + R_i + S_i$$

where, c_i represents the concentration of species *i* in the liquid (mol/m³), $c_{P,i}$ represents the amount adsorbed to solid particles (moles per unit dry weight of the solid). On the left-hand side of the above equation, the first two terms describe the accumulation of species within the liquid and solid phases, while the last term describes the convection due to the velocity field u. On the right-hand side of the above equation, the first term introduces the spreading of species due to mechanical mixing resulting from the porous media (dispersion), as well as diffusion and volatilization to the gas phase. The dispersion tensor is denoted as $D_{D,i}$ (m²/s) and the effective diffusion is represented by $D_{e,i}$ (m²/s).

The last two terms on the right-hand side of the above equation describe the production or consumption of the species. R_i is a reaction rate expression which can account for reactions in the liquid, solid, or gas phase, and S_i is an arbitrary source term, for example, due to a fluid flow source or sink (COMSOL, 2019).

Normally, the groundwater flow is firstly solved with a stationary solver to obtain a Darcy velocity field. Thereafter, the Darcy velocity field is applied to the advection term in the following solute transport calculation using a transient solver. Regarding the mesh, a tetrahedral mesh is used.

Both the equivalent continuous porous medium (ECPM) and discrete fracture matrix (DFM) methods are considered to represent the hydraulic and transport properties of fractured rock in this study. The upscaling is conducted by an in-house MATLAB code, *DFN2ECPM*, in which Oda's method is applied. In the upscaling, the uniform grid size is set to 50 m in all directions.

In the original modelling framework under development, it is planned to replace the numerical modelling part of the inside of the deposition hole with a surrogate model based on machine learning. However, since the development has not yet been completed, the application of a surrogate model based on machine learning has not been made in this study.

C.3 Benchmarks

C.3.1   1D Transport

In this problem, the numerical result of 1-D transient advection and dispersion of three tracers (conservative, decaying, and adsorbing) are compared to analytical solutions (Kolditz et al., 2015). As suggested in Task Specification (LaForce et al., 2022), a beam with dimension of 10 m × 1 m × 1 m is discretized into 200 hexahedral grid cells, each 0.05 m × 1 m × 1 m. The concentrations of the three tracers are set as 1,000 mol/m^3 at the inflow face (x=0) from 0 to 15,000 s (Fig. C-1). The concentration in model is then compared to the analytical solution at 20,000 s.
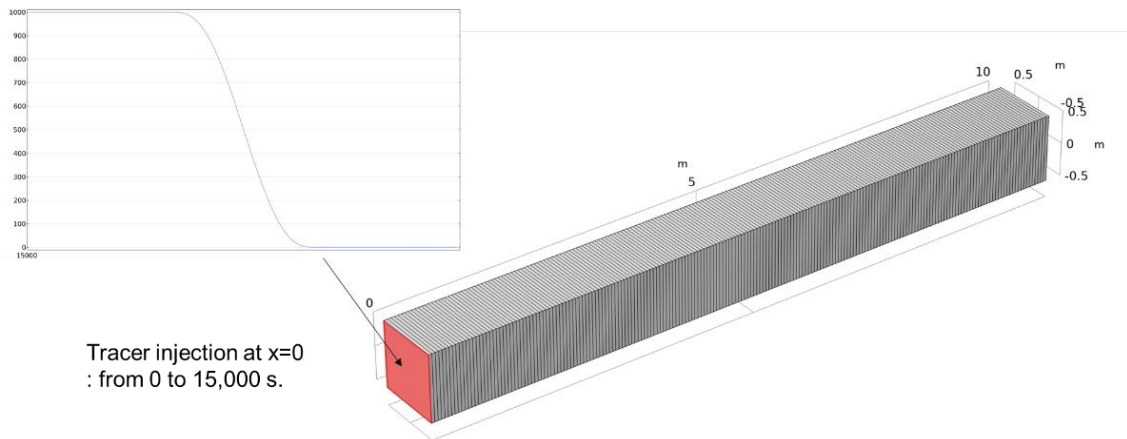
Fig. C-1. Geometry and boundary condition for 1D transport problem.

Fig. C-2 shows the result of 1D transient transport of three different tracers (conservative, decaying, and adsorbing). The numerical solutions are well matched with analytical solutions at 20,000 s.
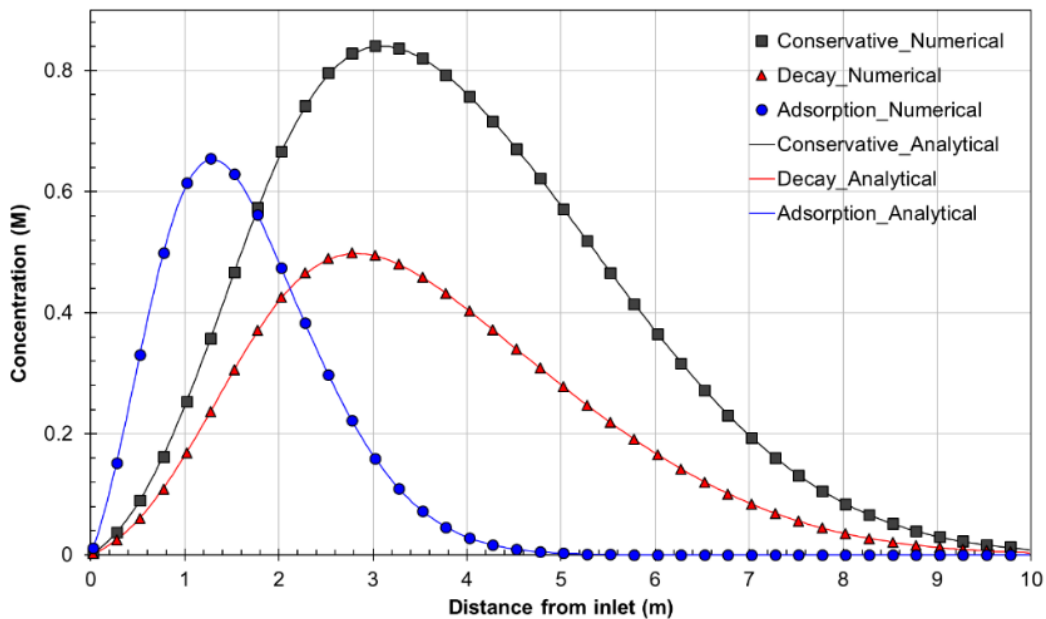
Fig. C-2. Results for 1D transient transport of conservative, decaying, and adsorbing tracers.

C.3.2   1D Fracture Plus Matrix Diffusion

In this problem, the numerical results of matrix diffusion are compared with the analytical solution by Tang et al. (1981). The mass is continuously injected at a concentration of 1.0 mol/L through the fracture inlet (x=0). Concentration profiles along the fracture (z > 0 m) and the rock matrix (x ≥ b) are compared to analytical solutions at

100, 1,000 and 10,000 days. The first set is compared with a flow velocity of 0.01 m/d along a 6 m fracture length at z = 2 m, with a domain of 2 m for the matrix. A second set is compared with a flow velocity of 0.1 m/d along a 60 m fracture length at z = 20 m with a domain of 1 m for the matrix. The approach for this problem is as follows.

- Equivalent continuous porous medium (ECPM)
- Boundary condition: Constant concentration (x=0), Outflow (x=end), No flux (sides).
- To decrease calculation time, the symmetry boundary is applied.

The fracture-matrix diffusion problem is solved twice, one with an average linear velocity in the fracture of 0.01 m/d and the other with an average linear velocity of 0.10 m/d. Concentrations of a conservative tracer are plotted at 100, 1000, and 10,000 days for each flow velocity (Fig. C-3) as a function of distance along the fracture and as a function of diffusion length into the matrix. All numerical results are well matched with analytical solutions.
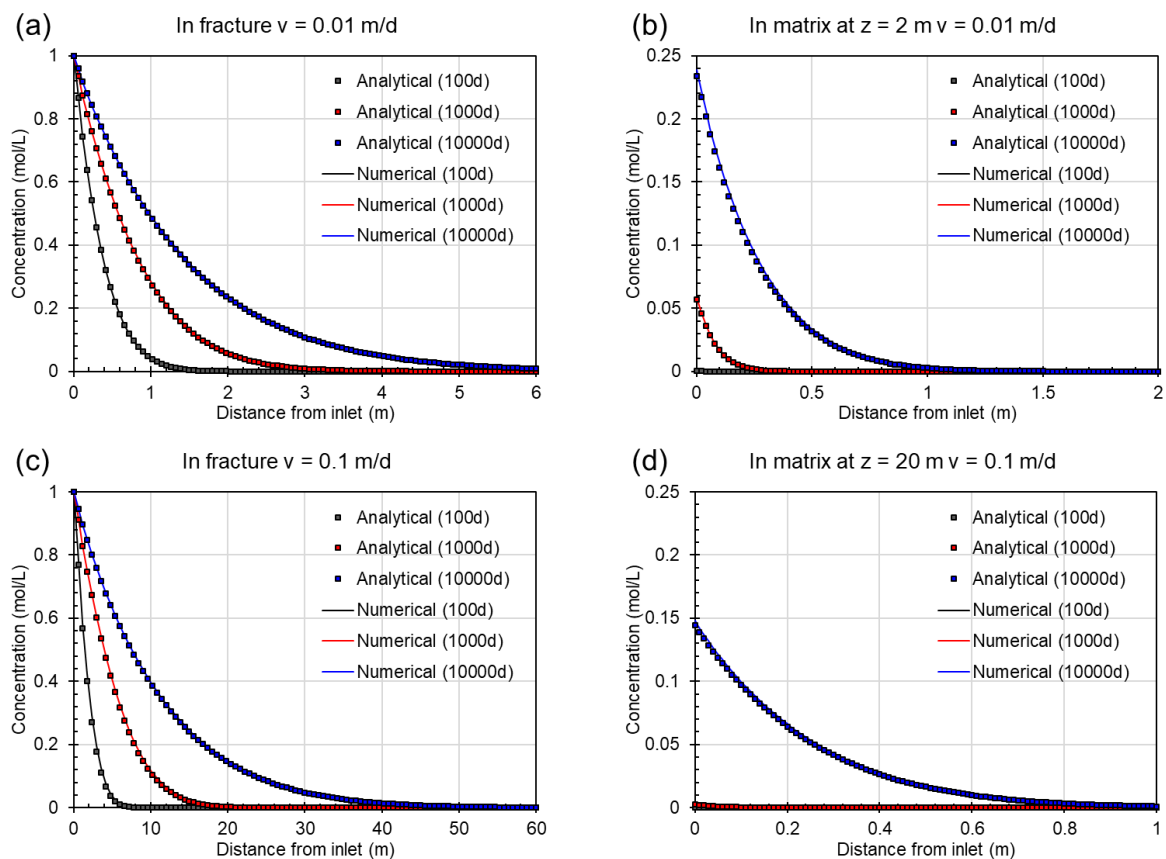
Fig. C-3. Tracer concentration as a function of distance along the fracture (a, c) and diffusion length into the matrix (b, d) for average linear velocities of 0.01 m/d (a, b) and 0.10 m/d (c, d).

In this study, the effect of mesh size representing fracture, by transforming the fractures into a fractured rock matrix in a continuum porous media, is also analysed (Fig. C-4). The equivalent porosity (ϕ') of fractured rock matrix can be defined as:

$$\phi' = ((b' - b) \cdot \phi + b)/b'$$

where, ϕ is rock matrix porosity, b is half of fracture width, and b' is the domain size of fractured rock matrix which can be equivalent to the mesh size in the continuum porous media. At fracture and fractured rock matrix (porous media), the mass flux (q) should be conserved as:

$$q = b'u = bv$$

where, u is Darcy's velocity in the fractured rock matrix and v is average linear velocity in the fracture. Then, the average linear velocity in the fractured rock matrix (v') will be derived as:

$$v' = \frac{u}{\phi'} = \frac{bv}{b'\phi'} = \frac{bv}{(b' - b) \cdot \phi + b} = \frac{v}{1 + \left(\frac{b'}{b} - 1\right)\phi}$$

The equation implies that the average linear velocity in the fractured rock matrix can be smaller than that in the fracture if the porosity of rock matrix is considered and the mesh size of the continuum porous media is greater than fracture width. And, the reduced average linear velocity will decrease the dispersion coefficient, which includes the product of dispersivity and average linear velocity. Accordingly, we could observe that the dispersion in the solute transport is underestimated as the mesh size (b'/b) increases. When the porosity of rock matrix is 0.01, the relationship for the average linear velocity in the fractured rock matrix can be depicted as Fig. C-5.
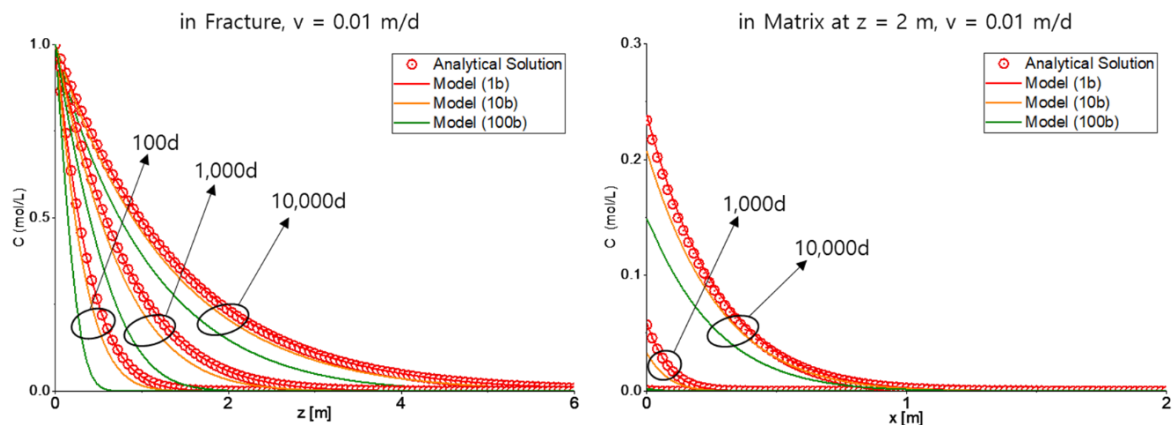
Fig. C-4. Tracer concentration as a function of distance along the fracture(left) and diffusion length into the matrix (right) for average linear velocities of 0.01 m/d depending on the mesh size (b'/b).
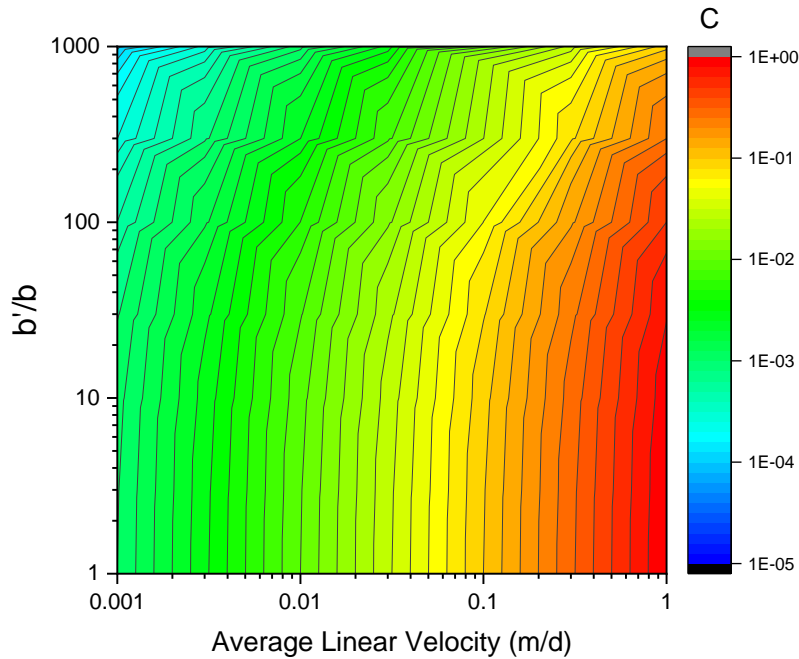
Fig. C-5. Contour map of the average linear velocity in the fractured rock matrix as function of the average linear velocity in the fracture and the mesh size (b'/b) in the equivalent continuum porous media.

C.3.3   Four-Fracture Transport

In this problem, the advection and diffusion of a conservative tracer through four fractures within a cubic domain are simulated. The Four-Fracture Transport problem is solved using two different fracture modelling methods: discrete fracture network (DFN) and equivalent continuum porous medium (ECPM). Fig. C-6 shows the initial and boundary conditions for the Four-Fracture Transport problem. Constant pressure (Dirichlet) boundary conditions are applied to the inflow and outflow faces to simulate groundwater flow. The mass is injected for 1 day through a single fracture on the west face (x = -500 m) of the domain, with a shape of step function.

Since the cells without fractures can't be removed from the domain in COMSOL, the mass transport through those cells is inevitably considered in the ECPM method. To minimize the transport through those cells, negligible values are input. The permeability and porosity of cells without fractures are set to $10^{-18}m^2$ and 10^{-10}, respectively.
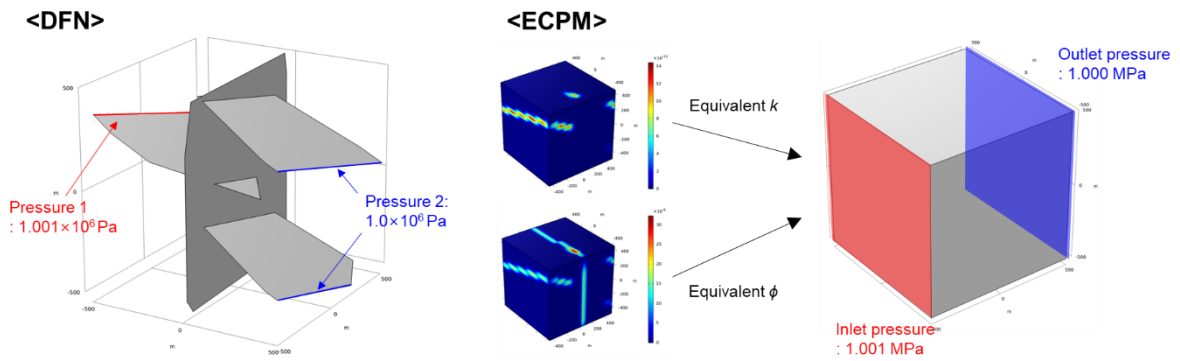
Fig. C-6. Initial and boundary condition of Four-Fracture Transport problem.

Fig. C-7 shows the breakthrough curves (BTCs) of Four-Fracture Transport problem using two different fracture modelling methods. In both methods, the injected mass starts to be flowed out from ~1 year, and more than 99.9% of mass is flowed out within ~50 years. However, there is slight difference between the BTCs of the two different fracture modelling methods. In the DFN method, the mass is transported faster compared to the ECPM method.
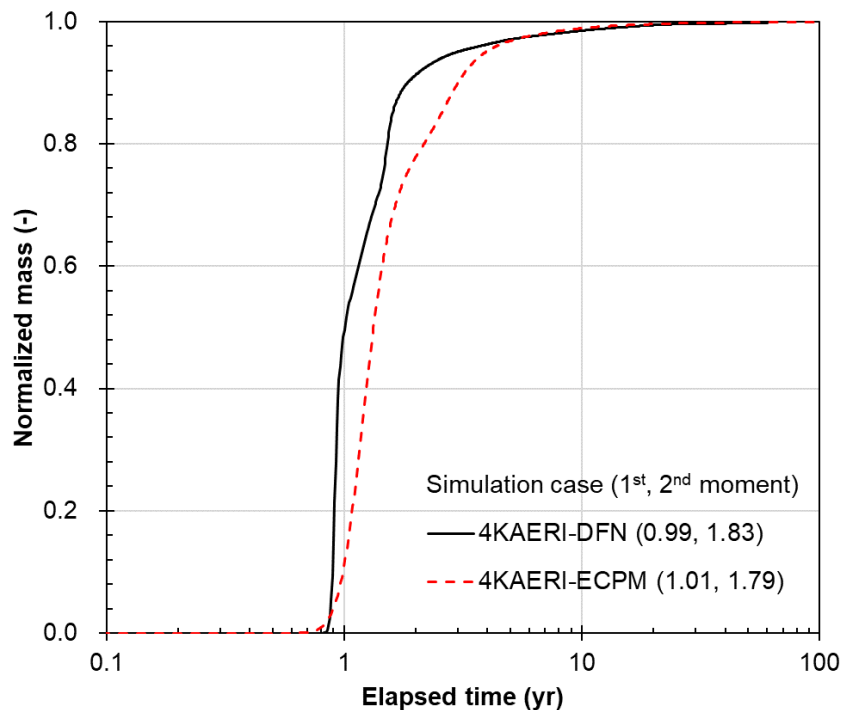
Fig. C-7. The breakthrough curves (BTCs) of Four-Fracture transport problem.

C.3.4   Four-Fracture Plus Stochastic Fractures

In this problem, the stochastically generated fracture set consisting of 1,085 fractures is added to the Four-Fracture Transport problem. Except for the addition of fracture set,

all boundary conditions and parameters remain the same as the Four-Fracture Transport problem. Additionally, the problem considers the advection and diffusion of conservative, decaying and adsorbing tracers.

For the Four-Fracture Plus Stochastic Fractures problems (C.3.4 and C.3.5), two different fracture modelling methods are adopted: the discrete fracture network (DFN) method and discrete-fracture matrix (DFM) method. In the DFN method, all fractures are represented as planar surfaces. On the other hand, the DFM method only represents four deterministic fractures as planar surfaces. The set of stochastic fractures is upscaled and input as hydraulic properties of porous media, such as porosity and permeability (Fig. C-8).
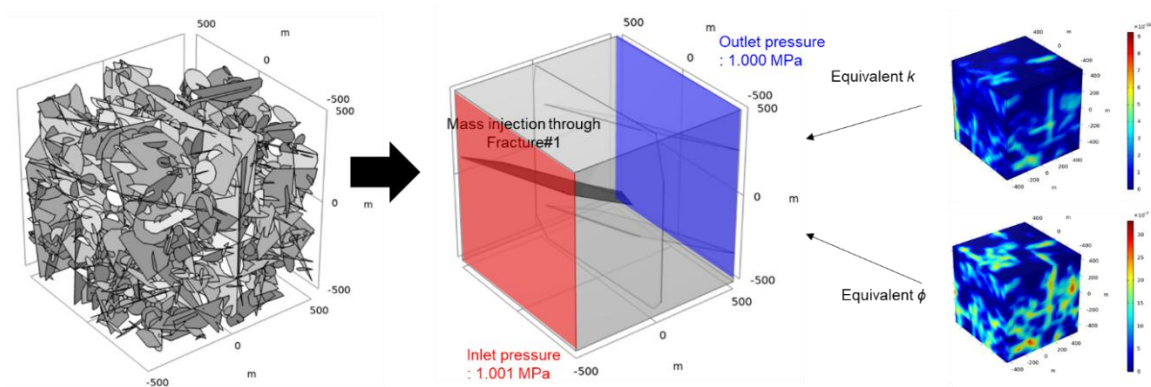
Fig. C-8. Description of discrete-fracture matrix (DFM) method.

Fig. C-9 shows the breakthrough curves (BTCs) of Four-Fracture Plus Stochastic Fractures problem. Although the BTCs shows a similar trend regardless of fracture modelling method, the BTCs slightly vary depending on the tracers. When compared to the conservative tracer, only ~98% of decaying tracer (~97% in DFM method) is discharged through the outlet due to its decay with half-life of 100 years. Meanwhile, the BTCs of the adsorbing tracer are delayed due to its adsorption onto the porous media. While it takes ~110 years for 99% release of conservative tracer, it takes ~330 years for the adsorbing tracer in DFN model.
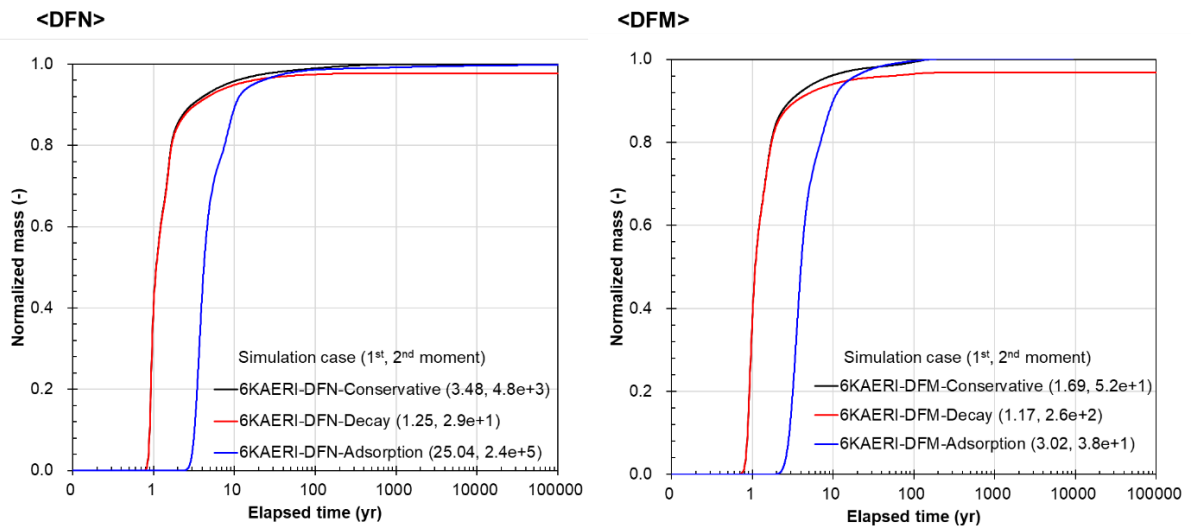
Fig. C-9. The BTCs of Four-Fracture Plus Stochastic Fractures problem.

To observe the effect of stochastic fractures on mass transport, the BTCs of Four-Fracture and Four-Fracture Plus problems are compared. As shown in Fig. C-10, the difference between the two BTCs (4-Fracture vs 4-Fracure+ (DFM) – Flux based) is not significant. This is primarily caused by the injection strategy. According to the Task Specification (LaForce et al., 2022), the permeability of deterministic fractures is much higher than that of stochastic fractures. Since this benchmark problem adopts a flux-based injection strategy as a boundary condition, the mass is injected in proportion to the Darcy's velocity at each fracture, which is directly related to the fracture permeability. However, when the mass is uniformly injected through all the fractures, the addition of stochastic fractures can delay the breakthrough of mass due to their lower permeability compared to the deterministic fractures. The vicinity of the failed canister in bentonite buffer can be considered as a condition of uniform mass injection strategy. In the vicinity of the failed canister, the released radionuclide can be uniformly injected into the surrounding fractures because the Darcy's velocity in the surrounding bentonite buffer is very low.
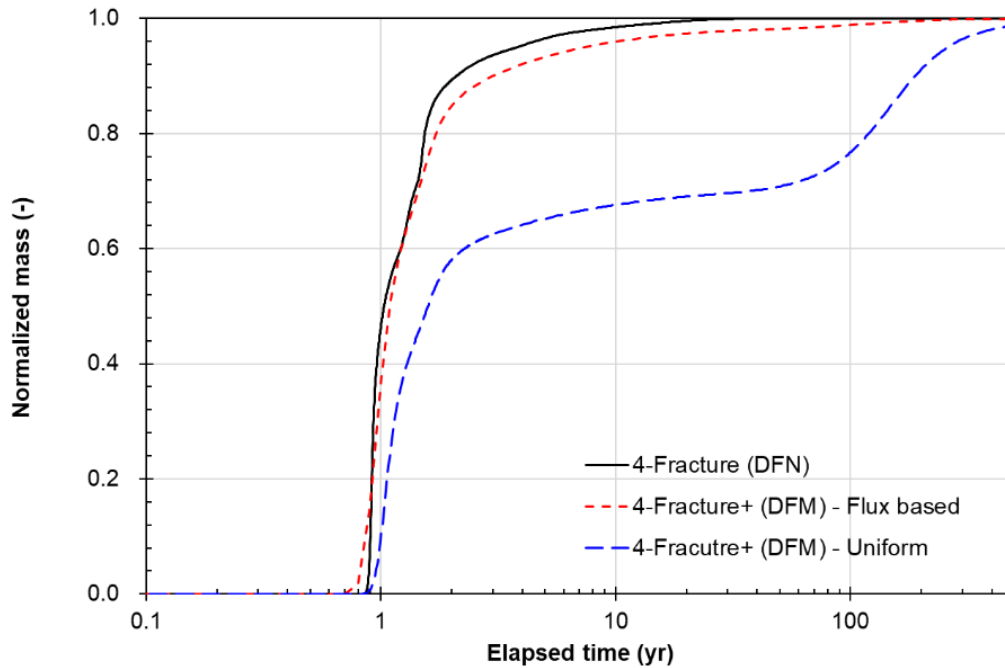
Fig. C-10. The BTCs of Four-Fracture and two Four-Fracture Plus Stochastic Fractures with different injection strategy.

C.3.5 Continuous Point Source

All conditions of this problem are the same with Four-Fracture Plus Stochastic Fractures problem, except for how the mass is introduced into the domain. In this problem, the mass is continuously injected through a point with coordinates (-500, 7.0, 248.25). Since injecting mass through a point is not possible in COMSOL, the mass is injected through a tiny edge defined by coordinates (-500, 7.0, 248.25) and (-500, 7.1, 248.225). The breakthrough curves (BTCs) of this problem are calculated by dividing the tracer mass exiting the domain at each time step by the mass introduced at each time step.

The BTCs obtained using both fracture modelling methods are similar to each other (Fig. C-11). It takes ~40 years and ~200 years for the conservative and adsorbing tracers, respectively, to achieve the steady state. Although the breakthrough curves reach plateau, there is still fluctuation, which makes the moment calculation diverge. The moment value in Fig. C-11 is calculated at the time when the BTC reaches its maximum value for the first time.
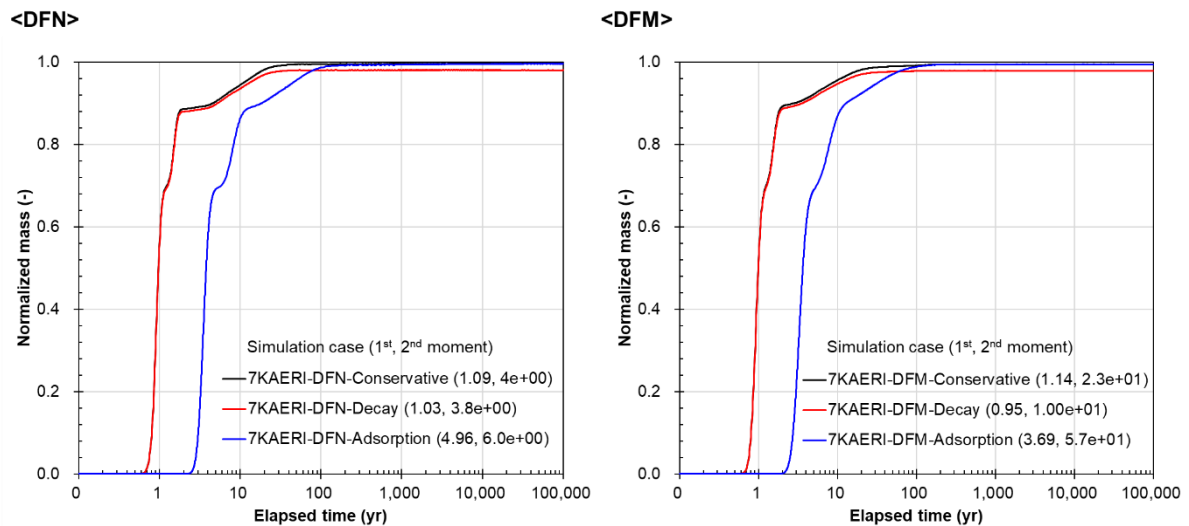
Fig. C-11. The BTCs of Four-Fracture Plus Stochastic Fractures with Continuous Point Source problem.

C.3.6 Radionuclide Source Term Benchmark

In this benchmark, the source term process specified in section 5.3 of the Task Specification (LaForce et al., 2022) is numerically simulated. First, the change in spent nuclear fuel (SNF) inventory for radionuclides in the 4N+1 decay chain and ^{99}Tc over time is calculated considering radioactive decay and ingrowth. Detailed information regarding the initial inventory of nuclides and the decay considered in this benchmark can be found in Table 5-10 of the Task Specification (LaForce et al., 2022).

Next, a waste package breach is simulated, followed by the release of radionuclides into the waste within the package. This calculation considers the instantaneous release fraction for ^{99}Tc, congruent release limited by the fuel matrix degradation rate, and the dissolution of radionuclides limited by elemental solubility limits. The input parameters for the release are provided in section 5.3 of the Task Specification (LaForce et al., 2022).

The amount of a radionuclide bounded within the SNF matrix can be described by a general governing equation as follows:

$$\frac{dM_i}{dt} = \sum_j I_{ij}\lambda_j M_j - (\lambda_i + r_i)M_i$$

where

M_i Amount of radionuclide i in a waste matrix [kg]

I_{ij} Branching ratio of radioactive decay from a radionuclide j [-]

λ_i Decay constant of radionuclide i [1/s]

r_i Release rate of radionuclide i from the waste matrix [1/s].

Similarly, the amount of a released radionuclide i in a waste package, m_i, can be expressed as

$$\frac{dm_i}{dt} = \sum_j I_{ij}\lambda_j m_j - \lambda_i m_i + r_i M_i + \text{transport}.$$

In this study, released radionuclides are assumed to be contained in a waste package so that the term of transport for a radionuclide is neglected. Assuming the inside of the waste package as a homogeneous porous medium, the set of the equations above can be written in a matrix form as

$$\dot{\boldsymbol{N}} = \boldsymbol{TN}(t)$$

where

$\boldsymbol{N}$ $1 \times \text{N}$ mass vector for radionuclides

$\boldsymbol{T}$ $N \times N$ transition matrix for decay and release.

The solution for the matrix equation is

$$\boldsymbol{N_{t+\Delta t}} = \exp(\boldsymbol{T}\Delta t)\,\boldsymbol{N_t}.$$

The matrix exponential function of $\exp(\boldsymbol{A}\Delta t)$ is calculated by $\mathtt{expm.m}$ function provided in MATLAB library. An approximation algorithm of $\mathtt{expm.m}$ is described in Al-Mohy and Higham (2009).

To consider of instantaneous release, $\boldsymbol{N}$ is updated at waste package breach time as bellow.

$$\boldsymbol{N}_{\text{updated}} = \begin{bmatrix} \boldsymbol{I} - \boldsymbol{IRF} & 0 \\ \boldsymbol{IRF} & \boldsymbol{I} \end{bmatrix} \begin{bmatrix} \boldsymbol{M}_{\text{previous}} \\ \boldsymbol{m}_{\text{previous}} \end{bmatrix}.$$

The concentration of a dissolved radionuclide is calculated as

$$C_i = \min\left(\text{sol}_i, \ \frac{m_i}{V_{\text{water}}}\right)$$

where

C_i Concentration of radionuclide i [kg/L]

sol_i Solubility limit of radionuclide i [kg/L]

V_{water} Volume of water [L].

The calculation of source term benchmark is implemented using an in-house MATLAB code. To verify the accuracy, the results from the MATLAB model are compared with a model built using GoldSim software. Both models show good agreement. Fig. C-12 illustrates the results for the decay and ingrowth of radionuclides in the 4N+1 decay chain, as well as the decay of ^{99}Tc. Since the waste package breach is not considered in this calculation, there is no discrete decrease in ^{99}Tc inventory due to the instant release fraction (IRF) or a gradual decrease of long-lived radionuclides due to the degradation of the SNF matrix.

It is important to carefully consider the decay and ingrowth of short-lived radionuclides with long-lived parents in the decay chain, such as ^{233}Pa and ^{241}Pu. The calculation results show a secular equilibrium between ^{237}Np and ^{233}Pa. In the case of ^{241}Pu, secular equilibrium with ^{245}Cm can be observed after the initial inventory decay. These results indicate that the use of expm.m function in the MATLAB for the source term benchmark is appropriate.

Fig. C-13 presents the inventory of ^{99}Tc in the SNF matrix, considering a waste package breach at 3,000 years. Unlike the results in Fig. C-12, a decrease in the inventory due to IRF and congruent release can be observed, showing good agreement with GoldSim.
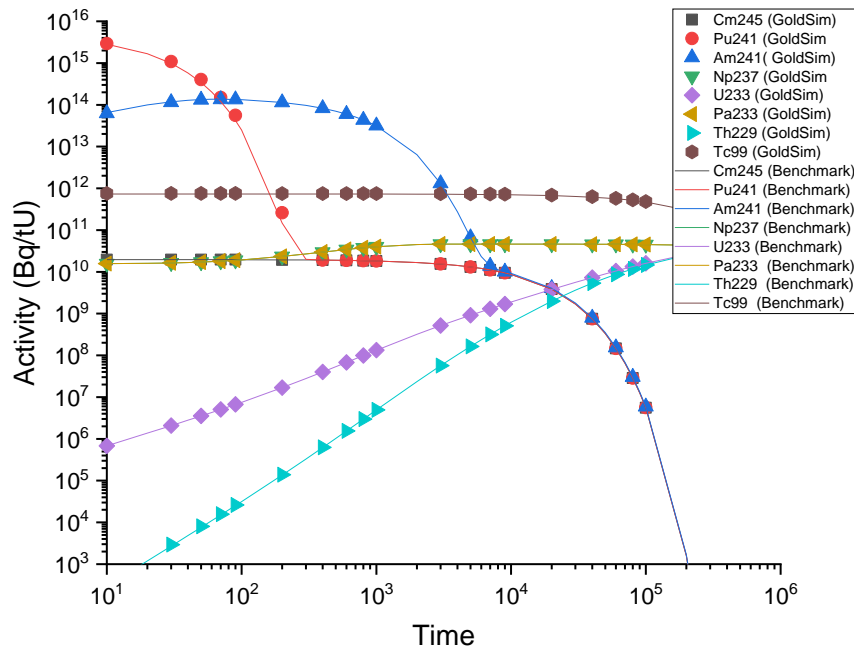
Fig. C-12. The decay and the ingrowth of radionuclides in SNF without the breach.
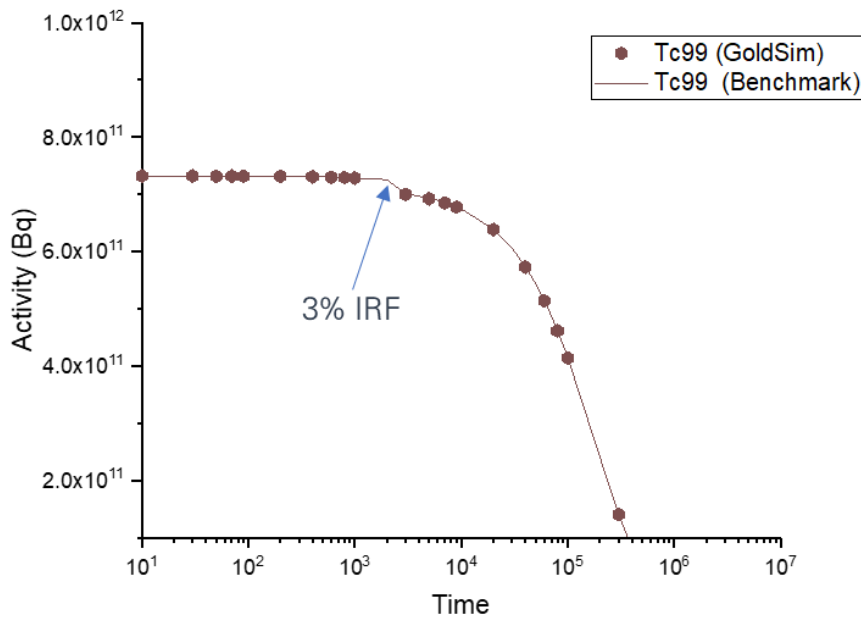
Fig. C-13. Change in ^{99}Tc inventory with consideration of the release after breach.

Fig. C-14 illustrates the changes in aqueous, precipitated, and fuel concentrations of each radionuclide in the waste package over time. As the package breaches at 3,000 years, the aqueous concentrations of radionuclides begin to increase. In the benchmark case, the calculated aqueous concentrations of ^{237}Np, ^{233}U, ^{229}Th, and ^{99}Tc reach their solubility limits. The model assumes that the release of radionuclides from SNF is not

limited by solubility, resulting in the released radionuclides directly contributing to the increase in precipitated concentration after the saturation of aqueous phases.
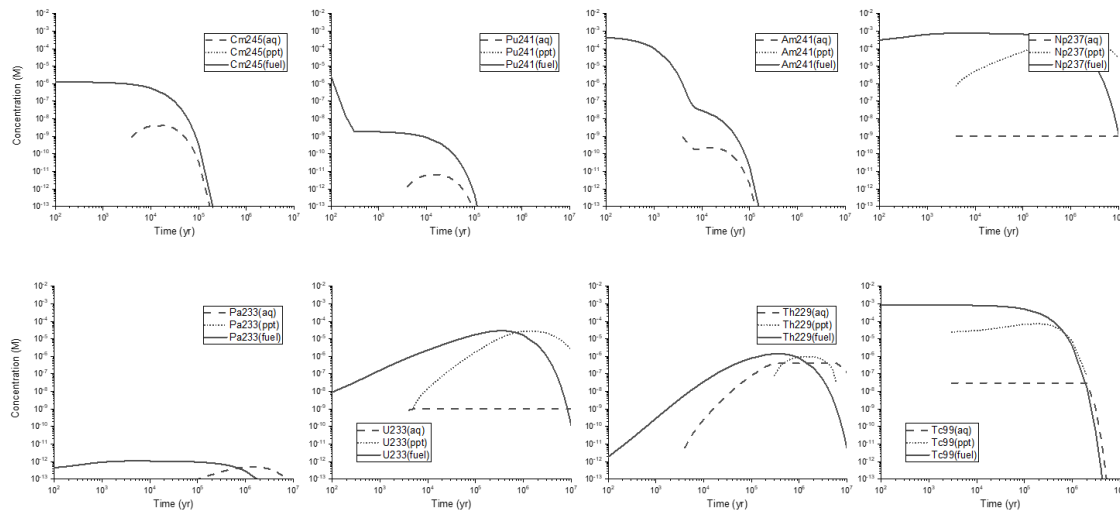
Fig. C-14. Concentration of radionuclides in the waste package.

C.4 Reference Case

C.4.1   Model Domain

In this study, the model domain is separated into the near-field component and far-field component in order to distribute the computing loads (Fig. C-15). The separated components are coupled by using the *Identity Mapping* function in COMSOL. Each component is calculated separately, and the hydraulic pressure for flow and solute concentration for transport calculated in the other component are set as boundary conditions at the surfaces in contact with each other in each calculation.
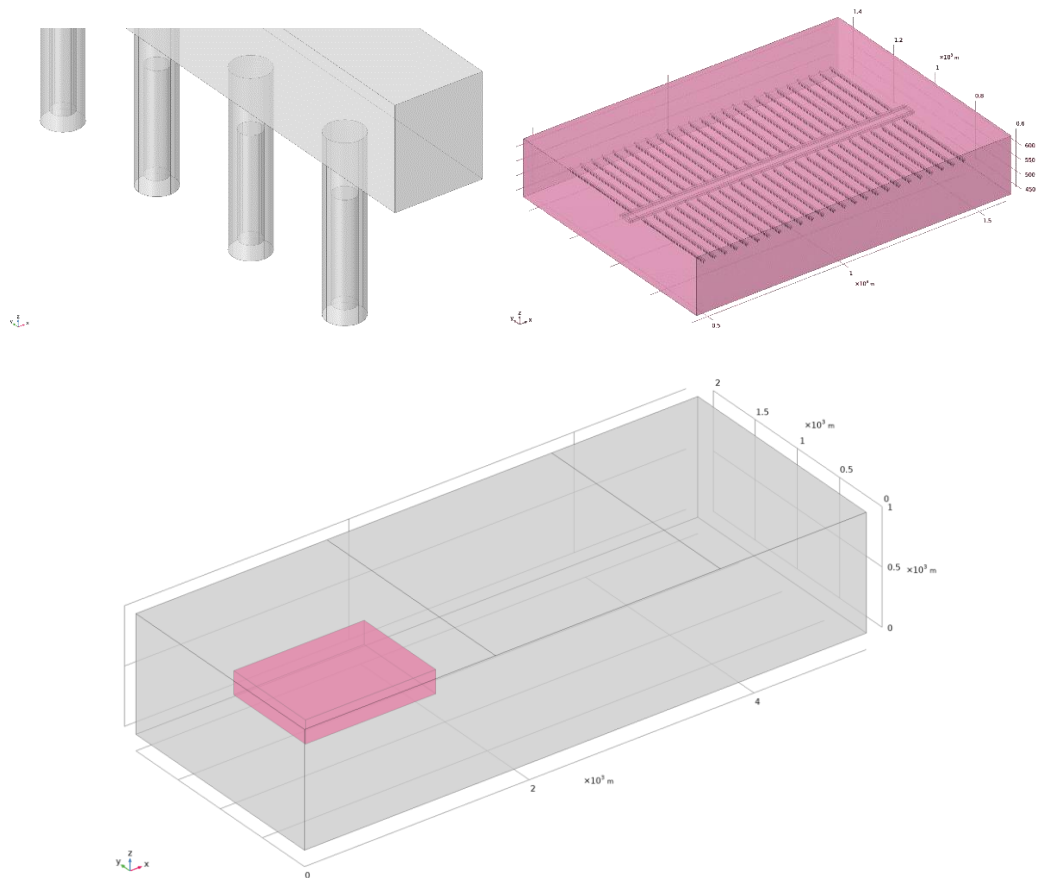
Fig. C-15. Domain components considered in this study (EBS, near-field, and far-field).

The waste package and the deposition hole are represented in a cylindrical shape based on their respective diameters and lengths as defined in the Task Specification (LaForce et al., 2022). The main tunnel and the deposition tunnel are represented in a rectangle shape based on their widths and heights as defined in the Task Specification (LaForce et al., 2022).

The hydraulic and transport properties of buffer and backfill, such as porosity, permeability, and effective diffusivity, are employed from the Task Specification (LaForce et al., 2022). For the properties inside of the waste package which is not defined in the Task Specification (LaForce et al., 2022), hypothetical values are applied with conservatism, such as 1 for porosity, 10^{-18} m^2 for permeability, and 10^{-9} m^2/s for effective diffusivity.

All meshes use tetrahedral elements with a fairly coarse mesh size; the maximum mesh sizes are set to 1 m for the waste package, 1 m for the buffer, and 5 m for the backfill. Although the geometry of the waste package is generated as a cylinder, the shape used in the calculations is actually a hexahedron because of the coarse mesh size for the

waste package. The total numbers of mesh elements for waste package, buffer, and backfill are 153,664, 844,091, and 672,366, respectively.

C.4.2   Fracture Network

Regarding the natural barrier system (NBS), both hydraulic conductor domains (HCD) and hydraulic rock mass domains (HRD) are considered as main pathway of the flow and transport. Unlike HCD which is deterministically defined in the Task Specification (LaForce et al., 2022), the 10 realizations of fracture networks for HRD which needs to be stochastically generated are supplied from Sandia National Lab. in this study.

Fig. C-16 depicts the cumulative distribution functions of permeability and aperture of the fracture networks for 10 realizations of HRD and those of 6 deterministic fractures for HCD. As shown in the figure, the properties of the HCD and the HRD are within the same range, so that HCD and HRD were grouped and upscaled to ECPM at once in this study. Then, the permeability and porosity of ECPM are adjusted to have the minimum values, 10^{-18} m^2 and 10^{-7}, respectively (Fig. C-17).

The mesh for the fractured rock is also applied in the shape of a tetrahedron with 50 m of the maximum mesh size. The total numbers of mesh elements of rock for near-field and far-field are 24,074,728 and 1,340,848, respectively.
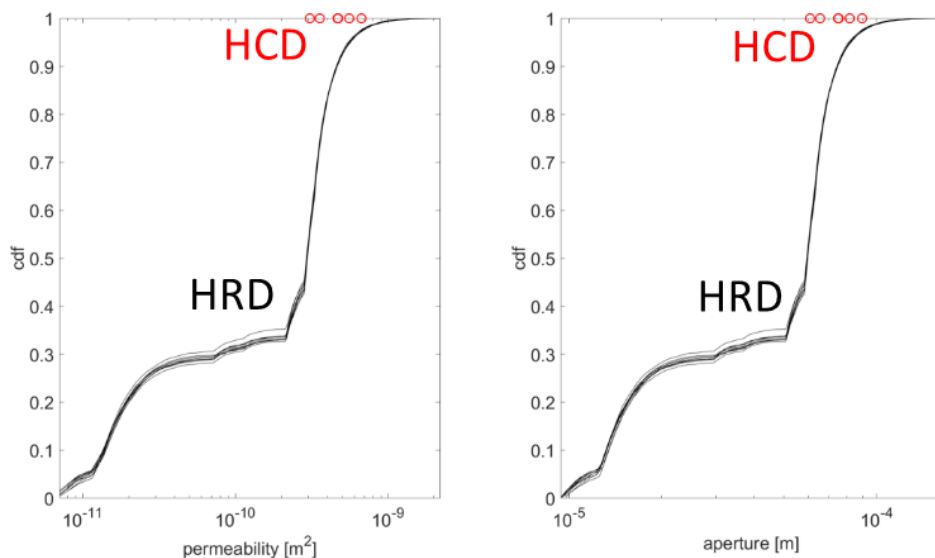
Fig. C-16. Cumulative distribution function of permeabilities and apertures of the fracture networks for 10 realizations of HRD and those of 6 deterministic fractures for HCD.
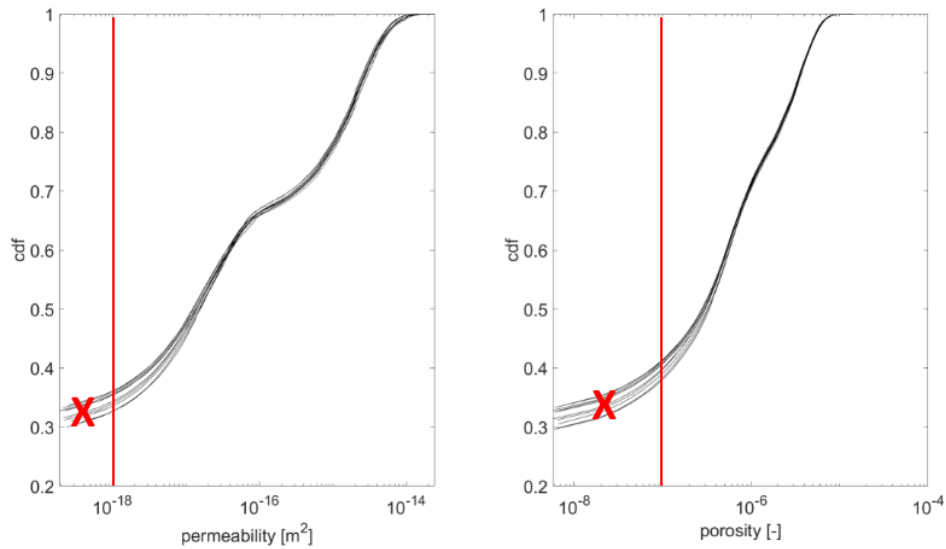
Fig. C-17. Cumulative distribution function of permeability and porosity of upscaled ECPM. Zones with the red cross were not used and instead the minimum value (red line) was used.

C.4.3   Flow Model

The steady state flow is simulated with *Darcy's Law* physics in COMSOL. The groundwater flow is assumed to occur through the saturated porous media. The steady state flow is established by using a constant hydraulic head boundary condition at the top surface of the domain. The hydraulic head is assumed to be same as the surface elevation, which is a function of distance as follows (LaForce et al., 2022).

- top of hill (0 m < x < 1,700 m): z = 1,020 m
- hillslope (1,700 m < x < 3,700 m): z = 10 · sin(π/2 + π/2000 · (x − 1,700 m)) + 1,010 m
- low point (3,700 m < x < 5,000 m): z = 1,000 m

No flow boundary condition is applied to all external boundary surfaces except for the top surface of the domain.

Fig. C-18 shows 3D contour maps of hydraulic pressure and streamlines of groundwater flow passing through the repository for 10 realizations. In all realizations, it is confirmed that most of the groundwater flow occurred along the deterministic fractures (HCD), and some effects of the stochastic fracture network (HRD) are also shown.

Fig. C-19 shows 2D contour maps of Darcy velocities in z-direction (m/yr) across the top surface for 10 realizations. As expected, it is confirmed that the inflow from the upper part of the hillslope and the outflow from the lower part of the hillslope are dominant. And, it is also confirmed that the groundwater flow is predominantly in the fracture

network constituting the HRD. In the inflow region, Darcy's velocity in z-direction is up to about 15E-3 m/yr. In the outflow region, Darcy's velocity in z-direction is about 10E-3 m/yr except Realization #2, in which the maximum outflow velocity reaches up to about 20E-3 m/yr.

Mean values and 95% confidence intervals are calculated for steady state flow rates at the top surface (Fig. C-20). It is confirmed that there is no large deviation for each realization and conservation of water mass is established as the sum of inflow and outflow is the same.
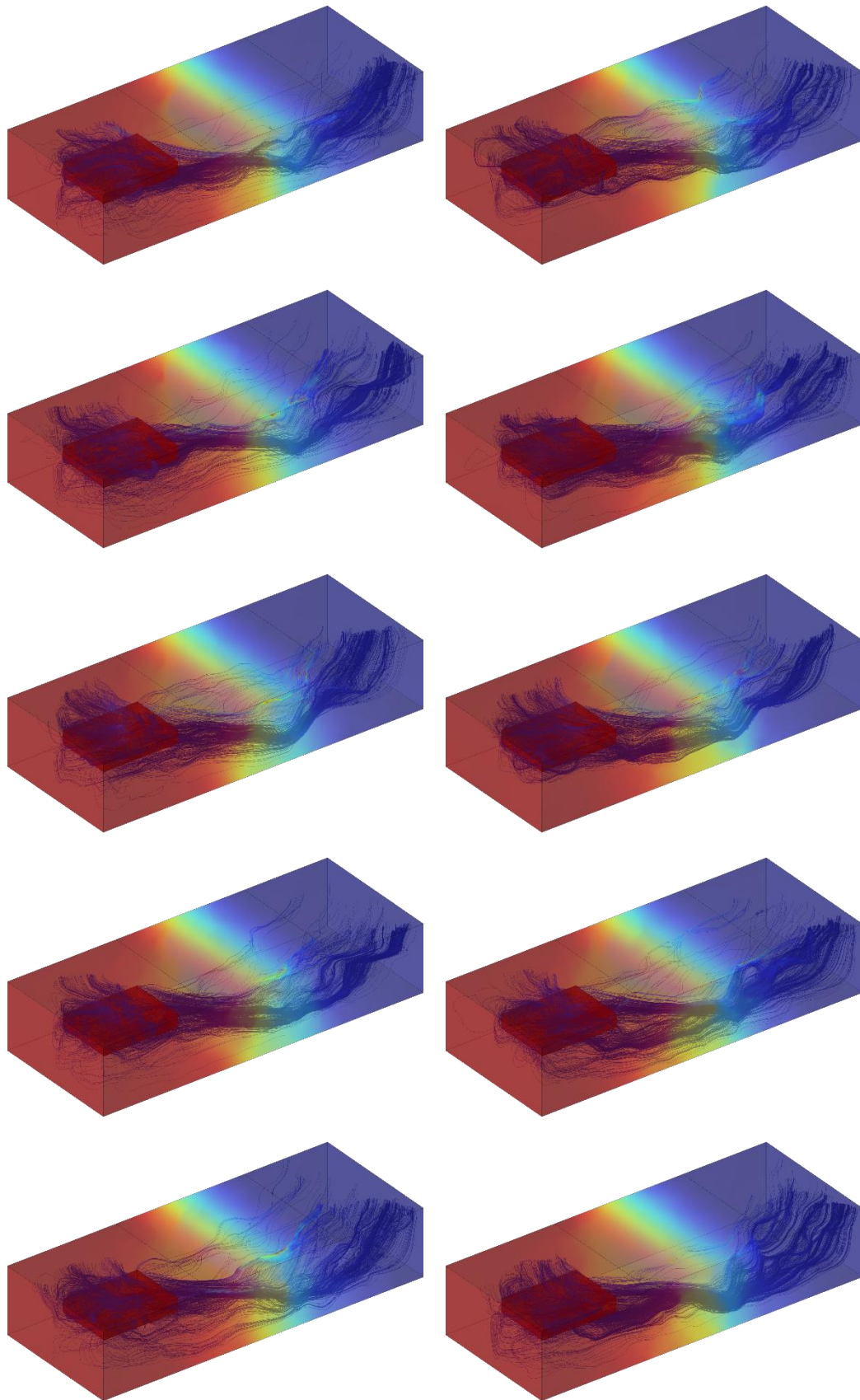
Fig. C-18. 3D contour maps of hydraulic pressure and streamlines of groundwater flow passing through the repository (10 realizations).
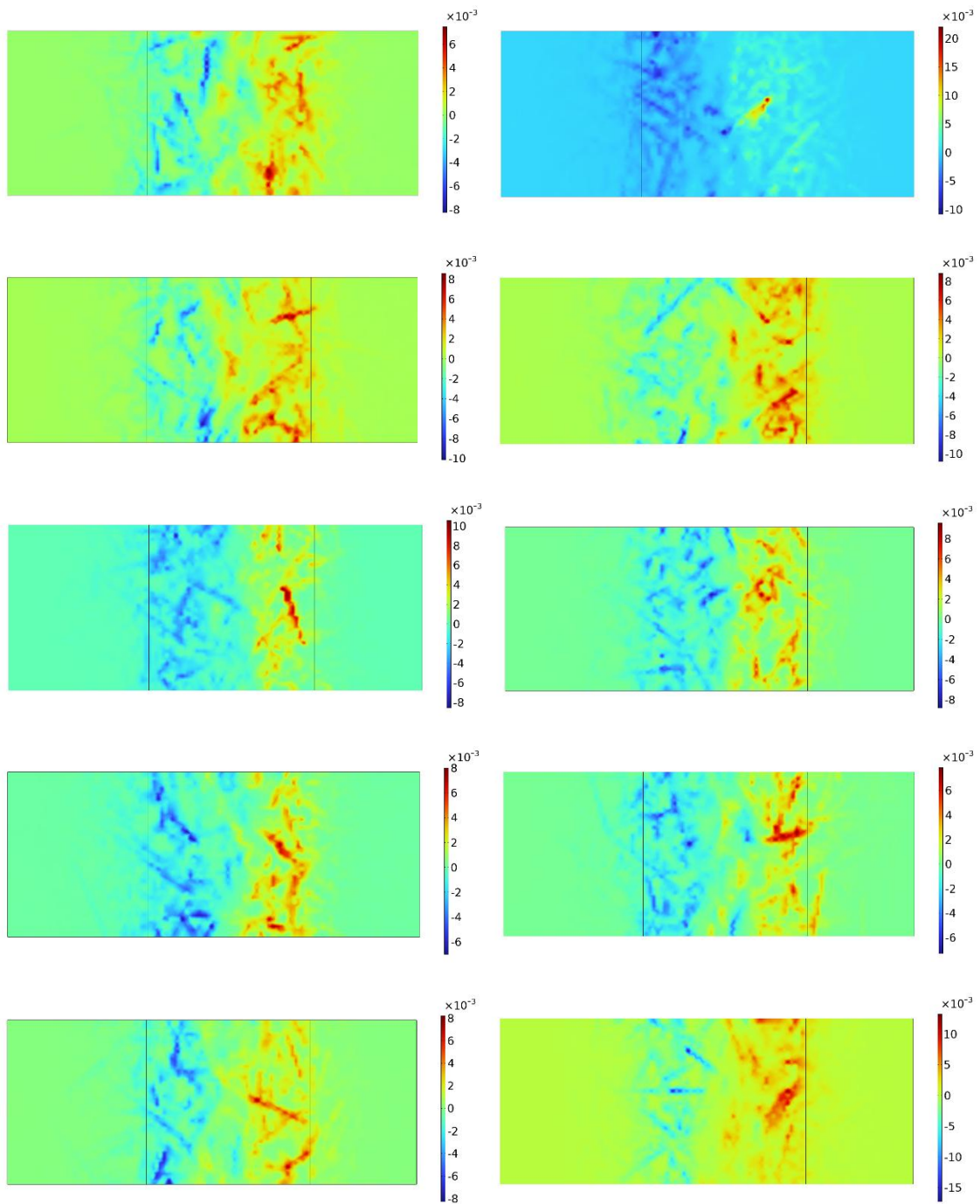
Fig. C-19. 2D contour maps of Darcy's velocities in z-direction (m/yr) across the top surface (10 realizations).
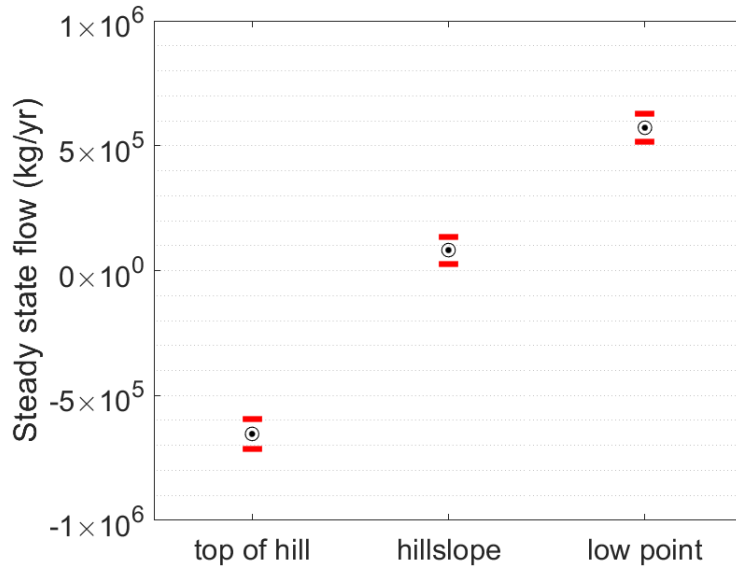
Fig. C-20. Mean (circle) and 95% confidence intervals (red line) for net steady state flow across top of hill, hillslope, and low point.

C.4.4   Tracer Release and Transport

The time-dependent transport is simulated with Transport of Diluted Species in Porous Media physics, which includes advection-diffusion equation, in COMSOL for 10^5 years. In this study, rock matrix diffusion is not considered. The boundary condition at the top surface is open boundary condition; if the normal flow velocity is positive, it is a no-gradient boundary condition, and if negative, it is a zero-concentration boundary condition. No flux boundary condition is applied to all external boundary surfaces except for the top surface of the domain.

As defined in the Task Specification (LaForce et al., 2022), both types of tracers are considered. Tracer 1 releases instantly, and Tracer 2 releases constantly based on the specific degradation rate, 10^{-7} /yr. In the model, it is assumed that all tracers release uniformly with a specific release rate per unit volume in the waste package domain. Therefore, instant release is changed to release having a smooth step function (F(t)) for 0.1 years. The release rate per unit volume (Q) of each tracer is as follows.

$$Q_{Tr_1} = 5.45[\text{g}]/128.9[\text{g/mol}] \times 10[\%] / V_{wp} \times \frac{dF(t)}{dt}$$

$$Q_{Tr_2} = 5.45[\text{g}]/128.9[\text{g/mol}] \times 90[\%] / V_{wp} \times 10^{-7}[1/\text{yr}]$$

where, V_{wp} is volume of the waste package (m3).

The overall simulations of tracer transport are performed using PARDISO direct solver in COMSOL, but it encounters a model convergence problem. In order to improve the

convergence, the time step could be decreased, but this causes another problem of significantly increasing the computing time. As one way to solve the model convergence problem, the applicability of an inconsistent stabilization technique is tested in this study. The inconsistent stabilization method provided by COMSOL is to add an artificial isotropic diffusion coefficient (D_{art}) to the diffusion term as follows.

$$\frac{\partial(\epsilon_p c_i)}{\partial t} + u \cdot \nabla c_i = \nabla \cdot \left[(D_{e,i} + D_{art}) \nabla c_i \right]$$

$$D_{art} = \delta_{id} h \|u\|$$

where, δ_{id} is a tuning parameter for the isotropic diffusion and h is mesh element size (m).

In this study, sensitivity analysis is performed to determine the effect of isotropic diffusion coefficient on the overall calculation result. Here, only δ_{id} is adjusted, since the number of mesh elements is desired not to be increased and the Darcy's velocity is a result from the flow model. Since the components of the near-field and far-field are separated, δ_{id} is also applied separately to each component. Preliminarily, it is confirmed that as δ_{id} is increased, the model convergence is improved and thus the computing time significantly decreases. Therefore, only the effect of δ_{id} on the model accuracy is analysed intensively in this study.

Firstly, the normalized cumulative mass flows of Tracer 1, which equal to cumulative outflow of Tracer 1 divided by the total inventory of Tracer 1, at the low point region are compared depending on the tuning parameters of near-field and far-field components (Fig. C-21). From the results, it is observed that the mass flow is highly affected by δ_{id} applied to near-field. On the other hand, it seems that there is no significant effect of δ_{id} applied to far-field. That is, it is expected that δ_{id} applied to far-field can be increased up to 10^{-4} without significantly affecting the model accuracy.

Since δ_{id} applied to near-field has a large sensitivity, its influence in near-field component is further investigated. Mass flux of Tracer 1 at an arbitrary point in the rock of near-field component are compared depending on the tuning parameters of near-field and far-field components (Fig. C-22). The mass flux is divided into convective and diffusive fluxes. As expected, convective flux is much more dominant rather than diffusive flux regardless of δ_{id} since matrix diffusion is not considered in this study. Since isotropic diffusion is artificially added to the diffusion term, it is expected δ_{id} to affect only the diffusive flux. Interestingly, however, it is observed that δ_{id} not only affects the diffusive flux, but also affects the convective flux in a similar ratio. Specifically, during the initial approximately 100 years, there is a significant disparity in flux influenced by δ_{id}, which then gradually decreases and maintains relative stability after around 100

years. For instance, the difference between cases with δ_{id} at 10^{-4} and δ_{id} at 10^{-7} (considered the most precise) exhibits an approximate 14-order separation within the initial 100 years, followed by a reduction to approximately a 3-order difference after about 100 years. It is considered that the effect of δ_{id} on the flux, especially convective flux, is ultimately transmitted to the overall modelling results.
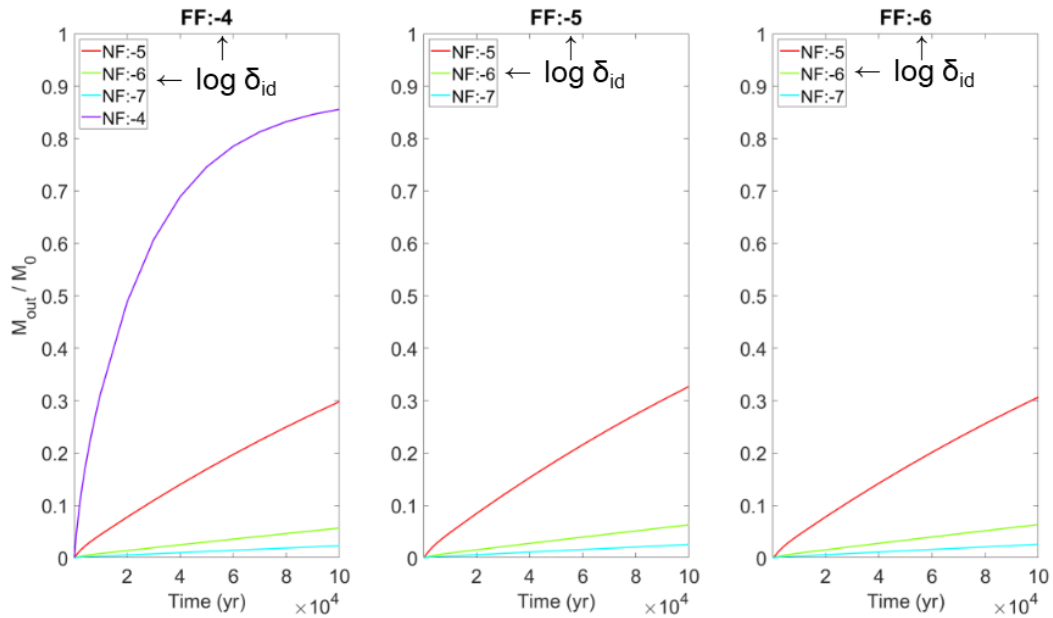
Fig. C-21. Normalized cumulative mass flow of Tracer 1 at the low point region depending on the tuning parameters of near-field and far-field components.
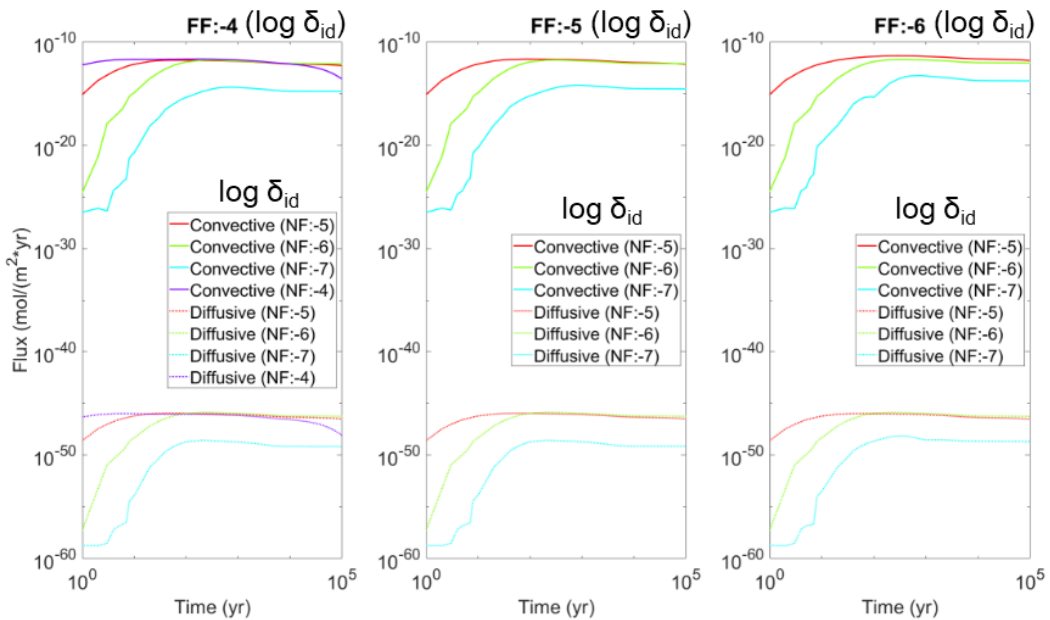
Fig. C-22. Convective and diffusive mass fluxes of Tracer 1 at an arbitrary point in the rock of near-field component depending on the tuning parameters of near-field and far-field components.

Subsequent calculations for 10 realizations of tracer transport necessitate setting δ_{id} to a significantly elevated value of 10^{-4} for computational stability. Given the influence of δ_{id} as analysed above, it is considered that the tracer transport calculated in this study may be highly exaggerated. Consequently, this factor must be taken into account while interpreting the results.

Fig. C-23 shows the relative iso-surface maps of Tracer 1 concentration in near-field and far-field components for Realization #1. Due to the high δ_{id}, it can be confirmed that within the near-field component, a prevalence of isotropic diffusion, occurring to a greater extent than originally anticipated, has become the dominant mechanism governing the tracer transport. On the other hand, within the far-field component, despite the high δ_{id}, it is evident that tracer transport driven by advection predominates over the isotropic diffusion.
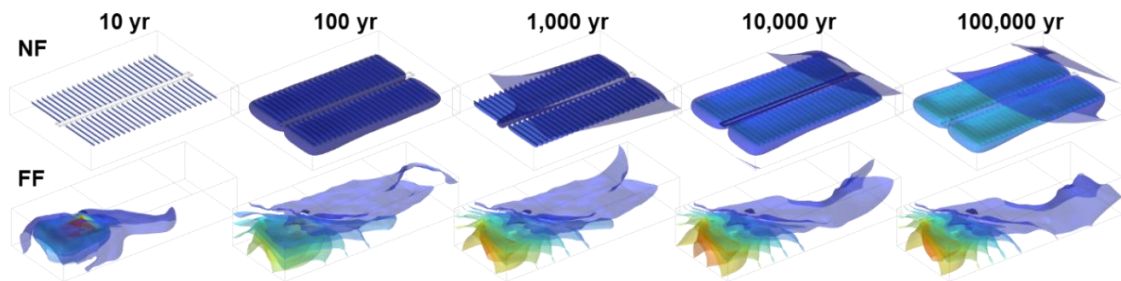
Fig. C-23. Iso-surface maps of Tracer 1 concentration in near-field(upper) and far-field(lower) components for Realization #1.

All the output metrics for comparison requested in the Task Specification (LaForce et al., 2022) are depicted in Fig. C-24 through Fig. C-29. Since a numerical error occurs in Realization #2, the mean and 95% confidence interval in the figures below are the results derived for the remaining 9 realizations except for Realization #2. As a result, it is evident that the deviations for the outcomes of the 9 realizations are not significantly large overall.

Fig. C-24 reveals that Tracer 1, released instantly, exhibits a peak in mass flux at approximately 1,000 years, while Tracer 2, released congruently, demonstrates a continuous increase in mass flux over the course of 100,000 years. And at the low point, the mass flux of all tracers is observed to be approximately one order of magnitude higher than that of the hillslope. The results of the maximum mass fluxes per unit area (Fig. C-26) and the concentration at arbitrary locations (Fig. C-28) also exhibit similar patterns.
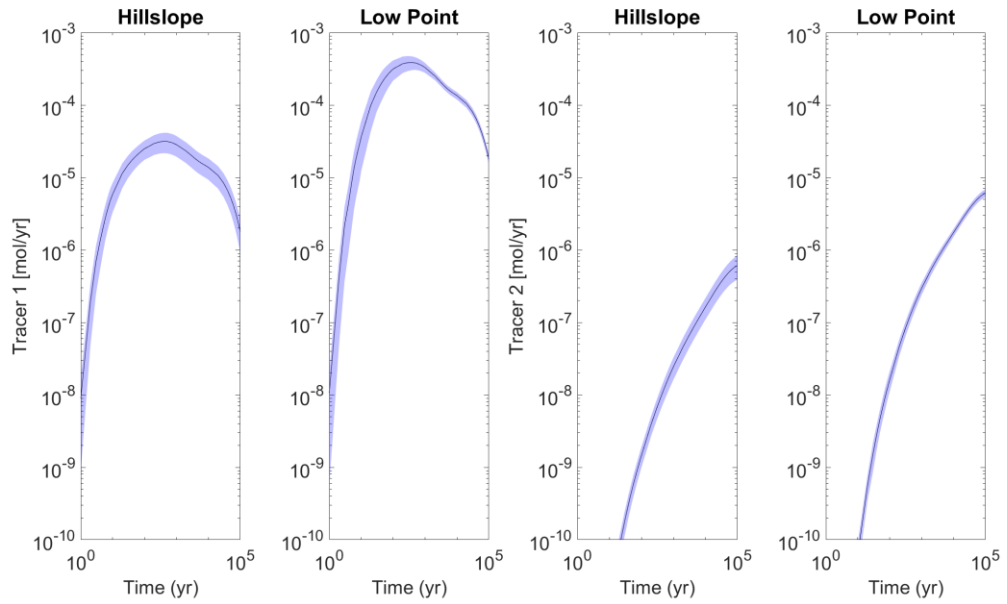
Fig. C-24. Mean and 95% confidence intervals for mass fluxes of Tracer 1 and Tracer 2 across hillslope and low point.
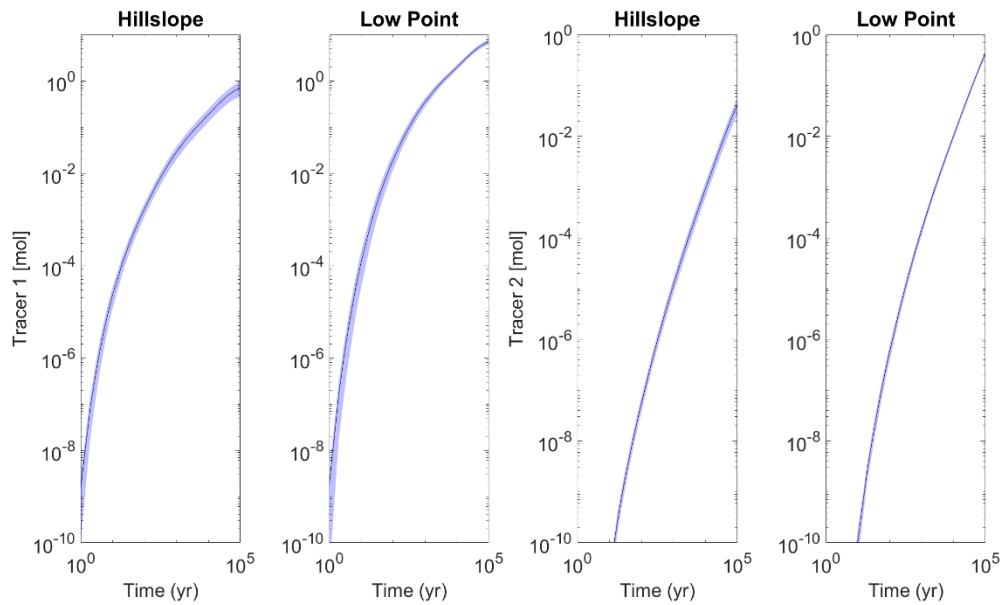
Fig. C-25. Mean and 95% confidence intervals for cumulative mass fluxes of Tracer 1 and Tracer 2 across hillslope and low point.
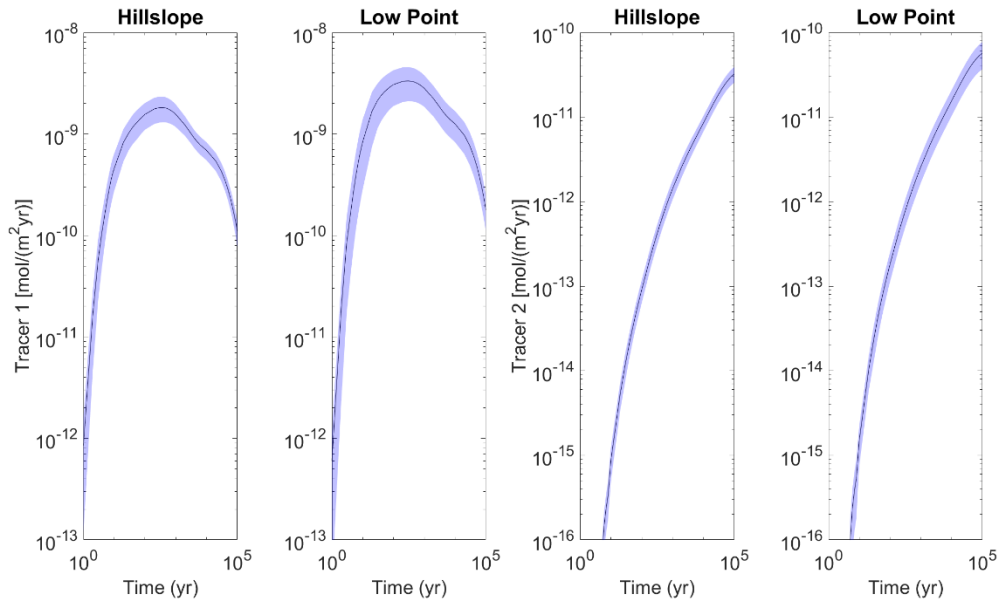
Fig. C-26. Mean and 95% confidence intervals for maximum mass fluxes per unit area of Tracer 1 and Tracer 2 across hillslope and low point.
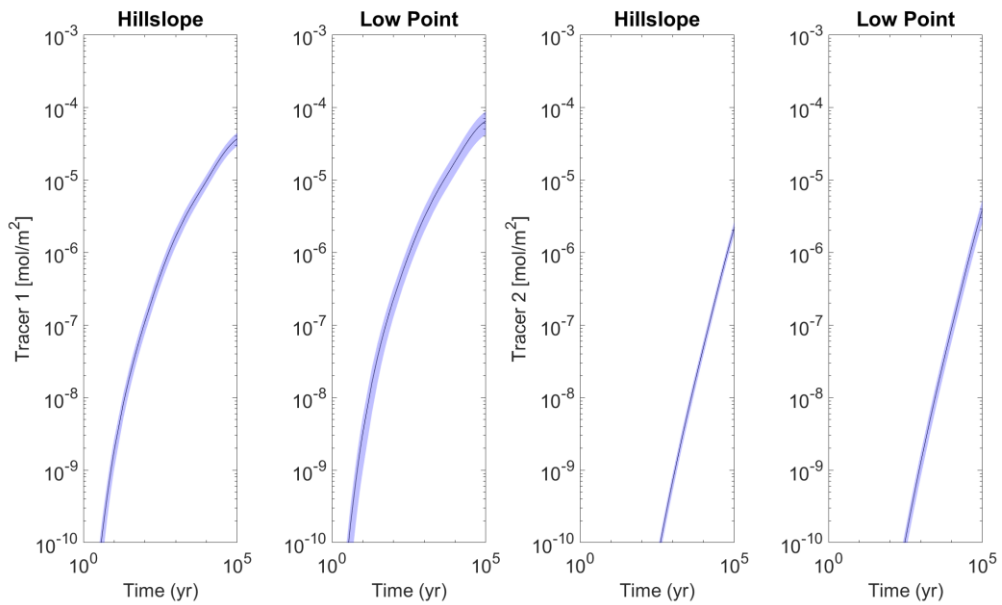
Fig. C-27. Mean and 95% confidence intervals for maximum cumulative mass fluxes per unit area of Tracer 1 and Tracer 2 across hillslope and low point.
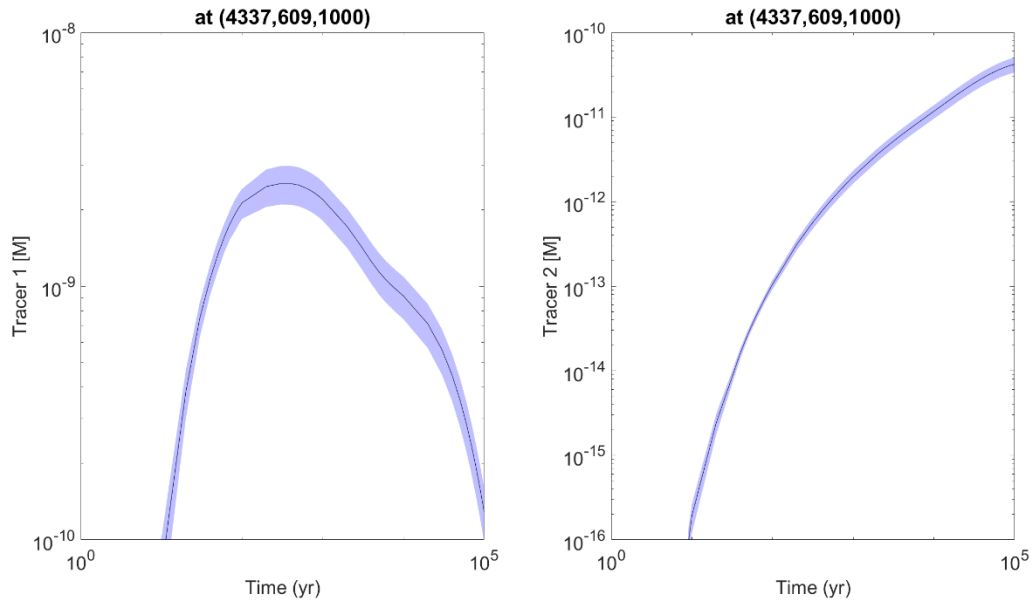
Fig. C-28. Mean and 95% confidence intervals for concentration of Tracer 1 and Tracer 2 at (4337, 609, 1000).

Fig. C-29 presents the cumulative amount of remaining tracers within each component in the near-field component. Specifically, the tracer amount in the buffer includes the amount remaining in the waste package, while the tracer amount in the backfill encompasses the amount remaining in both the waste package and the buffer. From the results, the instant release of Tracer 1 is found to result in nearly all tracers being transported outside the repository within 100,000 years. However, these findings are considered to be an outcome of overly conservative assumptions about transport properties within the waste package (porosity = 1, permeability = 10^{-18} m^2, and effective diffusivity = 10^{-9} m^2/s) and the addition of artificial isotropic diffusion for computational stability, which leads to an exaggerated calculation of tracer transport as illustrated in Fig. C-21 and Fig. C-22. Therefore, the results obtained in this study suggest that in the future, efforts should be made to improve the calculations by either not considering artificial isotropic diffusion or minimizing its influence.
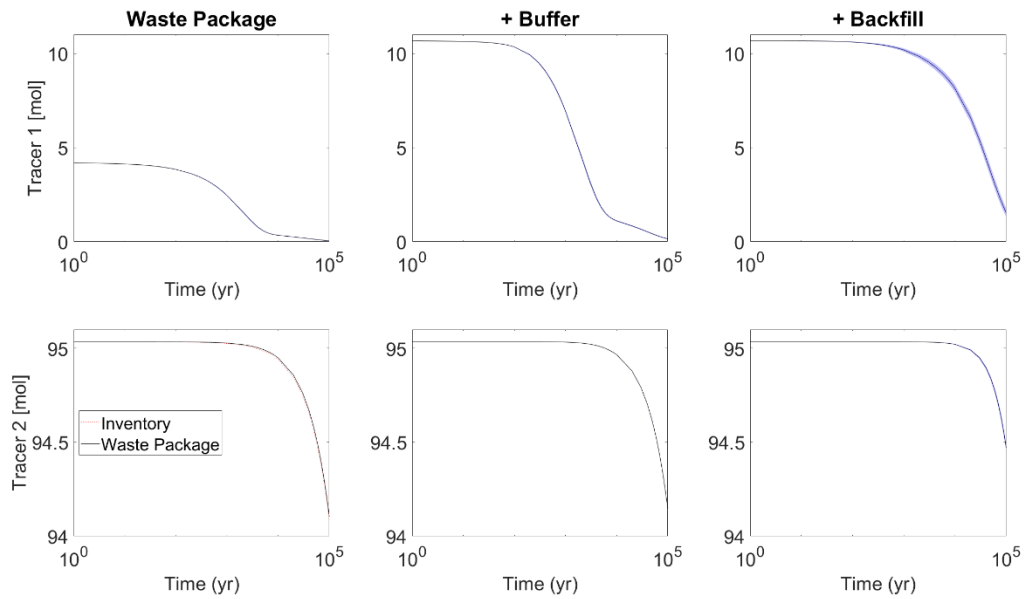
Fig. C-29. Mean and 95% confidence intervals for mass of Tracer 1 and Tracer 2 remained at waste package, buffer, and backfill (cumulative from left to right).

C.5 References

Al-Mohy, A.H. and N. J. Higham (2009), "A new scaling and squaring algorithm for the matrix exponential", SIAM Journal on Matrix Analysis and Applications, 31(3), pp. 970-989.

COMSOL, A. (2019) COMSOL Multiphysics Reference Manual. Version 5.5.

Kolditz, O., H. Shao, W. Wang, and S. Bauer (2015), Thermo-Hydro-Mechanical-Chemical Processes in Fractured Porous Media: Modelling and Benchmarking Closed-Form Solutions (O. Kolditz, H. Shao, W. Wang, & S. Bauer Eds.). Switzerland: Springer International Publishing.

LaForce, T., R. Jayne, R. Leone, P. Mariner, E.R. Stein, S. Nguyen, and T. Frank (2022), DECOVALEX-2023 Task F Specification - Revision 9, SAND2022-10439R. Sandia National Laboratories, Albuquerque, New Mexico.

Tang D.H., E.O. Frind, and E.A. Sudicky (1981), "Contaminant transport in fracture porous media: analytical solution for a single fracture". Water Resources Research, 17(3), 555-564. doi: 10:1029/WR017i003p00555

Appendix D. National Atomic Research Institute (NARI) for Taiwan Power Company

D.1 Introduction

Taiwan Power Company (TPC) is an electric power supplier in Taiwan who has responsibility for the final disposal of spent nuclear fuels of nuclear power plants. National Atomic Research Institute (NARI), a national research institute in Taiwan, was entrusted by Taipower Company to execute the design engineering and performance assessment for the final disposal of nuclear fuels. Based on previous work in Taiwan, the crystalline rock is considered as a potential host rock for deep geological disposal facility. The Swedish KBS-3 disposal concept has been considered as a potential disposal approach in Taiwan. Therefore, participating in the Task F1 is a good opportunity for improving the confidence of methods adopted by NARI/TPC.

D.2 Methods

We utilized DarcyTools (Svensson et al. 2010a), a finite volume code developed by the Swedish Nuclear Fuel and Waste Management Company, SKB, for generating stochastic fractures, upscaling to Equivalent Continuous Porous Medium (ECPM) properties, and simulating steady-state flow, as well as conducting particle tracking.

The Containment Transport (CT) module in GoldSim was employed to simulate mass transport in all cases.

D.3 Benchmarks

D.3.1   1D Transport

The Pipe pathway in the CT module of GoldSim was used to simulate this case. The simulation domain (10 m × 1 m × 1 m beam) was represented by 100 Pipe pathways. At the inflow surface, specifically at x = 0 m, three types of tracers were introduced, including conservative, decay, and adsorbing. The concentration of each solute was maintained at 1 mol/L from 0 seconds to 1.5×10^4 seconds, after which the concentration decreased to 0 mol/L. The water velocity was 10^{-4} m/s, the dispersion coefficient was

10^{-4} m^2/s, the porosity of the material was 4.0×10^{-1}, and the density of the material was 2.0×10^3 kg/m^3. The decay constant (λ) for the decay tracer was 5.0×10^{-5} s^{-1}, and the linear distribution coefficient for the adsorbing tracer was 6.8×10^{-4} m^3/kg. The simulated concentrations of tracers along the domain at 20,000 seconds are shown in Fig. D-1. It is noteworthy that the time at which the maximum concentration is reached for the decay tracer is comparable to that of the conservative tracer. However, in terms of concentration, the decay tracer exhibits a lower maximum concentration. This discrepancy arises from the fact that the observation time of 20,000 seconds surpasses the half-life of the decay tracer. On the other hand, the maximum concentration of the adsorbing tracer is lower than that of the conservative tracer due to adsorption considerations, leading to a slower transport rate. The results show a good agreement between the results simulated by GoldSim and analytical solutions.
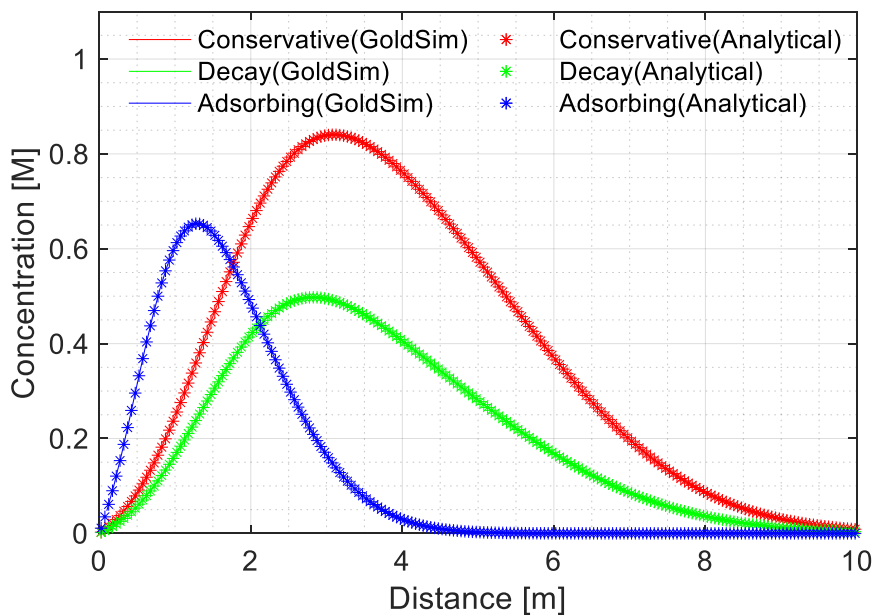
Fig. D-1. 1D transient transport benchmark results.

D.3.2   1D Fracture Plus Matrix Diffusion

The Cell pathway in the CT module of GoldSim was used to simulate this case, the schematic diagram is shown in Fig. D-2. The fracture zone was represented by 140 Cell pathways, with a length of 5.0×10^{-2} m in the low velocity case (0.01 m/day) and 5.0×10^{-1} m in the fast velocity case (0.1 m/day) in the z-direction for each cell. Each cell representing the fracture zone was coupled to 80 Cell pathways representing the matrix zone, where the tracer was transported between the Cell pathways representing matrix zone through diffusion. The first 10 Cell pathways representing matrix zone connected to the fracture zone had an x-direction length of 10^{-3} m, and subsequently, the length of

Cell pathways increased with depth. The total simulated depth of the matrix zone was 2.05 m.

When simulating advection/dispersion transport in fracture zone using Cell pathways, the dispersivity is related to the number of Cell pathways, which represents the level of discretization. The numerical dispersivity is half the length of one of the Cell pathways. When the number of Cell pathways is large enough and the numerical dispersivity is smaller than the desired dispersivity to be simulated, bidirectional virtual water flows should be established between each Cell pathway. This process is undertaken to attain the desired dispersivity. The virtual water flow rate is determined by multiplying the original flow rate in the Cell pathway with a dispersion factor. The dispersion factor can be calculated using the following equation (GTG, 2014b):

$$DispFactor = \left(\frac{n_{cell}\alpha}{L}\right) - 0.5 \qquad (1)$$

where *DispFactor* is dispersion factor [-], n_{cell} is the number of Cell pathways [-], α is the dispersivity [m], and *L* is the pathway length [m].

According to the equation above, the dispersion factors were set to 9.5 and 5.0×10^{-1} for the low velocity and fast velocity cases, respectively.

The concentrations of the tracer in fracture zone and matrix zone simulated using GoldSim are shown Fig. D-3. In this simulation case, it is assumed that the solute concentration is maintained at 1 mol/L at z = 0 m. Therefore, as the observation time increases, the concentration of solute in both the fracture and matrix will be higher. The concentrations of the tracer along fracture zone show a good agreement between the results simulated by GoldSim and analytical solutions. However, in the concentrations of tracer along the matrix zone, the discrepancy between the numerical results and analytical solutions increases at the depths where the x-direction length of the Cell pathway is increased. This discrepancy can be reduced by decreasing the x-direction length of the Cell pathway.
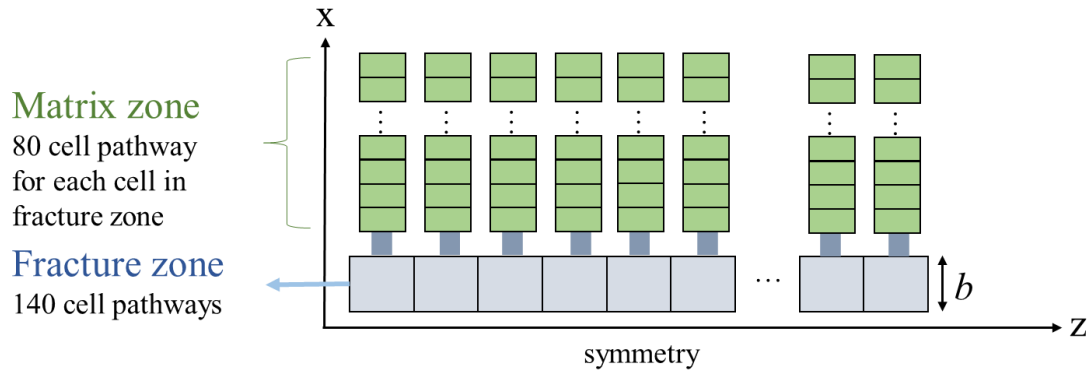
Fig. D-2. 1D Fracture Plus Matrix Diffusion simulation schematic diagram.
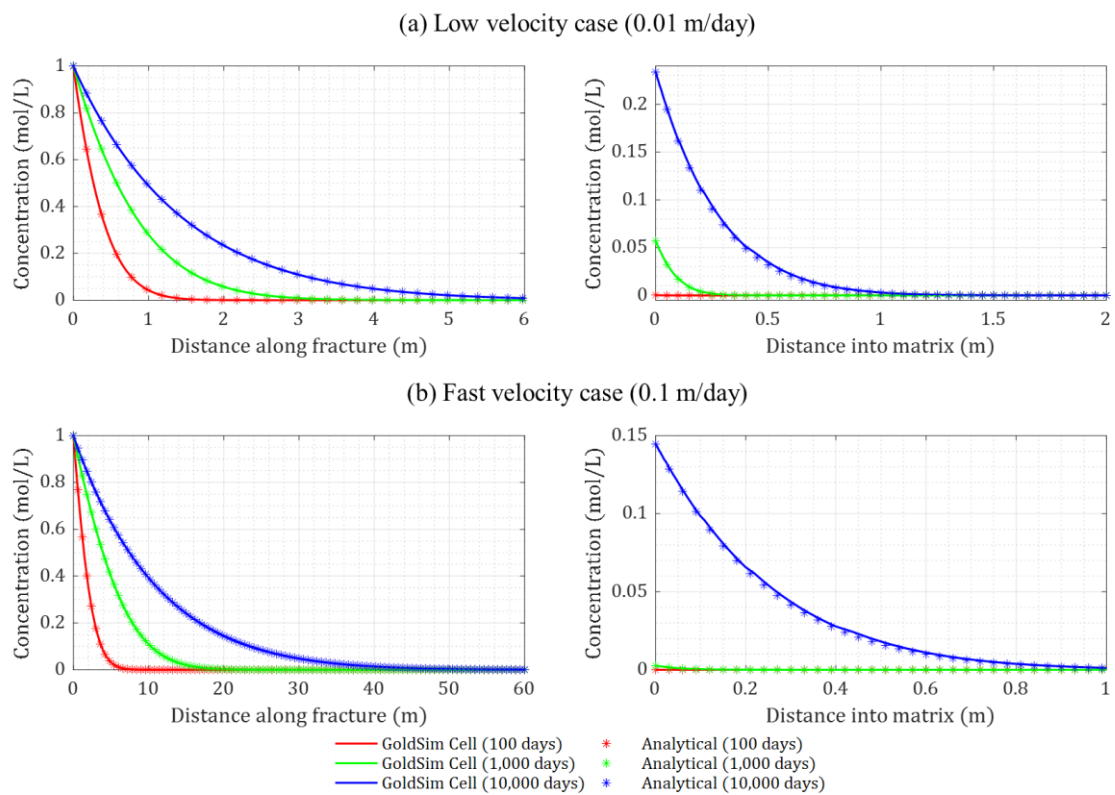
Fig. D-3. Concentrations of tracer as a function of distance in fracture zone and matrix zone for (a) the low velocity case (0.01 m/day) and (b) the fast velocity case (0.1 m/day).

D.3.3   Four-Fracture Transport

The Four-Fracture Transport case was simulated using DarcyTools. The four deterministic fractures were generated and upscaled to ECPM properties. In order to reduce the impact of cells not intersected by fractures, their permeability and porosity were set to negligible values. The permeability (k) was set to 10^{-27} m^2, and the porosity (ϕ) was tested at values of 10^{-14} and 10^{-20}. The modelled size of the domain was 1,024 m × 1,024 m × 1,024 m (range for x, y and z directions is from -512 m to 512 m). After

upscaling, the overall grid size is 8 m × 8 m × 8 m. To accurately simulate the boundary conditions, a smaller grid size of 4 m × 4 m × 4 m has been adopted near the positions x = -500 m and x = 500 m. The grid size is illustrated in Fig. D-4 and the total number of cells is 2,555,904. After upscaling, a pressure of $1.001×10^6$ Pa was applied at the x = -500 m, and a pressure of 10^6 Pa was applied at the x = 500 m to simulate the steady-state flow field, the result is shown in Fig. D-5. The particle tracking method has been adopted to simulate conservative tracer through four fractures. A total of 10,000 particles were uniformly placed along west face (x = -500 m) of inlet fracture. Trajectories of the particles are depicted in Fig. D-6. Fig. D-7 shows the normalized cumulative releases for two different porosities of cells not intersected by fractures. Only 95% of the total mass is released from the east boundary (x = 500 m) at the end of the simulation time when the porosity of cells not intersected by fractures is 10^{-14}. If the porosity is reduced to 10^{-20}, the total mass released from the east boundary at the end of the simulation time is increased to about 99.5%.
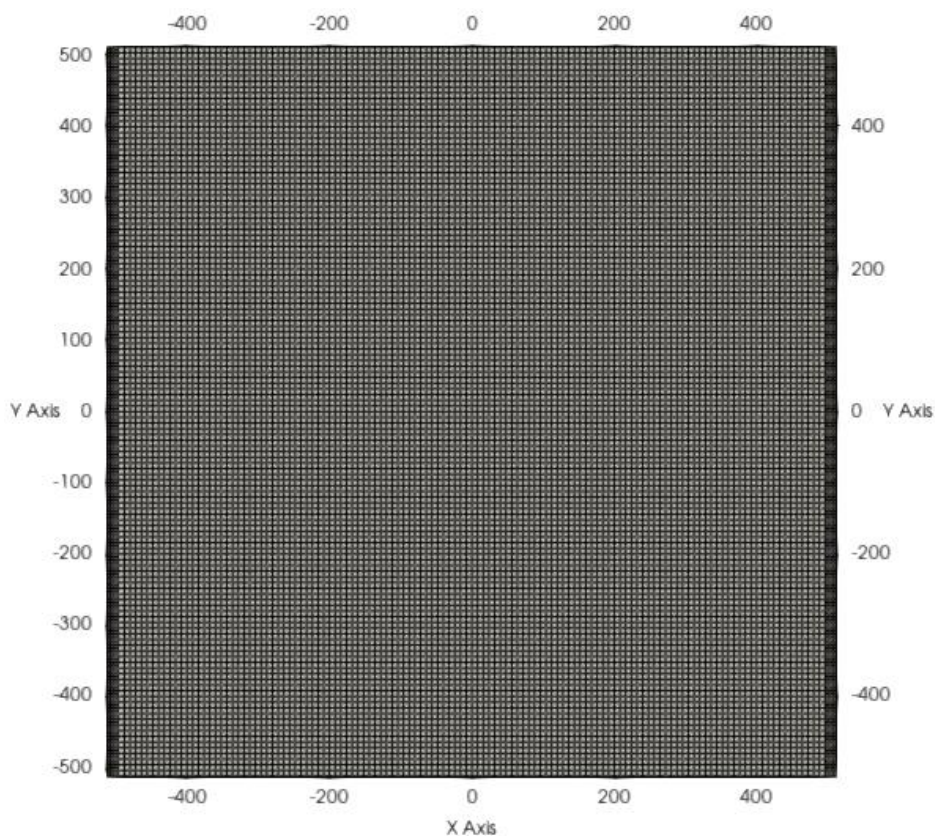
Fig. D-4. Grid in the Four-Fracture Transport case.
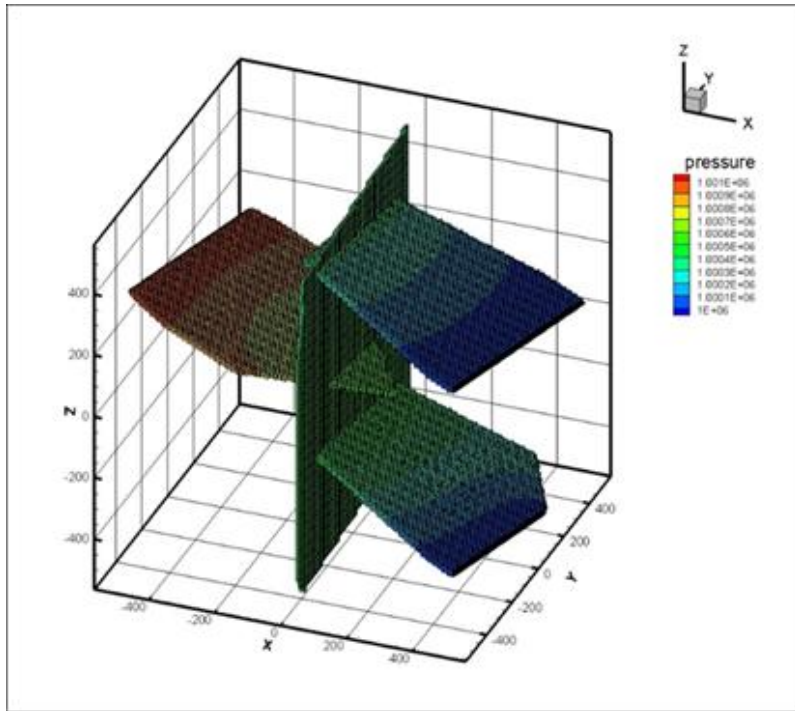
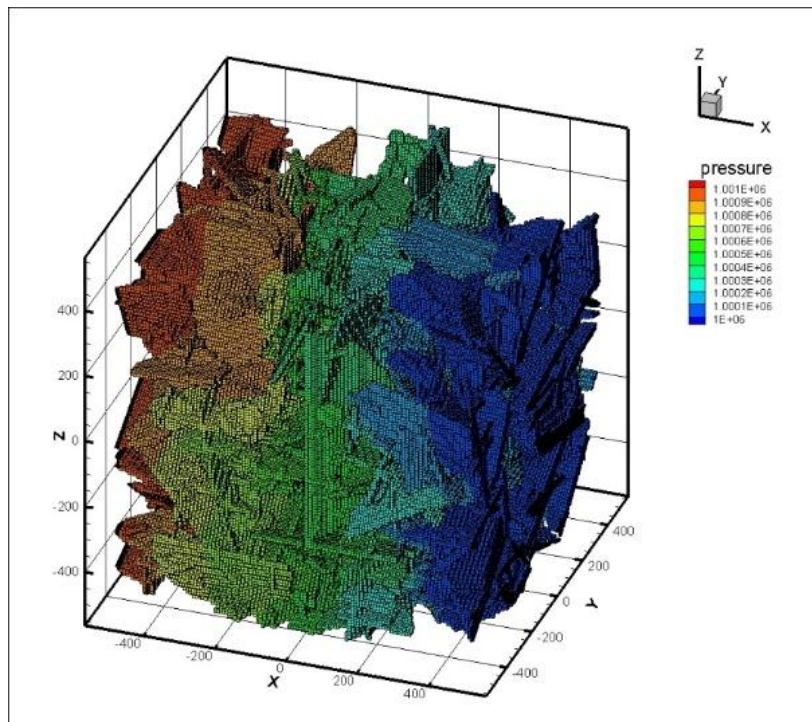**Fig. D-5. Steady-state flow field for the Four-Fracture Transport case simulated using DarcyTools.**
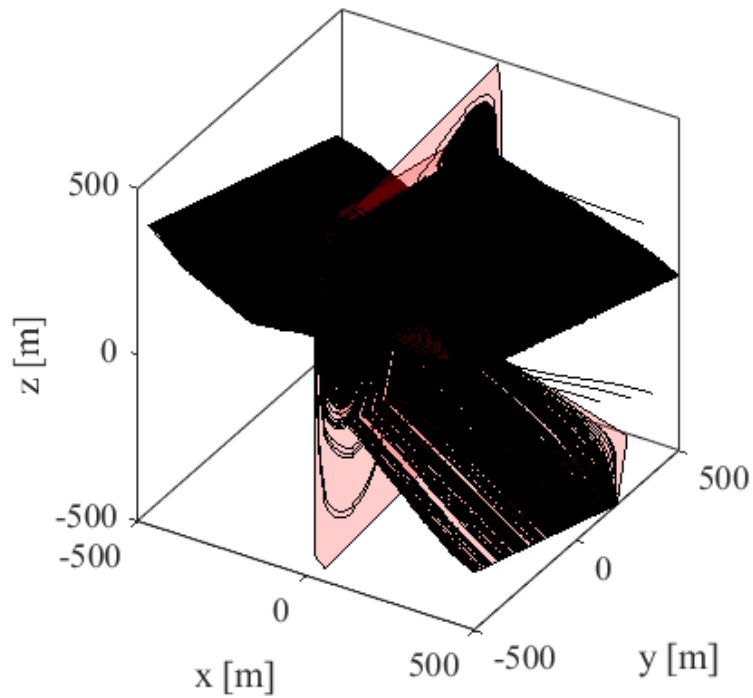
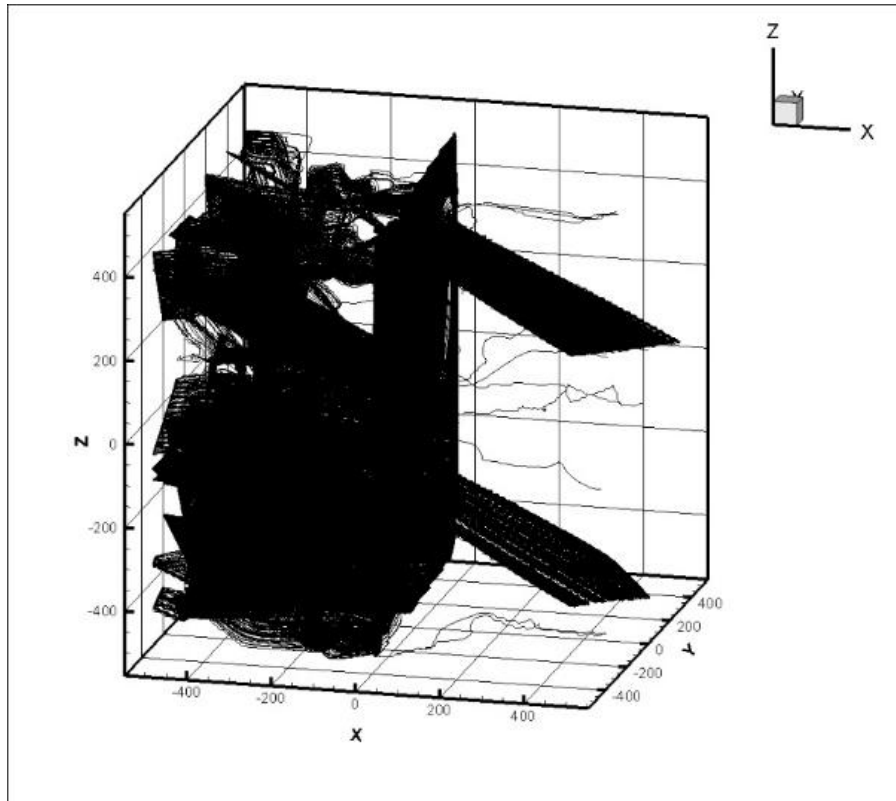**Fig. D-6. Trajectories of particles in the Four-Fracture case simulated using DarcyTools.**
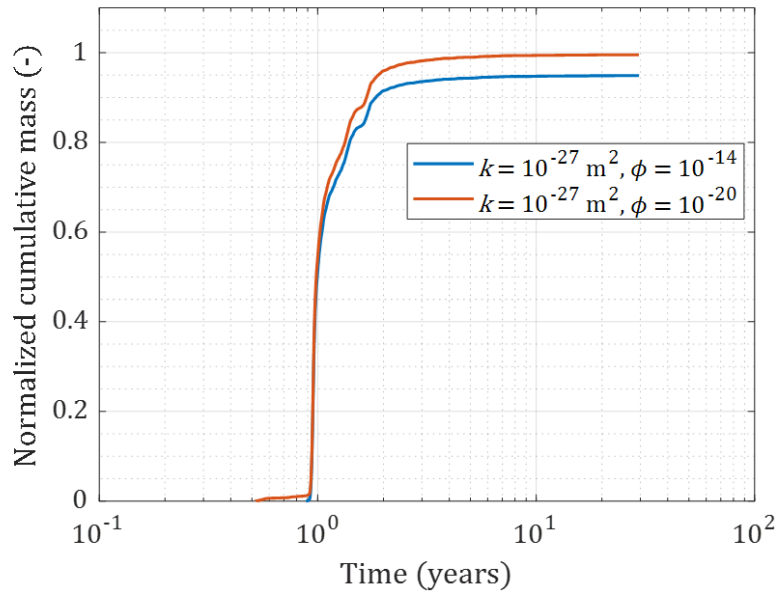
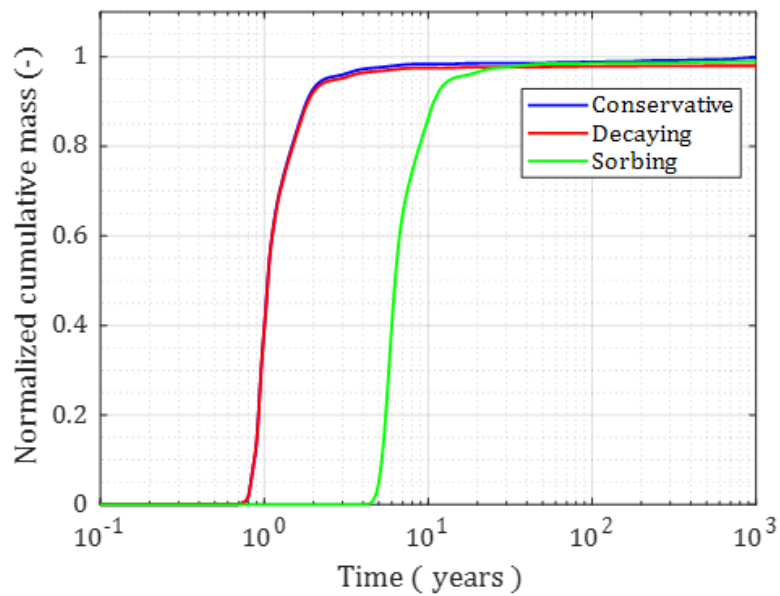**Fig. D-7. Breakthrough curves for the Four-Fracture Transport case using particle tracking method.**

D.3.4   Four-Fracture Plus Stochastic Fractures

The Four-Fracture Plus Stochastic Fractures case is simulated using DarcyTools and GoldSim. The stochastic fractures provided by SNL are imported into the Four-Fracture Transport case simulated using DarcyTools. The domain size in the model was 1,024 m × 1,024 m × 1,024 m. The overall grid size was 8 m × 8 m × 8 m. However, for the x-axis, a smaller grid size of 4 m × 4 m × 4 m was implemented before -488 m and after 496 m. In order to ensure accurate position of particles at the inlet face of fractures, a grid size of 2 m × 2 m × 2 m was adopted within the x-axis range from -512 m to -496 m. The grid size is visually represented in Fig. D-8 and the total number of cells amounts is 4,505,600. The permeability (k) and the porosity (ϕ) of cells not intersected by fractures were set to 10^{-27} m^2 and 10^{-20} m^2, respectively. The steady-state flow filed simulated by DarcyTools is shown in Fig. D-9. A particle was placed in the cells that intersected a fracture at the location x = -500 m. A total of 8,875 particles were placed at west face (x = -500 m) of inlet fractures. Fig. D-10 shows trajectories of the particles. After particle tracking, three parameters were estimated for each particle, including the flow-related transport resistance (F), the advective travel time (t_w), and the flow path length (L). The F is estimated by summing the values for all cells (i) along the flow path:

$$F = \sum_i F_i = \sum_i \left(\frac{a_r L}{q}\right)_i \tag{2}$$

where a_r is the flow-wetted surface per volume of rock [m^{-1}], L is the length of the cell [m], and q is the Darcy flux through the cell [m/yr].

The t_w is estimated by summation the time needed for a particle to traverse a cell i for all cells along the flow path:

$$t_w = \sum_i t_{wi} = \sum_i \left(\frac{L}{v_c}\right)_i \tag{3}$$

$$v_c = \frac{q}{\phi} \tag{4}$$

where t_w is the advective travel time [yr], v_c is the advective transport velocity in a cell [m/yr], q is Darcy flux [m/yr], and ϕ is the cell ECPM kinematic porosity [-].

The L is estimated by adding the length of each cell the particle traverses. After estimation, a total of 8,875 sets of the parameters are obtained. The transport of tracers was conducted using GoldSim with a Pipe pathway in the CT module. The input parameters used to describe the geometry of the Pipe pathway include length (L), width (W), cross-sectional area (A) and wetted perimeter (P) of the channel. The width (W) of the channel was arbitrarily assumed to be 1 m. The cross-sectional area (A) and wetted perimeter (P) of the channel were calculated based on the parameters provided by DarcyTools:

$$A = e_T W = \frac{2t_w}{F} W \tag{5}$$

$$P = 2(e_T + W) \tag{6}$$

where A is the cross-sectional area of the channel [m^2], e_T is the aperture of the channel [m], W is the width of the channel [m], and P is the wetted perimeter of the channel [m].

Water flux (v) and flow rate (Q) of the channel are given as:

$$v = \frac{L}{t_w} \tag{7}$$

$$Q = e_T W v \tag{8}$$

where v is the water flux of the channel [m/yr] and Q is the flow rate of the channel [m^3/yr].

The duration of the tracer injection was set at one day. Following 8,875 realizations of mass transport, the cumulative released masses of tracers for each particle were weighted based on the Darcy velocity at their respective initial positions, as estimated by DarcyTools. Subsequently, the weighted released masses were aggregated to

calculate the normalized total cumulative release mass. The results are shown in Fig. D-11. Notably, by the end of the simulation, the conservative tracer exhibited an arrival rate of approximately 99.91%.
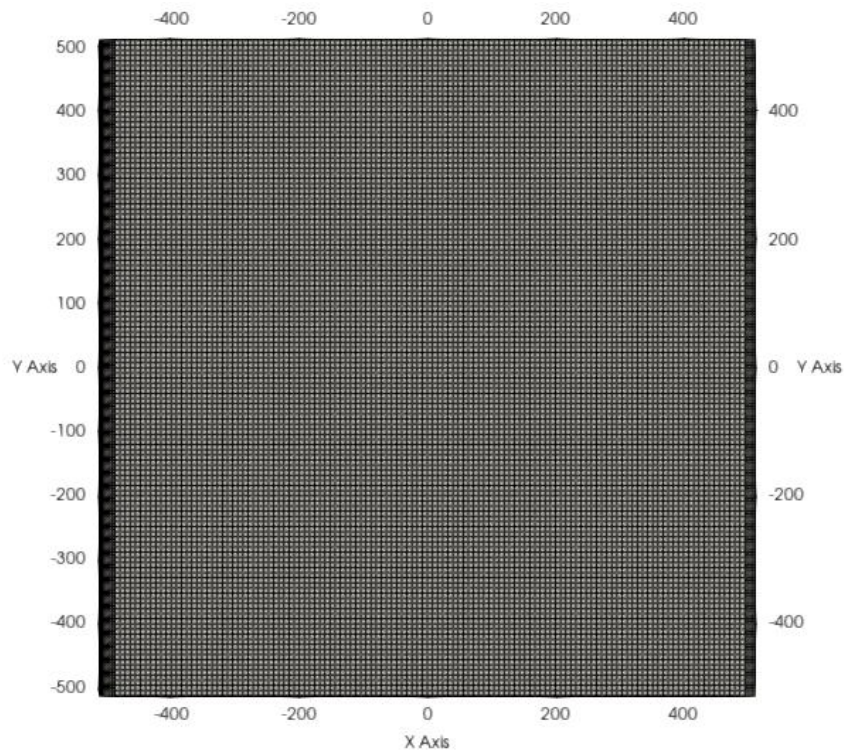
Fig. D-8. Grid in the Four-Fracture Plus Stochastic Fractures case.

Fig. D-9. Steady-state flow field for the Four-Fracture Plus Stochastic Fractures case simulated using DarcyTools.

Fig. D-10. Trajectories of particles in the Four-Fracture Plus Stochastic Fractures case simulated using DarcyTools.

Fig. D-11. Breakthrough curves of tracers for the Four-Fracture Plus Stochastic Fractures case.

D.3.5   Continuous Point Source

The overall simulation methods are similar to the Four-Fracture Plus Stochastic Fractures case, except for the initial positions of the particles in DarcyTools and the injection duration of the tracers in GoldSim. To simulate the point source using particle tracking in DarcyTools, 9,801 particles were uniformly distributed in a square region centered at (x = -497 m, y = 7 m, z = 248.25 m) and with a side length of 0.2 m, as depicted in Fig. D-12. The trajectories of these injected particles are shown in Fig. D-13. In the mass transport simulated using GoldSim, the tracers are injected continuously into the Pipe pathway. After 9,801 realizations of mass transport, the release rates of particles were summed to obtain the normalized total release rate. The results of the normalized breakthrough curves for tracers are shown in Fig. D-14.
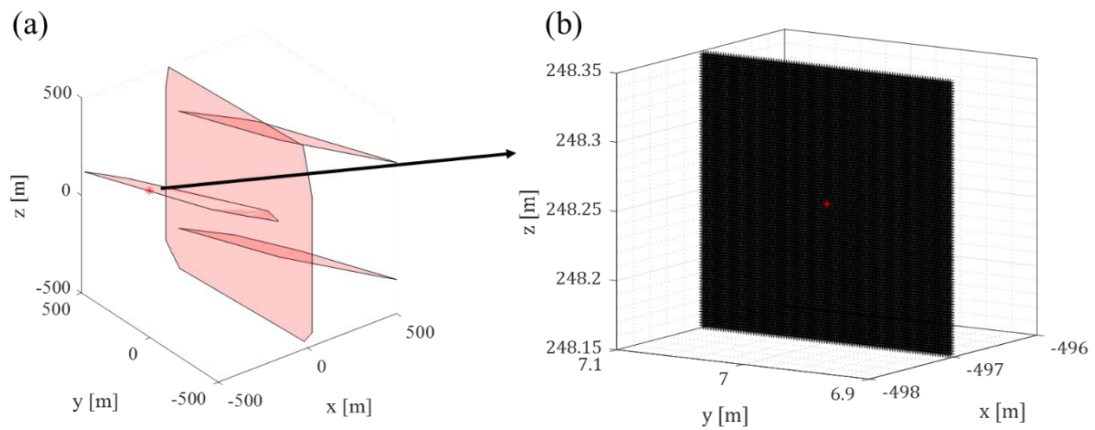
Fig. D-12. (a) Red star indicates the precise location of point source specified in Task specification report, (b) Positions of particles used to simulate the point source in DarcyTools. Note: the stochastic fractures are not shown in this figure.
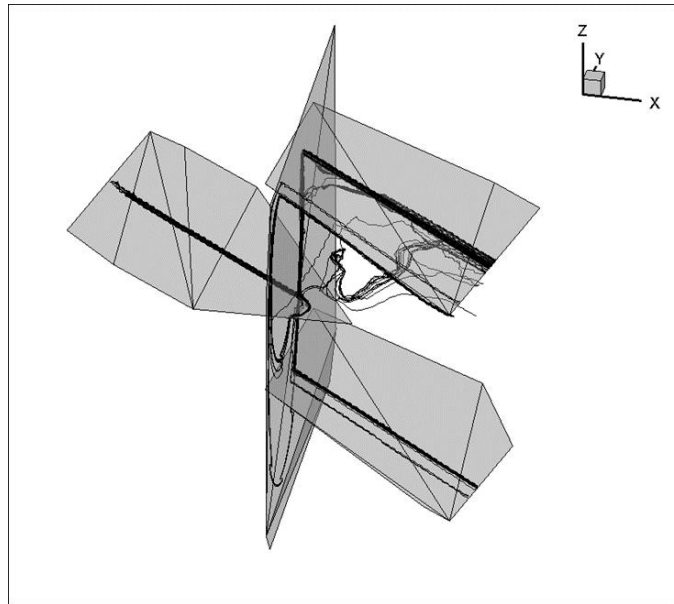
Fig. D-13. Trajectories of particles in the Continuous Point Source case simulated using DarcyTools. Note: the stochastic fractures are not shown in this figure.
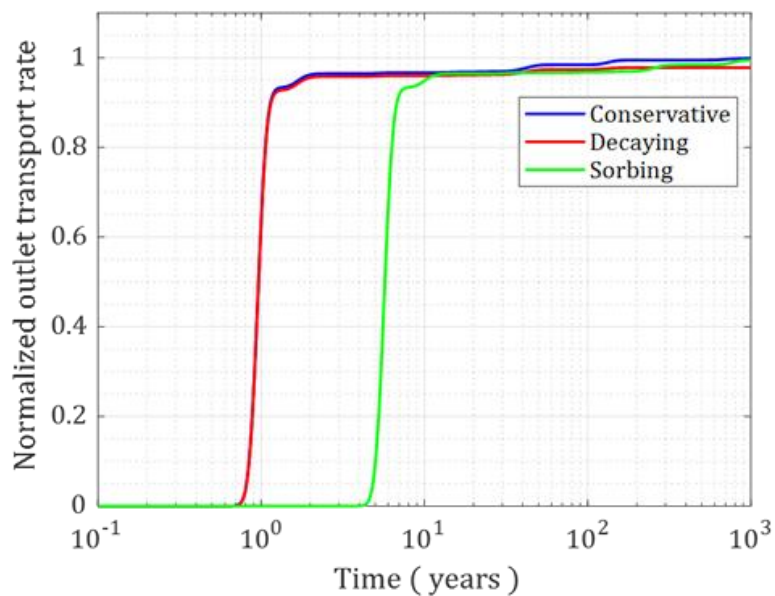
Fig. D-14. Breakthrough curves of tracers for the Continuous Point Source case.

D.3.6 Radionuclide Source Term Benchmark

The Radionuclide Source Term Benchmark case is simulated using GoldSim. A Cell pathway has been used to simulate the activity of 4n+1 decay chain radionuclides and Tc-99 over time in a waste package with 10^4 m^3 of water. The initial activities of radionuclides were specified according to the Table 5-10 in section 5.3 of Task specification report (LaForce et al. 2023). The results simulated using GoldSim are

compared with results extracted from Anttila (2005) and shown in Fig. D-15 and these results exhibit excellent agreement.

A Source element in GoldSim was used to simulate the waste package breach time (3,000 years) and release mechanisms of radionuclides from fuel matrix (instant/continuous release), which includes a Cell pathway used to dissolve the radionuclide released from fuel matrix. The amount of water in the Cell pathway was specified as 10^4 m^3. The initial activities of radionuclides in fuel matrix were specified according to the Table 5-10 in section 5.3 of the Task specification report. A release fraction of 10^{-6} yr^{-1} was specified for the fuel matrix and 3% of Tc-99 was released from fuel matrix into water in the Cell pathway immediately upon waste package breach. The solubility limits listed in the Table 5-10 were also applied to the water in the Cell pathway. The total, fuel, aqueous and precipitated concentrations of different radionuclides over time simulated using GoldSim are shown in Fig. D-16.
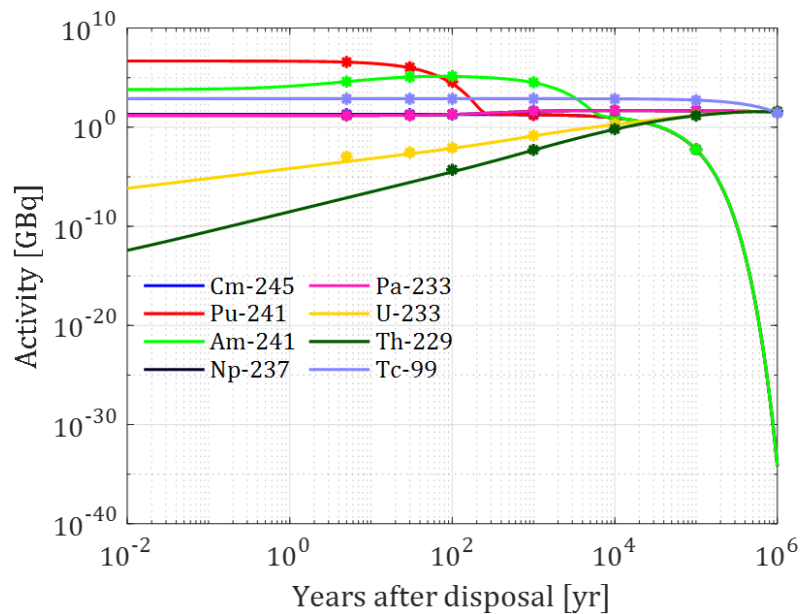
Fig. D-15. Activity of radionuclides for the Radionuclide Source Term Benchmark case. The lines represent simulated results obtained through GoldSim. The dots represent results extracted from Anttila (2005).
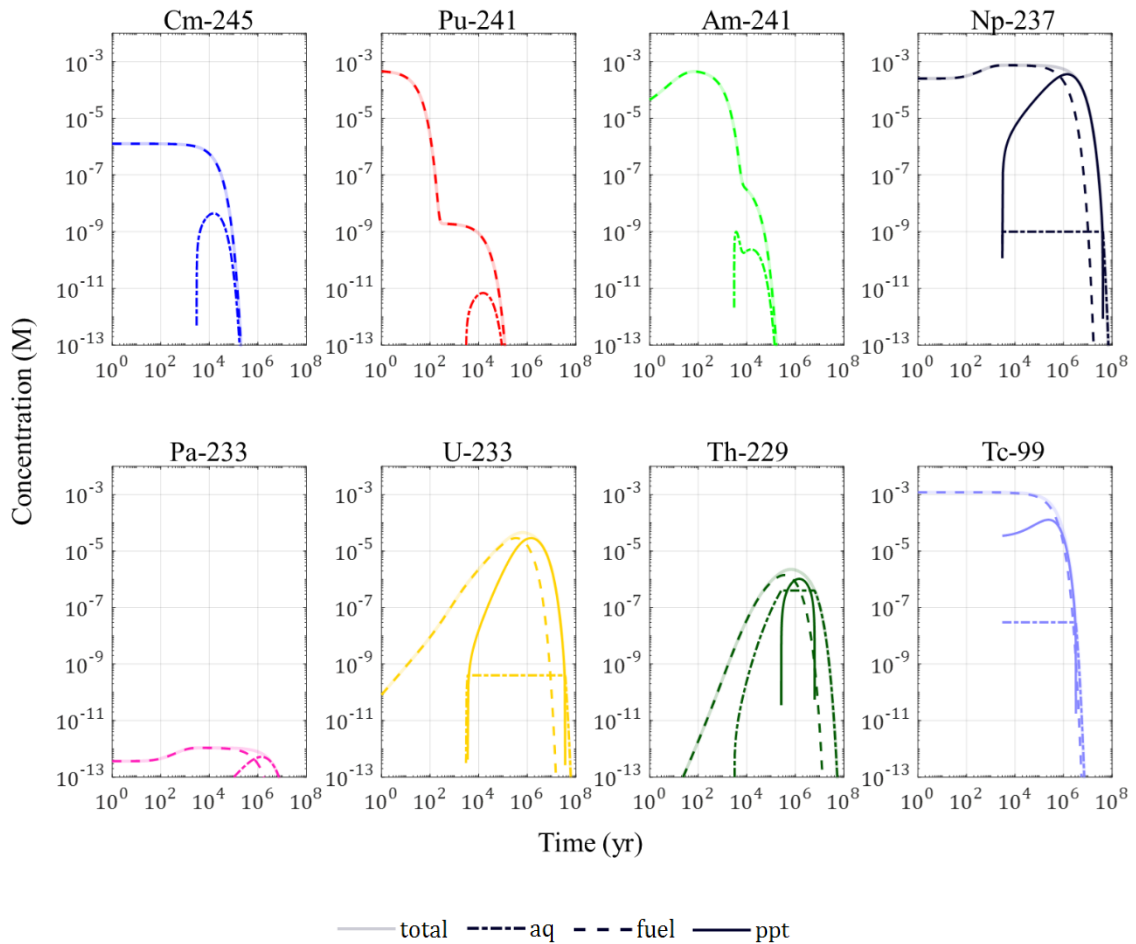
Fig. D-16. Concentration of radionuclides in the waste package simulated using GoldSim. Note: total = total concentration, aq = aqueous concentration, fuel = fuel concentration, and ppt = precipitated concentration.

D.4 Reference Case

D.4.1   Model Domain

The layout of the repository was established using SketchUp as outlined in section 3.4 of the Task F specification report (LaForce et al. 2023, Table 3-4), as shown in Fig. D-17. The layout was output as STL format and imported by DarcyTools.

The computational grid in DarcyTools is an unstructured adaptive Cartesian grid. At the beginning of grid generation, a single cell covers the entire domain. After that, the grid generator splits cells requiring refinement in two half cells. This procedure will be repeated until the specified cell size is reached. The refinement was hierarchically applied from the default cell size (32 m × 32 m × 32 m) to the maximum cell size (8 m × 8 m × 8 m) in the fractures. On the top of the domain, the size of cells belong to

hillslope area was reduced to 2 m × 2 m × 1 m. Then the cell size of 1 m × 1 m × 1 m was globally applied in the repository zone and cell size of 0.25 m × 0.25 m × 0.50 m was applied around deposition holes.
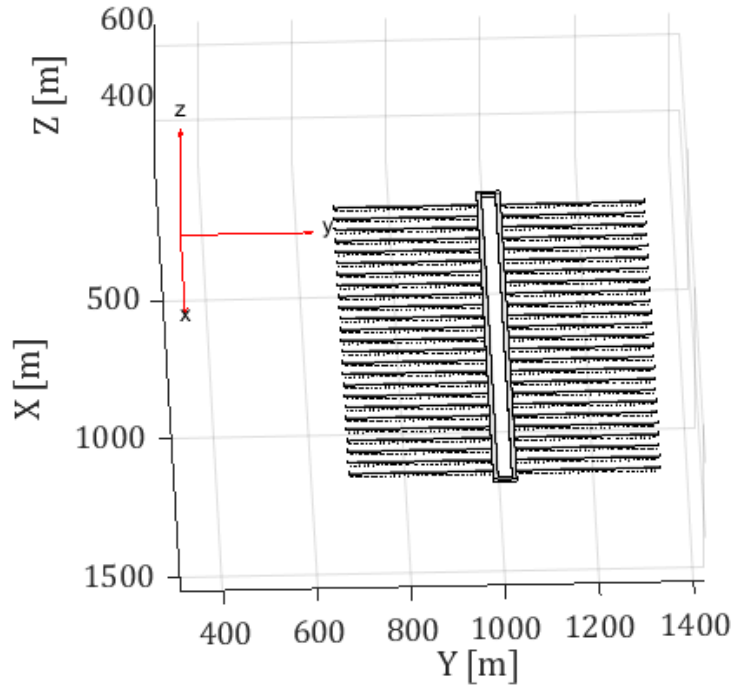
Fig. D-17. The layout of the repository established using SketchUp.

D.4.2   Fracture Network

The deterministic fractures in the Reference case were included in the simulation. Based on the DFN recipe listed in the Task F specification report (LaForce et al. 2023, Table 3-4), the stochastic fractures were generated by DarcyTools. The information used to generate the stochastic fractures were dependent on the depth of the simulation domain. From the top surface to z = 850 m, from z = 850 m to z = 700 m and from z = 700 m to z = 0 m, the information of Depth Zone 2, 3 and 4 were used, respectively. Sizes of generated fractures obey the power law size distribution:

$$f(r) = \frac{kr_0^k}{r^{k+1}}, k \geq 2, r_0 < r < \infty \tag{9}$$

where r is fracture radius [m], r_0 is the minimum radius [m], and k is the scaling characteristics of fractures as a function of size [-].

The lower and upper limit of fracture radius implemented in the Reference case were 30 m and 574 m, respectively. The fracture intensity (P_{32}) within this size interval was adjusted by:

$$P_{32}[r_{min}, r_{max}] = \frac{\pi n_0 k r_0^k}{2-k}\left(r_{max}^{2-k} - r_{min}^{2-k}\right) \tag{10}$$

where r_{min} is lower limit of fracture radius [m], r_{max} is upper limit of fracture size [m], and n_0 is average number of fractures per unit volume of rock [-].

The fractures generated by DarcyTools were assumed to be squares with length (L_f) and aperture (e_T). The equivalent length of a square fracture was calculated by:

$$L_f = r\sqrt{\pi} \tag{11}$$

The orientations of the generated fractures obey the Univariate Fisher orientation distribution. Isolated single fractures or fractures of isolated clusters were removed from the generated fracture network.

The fracture transmissivity is a function of fracture size. A semi-correlated power law model was adopted in DarcyTools to calculate the fracture transmissivity:

$$T = \min\left[a_T 10^{d_T Uni}\left(\frac{L_f}{100}\right)^{b_T}, c_T\right] \tag{12}$$

where T is the fracture transmissivity [m²/s], a_T is the transmissivity of a 100 m large fracture [m²/s], b_T is the power law exponent [-], c_T is a threshold transmissivity value [m²/s], d_T is a dimensionless coefficient that determines the spread of generated random deviates using a uniform distribution (Uni), and L_f is the fracture size [m].

A fully-correlated relationship of fracture radius and transmissivity is required in the Reference case. Thus, the parameters imported into the above equation were modified to enable DarcyTools to calculate the fracture transmissivity based on a fully-correlated relationship. The parameters were calculated or are imported according to following table:

Tab. D-1. Parameters used in calculation of fracture transmissivity.

Parameter	a_T	b_T	c_T	d_T
Equation or Value	$b^T\left(\frac{100}{\sqrt{\pi}}\right)^{b^T}$	b_T	1	0

The coefficients (a_T and b_T) used to calculate the transmissivity of the deterministic fractures were taken from the EW fractures in Depth Zone 3 listed in the Task Specification (LaForce et al. 2023, Table 3-4).

The aperture of the fractures was calculated based on the transmissivity of the fractures using the cubic law (Bear et al. 1993):

$$e_T = \left(12T\frac{\mu}{\rho g}\right)^{\frac{1}{3}} \tag{13}$$

where e_T is fracture aperture [m], μ is viscosity of water [Pa. s], ρ is density of water [kg/m³], and g is the acceleration due to gravity [m/s²].

After assigning the transmissivity and aperture values to the fractures and the porosity to the rock matrix, effective continuum porous media (ECPM) upscaled from DFN was performed in DarcyTools. The porosity of a cell intersected by a fracture was calculated by (Svensson et al. 2010b):

$$\phi = V_I/V_{cell} \tag{14}$$

where ϕ is the porosity of the cell intersected by a fracture aperture [-], V_I is the fracture intersecting volume of a cell [m³] and V_{cell} is the volume of a cell [m³].
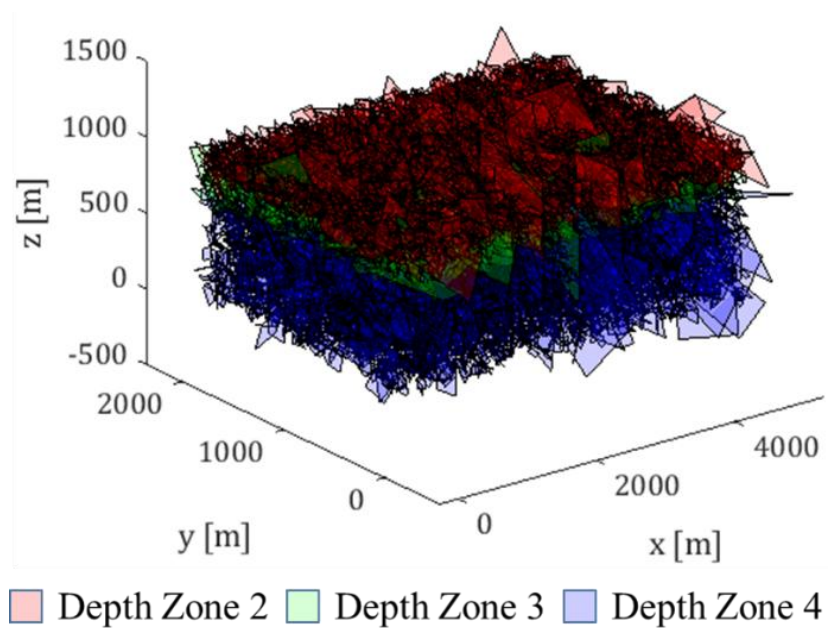
Fig. D-18. A stochastic DFN realization generated using DarcyTools.

D.4.3   Flow Model

The model, constructed using DarcyTools, was run transiently for a sufficient duration to achieve a state of steady flow.

To calculate the steady state water flow through specified regions of the top surface, the domain was divided into three regions along the x direction. The range of x of each

region is 0 m < x < 1,700 m (top area), 1,700 m < x < 3,700 m (hillslope area) and 3,700 m < x < 5,000 m (low point area), respectively.

Fig. D-19 illustrates the grids at the left boundary of the reference case domain. In order to prevent numerical errors from occurring in the cells at the domain boundary, the cells with centers located at depths of 1,017 m and 997 m were used to calculate the steady-state water flow through the top and low point areas, respectively. For the steady-state water flow through the hillslope area, the height of the topmost cells differs along x-direction, shown in Fig. D-20. Therefore, for each column of cells along the x-direction, the water flow was calculated by selecting the cells at the third depth from the top. Based on our extensive testing, we have observed that the steady-state water flow through the hillslope area varies across different DFN realizations, resulting in a diverse range of results. To tackle this issue, it was necessary to recalculate the steady-state water flows of the hillslope for different DFN realizations. This was done under the assumption that water flow is conserved, ensuring that the total inflow matches the total outflow.

Tab. D-2. Steady-state water flows through different surface regions.

DFN realization	Flux [kg/yr]		
	Top area	**Hillslope area**	**Low point area**
1	-6.11E+05	1.45E+05	4.66E+05
2	-1.01E+06	8.17E+05	1.91E+05
3	-8.74E+05	4.35E+05	4.38E+05
4	-1.01E+06	4.64E+05	5.45E+05
5	-8.11E+05	-7.09E+04	8.82E+05
6	-3.36E+05	1.67E+05	1.69E+05
7	-1.49E+06	9.16E+05	5.76E+05
8	-1.32E+06	7.75E+05	5.47E+05
9	-8.20E+05	1.65E+05	6.54E+05
10	-1.21E+06	7.14E+05	4.95E+05
Mean	-9.49E+05	4.53E+05	4.96E+05
Standard deviation	3.40E+05	3.42E+05	2.08E+05

Note: the flux through the hillslope area is calculated based on the fluxes of top and low point areas.
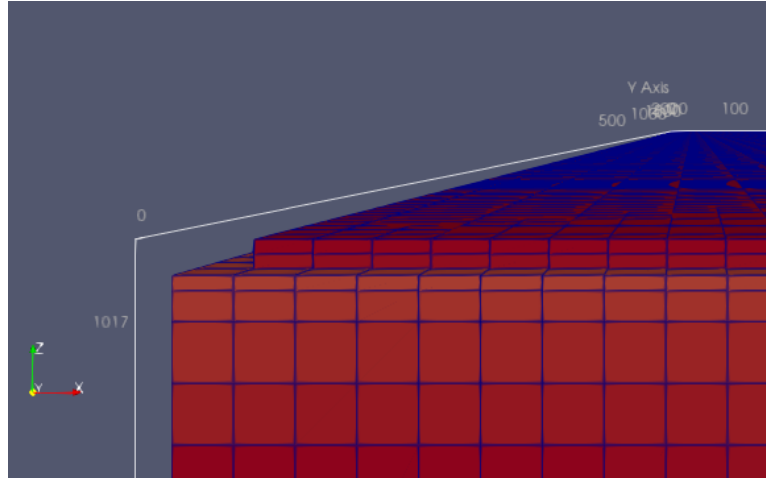
Fig. D-19. The grids at the boundary of the domain of the reference case.
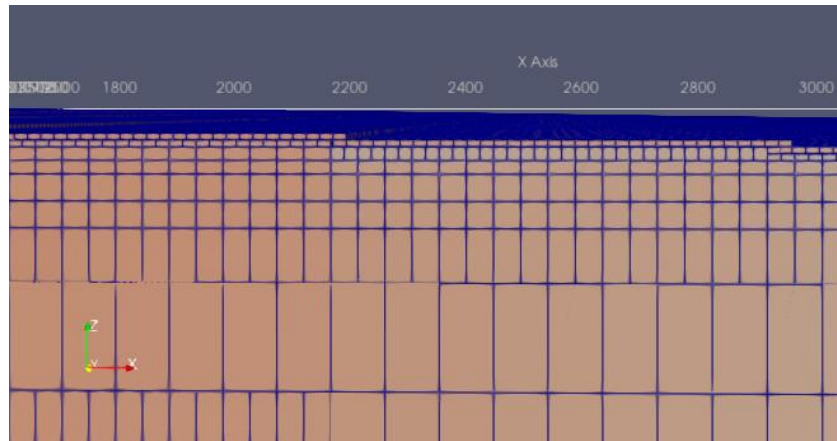
Fig. D-20. The grids at the front and top boundaries of the hillslope area.

D.4.4   Tracer Release and Transport

In order to facilitate the flow information required for the mass transport simulation software, GoldSim, particle tracking was employed through DarcyTools. This process involves placing a single particle within each deposition hole, from which we obtain two near-field parameters and three far-field parameters for each particle.

The near-field parameters, namely the equivalent initial flux (U) and the equivalent flow rate (Q_{eq}), play a crucial role in the near-field models of mass transport. U represents the average Darcy velocity surrounding the deposition hole. On the other hand, Q_{eq} signifies the rate at which mass is transferred from a deposition hole as a result of water seeping into the fracture intersecting the deposition hole (Neretnieks et al., 2010). To calculate Q_{eq}, the following equation is adopted:

$$Q_{eq} = 2UH\sqrt{2D_w t_{DH}}$$ (15)

where Q_{eq} is the equivalent flow rate [m³/yr], U is the equivalent initial flux [m/yr], H is the height of the deposition hole [m], D_w is the diffusivity in the water, and t_{DH} is the time that the water is in contact with the deposition hole [yr].

The far-field parameters, including the flow-related transport resistance (F), the advective travel time (t_w), and the flow path length (L), are calculated along the flow path. The estimations of these parameters have been mentioned in section D-3.4. After estimation, each deposition hole has a set of flow information. Total of 2,500 sets of flow information are obtained for each DFN realization. Fig. D-21 shows the cumulative fraction of flow-related transport resistance (F), advective travel time (t_w) and flow path length (L) for 10 DFN realizations. The results show that variations in fracture properties across different realizations lead to significant variability in F, t_w and L. Specifically, realization 1 exhibits lower F and t_w values, while realization 6 demonstrates higher values in comparison. Fig. D-22 shows the cumulative fraction of F, t_w and L for particles released from hillslope and low point areas in 10 different DFN realizations. The results show that particles released from the low point area have higher values of F, t_w and L.
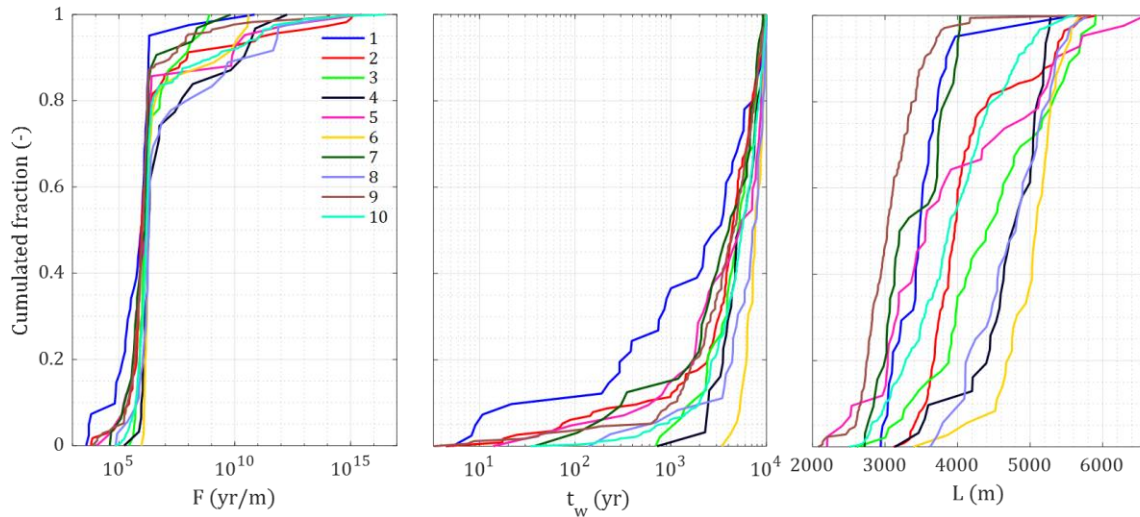
Note: Only the data of particles with advective travel time (t_w) less than 10^5 years are shown.

Fig. D-21. Cumulative fraction of flow-related transport resistance (*F*), advective travel time (*t_w*) and flow path length (*L*) for 10 DFN realizations.
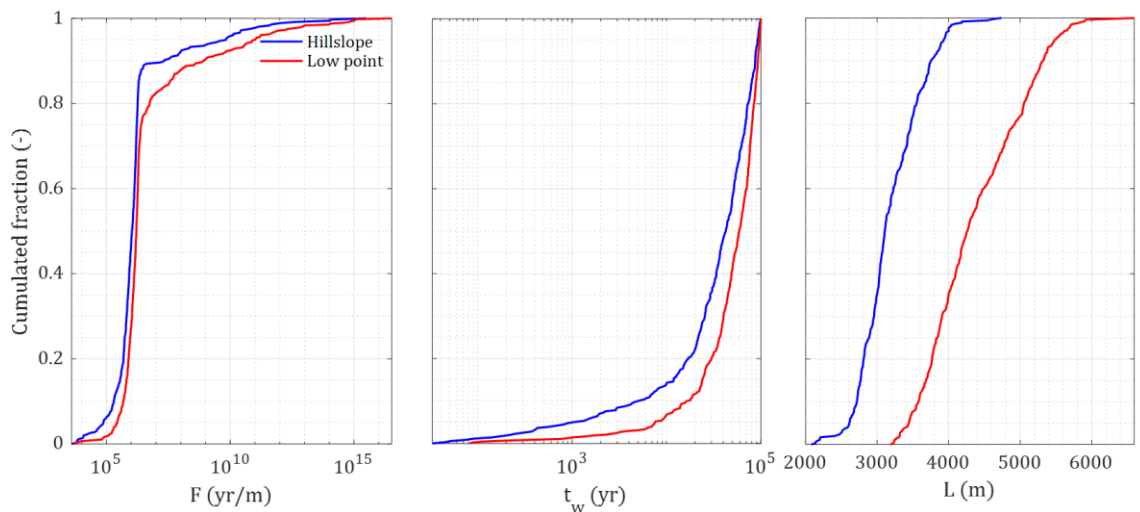
Note: Only the data of particles with advective travel time (t_w) less than 10^5 years are shown.

Fig. D-22. Cumulative fraction of flow-related transport resistance (*F*), advective travel time (*t_w*) and flow path length (*L*) for particles released from hillslope (blue line) and low point (red line) areas in 10 different DFN realizations.

The mass transport was conducted using GoldSim with the CT module. Two near-field models were established based on the conditions of deposition hole, including deposition hole without fracture intersection and deposition hole with a fully crossing fracture.

In the CT module, the Cell pathway serves as a means to simulate a mixing cell. This pathway represents the various components within a deposition hole, including the canister (represented as a void volume in our simulations), the buffer, and the backfill

material. It is important to note that the deposition tunnel was not accounted for in the near-field models of mass transport.

The first near-field model, deposition hole without fracture intersection, was established by referring to POSIVA (Poteri et al. 2014). The void volume(V) in a deposition hole is filled with water and specified to be:

$$V = r^2 \pi h \tag{16}$$

where V is the void volume in the deposition hole [m^3], r is the radius of the canister [m] and h is the height of the canister [m].

The dimensions of the Cell pathways, which represent the elements in the deposition hole, are illustrated in Fig. D-23. The figure is plotted based on a cylindrically symmetric configuration and further detailed in Tab. D-3 and Tab. D-4. Only diffusion was taken into account for mass transport in a deposition hole. The blue arrows in Fig. D-23 represent the diffusion transport that was taken into account between the void volume in the deposition hole and the buffer compartments surrounding the canister.
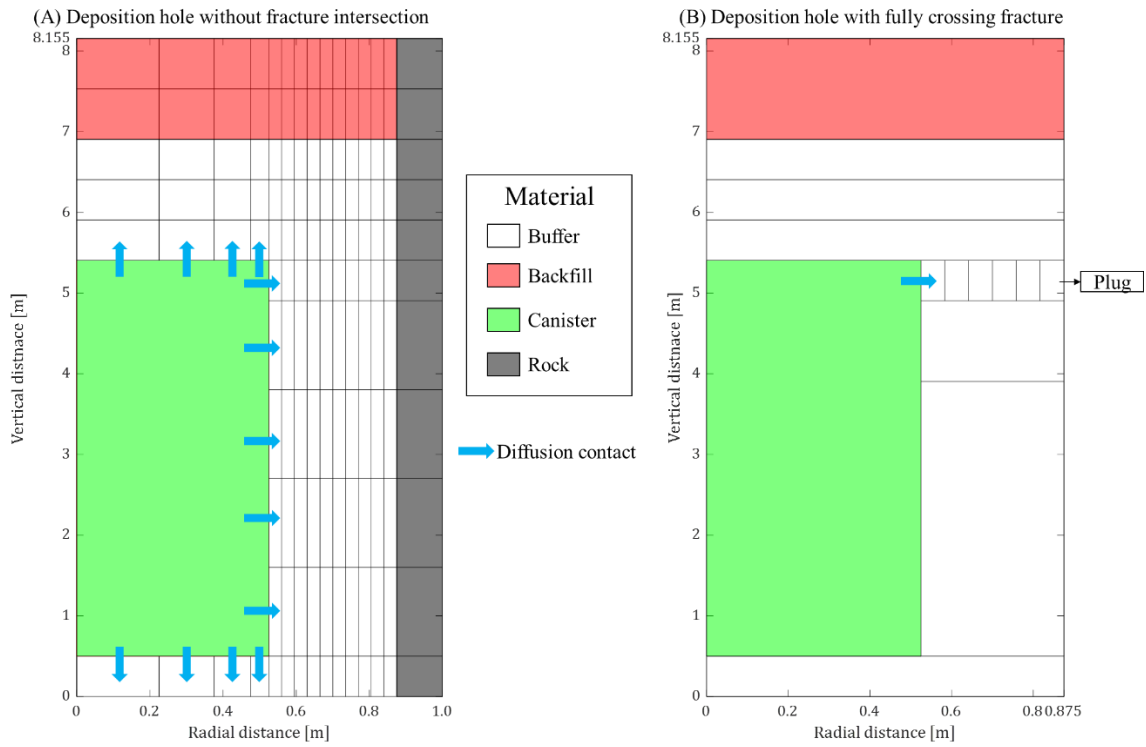
Note: The blue arrows represent the diffusion transport that has been taken into account between the canister (void volume in the deposition hole) and the buffer compartments surrounding the canister.

Fig. D-23. The dimensions and materials of the Cell pathways in two near-field models: (A) deposition hole without fracture intersection and (B) deposition hole with a fully crossing fracture.

Tab. D-3. Points in near-field model of deposition hole without fracture intersection.

Vertical distance [m]	Radial distance [m]
0.0	0.0
0.50	0.225
1.60125	0.375
2.7025	0.475
3.80375	0.525
4.905	0.560
5.405	0.595
5.905	0.630
6.405	0.665
6.905	0.70
7.530	0.735
8.155	0.770
	0.805
	0.840
	0.875
	1.0

*The vertical and radial distances are not applicable within the region that represents the canister

Tab. D-4. Points in near-field model of deposition hole with a fully crossing fracture.

Vertical distance [m]	Radial distance [m]
0.0	0.0
0.50	0.5250
3.905	0.5833
4.905	0.6417
5.405	0.70
5.905	0.7583
6.405	0.8167
6.905	0.8750
8.155	

*The vertical and radial distances are not applicable within the region that represents the canister.
*The radial distance is specifically applicable to the canister and uppermost buffer compartments surrounding the canister.

The second near-field model, deposition hole with a fully crossing fracture, was established by referring to SKB (SKB 2010). The dimensions of the Cell pathways are illustrated in Fig. D-23(B) and Tab. D-4. When tracers in the buffer diffuse into rock fracture through the uppermost buffer compartments, the majority of the transport resistance occurs at the entrance of the rock fracture. To simplify the process and avoid excessive discretization, a Cell pathway represents an equivalent transport resistance plug is connected to the uppermost and outermost buffer compartment surrounding the canister (SKB 2010). The length (P_L) and the area (P_A) of this equivalent transport resistance plug can be calculated by the following equations:

$$P_L = \left[1 - 1.35 \log_{10}\left(\frac{b}{a}\right) + 1.6 \log_{10}\left(\frac{d}{a}\right)\right] b \tag{17}$$

$$P_A = \pi(2r_d)(2b) \tag{18}$$

where a is the height of the buffer compartment in connection with the rock fracture [m], b is the half-width of the fracture aperture [m], d is the thickness of the buffer [m], P_A is the area of the equivalent transport resistance plug [m^2], P_L is the length of the equivalent transport resistance plug [m] and r_d is the radius of a deposition hole [m].

When a disposal hole is completely intersected by a fracture, the model of the deposition hole with a fully crossing fracture is used to simulate the near-field mass transport of the disposal hole. Conversely, if it is only partially intersected or not

intersected at all by a fracture, the model of the deposition hole without fracture intersection is adopted.

A Pipe pathway within CT module was utilized to represent the rock fracture in far-field. The function of the Pipe pathway is to solve the one-dimensional advection-dispersion equation (ADE) coupled to a diffusion equation in the direction perpendicular to the advection with Laplace transform method. The Pipe pathway was assumed to be a rectangular flow channel. The input parameters used to describe the geometry of the Pipe pathway were calculated based on the output parameters of DarcyTools and have been mentioned in section D-3.4.

In order to minimize longitudinal dispersion for each transport pathway, one single flow pathway in rock was divided to 10 sub Pipe pathways.

In the first near-field model, deposition hole without a fracture intersection, advective flux links with an outflow rate were created from Cell pathways at the boundary of near-field model to the first sub Pipe pathway. The outflow rate of each Cell pathway was specified to be the envelope surface of the cylindrical shell multiplied by equivalent initial flux (U). In the second near-field model, a deposition hole with a fully crossing fracture, an advective flux link with an outflow rate, which was the equivalent flow rate (Q_{eq}), was created from the Cell pathway that represents the equivalent transport resistance plug to the first sub Pipe pathway.

The release of tracers from the waste package into the water within the void volume of the deposition hole commences at the start of the transport simulation. Tracer 1, with an inventory of 0.545 g, was instantly released. On the other hand, the inventory of Tracer 2, amounting to 4.90 g, was gradually released throughout the transport simulation at a fractional rate of 10^{-7} yr^{-1}.

For each DFN realization in the reference case, 2,500 realizations of mass transport were conducted in GoldSim. In each realization of mass transport, the near and far-field flow information of a pathway was imported into GoldSim to simulate mass transport. The total simulation time was 100,000 years.

To estimate the tracers and radionuclides remaining in the repository region over time, the repository boundaries were defined in DarcyTools. The x-coordinate ranges from 500 m to 1,540 m, the y-coordinate ranges from 669 m to 1,331 m, and the z-coordinate ranges from 541.25 m to 557 m. These boundary ranges are shown in Fig. D-24. The results of the masses of tracer 1 and tracer 2 left in the repository region over time are shown in Fig. D-25. The variations among various DFN realizations arise from spatial variability and become more pronounced over time. On average, at 100,000 years, tracer 1 and tracer 2 have about 88.27% and 99.93% mass left in the repository region,

respectively. Tracer 1 was instantly released at the start of the transport simulation, thus it has less mass left in the repository region.
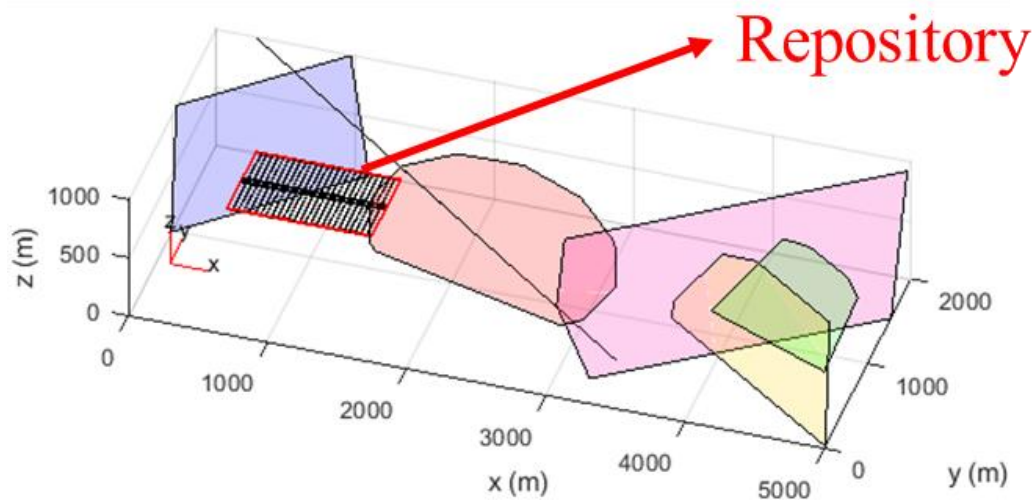
Fig. D-24. The boundaries of repository in the reference case.
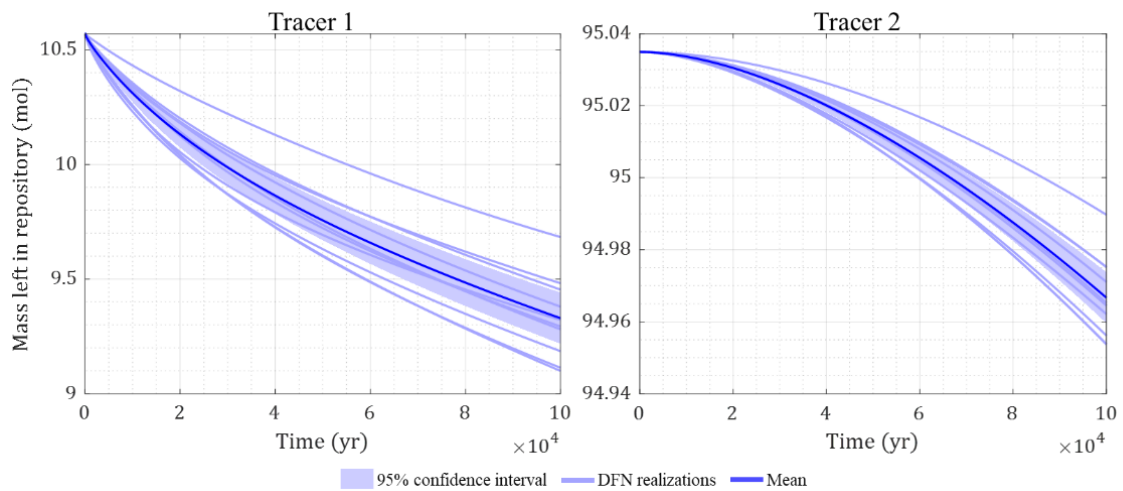

Fig. D-25. Mass of tracers left in the repository region over time.

DarcyTools conducts particle tracking to determine the final positions of released particles and flow-related transport parameters for mass transport simulations. Meanwhile, GoldSim performs mass transport simulations, providing the mass flow rate of a release path at its endpoint. By conducting 2,500 realizations, we were able to identify the endpoint locations of particles with mass flow rates within a specific area for each DFN realization.

To further analyse the mass flow rate across the hillslope and low point area, we cumulatively calculated it based on the endpoint locations of release paths. This

calculation allows us to gain a comprehensive understanding of the mass flow changes over time. Fig. D-26 and Fig. D-27 show the mass flow and cumulative mass across the hillslope and low point area, respectively. The mass of tracer 1 was released immediately at the beginning of the mass transport simulations, leading to peaks in the mass flow of tracer 1 over time. The maximum mean mass flow of tracer 1 is higher in the hillslope area and also occurs earlier (around 1,500 years) as depicted in Fig. D-22.
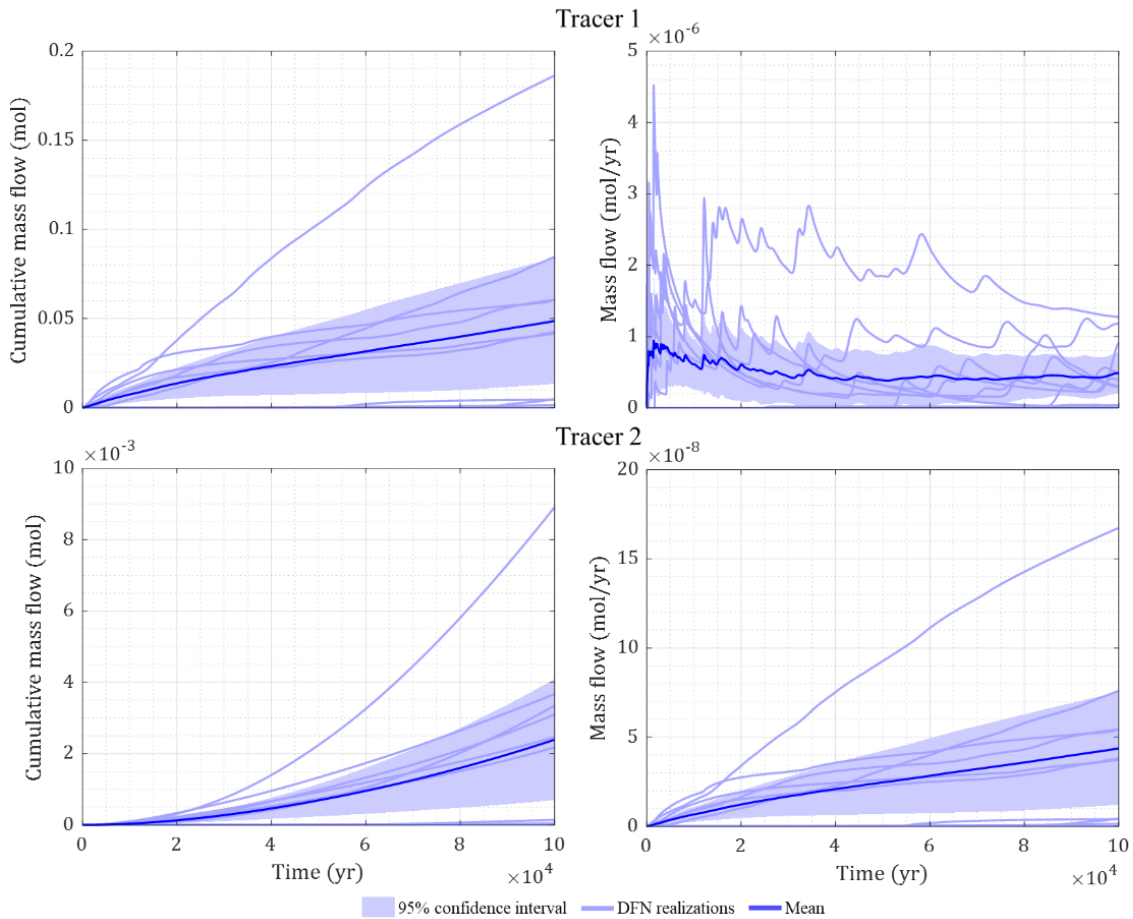
Fig. D-26. Cumulative mass and mass flow across the hillslope area.
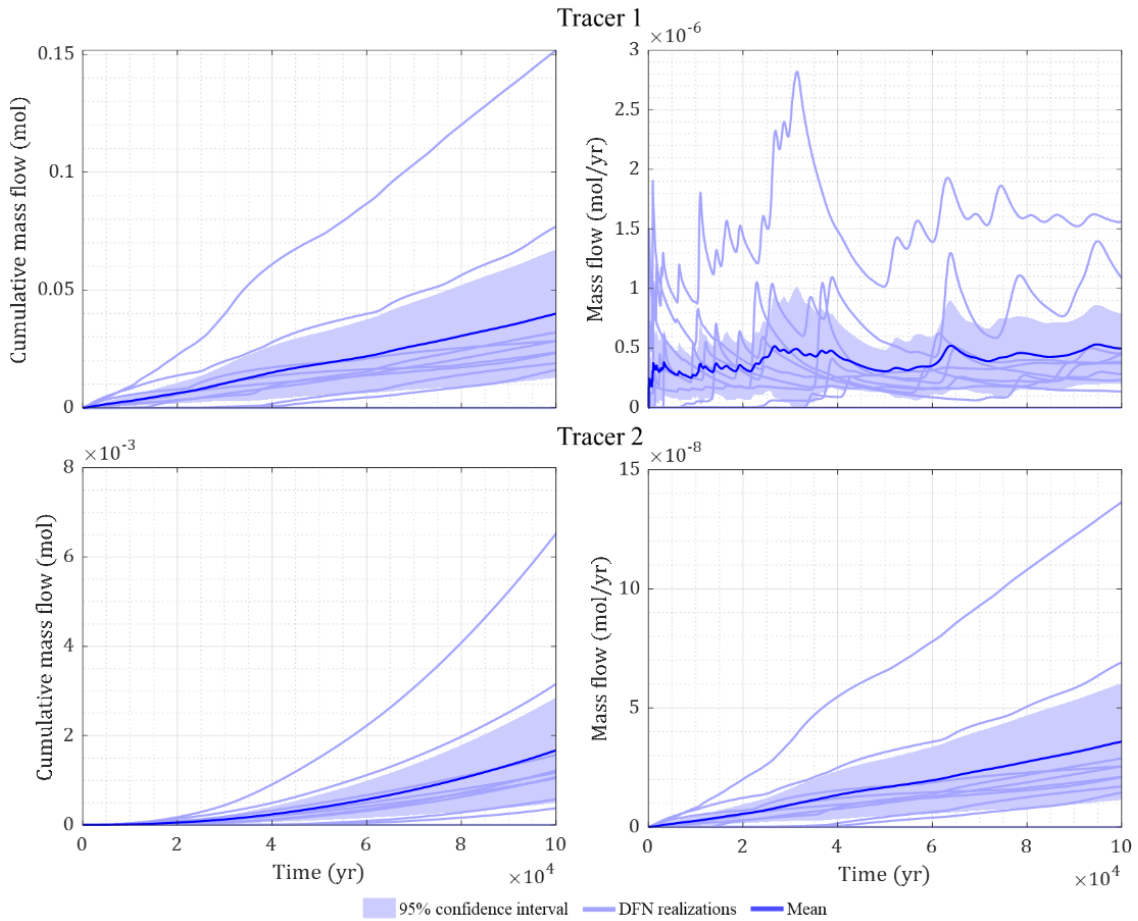
Fig. D-27. Cumulative mass and mass flow across the low point area.

In the Task specification report, it is required to identify the cell locations on the surface of the hillslope and low point area where the tracer mass flow is the greatest in each DFN realization. Subsequently, the mass flow (moles/year) of each tracer across the top surface of a cell need to be normalized by the area of the cell to estimate the mass flow per unit area (moles/year/m^2). This data should then be plotted as a function of time. During the mass transport simulation conducted using GoldSim, the mass flow (moles/year) was estimated for each particle at its final location. The end locations of particles estimated using DarcyTools provide information to identify the location on the surface where the tracer mass flow is the greatest, as required for the assessment in Task specification. The cross-sectional areas of the fracture simulated by GoldSim were used to calculate the mass flow per unit area (moles/yr/m^2). For the purpose of comparison with the results from the ECPM model, we have upscaled the cross-sectional areas of the fractures to fit within a unit area (1 m^2 square), and the cross-sectional areas of the fractures are eliminated in calculations. Fig. D-28 and Fig. D-29 depict the maximum mass flow and cumulative mass per unit area at a cell in the hillslope and low point area over time, respectively. It should be noted that the mass transport of tracers released from each deposition hole in the geosphere was simulated in a 1-dimensional

manner. Therefore, the maximum mass release and its location considered in this assessment only account for the contribution of tracers released from a single deposition hole. The cumulative maximum mass per unit area for tracer 1 in hillslope and low point areas demonstrates that, in certain scenarios, mass of tracer 1 in a deposition hole was completely released from the release point.
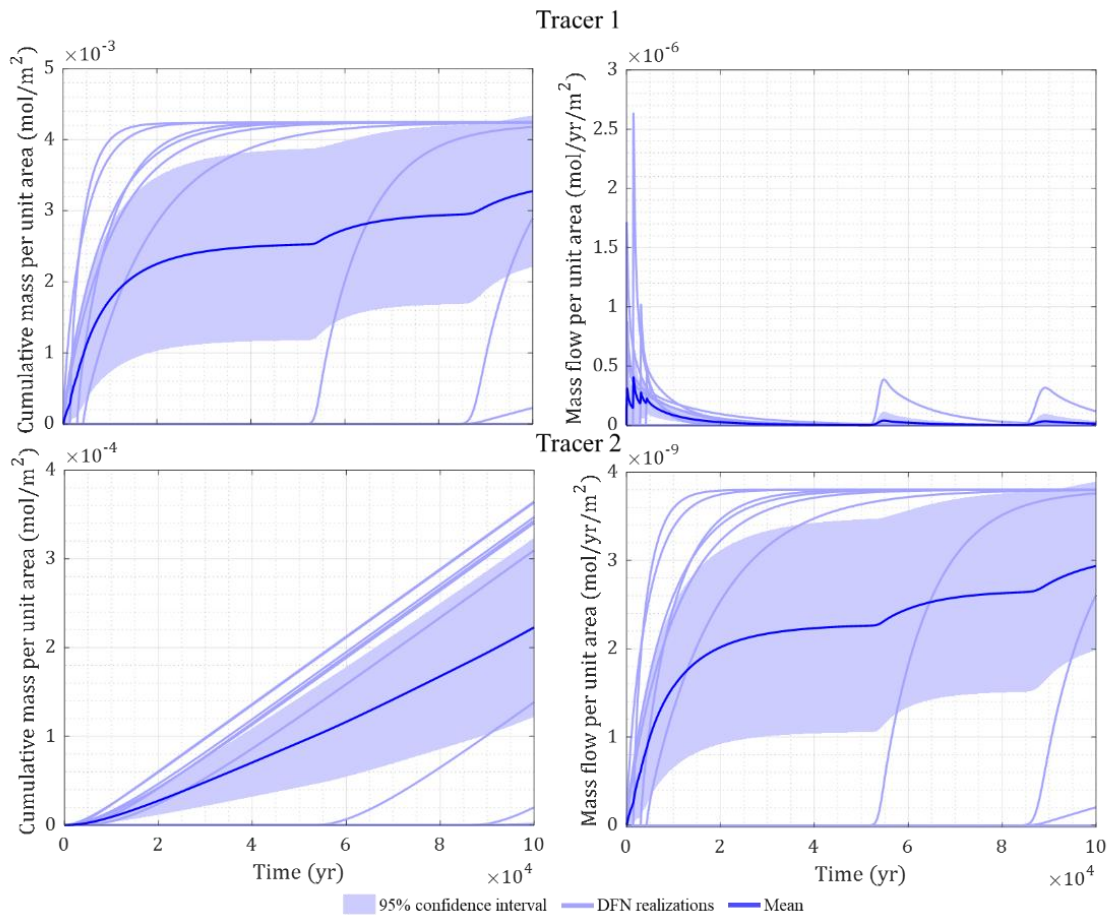
Fig. D-28. Maximum mass flow and cumulative mass across the hillslope area.
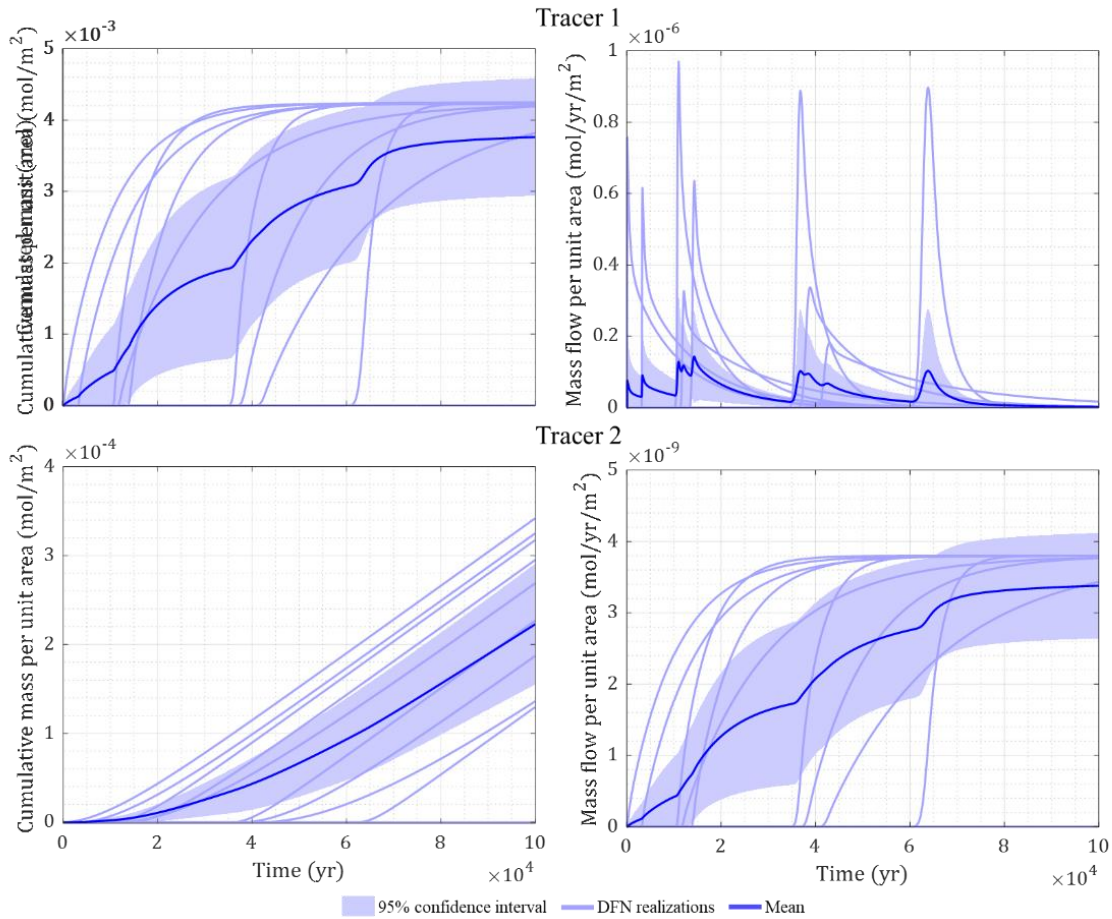
Fig. D-29. Maximum mass flow and cumulative mass across the low point area.

In order to analyse the concentration of tracers and radionuclides in the vicinities of two specified points on the hillslope area with coordinates (3500, 831, 1000) and on the low point area with coordinates (4337, 609, 1000), the end points of particles within a 50-meter radius around the specified points were identified. The total mass release estimated based on the flow-related information of these particles was then divided by the total water flow rate of the cells within the 50-meter radius around each specified point. The total water flow rates of the cells around the specified points in the hillslope area and the low point area were obtained from DarcyTools and are listed in Tab. D-5. The analysed results are shown in Fig. D-30. The results indicate that tracers exhibit earlier release concentrations around the observation points on the hillslope, while it takes approximately over 50,000 years to observe higher average concentration around the observation point on the low point area.

Tab. D-5. Total water flow rate of the cells in the vicinities of the specified points.

DFN realization	1	2	3	4	5	6	7	8	9	10
Hillslope (3500, 831, 1000)										
Flow rate [m³/yr]	187	164	481	849	201	442	486	111	972	278
Low point (4337, 609, 1000)										
Flow rate [m³/yr]	18,051	6,675	11,237	16,598	19,021	12,792	15,098	7,981	8,531	19,598
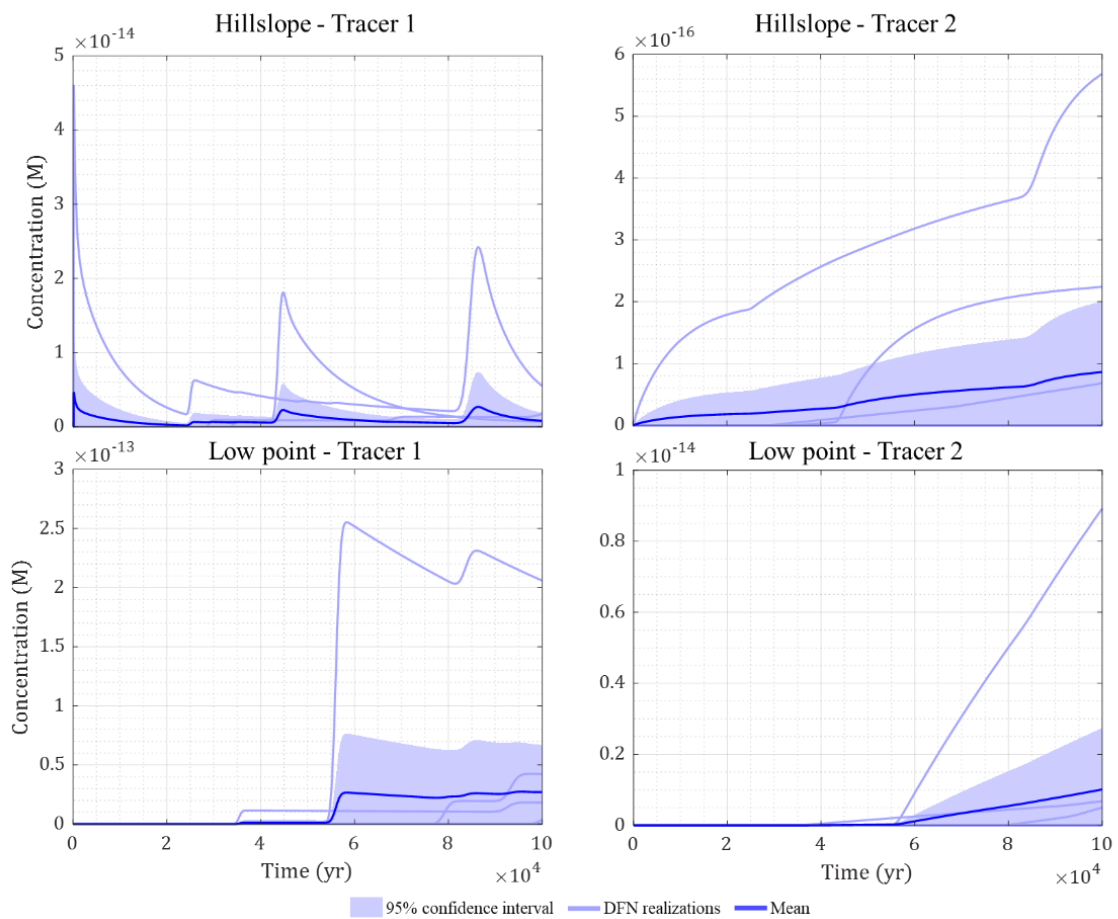
Fig. D-30. Concentrations of tracers around two observation points on hillslope and low point area.

D.5 References

Anttila, M. (2005). *Radioactive Characteristics of the Spent Fuel of the Finnish Nuclear Power Plants*. Working Report 2005-71. Posiva Oy, Olkiluoto, Finland.

Bear, J. (1993). *Flow and Contaminent Transport in Fractured Rocks*, Academic Press: 1-37.

LaForce, T., Jayne, R., Leone, R., Stein, E., and Nguyen, S. (2023). *DECOVALEX-2023 Task F Specification*, Revision 10. SAND2023-04005R. Sandia National Laboratories, Albuquerque, New Mexico.

Neretnieks, I., Liu, L., and Moreno, L. (2010). *Mass transfer between waste canister and water seeping in rock fractures Revisiting the Q-equivalent model*. TR-10-42. Svensk Kärnbränslehantering AB, Stockholm.

Poteri, A., Nordman, H., Pulkkanen, V. M., and Smith, P. (2014). *Radionuclide Transport in the Repository Near-Field and Far-Field*. POSIVA 2014-02. Posiva Oy, Olkiluoto, Eurajoki.

Svensson, U., Kuylenstierna, H. O., and Ferry, M. (2010a). *DarcyTools version 3.4–Concepts, Methods and Equations*. R-07-38. Svensk Kärnbränslehantering AB, Stockholm.

Svensson, U., and Ferry, M. (2010b). *Darcy Tools version 3.4 User's Guide.* R-10-72. Svensk Kärnbränslehantering AB, Stockholm.

SKB (2010). *Radionuclide transport report for the safety assessment SR-Site*. TR-10-50. Svensk Kärnbränslehantering AB, Stockholm.

Appendix E. Sandia National Laboratories (SNL) for the US Department of Energy

E.1 Introduction

The United States Department of Energy (DOE) is responsible for permanent disposal of commercial spent nuclear fuel. Since 2010, the DOE has engaged the national laboratories (including SNL and LANL) to pursue a generic site-independent research and development program focusing on three host rock types for deep geologic disposal of nuclear waste: argillite (also called shale or clay), salt (including bedded and domal), and crystalline rock. The strategic objectives of the program include developing a sound technical basis for multiple viable disposal options in the US, increasing confidence in the robustness of generic disposal concepts, and developing the tools needed to support disposal concept implementation.

SNL, supported by DOE, proposed DECOVALEX-2023 Task F. SNL leads and participates in the various activities of each branch, F1 (crystalline) and F2 (domal salt). Participation in Task F benefits DOE because it motivates development of the capabilities (skills and software) needed for quantitative safety assessment of a mined repository, tests current and developing capabilities against approaches used by other participants, provides useful benchmarks that build confidence in modelling capabilities, and may help direct future development of modelling capabilities.

E.2 Methods

PFLOTRAN, a massively parallel flow and reactive transport model (Hammond et al. 2014) was used to run all simulations. PFLOTRAN is a finite volume code and Richard's flow was used to simulate steady state flow for all simulations. Tracer transport was run using either global implicit reactive transport or the UFD Decay Process Model. To simulate source term release the Waste Form Process Model in PFLOTRAN was utilized. Stochastic and deterministic fractures are generated using Los Alamos National Laboratories (LANL) dfnWorks (Hyman et al. 2015). Upscaling to an Equivalent Continuous Porous Medium (ECPM) was done via a python script called mapdfn.py (Stein et al. 2017).

E.3 Benchmarks

The SNL team simulated the full set of benchmark problems developed for DECOVALEX-2023 Task F1. The following subsections summarize and discuss the approaches taken by the team for each of those benchmarks and the results obtained. The benchmark problems are described in full in LaForce et al. (2023) and are compared to the results of other teams in the parent report of this appendix.

E.3.1   1D Transport

For the 1D transport benchmark the Reactive Transport mode in PFLOTRAN was used to simulate the tracers. 200 grid cells were used to discretize the 10 m beam, and a maximum time step size of 1 second was implemented. The maximum time step size was found to have a direct impact in matching the solution with the analytical solution. Results are shown in Fig. E-1. The displayed curves reflect the improved results achieved through a lower maximum time step size.
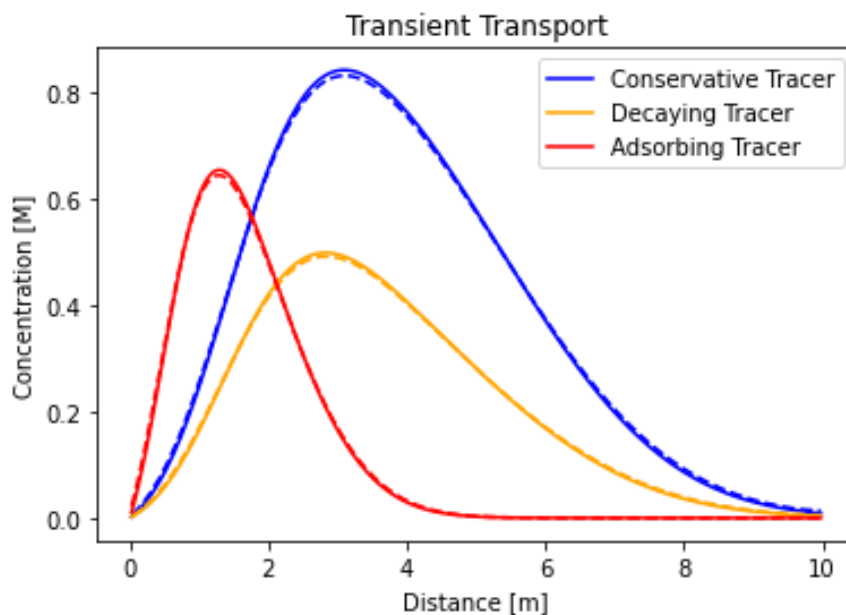
Fig. E-1. 1D Transient benchmark results. Solid lines represent the analytical solution and dashed lines represent PFLOTRAN solution.

E.3.2   1D Fracture Plus Matrix Diffusion

To simulate the 1D Fracture Plus Matrix Diffusion benchmark, PFLOTRAN uses a multiple continuum model that models a primary continuum (fracture) coupled to a secondary continuum (matrix) using a Dual Continuum Disconnected Matrix (DCDM) model (Iraola

et al. 2019). The simulation ran with a maximum time step size of 0.1 days and 100 in the secondary continuum for the fast and slow velocity, respectively.

The analytical solution and PFLOTRAN solution for the slow velocity case are compared in Fig. E-2. The PFLOTRAN simulations are verified to agree between 0.1-15% relative error for concentrations in the fracture with higher values of relative error being associated with small concentrations values further along the fracture. When only looking at concentrations above 0.1 the greatest relative error is ~8%. For the high velocity case (Fig. E-3), the PFLOTRAN simulations agree between 0.05-15% relative error in the fracture, with larger relative errors again being associated with smaller concentration values. Looking at values between 0-5 m down the fracture, relative error is less than 1%.
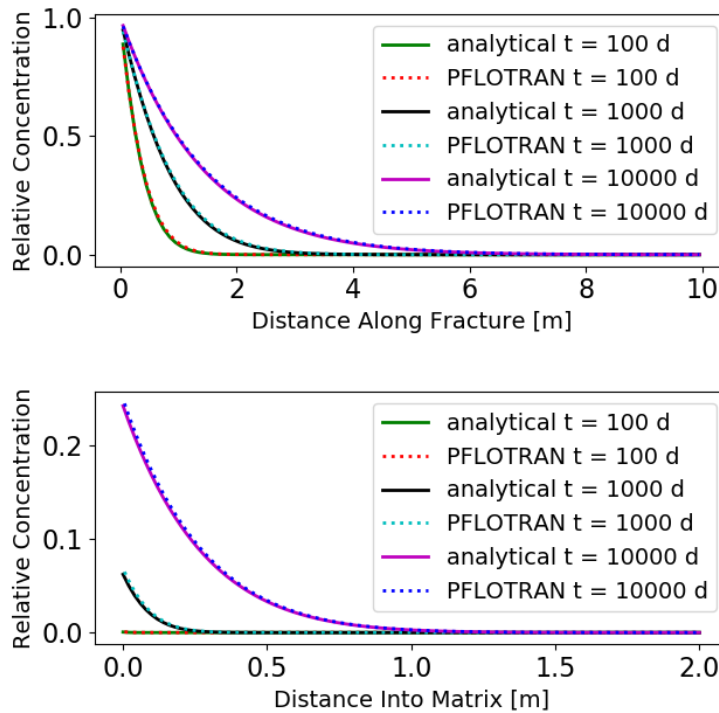
Fig. E-2. Concentrations in the fracture (above) and in the matrix 2 m into the fracture (below) for low velocity case (0.01 m/d).
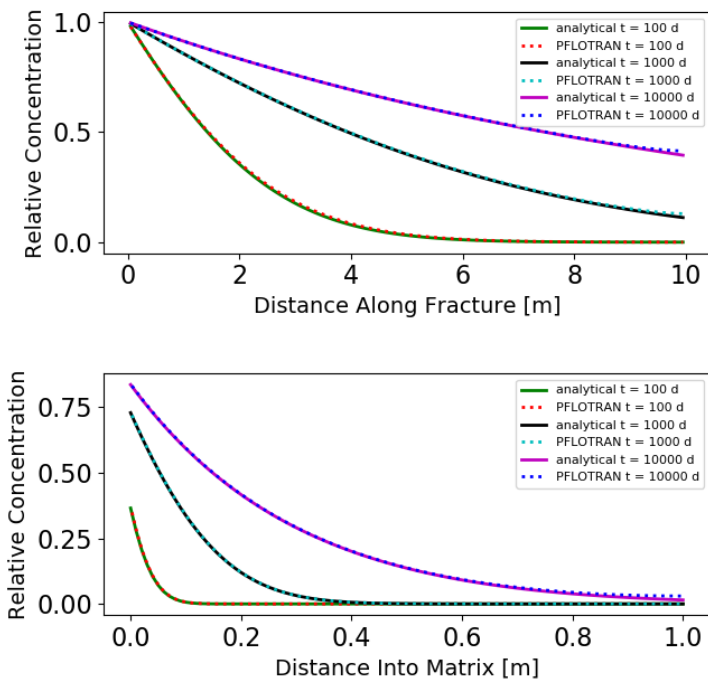
Fig. E-3. Concentrations in the fracture (above) and in the matrix 2 m into the fracture (below) for fast velocity case (0.1 m/d).

E.3.3   Four-Fracture Transport

Three methods were used to simulate the Four-Fracture Transport benchmark:

- Discrete fracture network (DFN) with particle tracking
- DFN with the advection-dispersion equation (ADE)
- Equivalent continuous porous medium (ECPM) with ADE

The four fractures were generated using Los Alamos National Laboratories (LANL) dfnWorks (Hyman et al. 2015). dfnWorks uses PFLOTRAN to solve for the steady state flow field solution. Fig. E-4 and Fig. E-5 show the fracture domain pressure solution in the DFN and ECPM, respectively.

A pulse of tracer is introduced on the west face (x = -500) of the domain at the beginning of the simulation by changing the tracer concentration to 1 mol/L in the incoming water for one day. The concentration at the west face is zero for all other times. A zero-gradient boundary condition is prescribed at the west face to prevent diffusive loss of tracer out the west face.
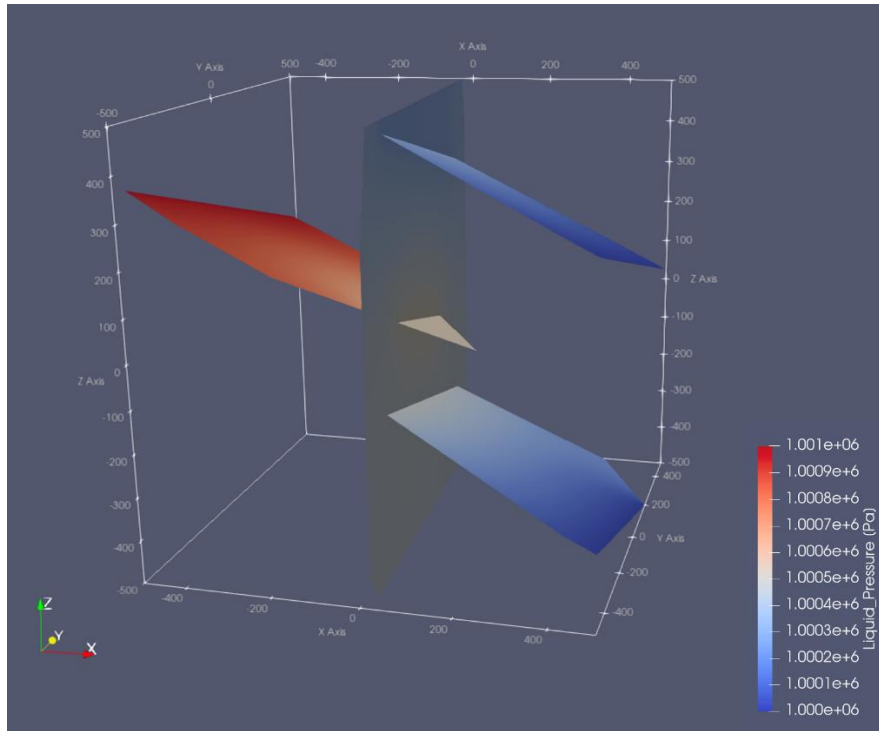
Fig. E-4. Steady state flow field of the DFN for the Four-Fracture DFN.
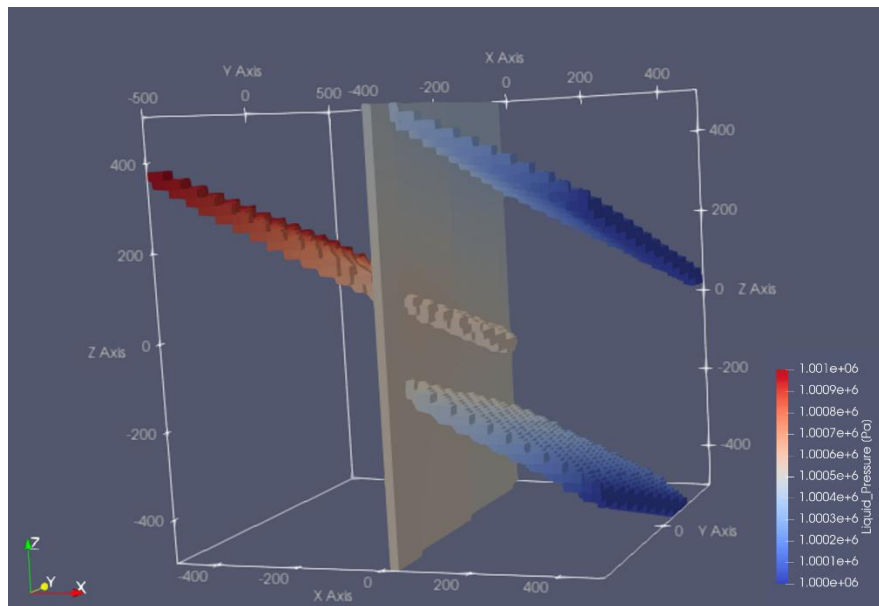
Fig. E-5. Steady state flow field of the ECPM for the Four-Fracture DFN.

Each of the two DFN simulations use 175,920 2-D finite volume elements to simulate the four fractures. The particle tracking approach utilizes dfnWorks particle tracking software dfnTrans (Lagrangian reference frame). The dfnTrans software takes the flow field and fracture information and outputs particle travel times in the domain. The second method uses the advection-dispersion equation (ADE) in PFLOTRAN (Eulerian reference frame). With the ECPM approach a python script called mapdfn.py (Stein et

al. 2017) was used to upscale the fractures into a uniform grid. Using output from dfnWorks (apertures, permeabilities, radii, the unit vector defining the normal vector to the fractures, and coordinates of the fracture center) along with user input defining the domain and grid cell size, mapDFN.py outputs upscaled anisotropic permeability, porosity, and tortuosity based on the intersection of fractures within grid cells. A cell length of 20 m was chosen which resulted in a total of 9704 active hexahedrons to represent the four fractures. A stairstep correction was applied to the ECPM to more accurately simulate fracture path lengths.

First and second moments are found in Tab. E-1 and breakthrough curves are shown in Fig. E-6. Overall, the three methods show good agreement with one another. Using the stairstep correction in the ECPM simulation provided a better match to the DFN simulations.

Tab. E-1. First and second moments for the Four-Fracture Transport problem.

Method	1st Moment	2nd Moment
DFN Particle Tracking	1.07	3.0
DFN ADE	1.01	2.3
ECPM	1.05	2.0
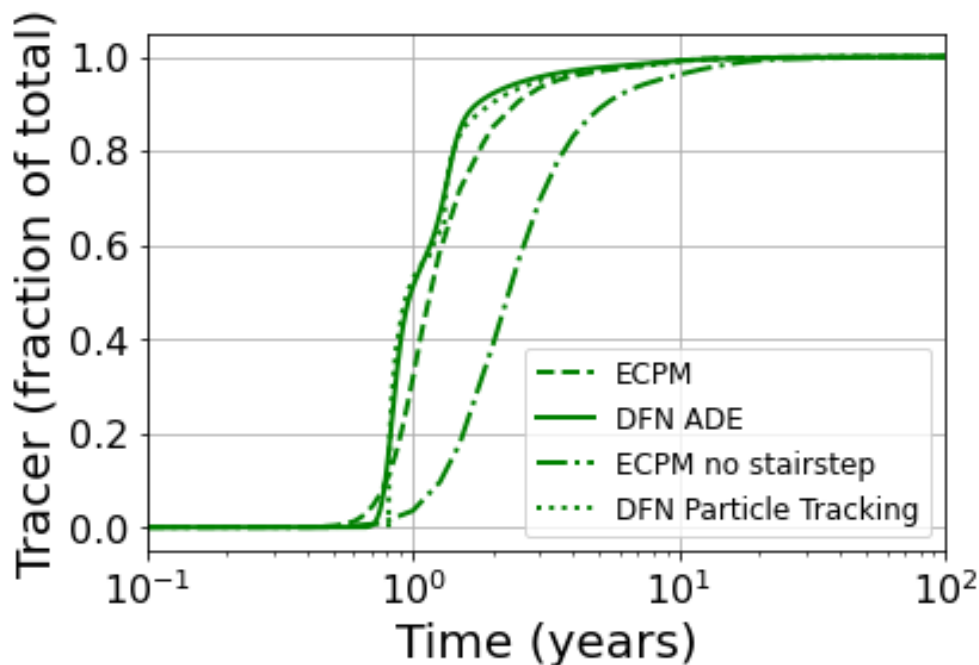
Fig. E-6. Breakthrough curves for the 4-Fracture benchmark using three different modelling methods.

E.3.4   Four-Fracture Plus Stochastic Fractures

This benchmark uses the same four deterministic fractures as the Four Fracture benchmark but adds dozens of stochastically generated fractures as shown in Fig. E-7. The stochastic fractures are generated using dfnWorks. Methods used to generate stochastic fractures are discussed in detail in the Reference Case section later in this appendix (Section E.4.2).

Two approaches were taken for this benchmark:

- DFN for all deterministic and stochastic fractures with ADE
- ECPM for entire block with ADE

The DFN uses 4,647,375 2-D cells. The ECPM uses 49,685 active hexahedrons (cells with no intersecting fractures are inactivated). Active cells are shown in Fig. E-8. A zero-gradient boundary condition is prescribed at the west face to prevent diffusive loss of tracer out the west face.

The decaying and sorbing tracers are modelled via PFLOTRAN Reactive Transport mode. To get the constant retardation coefficient of 5 in the ECPM model, PFLOTRAN uses a dummy mineral with the porosity values input as the initial volume fraction to correctly calculate the distribution coefficient. First and second moments are found in Tab. E-2 and breakthrough curves are shown in Fig. E-9.
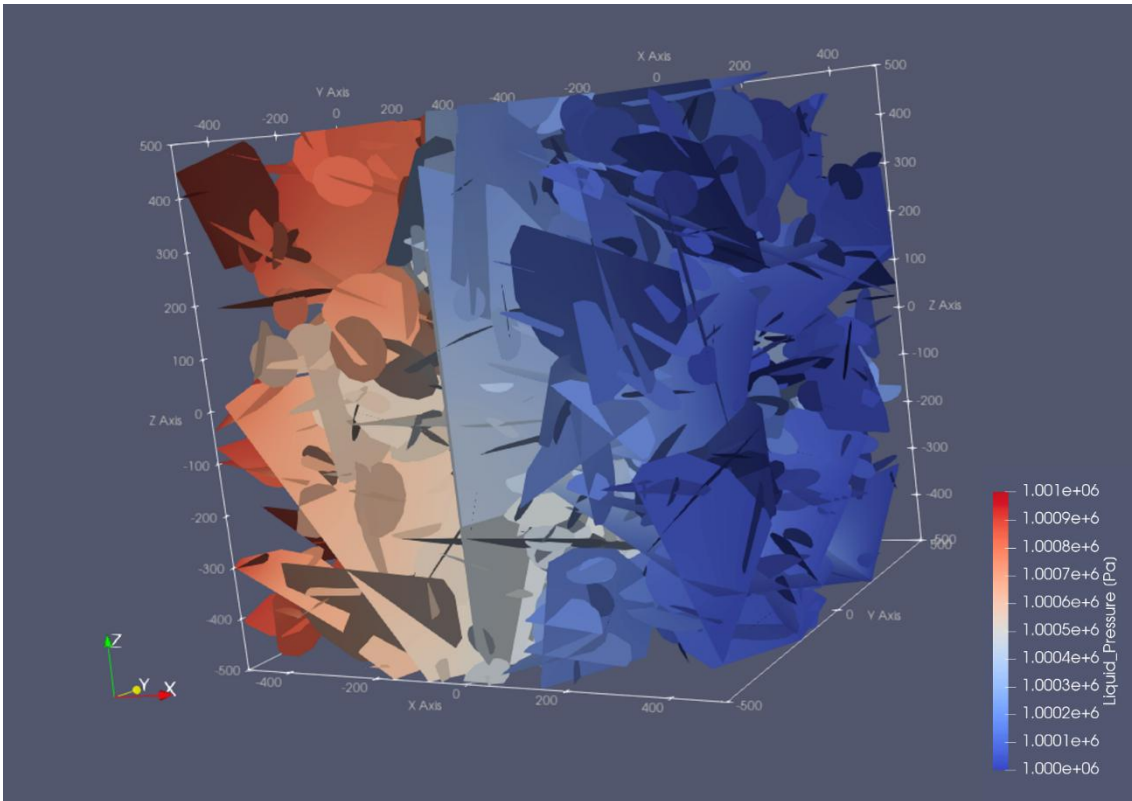
Fig. E-7. Steady state flow field of the DFN for the Four-Fracture Plus Stochastic Fractures benchmark.
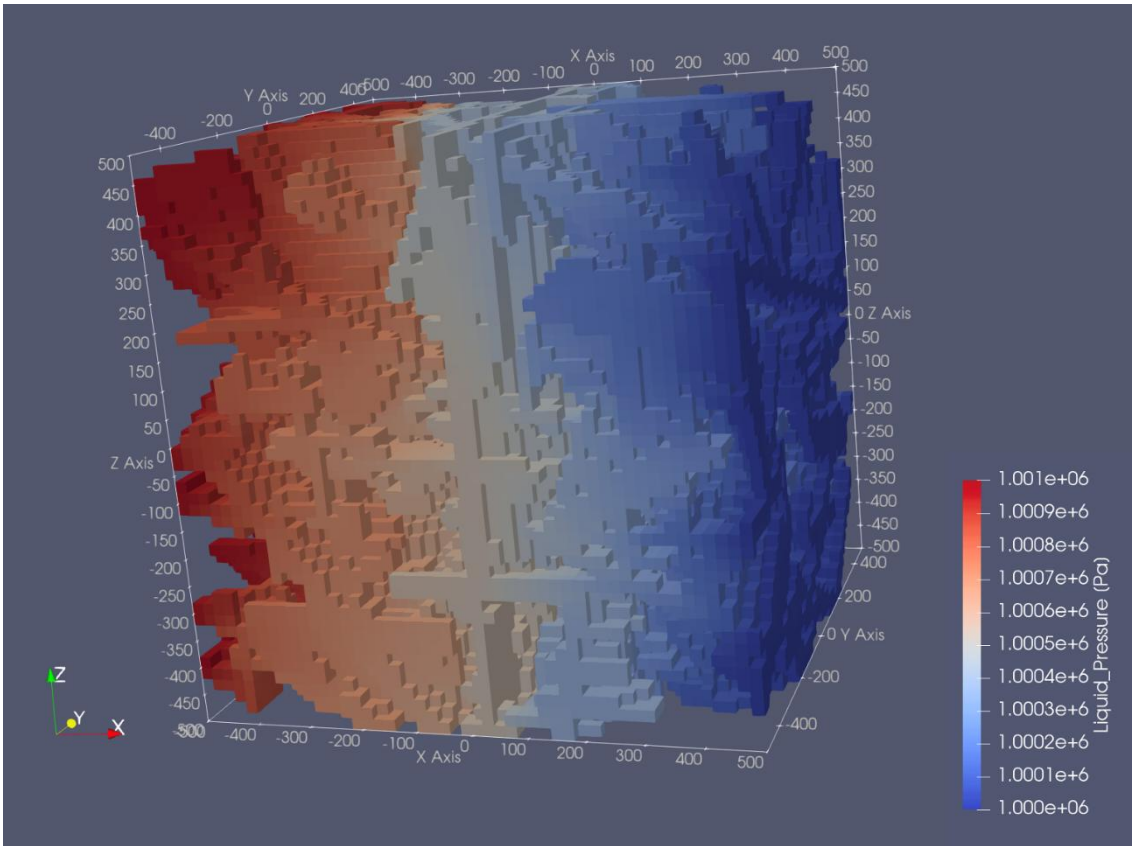
Fig. E-8. Steady state flow field of the ECPM for the Four-Fracture Plus Stochastic Fractures benchmark.

Tab. E-2. First and second moments (truncated at 1000 years) for the Four-Fracture Plus Stochastic Fractures problem.

Method	1st Moment Conserv. Tracer	1st Moment Decaying Tracer	1st Moment Sorbing Tracer	2nd Moment Conserv. Tracer	2nd Moment Decaying Tracer	2nd Moment Sorbing Tracer
DFN ADE	0.93	0.80	4.31	26.4	4.0	142
ECPM	1.02	0.85	4.81	27.0	6.6	291
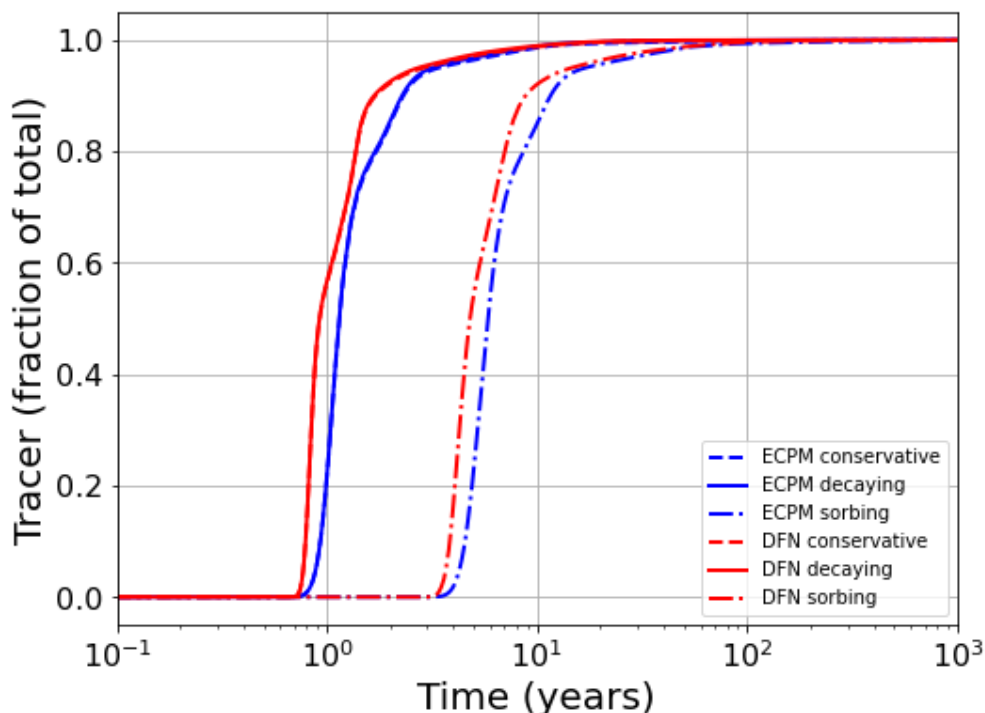
Fig. E-9. Breakthrough curves for Four-Fracture Plus Stochastic Fractures benchmark.

E.3.5   Continuous Point Source

This benchmark is the same as the Four-Fracture Plus Stochastic Fractures benchmark except for a change in how the tracers are introduced. To simulate a continuous point source, a source/sink is defined at the coordinates specified (-500,7.0, 248.25). As in the Four-Fracture Plus Stochastic Fractures benchmark, the two modelling approaches are DFN and ECPM, both with ADE. A zero-gradient boundary condition is prescribed at the west face to prevent diffusive loss of tracer out the west face.

For the ECPM approach, tracer introduction includes the entire grid cell that intersects the coordinate. A water flux of 1 kg/yr spiked with tracer concentrations of 1000 mol/L is injected continuously into the cell. For the DFN approach, a water flux of 0.001 kg/yr spiked with tracer concentrations of 1 mol/L is injected continuously into the cell intersecting the coordinates. First and second moments are found in Tab. E-3, and breakthrough curves of flux in versus flux out are shown in Fig. E-10. The higher fidelity DFN approach shows sharper initial breakthrough and much more tailing.

Tab. E-3. First and second moments (truncated at 1000 years) for the Continuous Point Source benchmark.

Method	1st Moment Conserv. Tracer	1st Moment Decaying Tracer	1st Moment Sorbing Tracer	2nd Moment Conserv. Tracer	2nd Moment Decaying Tracer	2nd Moment Sorbing Tracer
DFN ADE	1.63	1.27	8.08	695	10.5	5994
ECPM	0.88	0.80	4.34	11.1	3.5	159
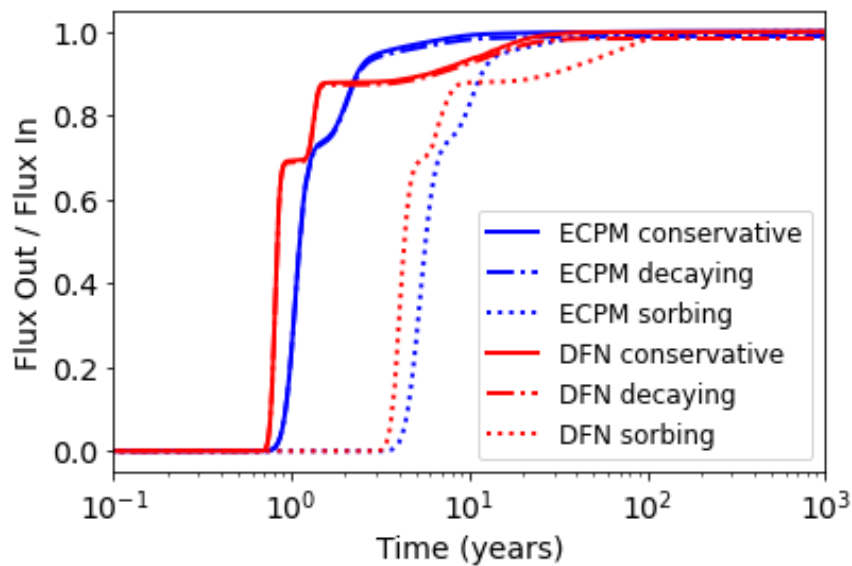
Fig. E-10. Breakthrough curves for the Continuous Point Source benchmark.

E.3.6   Radionuclide Source Term Benchmark

A test case for the radionuclide source term was developed as documented in Section 5.3 of LaForce et al. (2023). This benchmark is designed to test the implementation of radioactive decay and ingrowth, waste package breach time, instant release fraction, fuel matrix degradation rate, and solubility limitations.

Fig. E-11 shows that calculated radionuclide activities match the activities calculated in Anttila (2005, Table 2.2.2.4) at 5, 30, 10^2, 10^3, 10^4, 10^5, and 10^6 years. Fig. E-12 indicates that at 3000 years, waste package breach occurs as prescribed and there is an immediate release of 3% of the ^{99}Tc from the fuel, also as prescribed. The fuel matrix is shown not to degrade before waste package breach and is shown to be 64% degraded at one million years; the expected degradation is 63.1% based on analytical solution. Radionuclide release from fuel degradation is shown to be congruent. As indicated in Fig. E-13, aqueous concentrations are limited by prescribed element solubility limits. The

isotope partitioning model of PFLOTRAN distributes the isotopes of the same element in each cell such that their ratios are equivalent in all phases (i.e., maximum entropy).
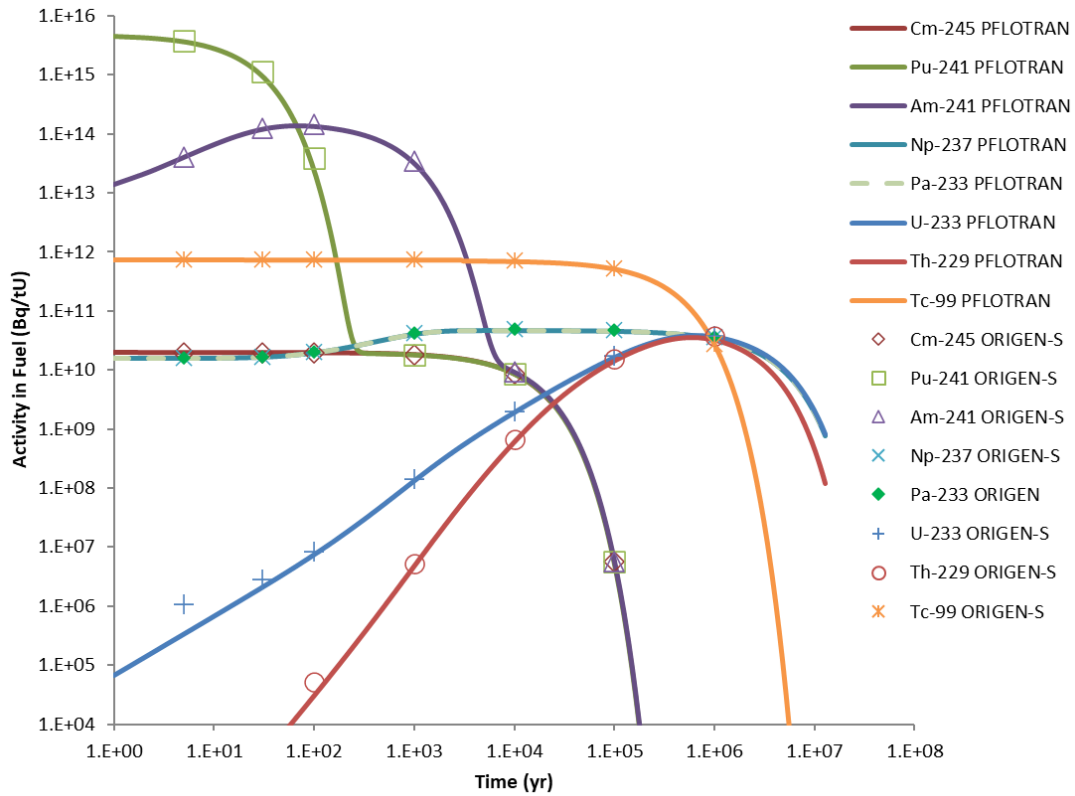
Fig. E-11. Calculated decay and ingrowth for the Radionuclide Source Term benchmark compared to the ORIGEN-S calculations of Anttila (2005, Table 2.2.2.4).
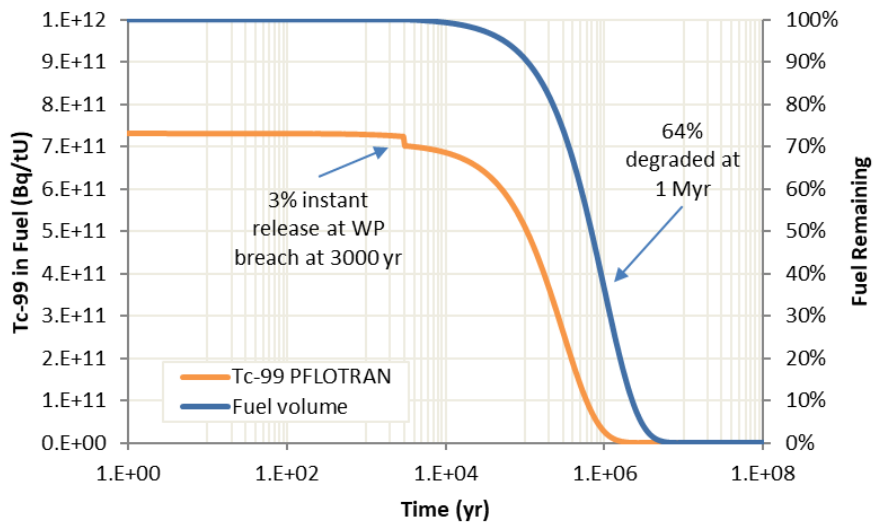
Fig. E-12. Calculated ⁹⁹Tc activity in the fuel and fuel volume remaining over time in the Radionuclide Source Term benchmark.
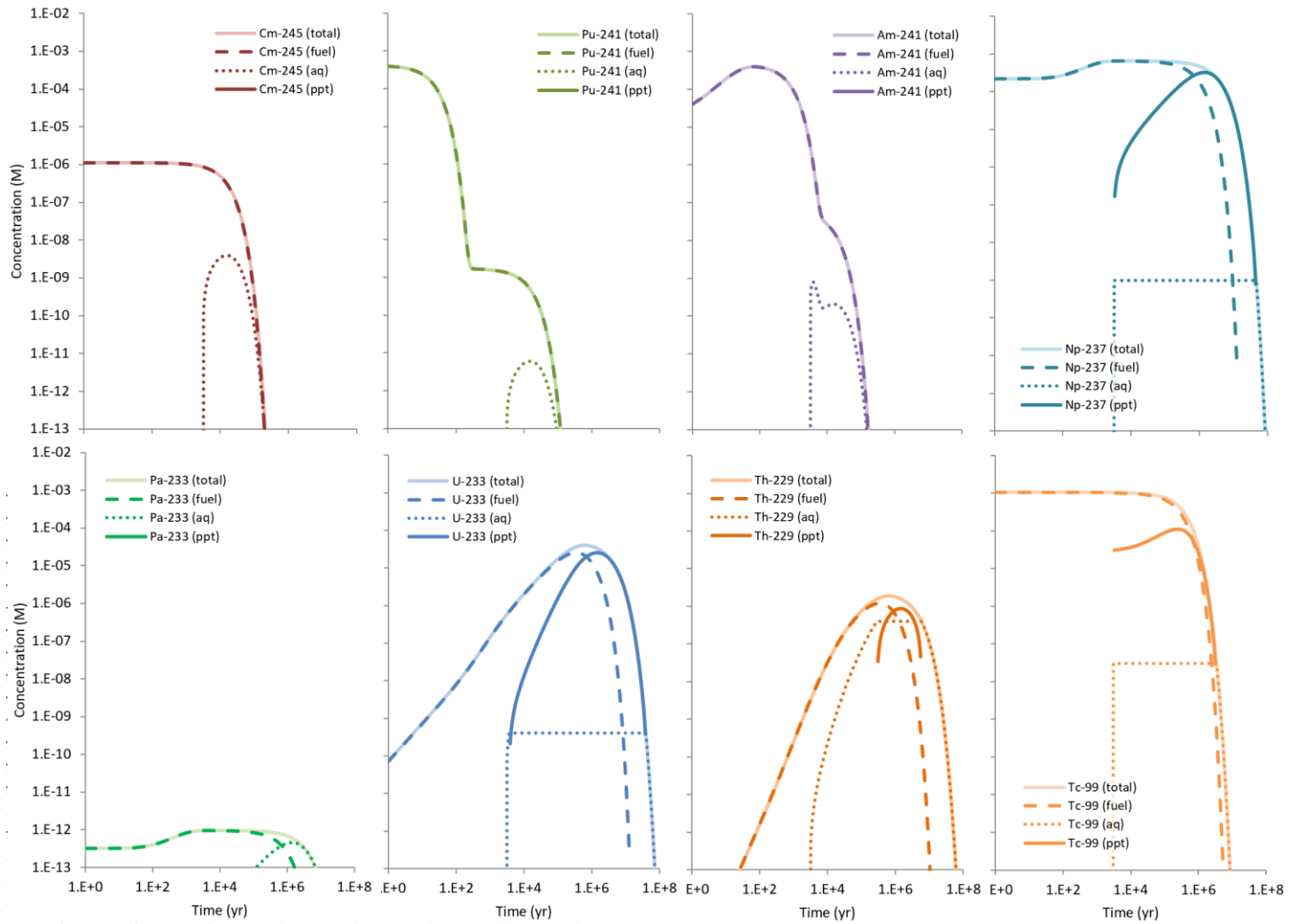
Fig. E-13. Calculated phase partitioning for the Radionuclide Source Term benchmark as affected by release rate and solubility limitations.

E.4 Reference Case

E.4.1 Model Domain

The repository is discretized using CUBIT, a Sandia meshing software, and converted to an unstructured mesh that can be input into PFLOTRAN, a massively parallel flow and reactive transport model (Hammond et al. 2014). Fig. E-14 shows an image in Paraview of the drifts and deposition holes in the repository. The deposition holes and waste packages are discretized to a cell size of 0.93 or 0.74 m, the deposition drifts are discretized to 2.7 or 2.2 m, and the near field is discretized to 8.3 or 6.7 m (Fig. E-15). A minimum radius of 10 m is used to generate the fractures in the near field and then upscaled to a 25/3 or 20/3 m grid (Fig. E-16).
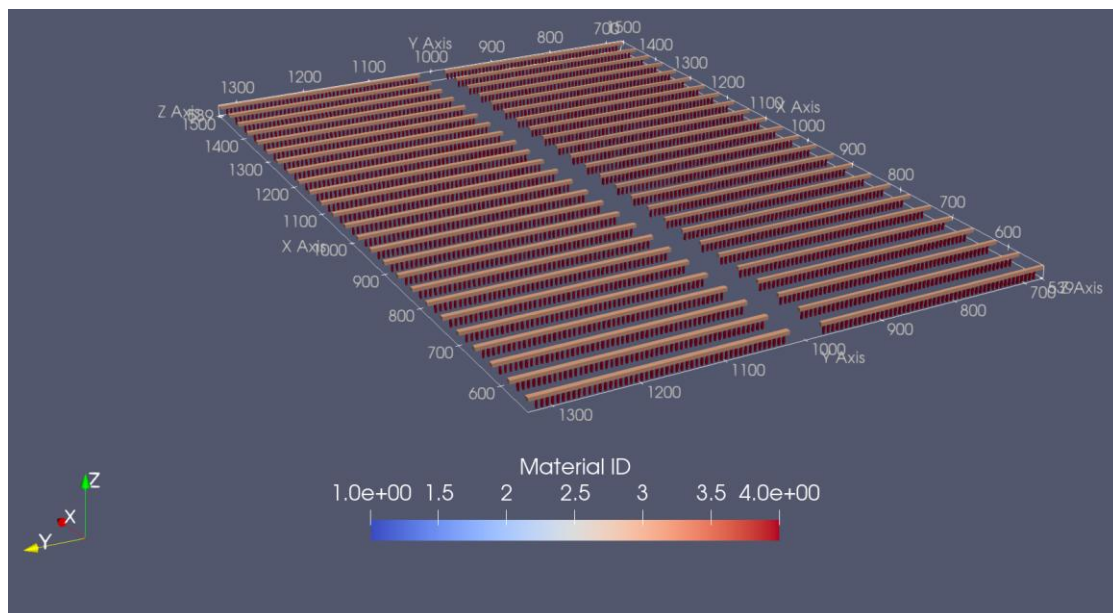
Fig. E-14. Discretization of the repository with 20 m far field cell size.
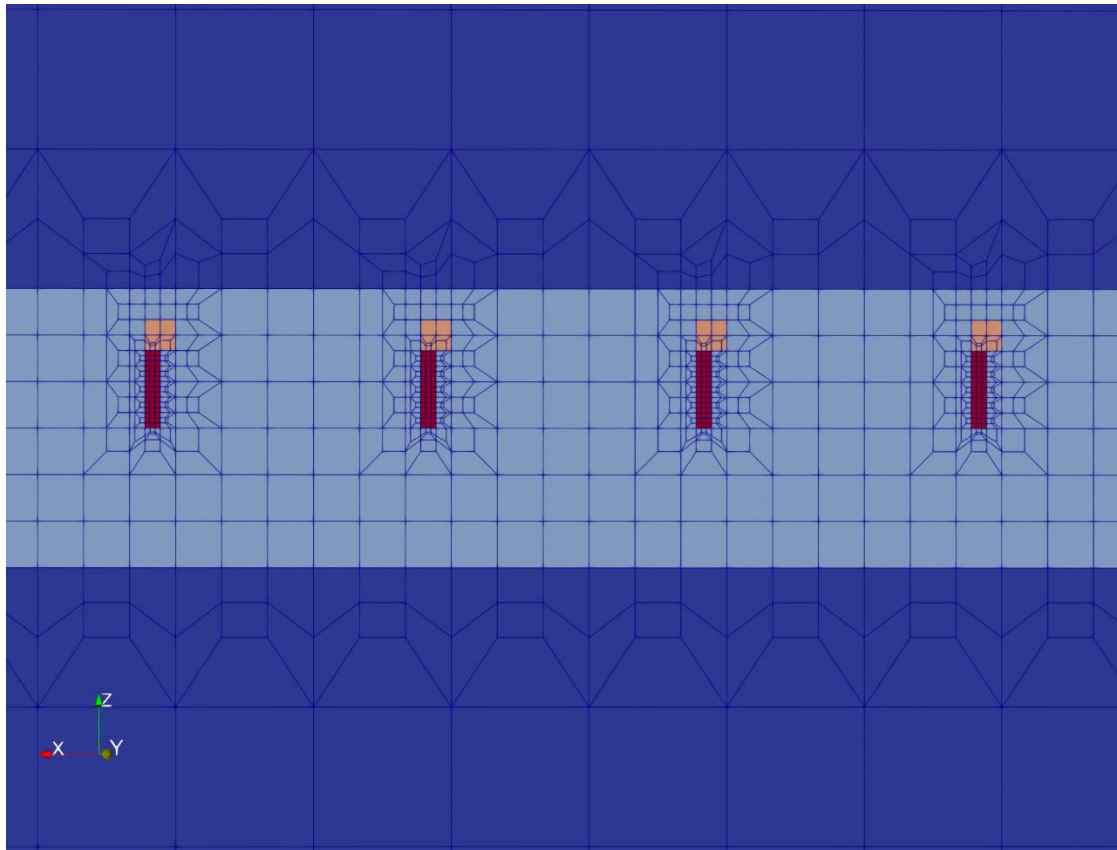
Fig. E-15. Discretization of deposition holes and drifts with 20 m far field cell size.
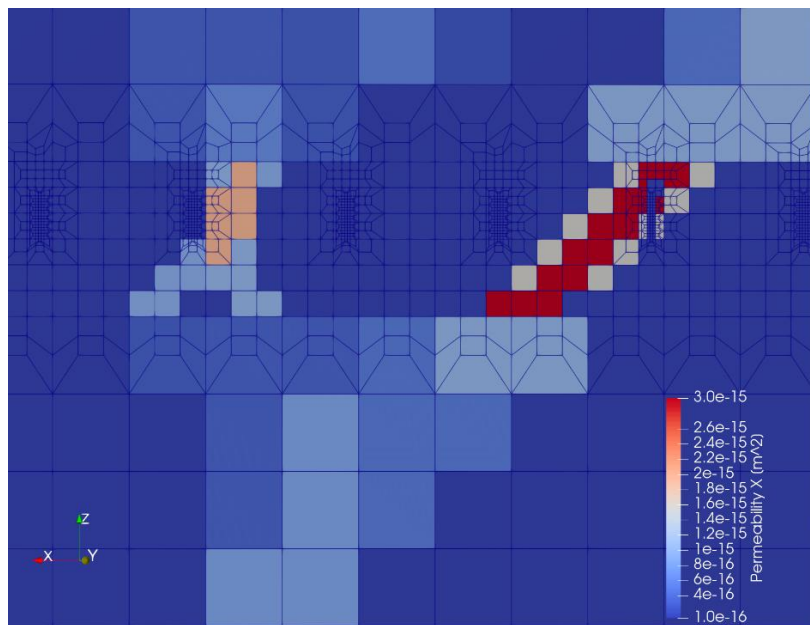
Fig. E-16. Upscaled repository using cell size of 20/3 m.

Tab. E-4 shows the grid value of each parameter based on a 20 or 25 m grid size vs the value specified in the task specification. The 20 m grid cell size results in closer sizing to the task specification for all parameters except for the volume of the canister. Therefore, both grid sizes were implemented and tested to see if the smaller volume of canister in

the 20 m grid affects the transport results. The grid sizing was found to have minimal impact on the transport solution but the 25 m grid size offered a significant speed up in simulation runtime.

Tab. E-4. Sizes of parameters meshed in Cubit vs Task Specification.

Parameter	Value with Grid Size 20 m [m]	Value with Grid Size 25 m [m]	Value in Task Specification [m]
Deposition hole spacing	5.93	5.55	6
Canister dimensions	0.74 × 5.18	0.9 × 5.55	1.05 × 4.9
Drift spacing	40	41.66	40
Drift floor (z value)	551.11	550	550
Drift tunnel dimensions	4.44 × 4.44	5.55 × 5.55	4.2 × 4.8
Deposition hole dimensions	2.22 × 8.88	2.77 × 8.33	1.75 × 8.155

E.4.2   Fracture Network

Stochastic and deterministic fractures are generated using Los Alamos National Laboratories (LANL) dfnWorks (Hyman et al. 2015). dfnWorks takes inputs of probability distributions for fracture radius and orientation, fracture density, and fracture transmissivity. Fracture orientation is sampled from a Fisher distribution which is parameterized by mean direction (characterized by mean trend φ, the angle the projection of the pole onto the x-y plane makes with the x axis and mean plunge θ, the angle the pole makes with x-y plane), and a concentration parameter κ. Fracture radius is sampled through a truncated power law distribution, with the form of (Follin et al. 2007),

$$f(r) = \frac{kr_0^k}{r^{k+1}}$$

where r0 is the minimum radius and k is a constant, respectively. Fracture intensity is expressed as fracture area per unit volume of rock (P32 [m^2/m^3]). The P32 values for the task specification assume r0 = 0.04 m and maximum radius (rmax) of 564 m. P32 is related to the average number of fractures per unit volume of rock (n0) by (Swiler et al. 2020):

$$P_{32} = n_0 \int_{r_0}^{r_{upper}} p(r)\pi r^2 dr = n_0 \int_{r_0}^{r_{upper}} \frac{kr_0^k}{r^{k+1}}\pi r^2 dr = \frac{n_0 \pi k r_0^k}{2-k}[r^{2-k}]_{r=r_0}^{r=r_{upper}}$$

The P32 over the range r0 = 0.04 m to rmax = 564 m is equivalent to billions of fractures per km^3, the vast majority of which have radii < 1 m. We calculated the P32 for a smaller

range of radii (e.g., minimum radius, rmin = 30 m to rmax = 564 m), by integrating the above over the range rmin to rmax (Swiler et al. 2020):

$$P_{32}[r_{min}, r_{max}] = \frac{\pi n_0 k r_0^k}{2-k}[r_{max}^{2-k} - r_{min}^{2-k}]$$

Fracture transmissivity (T [m²/s]) is a function of fracture radius. The reference case uses the fully-correlated relationship defined in Follin et al. (2007):

$$\log T = \log a r^b$$

where r is radius [m] and the coefficients a and b are dimensionless constants. Fracture aperture is calculated from the transmissivity using the cubic law (Bear et al. 1993):

$$\text{aperture} = \left(12T\frac{\mu}{\rho g}\right)^{\frac{1}{3}}$$

where μ is viscosity of water [Pa s], ρ is density of water [kg/m³], and g is the acceleration due to gravity [m/s²]. Permeability (k [m²], not to be confused with the exponent in the power law) is defined as,

$$k = \frac{\text{aperture}^2}{12}$$

The dfnWorks output must be post processed to allow for the depth dependent transmissivity, aperture, and permeability. Deterministic fractures are entered by specifying normal vectors, radii, and translation from the origin. Stochastic fractures are randomly distributed in the domain until the target fracture density is reached. Isolated fractures and fracture clusters not connected to faces in the domain are discarded. Fracture apertures, permeabilities, normal vectors, and coordinates are outputted. Fig. E-17 shows an image of the DFNs generated from one realization.
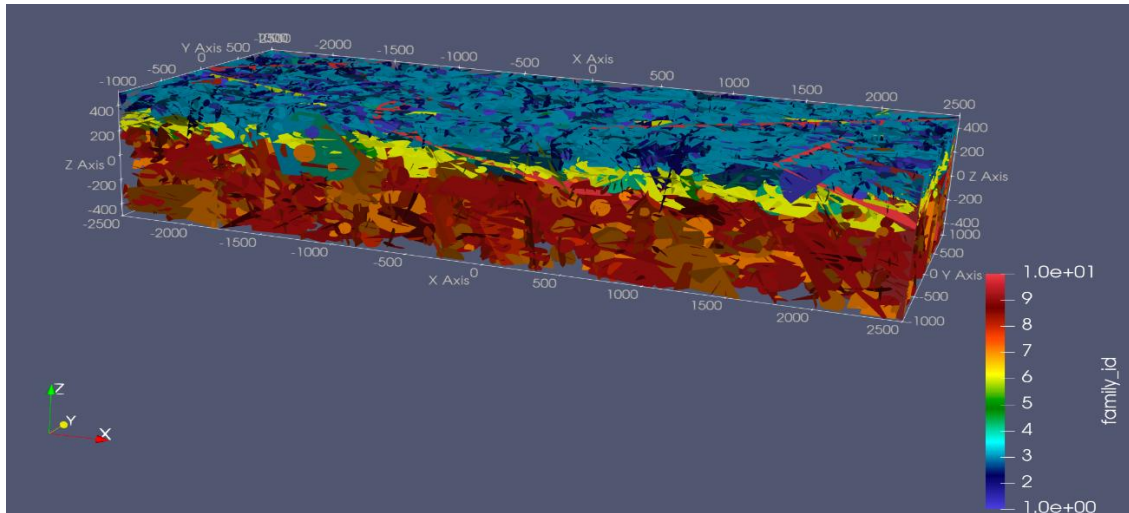
Fig. E-17. dfnWorks output of fracture families for one realization (stochastic and deterministic).

Fractures are upscaled using a Python script called mapdfn.py (Stein et al. 2017), which takes dfnWorks input and ECPM model domain and discretization (origin, domain, length, and length of cubic grid cells) and outputs grid cell permeability, porosity, and tortuosity. Cell properties are calculated by determining the fractures that extend over the ECPM grid cell It is assumed any fracture completely crossing the grid cell or a fracture must extending beyond the cell center will be mapped to that cell. For each fracture in a cell, intrinsic transmissivity (Tf [m3]) is calculated as,

$$T_f = k_f b_f$$

where kf is fracture permeability [m^2] and bf is fracture aperture [m]. Intrinsic transmissivity is described as a diagonal transmissivity tensor, where the coordinates are then rotated into the coordinates of the grid. Off-diagonal terms are discarded, and the diagonal tensor describe cell permeability is calculated as,

$$\begin{bmatrix} k_{xx} & & \\ & k_{yy} & \\ & & k_{zz} \end{bmatrix} = \frac{1}{d} \sum \begin{bmatrix} T_{xx} & & \\ & T_{yy} & \\ & & T_{zz} \end{bmatrix}_f$$

where d is the length of the cell side, and the sum is over all fractures intersecting the cell. A stairstep correction may be added to the permeability which accounts for the artificially low flux calculated from the ECPM due to fractures being characterized as staircases. The correction is derived from Sweeney et al. 2020, where the amount of correction needed is determined by the dot product between each fracture in the grid cell and the normal vector to each coordinate axis and is applied based on the angle closest to 45°. Fracture porosity for each grid cell is calculated as,

$$\phi = \frac{1}{d} \sum b_f$$

And cell tortuosity (τ) is calculated so the effective diffusion coefficient (De) is homogeneous everywhere in the fractured rock. In PFLOTRAN tortuosity is a number less than one so that,

$$D_e = \phi \tau D_m$$

where D_m is the molecular diffusion coefficient in water. Cells not intersected by fractures are assigned matrix permeability and porosity. For the reference case, an upscaled grid cell size of 20 and 25 m was used.

A test using the multiple continuum model in PFLOTRAN was also applied to the reference case. The multiple continuum model in PFLOTRAN models a secondary continuum (matrix) coupled to the primary continuum (fracture) modelled as a disconnected one-dimensional domain which is referred to as the DCDM (Dual Continuum Disconnected Matrix) model (Lichtner, 2000). Transport in the fractures occur due to advection and diffusion, transport in the matrix occurs due to diffusion only. The secondary continuum is modelled as a one-dimensional domain where diffusive fluxes occur perpendicular to the fracture wall. Each primary continuum cell has a corresponding set of secondary continuum cells attached to it. The secondary cells cannot interact with secondary cells associated with other primary cells. The equations for the primary and secondary continuum are solved separately and coupled together by a mass exchange flux assuming symmetry along the axis dividing them (Iraola et al., 2019). The DCDM uses the 25 m mesh created in Cubit and the upscaled porosity values from the ECPM were used as input into the DCDM model for the fracture volume fraction. Cells that did not have any fractures in them were set to inactive and the multiple continuum model was turned off in the repository. The DCDM model uses the steady state water flow from the ECPM.

E.4.3   Flow Model

Steady state flow is implemented using PFLOTRAN Richards' mode. The initial conditions are created by running the top pressure boundary condition on a 2-D model to steady state. The tracer advects out of the top boundary condition while no-flow boundary conditions are applied to all other faces. Fig. E-18 shows the water flux for all realizations for the 25 m grid, and Tab. E-5 compares the mean and standard deviation of the fluxes for the 20 and 25 m grid. Positive values represent outflow and negative values represent inflow.
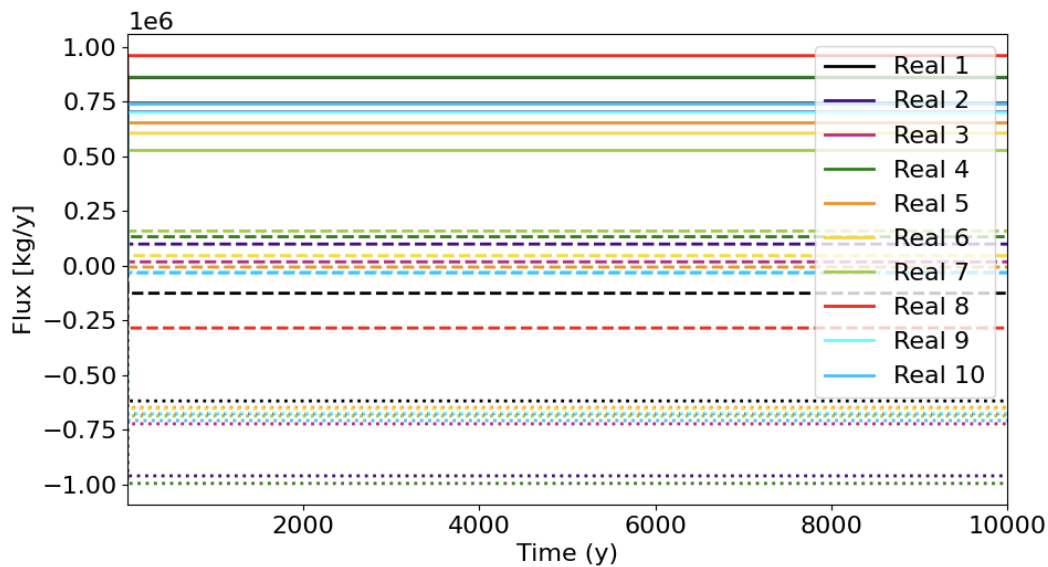
Fig. E-18. Steady state fluxes for 25 m grid over all realizations. Solid lines represent the low point, dashed lines represent the hillslope, and dotted lines represent the high point.

Tab. E-5. Mean and standard deviation for the water fluxes on the three surfaces of interest.

Surface	Mean Flux 20 m grid [kg/y]	Standard Deviation 20 m grid [kg/y]	Mean Flux 25 m grid [kg/y]	Standard Deviation 25 m grid [kg/y]
High Point	-643643	104755	-733756	125180
Hillslope	-21756	111360	-1959	123889
Low Point	665399	119680	735715	122949

E.4.4 Tracer Release and Transport

Transport for the conservative tracers is simulated using PFLOTRAN reactive transport mode, and the source terms for the tracers are simulated in PFLOTRAN using the Waste Form Process Model. The model contains three main components: the waste form canister, waste form object, and the waste form release mechanism. The waste form canister controls the timing of the canister breach and performance of the canister after the breach. The waste form object contains only information required by all waste form types (such as location, volume, and exposure factor) and points to the waste form mechanism and stores concentrations of the radionuclide inventory. Once the canister breaches, the waste form object degrades according to the degradation model defined by the waste form mechanism. The waste form mechanism contains information which

defines behaviour of each specific waste form type and contains the density, initial radionuclide concentrations, and pointer to the waste form degradation model.

Fig. E-19 shows the mass remaining in the repository for the 20 m grid. The mass remaining of Tracer 2 had to be post-processed since the mass balance file output by PFLOTRAN does not include the amount remaining in the waste packages. There is little variance between fracture realizations early on. At the end of the simulation the difference increases to about ~0.1 moles for Tracer 1 and ~0.001 moles for Tracer 2. When comparing the mass in the repository for different upscaling lengths (Fig. E-20), we see that there is more mass remaining in the repository for the 25 m grid compared to the 20 m grid. This is due to the way the repository was discretized in Cubit. The 25 m grid is ~40 m larger in the x-direction than the 20 m grid.
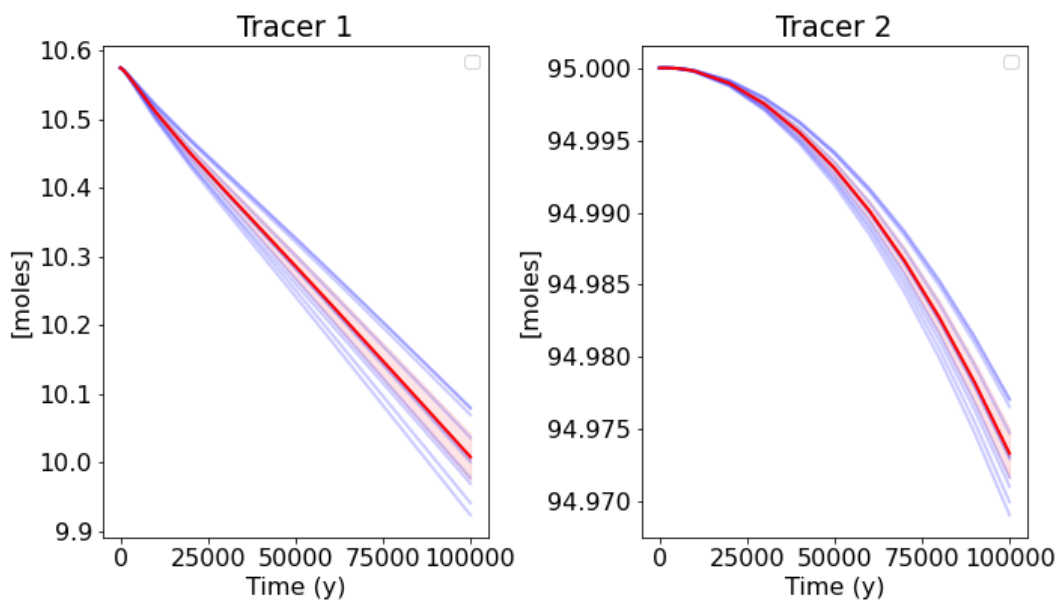
Fig. E-19. Mass remaining in the repository for the 20 m grid. Bold red line is the mean, shaded red region is the 95% confidence interval of the mean, and blue lines represent fracture realizations.
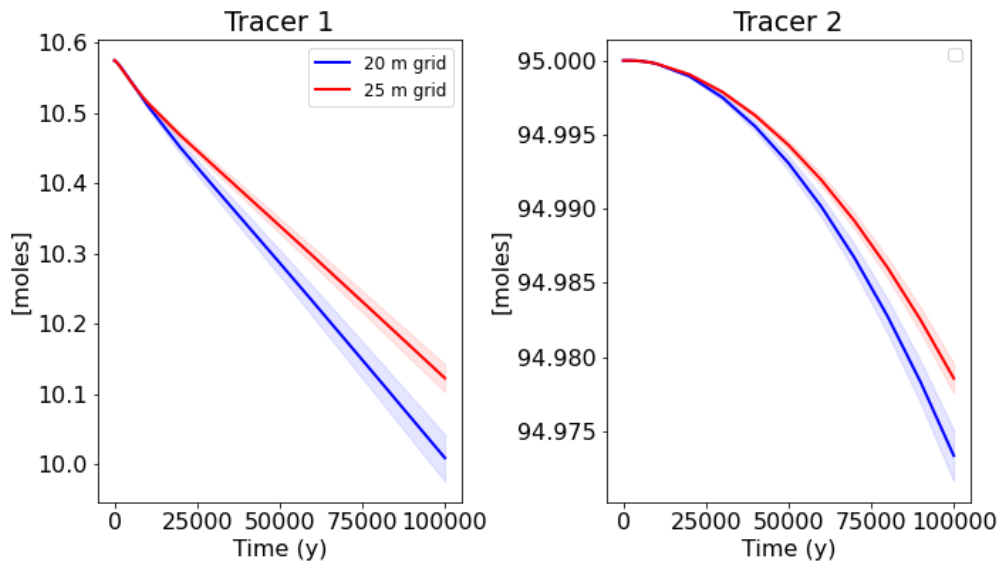
Fig. E-20. Mean and 95% confidence interval of mass remaining in the repository for the 20 m grid (blue) and 25 m grid (red).

The cumulative mass (moles) and mass flow (moles/year) across the hillslope for the 20 m grid can be seen in Fig. E-21. We see a large difference in the realizations with a range of ~ 0.035 moles for Tracer 1 cumulative mass. There is a steady increase of mass flow for Tracer 2 while Tracer 1 has a spike in the beginning of the simulation and then steadily increases. When comparing the different upscaling lengths (Fig. E-22) we see no difference in the mean and 95% confidence intervals except at late times where the 20 m grid is slightly higher than the 25 m grid.
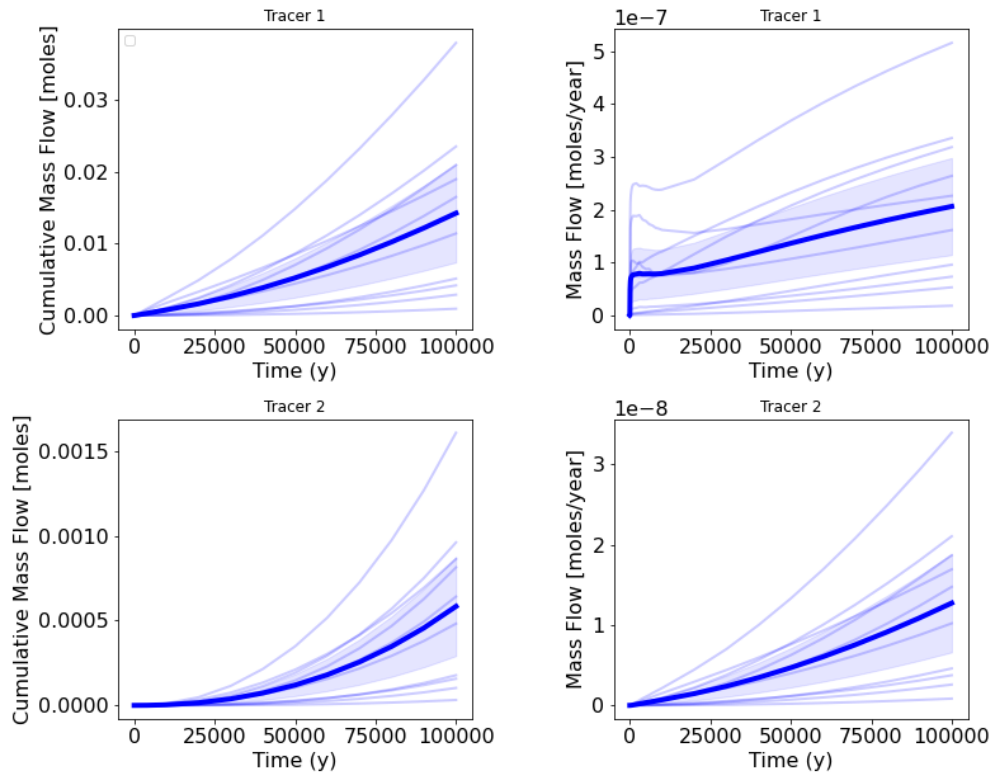
Fig. E-21. Cumulative mass (moles) and mass flow (moles/year) across the hillslope for the 20 m grid.
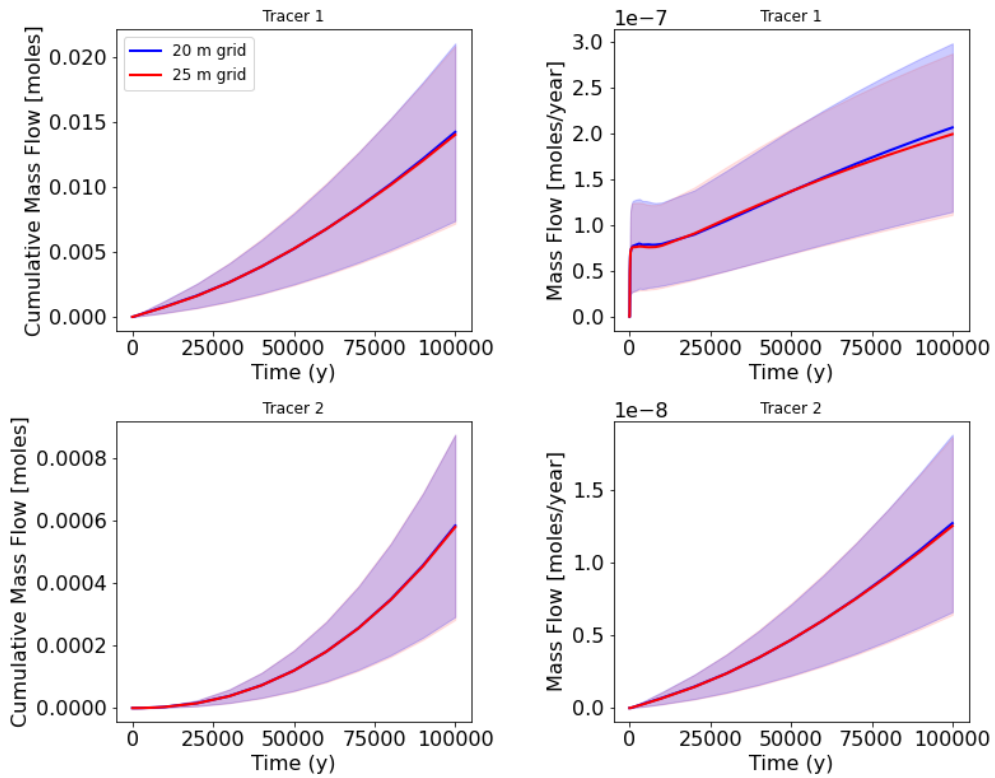
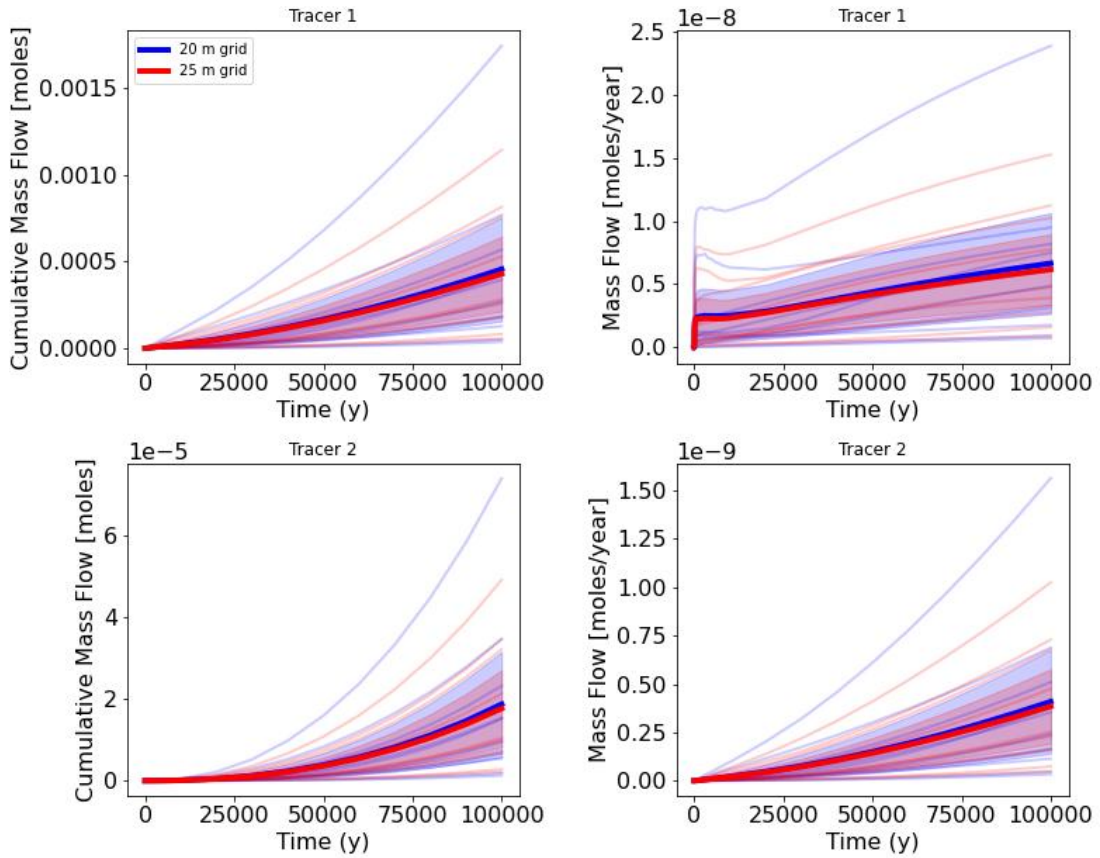**Fig. E-22. Cumulative mass (moles) and mass flow (moles/year) across the hillslope for the 20 m grid (blue) and 25 m grid (red).**

The cumulative mass flow and mass flow for the low point for the 20 m grid is plotted in Fig. E-23. We see quite a lot of variance in the realizations with a range of ~0.05 mole. As expected, the low point has higher fluxes than the hillslope and the tracer is concentrating in the south-west portion of the low point surface (Fig. E-24). Comparing the two upscaling lengths across the low point (Fig. E-25) the 25 m grid has a slightly higher mean which is likely due to more false connections occurring in the domain. However, the means and 95% confidence intervals are still quite close to each other, proving the 25 m grid to be advantageous over the 20 m grid due to the faster run time.
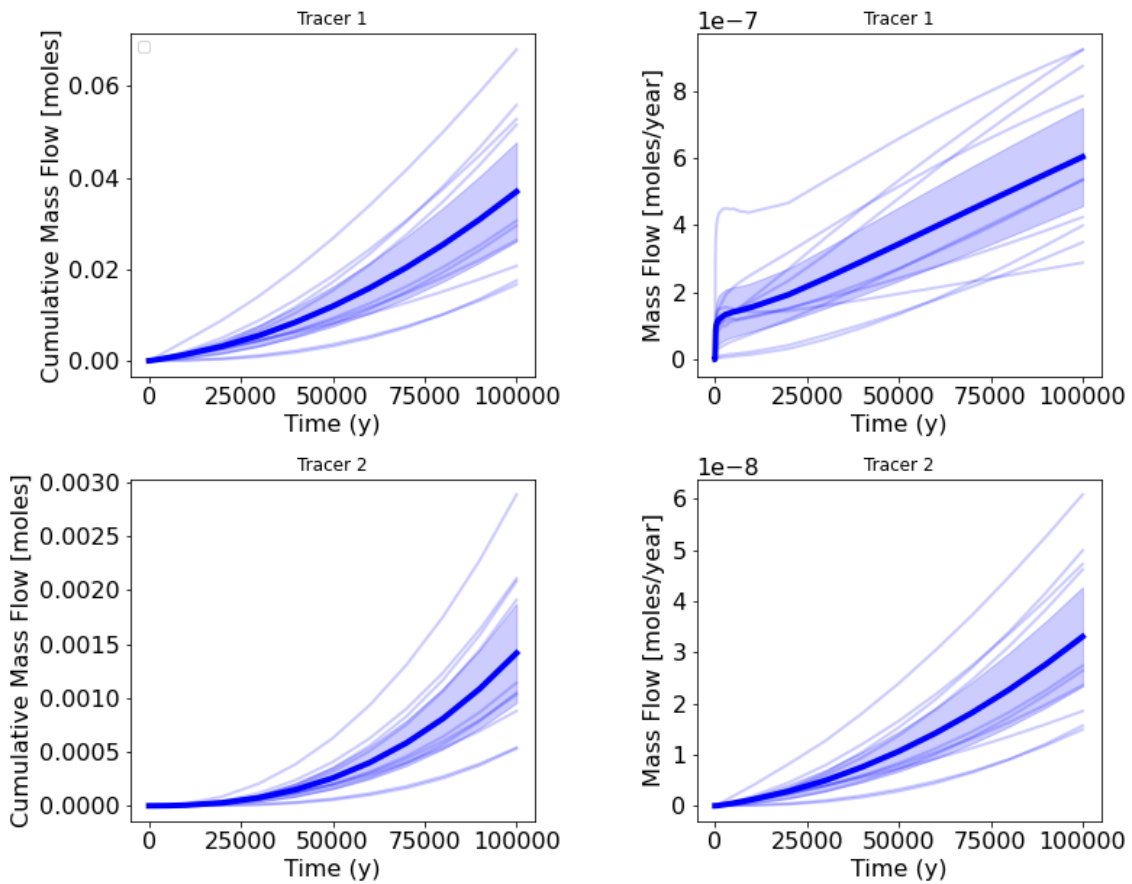
Fig. E-23. Cumulative mass (moles) and mass flow (moles/year) across the low point for the 20 m grid.
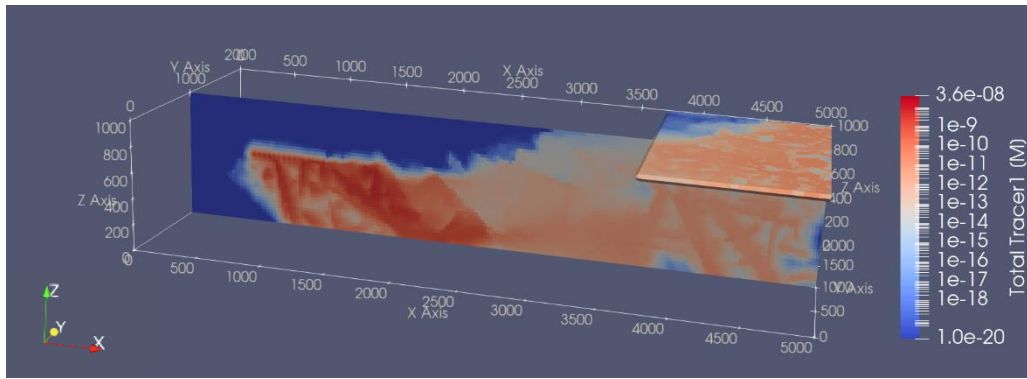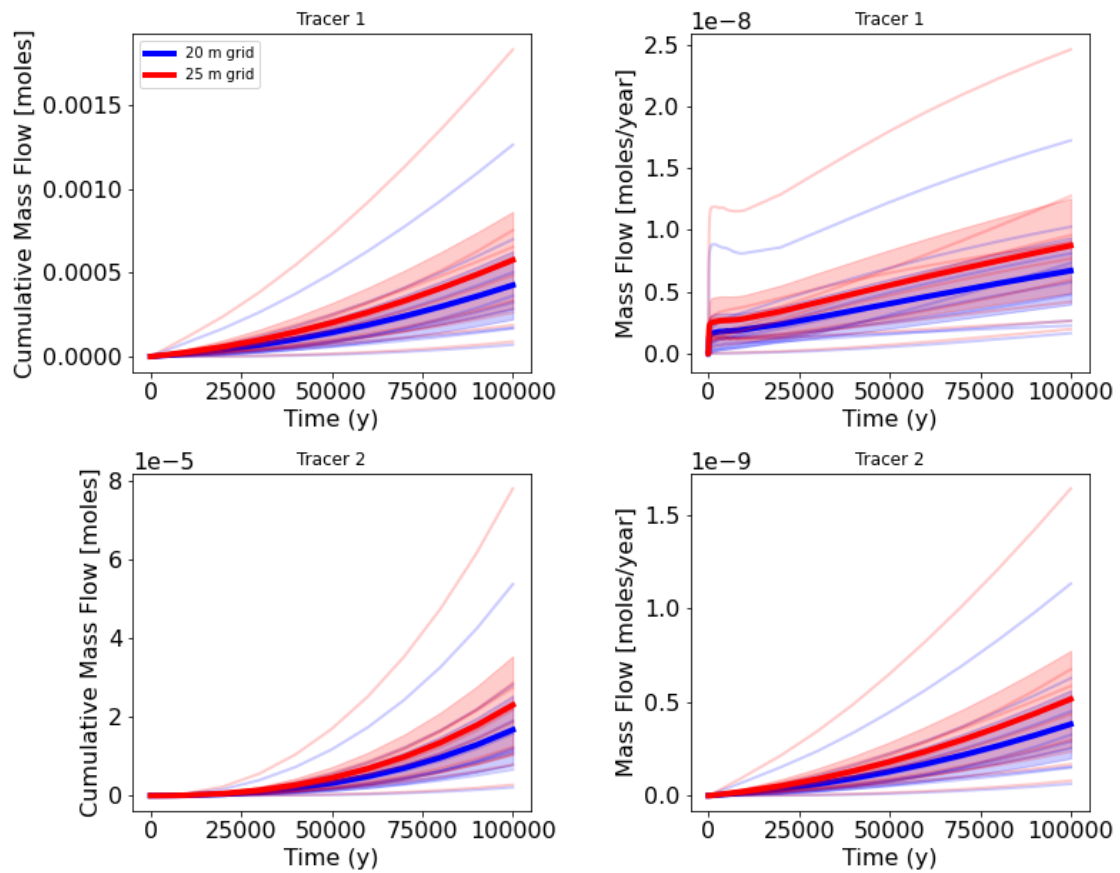
Fig. E-24. Tracer 1 at 100000 years for realization one.
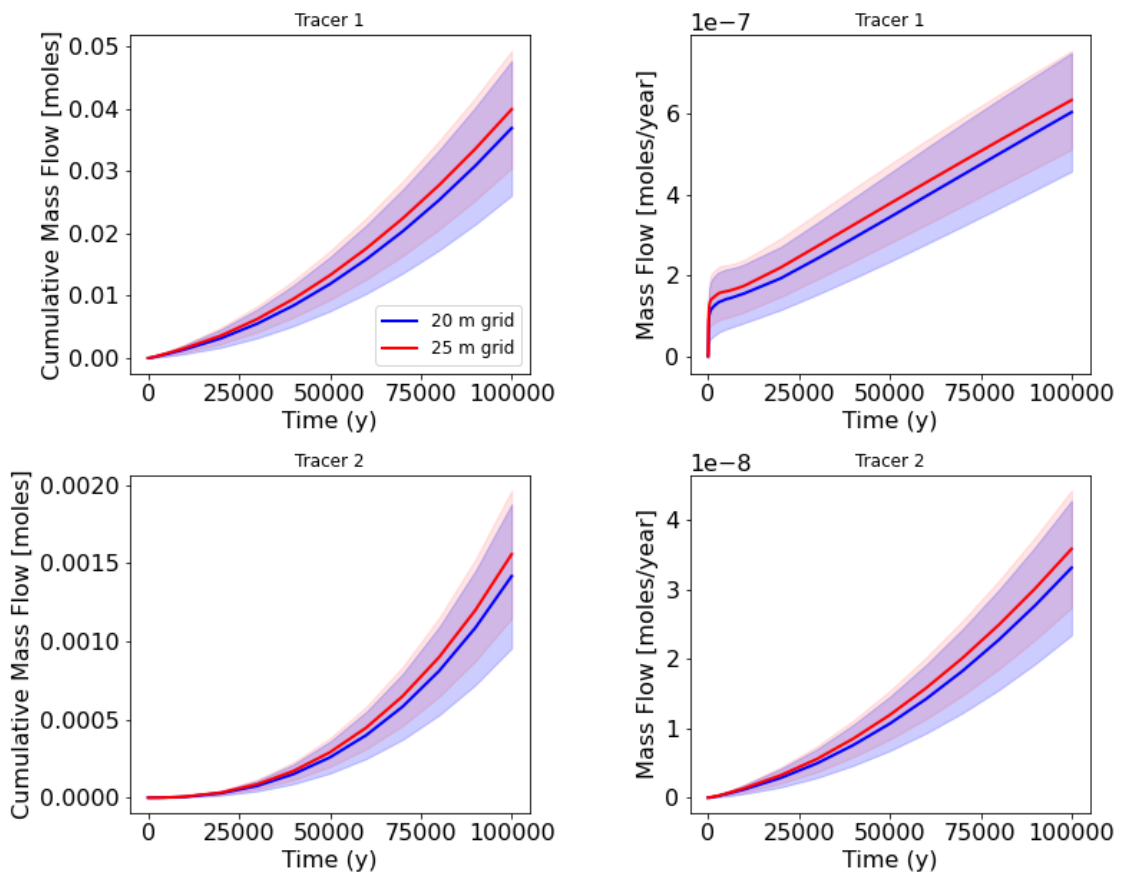
Fig. E-25. Cumulative mass (moles) and mass flow (moles/year) across the low point for the 20 m grid (blue) and 25 m grid (red).

To obtain the maximum tracer flux over the hillslope and low point, observation points across the entire two surfaces were post processed to find maximum mass flow at 100,000 years. The results for the hillslope calculated using both grid sizes is shown in Fig. E-26. The means and 95% confidence interval of the 25 m grid overlap with the 20 m grid, with realization 9 having the highest cumulative mass flow and mass flow. Looking at a slice through the domain at this point we see a large stochastic fracture intersecting a deterministic fracture which is likely causing the high mass flow. Looking

at the maximum mass flow results for the low point (Fig. E-27), the 25 m grid is visibly higher than the 20 m grid with realization 9 again having the highest mass flow. Taking a slice in the domain where this maximum mass flow occurs shows that it's less due to a deterministic fracture and more due to a large stochastic fracture cluster.

Fig. E-26. Maximum cumulative mass (moles) and mass flow (moles/year) across the hillslope for the 20 m grid (blue) and 25 m grid (red).

Fig. E-27. Maximum cumulative mass (moles) and mass flow (moles/year) across the low point for the 20 m grid (blue) and 25 m grid (red).

Two observation points on the hillslope and low point were also selected to compare concentrations at. These locations represent places where deterministic fractures intersect with the top surface. Fig. E-28 shows the results comparing the two grid sizes and realizations. We see a large range in realizations, ~1.59×10^{-13} M for Tracer 1 on the hillslope and ~1.15×10^{-11} M for Tracer 1 on the low point. However, all concentrations remain low with nothing higher than 1×10^{-10} M.
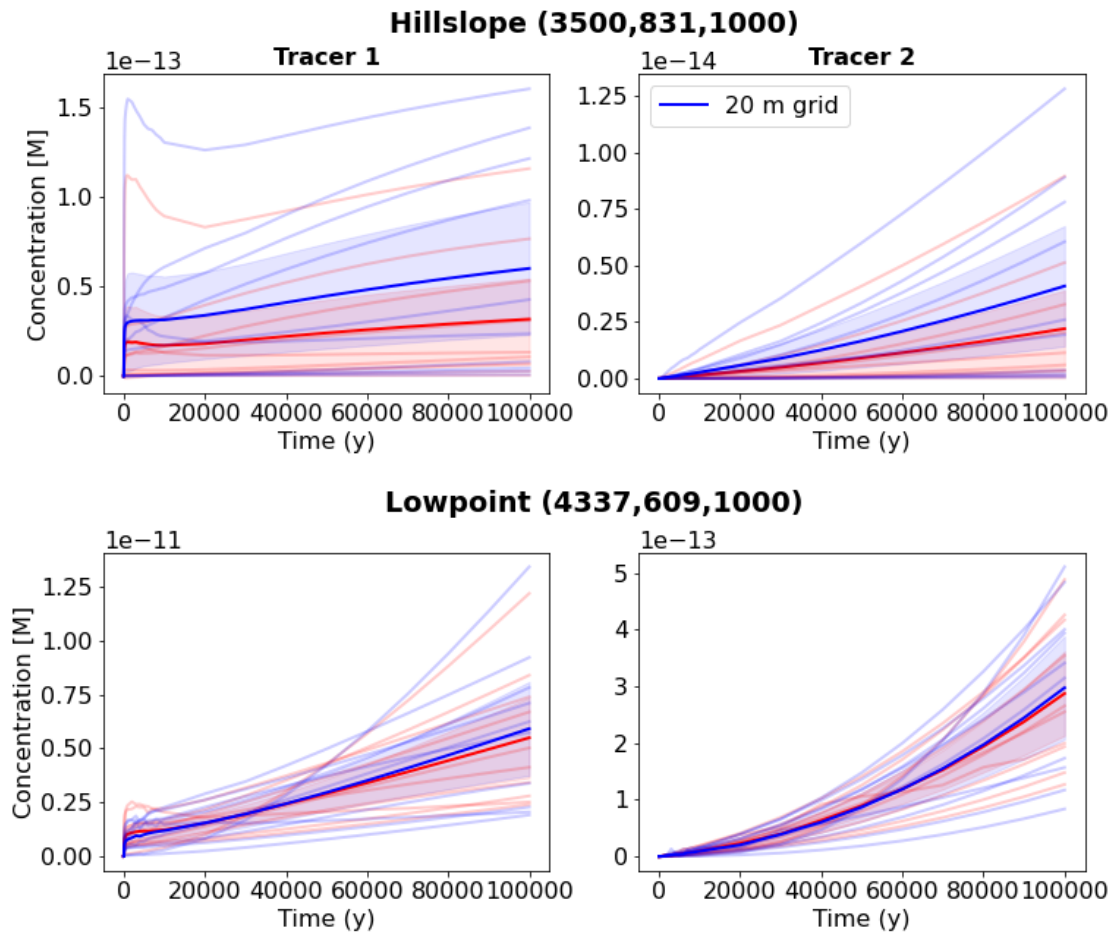
Fig. E-28. Observation points on the hillslope and low point comparing the 20 m grid (blue) and 25 m grid (red).

The DCDM model was compared against the ECPM 25 m grid. The DCDM model was not included over the repository region. Outside the repository region, cells that had no fractures intersecting them were made inactive. The secondary continuum was discretized using 100 cells with matrix properties as stated in the task specification. Fig. E-29 shows the mean and 95% confidence intervals of the fluxes over the hillslope comparing the ECPM and DCDM models. The DCDM shows slightly higher means of at the hillslope than the ECPM. This could be due to less numerical diffusion in the DCDM model due to the matrix cells being set to inactive. At 100,000 years the cumulative mass flow for Tracer 1 for the DCDM is about ~0.005 moles higher. Fig. E-30 shows the fluxes over the low point, where the DCDM is very similar to the ECPM. Although the DCDM represents fracture-matrix diffusion at the cm scale, the effective diffusion coefficient specified in the task specification is quite low ($10^{-13.7}$ m^2 s^{-1}), therefore it is not surprising that the ECPM and DCDM give similar results.
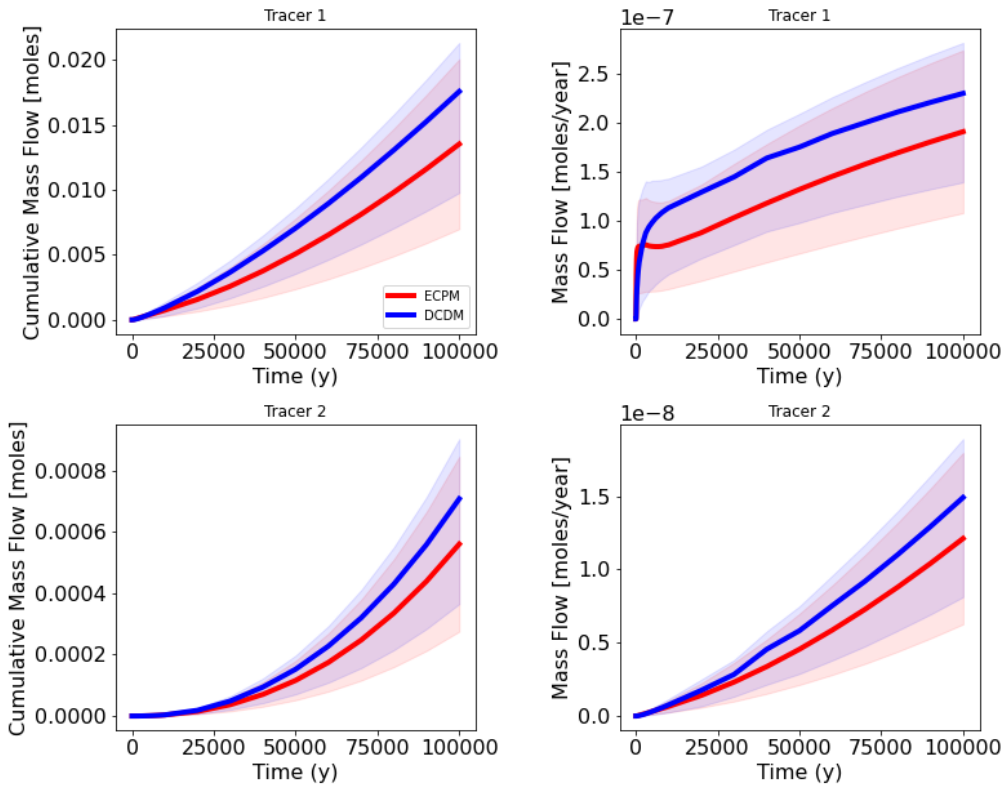
Fig. E-29. Means and 95% confidence intervals for the DCDM (blue) and ECPM (red) for the fluxes over the hillslope.
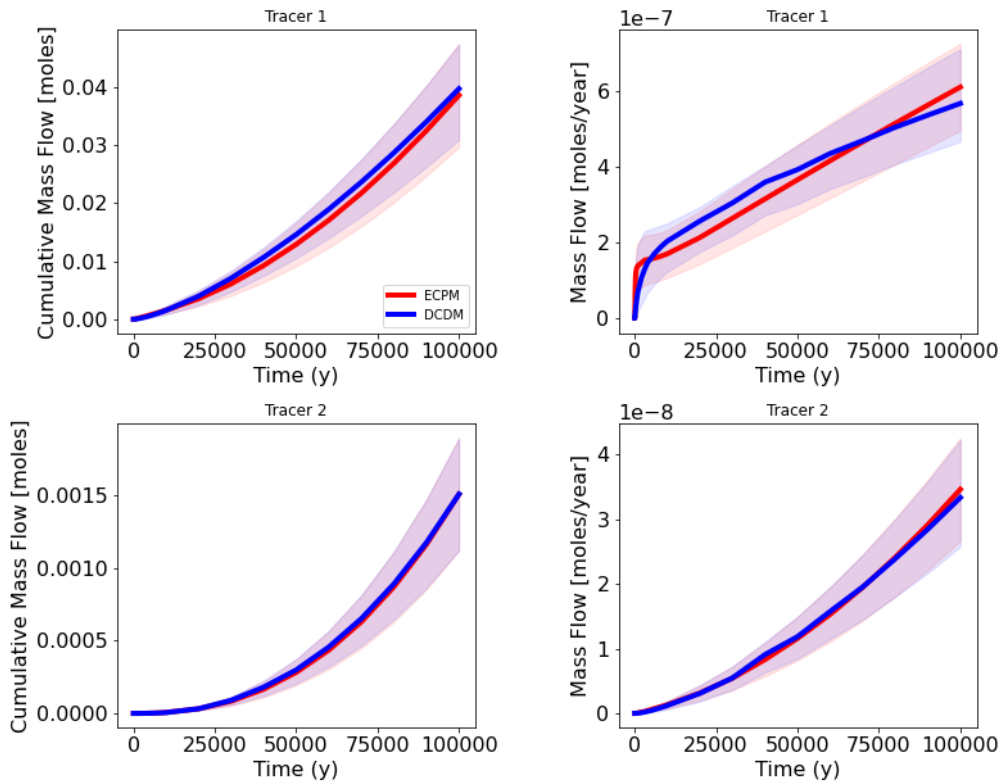
Fig. E-30. Means and 95% confidence intervals for the DCDM (blue) and ECPM (red) for the fluxes over the low point.

E.4.5   Radionuclide Release and Transport

The radionuclide inventory was implemented on the ECPM 25 m grid for all ten realizations. The UFD Decay Process Model in PFLOTRAN was used to simulate the radionuclide behaviour over the simulation. The UFD Decay Process Model differs from the reactive transport mode in PFLOTRAN because it decays all the phases instead of only the aqueous and adsorbed phase, and distribution coefficients can be specified by material and isotope.

The radionuclide mass left in the repository was found to be the same for all realizations (Fig. E-31). This could be due to the larger portion of tracer remaining in the waste package compared to the conservative tracers, or the adsorption occurring in the buffer. The cumulative mass flow and mass flow across the hillslope is plotted in Fig. E-32. The fluxes show no observable amount before 50,000 years where only one waste package has breached at time zero due to an undetected defect, and then we observe a spike in the flux after all the waste packages breach. There is a large difference between the realizations, a range in ~1 mole for ^{129}I and ~20 moles for ^{238}U. The cumulative mass flow and mass flow across the low point plotted to one million years is shown in Fig. E-33. When plotted to a million years we see that the mass flow ^{129}I is still increasing but for all other radionuclides it has started to decrease where the maximum mass flow occurred at ~200,000 years. A wide difference in realizations remains with more than 40 moles range for ^{129}I and ~5,000 moles range for ^{238}U. The observation points for the hillslope and low point are plotted in Fig. E-34 to one million years. ^{129}I shows the highest concentration with the largest realization reaching over 4×10^{-9} M and 1.5×10^{-11} M at the hill slope and low point observation point respectively. ^{226}Ra and ^{230}Th are not plotted because not a significant amount of concentration has been observed at these points.
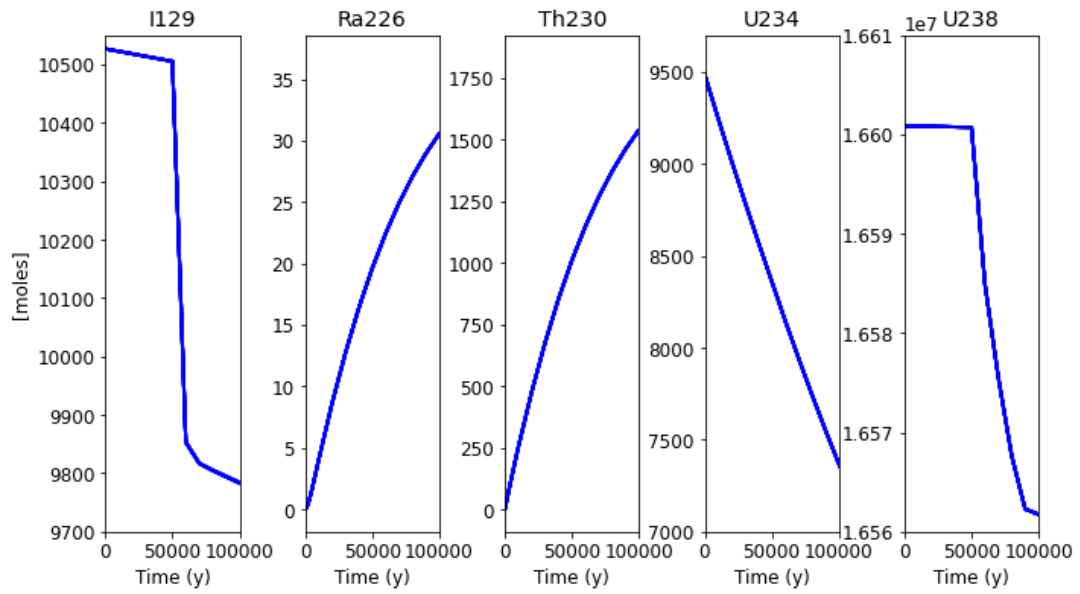
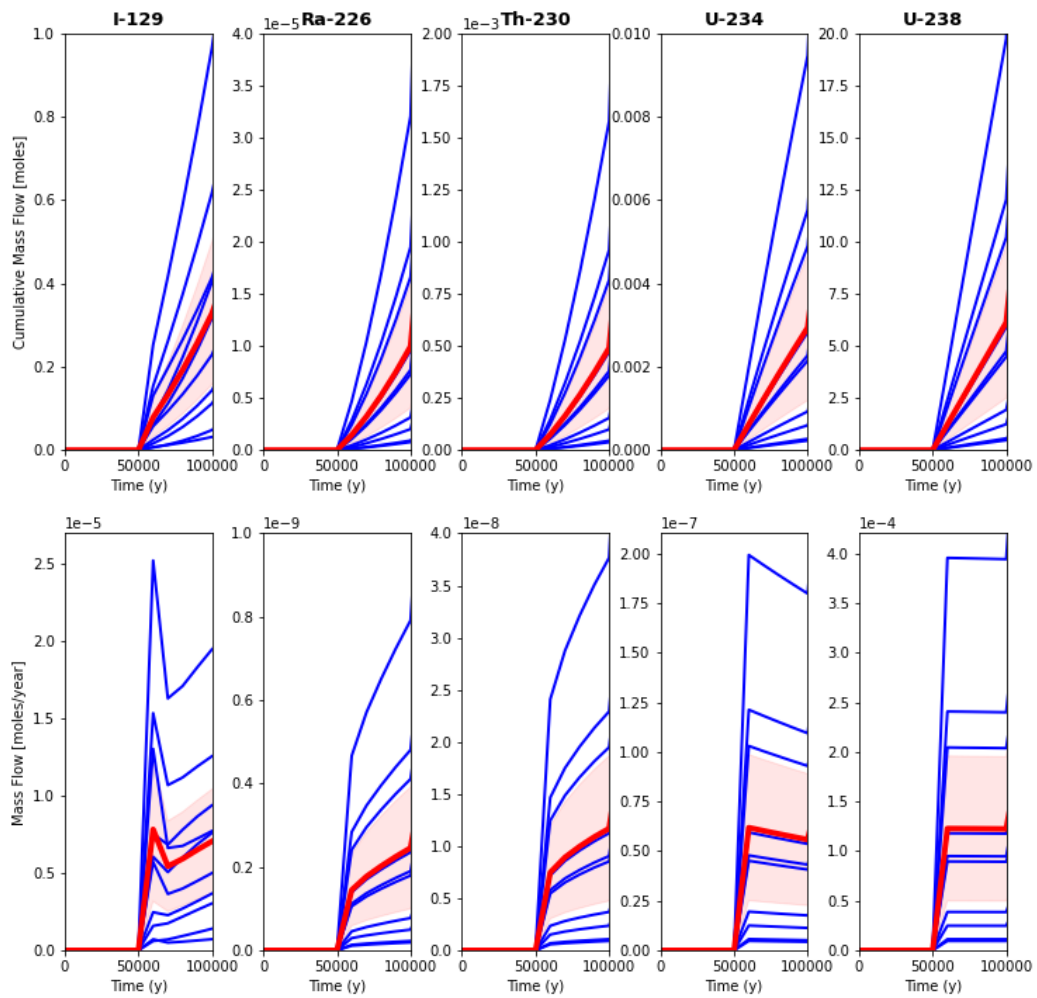**Fig. E-31. Mass of each radionuclide remaining in the repository.**

Fig. E-32. The cumulative mass flow and mass flow across the hill slope for radionuclide inventory.
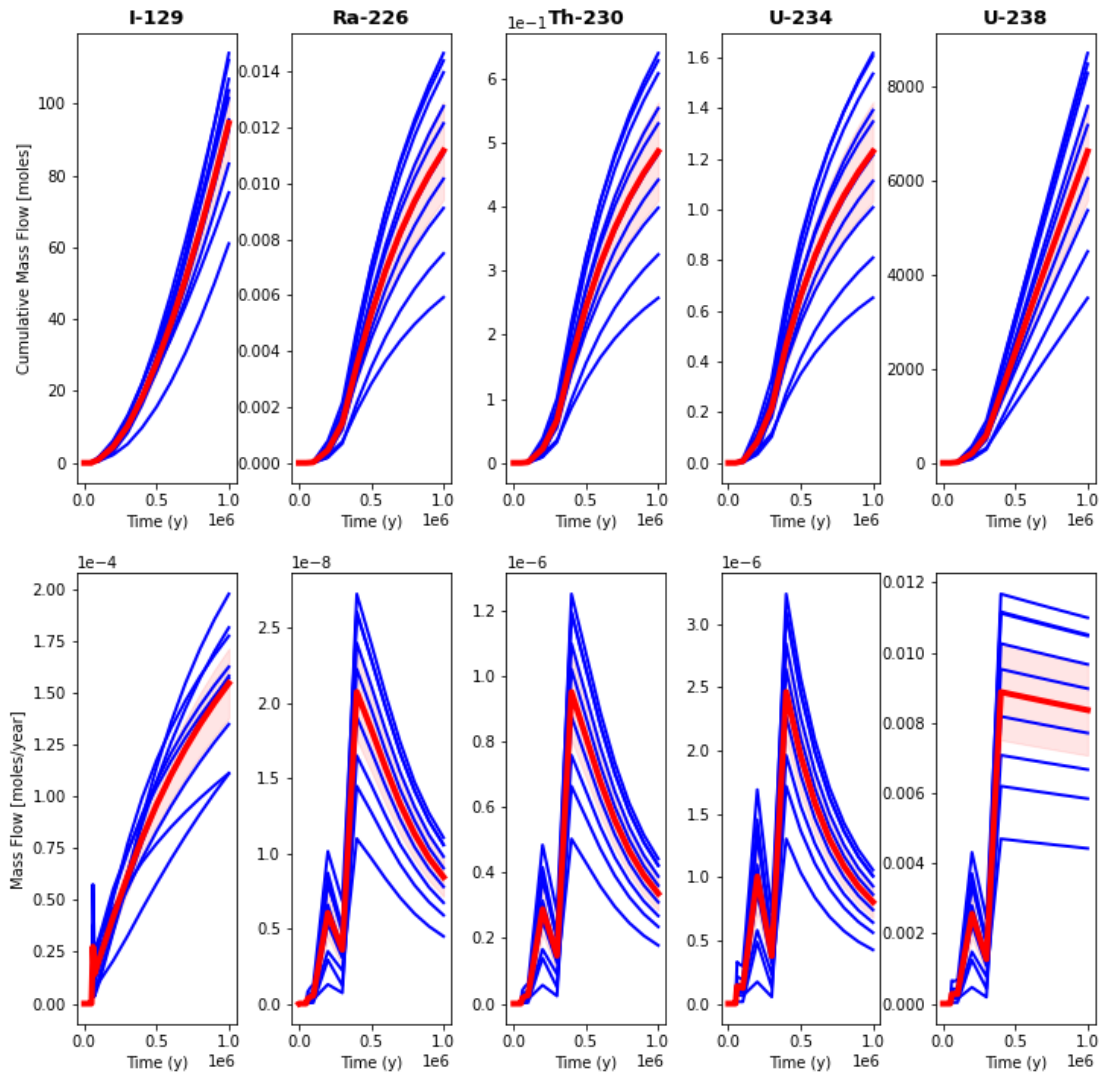
Fig. E-33. The cumulative mass flow and mass flow across the low point for radionuclide inventory. Plotted to 1,000,000 years.
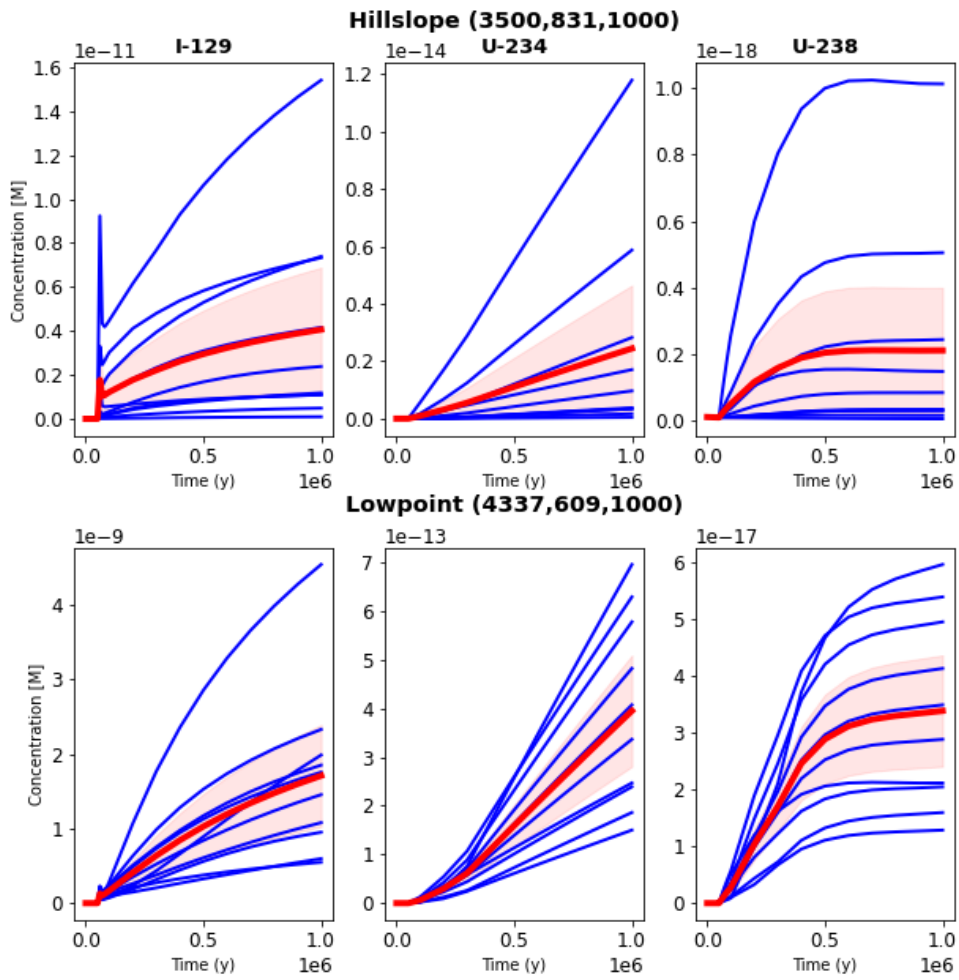
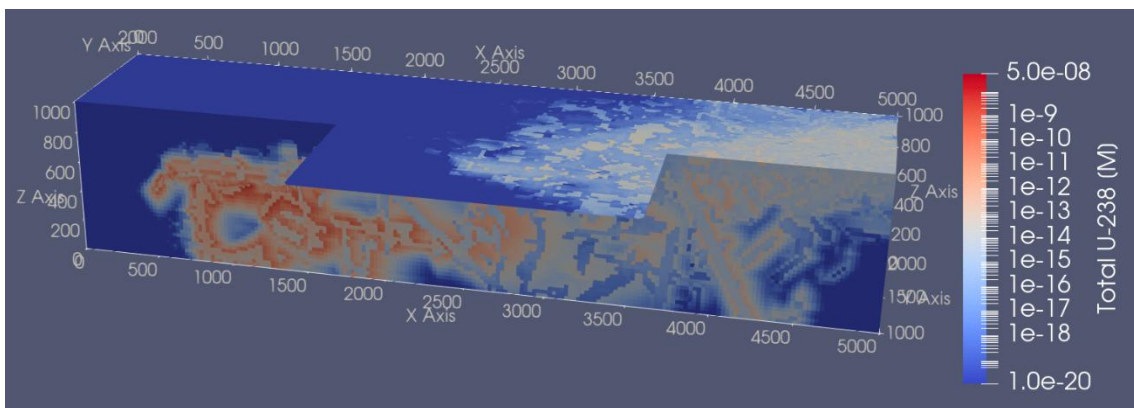**Fig. E-34. Observation points on the hillslope and low point for the radionuclide inventory.**

Fig. E-35. U-238 at 100000 years.

E.5 References

Anttila, M. 2005. Radioactive Characteristics of the Spent Fuel of the Finnish Nuclear Power Plants. Working Report 2005-71. Posiva Oy, Olkiluoto, Finland.

Hammond, G.E., Lichtner, P.C., and Mills, R.T. 2014. Evaluation the performance of parallel subsurface simulators: An illustrative example with PFLOTRAN. *Water Resources Research,* 50(1), 208-228.

Iraola, A., P. Trinchero, S. Karra and J Molinero. 2019 Assessing dual continuum method for multicomponent reactive transport. *Computers & Geosciences.* 130: 11-19

LaForce, T., R.S. Jayne, R. Leone, Stein, E., and Nguyen, S. 2023. DECOVALEX-2023 Task F Specification Revision 10. SAND2023-04005R. Sandia National Laboratories, Albuquerque, New Mexico.

Lichtner, P.C. 2000. Critique of Dual Continuum Formulations of Multicomponent Reactive Transport in Fractured Porous Media. *Dynamics of Fluids in Fractured Rock*, Geophysical Monograph 122, 281-298.

Stein, E. R., J. M. Frederick, G. E. Hammond, K. L. Kuhlmann, P. E. Mariner, and S. D. Sevougian 2017. April 9-13, 2017. *Modeling Coupled Reactive Flow Processes in Fractured Crystalline Rock*. Paper presented at the International High-Level Radioactive Waste Management Conference, Charlotte, NC.

Sweeney, M.R., Gable, C. W., Karra, S., Stauffer, P.H., Pawar, R.J., & Hyman, J.D. 2020. Upscaled discrete fracture matrix model (UDFM): an octree-refined continuum representation of fractured porous media. *Computational Geosciences*, 24(1), 293-210.

Appendix F.   Radioactive Waste Management Authority in Czech Republic (SÚRAO)

F.1 Introduction

The Czech Deep Geological Repository (DGR) project envisages the disposal of waste in a crystalline rock environment based on the Swedish KBS-3 model, which also envisages the disposal of spent nuclear fuel (SNF) in metal, hermetically-sealed waste packages in boreholes sealed with a bentonite buffer. With regard to performance assessment (PA), SÚRAO already has extensive experience in the management of its low- and intermediate-level waste repositories. However, both PA activities and the creation and validation of mathematical models related to the deep geological repository project are still in the early stages of development. Therefore, the main reason for SÚRAO's involvement in the crystalline reference case task is to gain more experience regarding the preparation and application of PA modelling methods and the validation of models in the context of the Czech DGR development programme.

F.2 Methods

The main simulating tool employed for Task F comprised PFLOTRAN, which uses the finite volume method (Lichtner et al. 2020). The RICHARDS, GIRT and REACTION SANDBOX (Hammond 2020) mode was used for the benchmark and Reference Case models. The RICHARDS mode is used for the flow, and all of the transport models were implemented applying the GIRT (Global Implicit Reactive Transport) mode.

The mass conservation equation, together with the Darcy flux were implemented in the RICHARDS mode. Mass conservation was introduced via:

$$Q_w = \frac{\partial}{\partial t}(\varphi s \gamma) + \nabla \cdot (\gamma \boldsymbol{q})$$

where Q_w denotes the source/sink, φ the porosity, s saturation, γ the molar water density and $\boldsymbol{q}$ the Darcy flux, described as:

$$\boldsymbol{q} = -\frac{kk_r(s)}{\mu}\nabla(P - \rho g z)$$

where k is the intrinsic permeability, k_r the relative permeability, μ the viscosity, P the pressure, ρ the mass water density, g gravity and z the vertical distance (Lichtner et al. 2020). The governing equation for the solute transport of the tracer was given by:

$$Q_C = \frac{\partial}{\partial t}\varphi C + \nabla \cdot (\boldsymbol{q}C - \varphi s\tau D\nabla C)$$

where Q_C denotes the source/sink for the tracer, C the concentration, τ tortuosity and D the diffusion/dispersion coefficient (Lichtner et al. 2015).

The source density $Q_C(t,x)$, $[m^{-3}\,s^{-1}]$ is non-zero within the Ω_Q domain, which represents the repository. Its value in a finite volume E is given by the diffusion flux through the bentonite buffer. The flux is driven by the difference between the immobile concentration C_{im} in the container and the concentration in the surrounding rock C:

$$Q_C(t,x) = k\chi(\Omega_Q)(C_{im}(t,x) - C(t,x)).$$

Diffusion is approximated via this linear relationship with an effective diffusion coefficient

$$k = \frac{ND_bS}{|E|d}$$

where D_b $[m^2 s^{-1}]$ denotes the diffusion coefficient of the bentonite, $S = 2\pi r(l+r)$ represents the surface area of the bentonite barrier, and d is its thickness. We assumed a discretization that respects the periodicity of the repository. Therefore, all the source cells E have the same internal structure, which contain N containers.

The immobile concentration C_{im} can be supplemented by the slow dissolution of the waste matrix:

$$\frac{dC_{im}}{dt} = -Q_C + \lambda C_W, \quad \frac{dC_W}{dt} = -\lambda C_W,$$

where λ is the kinetic rate of dissolution and C_W denotes the mass of the tracer in the dissolving waste.

```
CHEMISTRY
 PRIMARY_SPECIES
  Tracer_2
 /
 IMMOBILE_SPECIES
  Tracer_2_im
 /
 REACTION_SANDBOX
 DISTRIBUTED_WASTE_PACKAGE
    # dissolved species
   MOBILE_NAME Tracer_2
    # immobile species
   IMMOBILE_NAME Tracer_2_im
    # aux. mineral to specify space-dependent diffusion coef.
   DIFFUSION_SCALE_MINERAL DIFF_SCALE(s)
    # mineral used for Waste content
   WASTE_MINERAL Fractional(s)
    # fractional dissolution rate mol*s^-1
   WASTE_RATE 3.17e-15
 /
 /
```

Fig. F-1. Example of the DWP module configuration.

The multi-continuum approach described was successfully implemented in PFlotran, version 4.0.0 applying the custom Reaction Sandbox DWP (Distributed Waste Package) module. Fig. F-1 provides an example of the DWP module configuration card in the PFlotran input file. In order to utilize the module it is necessary to provide specific species names for the mobile and immobile concentrations. The spatially variable diffusion rate is determined through the volume fraction of an auxiliary mineral, which is specified by the DIFFUSION_SCALE_MINERAL keyword. The waste dissolution rate λ is set using the WASTE_RATE keyword, and the internal waste mass C_W is represented by the mineral, which is denoted WASTE_MINERAL, the volume fraction of which is updated after each time step applying the DWPUpdateKineticState method. The mobile and immobile concentrations were calculated applying the core PFLOTRAN solver via the DWPEvaluate method, thus providing both residual and Jacobian information. The modified PFLOTRAN source code is available for a forked repository, https://github.com/flow123d/pflotran_JB. The construction of a custom Docker image was integrated into the simulation repository, which is described in the following section.

F.2.1   Homogenization of DFN

A discrete fracture network (DFN) sample generated using the pydfnworks library (Hymann et al. 2015) was upscaled so as to form an effective heterogeneous continuum. Anisotropic grid stepping was required in order to align the grid with the geometry of

the repository. This feature was not, however, supported by the original mapDFN script developed by SNL (Stein & Kulman 2021). Therefore, in order to address this limitation, we extended the algorithm so as to accommodate anisotropic grids. The cell corners were transformed into the local coordinate system of the fracture, for which a simplified intersection test was performed. The simplification of the code applying vector operations provided for the significant acceleration of the calculation. Moreover, the homogenization process was refactored into a reusable module: mapdfn.py, while the main.py script handled the configuration of the model from a YAML file and the output of the PFLOTRAN input fields. The model input scripts, a docker image for the custom PFLOTRAN fork, the problems surrounding the testing, and repository model inputs can be accessed in the repository (Březina 2023; https://github.com/GeoMop/Decovalex2023).

F.3 Benchmarks

F.3.1   1D Transport

The 1D transport benchmark was simulated with the Reactive transport mode only and, due to the geometrical simplicity problem, it was the only benchmark for which the RICHARDS flow mode was not applied and for which the Darcy velocity was set explicitly. The model domain comprises a beam with dimensions of 10 m in the X axis and 1 m in the Y and Z axes. The discretization of the beam was applied as suggested in the Task Specification in 0.05 m, 1 m, 1 m grid cells, thus resulting in a total of 200 hexahedral cells. The results of each of the three simulations (conservative, decaying and sorbing tracer) evinced good matches with the analytical solution (Fig. F-2). The model breakthrough curve was slightly more dispersed in all the cases when compared to the analytical solution, which is caused by taking too large timesteps to match the analytical solution with PFLOTRAN. The mismatch could be solved by reducing the maximum timesteps.
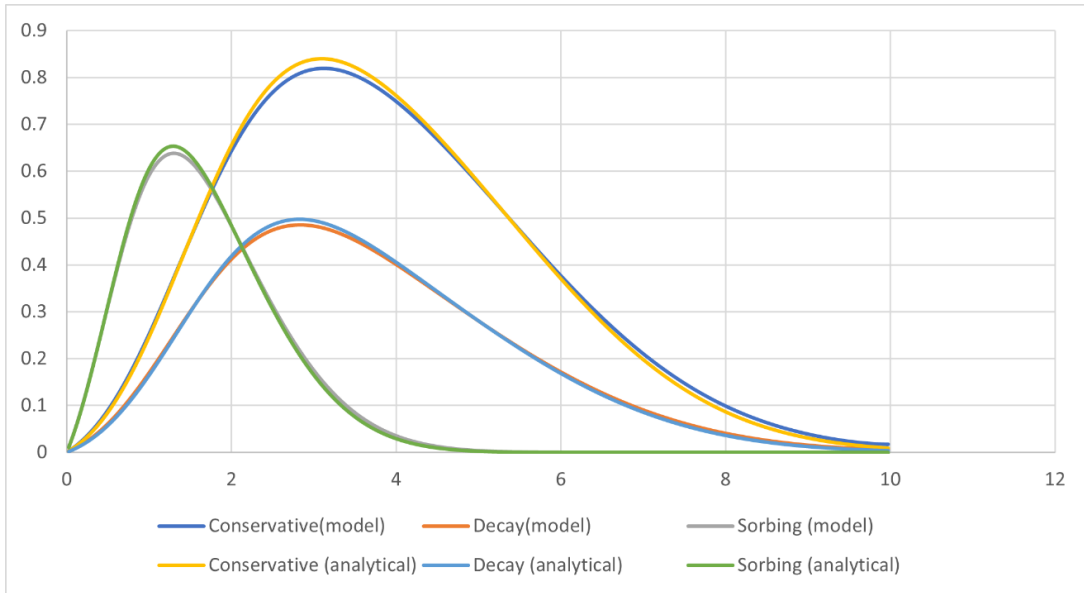
Fig. F-2. Comparison of the model and analytical breakthrough curves.

F.3.2   1D Fracture Plus Matrix Diffusion

The Fracture-Matrix Diffusion benchmark was considered as an axisymmetric problem. The grid was gradually refined in the Y direction towards the cells that represented the fracture and in the X direction towards the inflow cells, with the smallest cells of 0.01 m, 0.005 m and 1 m in size and the largest cells of 1 m, 0.2 m and 1 m in size. The fracture porosity was set at 0.01 according to the 0.005 m Y cell face (Fig. F-3). The matrix porosity was the same (see the Task Specification) and the matrix permeability was set at the very low value of 1×10^{-22}.

```
#=========================== discretization ==================================
GRID
  TYPE structured
  ORIGIN 0.d0 0.d0 0.d0
  NXYZ 58 38 1
  DXYZ
    10@0.01 10@0.02 14@0.05 10@0.1 10@0.2 4@1
    10@0.005 5@0.01 18@0.05 5@0.2
    1.d0
  /
END
```

Fig. F-3. Discretization scheme for the matrix diffusion benchmark.

The Darcy velocity was simulated implicitly by the Dirichlet pressure boundary condition of 108238 Pa at the inflow face and 100000 Pa at the outflow, with a fracture permeability of 1×10^{-15} m^2. The tracer source was modelled by the Dirichlet condition as

a constant concentration at the inflow face. The concentrations at the observations points along the fracture are shown in (Fig. F-4), and into the matrix in (Fig. F-5) for velocities of 0.01 m/s and 0.1 m/s.
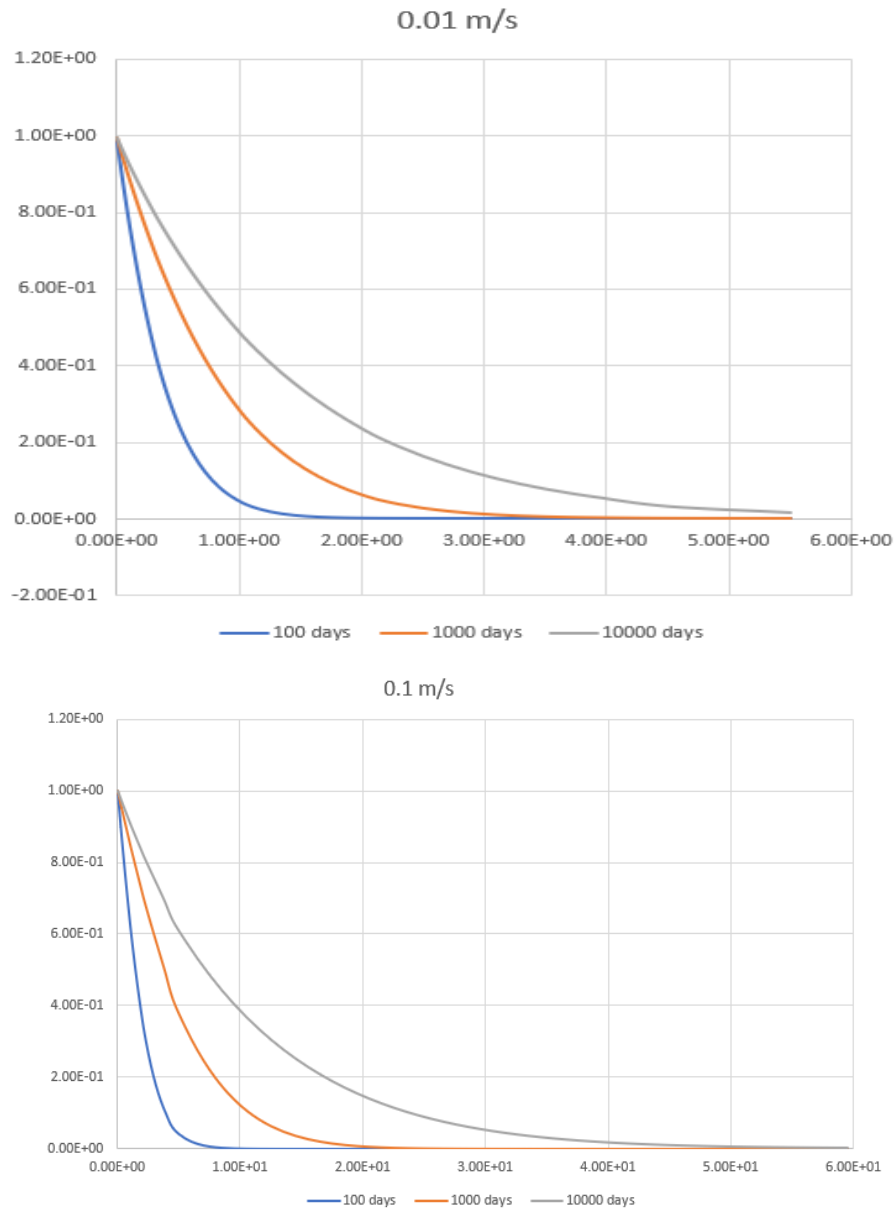
Fig. F-4. Concentration along the fracture at low (top) and high (bottom) velocities.
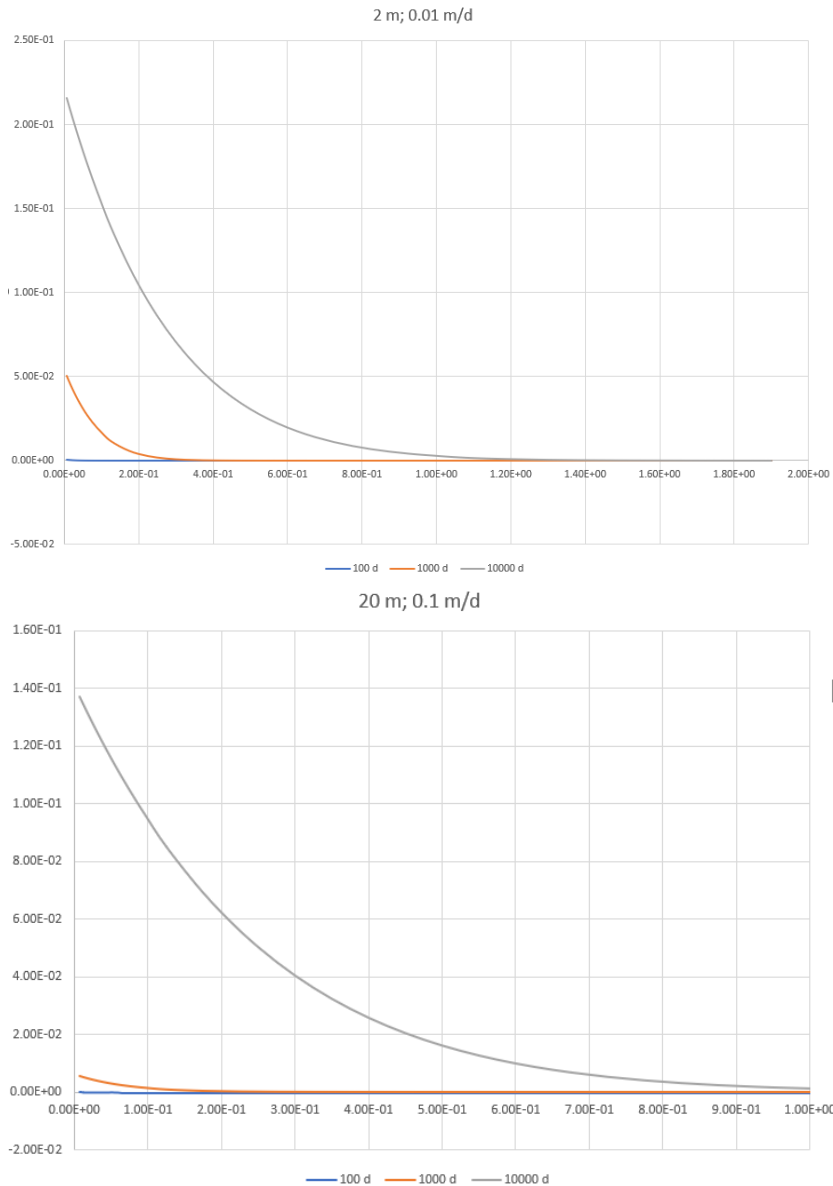
Fig. F-5. Concentration into the matrix at low velocity and a distance of 2 m (top) and at the high velocity and a distance of 0.2 m (bottom).

F.3.3   Four-Fracture Transport

The 4-fracture problem was simulated using the PFLOTRAN and DFNWorks framework with the pydfnworks user interface. The pydfnworks library was used only for the generation of the fractures and the creation of the input files for the upscaled CPM model. The transport simulation was conducted using the homogenized CPM model (Fig. F-7). The domain was discretized and the material properties were calculated into the 10 × 15.625 × 12.5 m cell grid, thus resulting in a model with 512 000 elements. The motivation for using these non-cubic block cells concerned the testing of the functionality and accuracy of the modified upscaling method that will be used later in

the reference case model. The cells without fractures were deactivated for the purpose of the comparative team pore volume calculations.

The liquid flow boundaries were set over the entire left (inflow) and right (outflow) faces. No flow boundary was considered for the other faces. The effect of gravity on the hydrostatic pressure was not considered. Dirichlet constant pressures were defined of 1.001 MPa at the inflow and 1 MPa at outflow. The model was hydraulically in the steady-state regime and the active cells were fully saturated.

The transport of the conservative tracer was simulated with the advection-dispersion equation, while neglecting the matrix diffusion. The tracer was injected with a 1-day long pulse and a l mol/L concentration as the constant Dirichlet boundary condition over the entire cross-section of the fracture and the inflow face of the model domain. A zero diffusive gradient was applied at the outflow face.
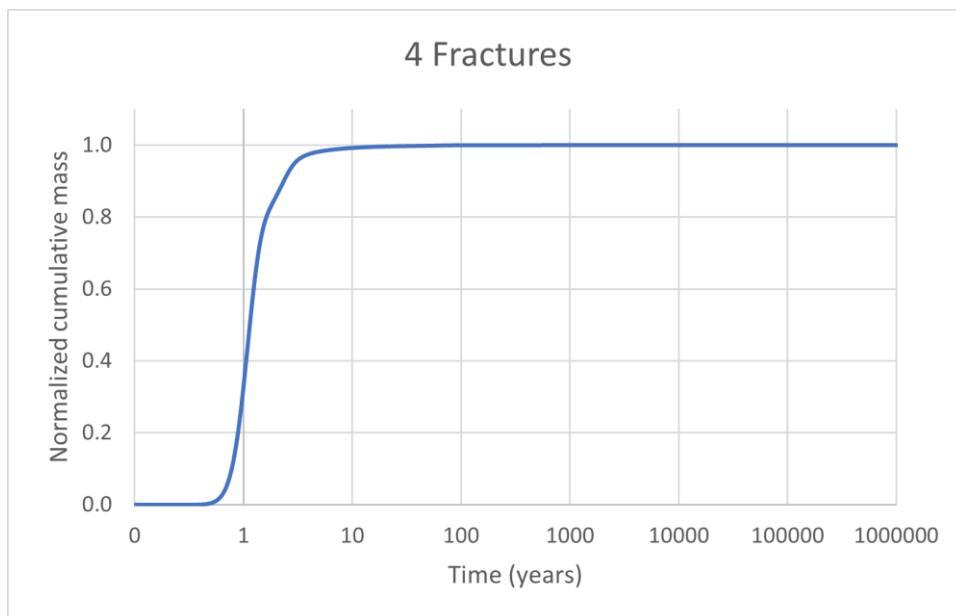
Fig. F-6. Normalized cumulative breakthrough curve of the 4-Fracture problem.

F.3.4   Four-Fracture Plus Stochastic Fractures

The four-fracture plus problem consisted of a continuation of the four-fracture problem, which introduced the stochastically generated fracture network to the previous deterministic fractures case. The deterministic and stochastic fractures were generated using the pydfnworks library. The same discretization and upscaling was used as in the previous 4-fracture problem.
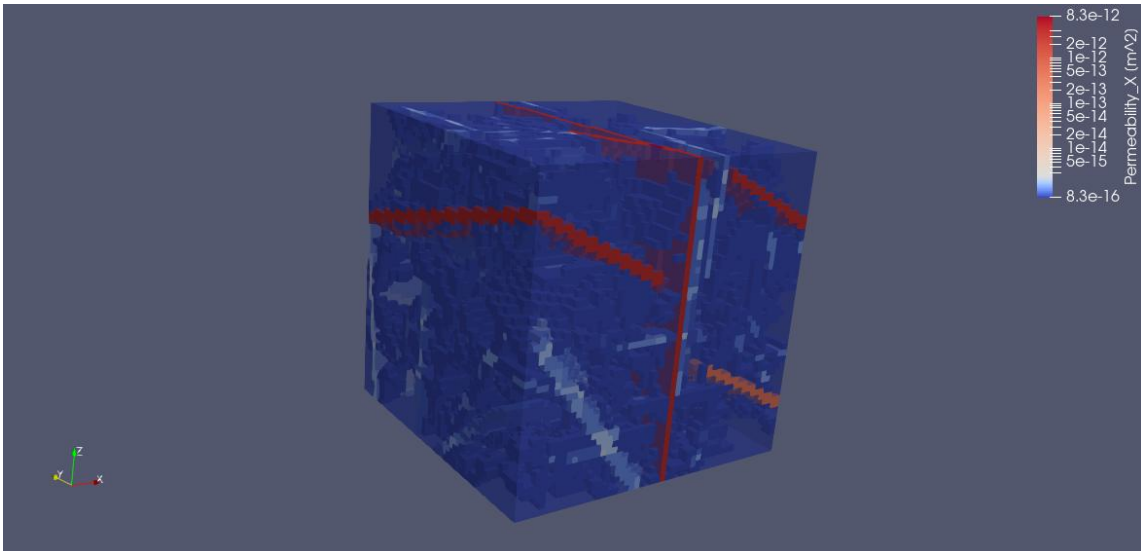
Fig. F-7. Permeability field of the 4-Fracture Plus model.

In addition to the extension of the fracture network, the benchmark case was also extended by adding two new tracers to the transport simulations – decaying and sorbing tracers. The decaying tracer had a half-life of 100 years. The sorbing tracer (with a retardation coefficient of 5) was modelled applying a linear distribution coefficient (the coefficient distributed the mass by the ratio of the mass sorbed on the fracture area and the mass that dissolved in the water) of 4, following conversion by Tang et al. (1981). The spatial distribution of the coefficient was derived from the porosity, for which the KD_MINERAL_NAME parameter was used where the distribution coefficient for each fracture is derived from a "dummy mineral" volume fraction, which was calculated internally in PFLOTRAN as:

$$K_d = (R - 1)\rho_w\, \rho_r (1 - \varphi) 10^3 V_m$$

Where R denotes the retardation factor, ρ_w the water density, ρ_r the rock density, φ the porosity and V_m the mineral volume fraction. The volume fraction was calculated for each cell as the ratio of the fracture aperture that crosses the cell and the cell side length, which gives the same number as the cell porosity value.

The flow was driven by the pressure difference of 0.001 MPa between the inflow and the outflow faces. Flow occurred only if the cells crossed by the fractures and all the other cells were deactivated. The conservative, sorbing and decaying tracers were included via a constant concentration of 1 mol/L, which lasted one day (the Dirichlet concentration boundary condition) over the inflow surface. A zero diffusive gradient was applied to the outflow face, thus allowing advective flux out of the domain only.

The cumulative breakthrough curves were normalized by the introduced tracer mass. Most of the mass passed the domain in less than 10 years (Fig. F-9). The moment analysis

showed the first moment values as 1.03 for the conservative tracer and 0.85 for the decaying tracer. The first moment value of the sorbing tracer was 4.73, which approximately fit to the expectation given by the retardation factor of 5 in each fracture. The effect of sorption is visualized in Fig. F-8, which compares the conservative and the sorbing tracers that had propagated through the domain after 1 year. The differences in the breakthrough between the conservative and the decaying tracers are barely detectable, which is due to fact that the half-life of the decaying tracer is 100 times longer than the peak of the breakthrough curve.
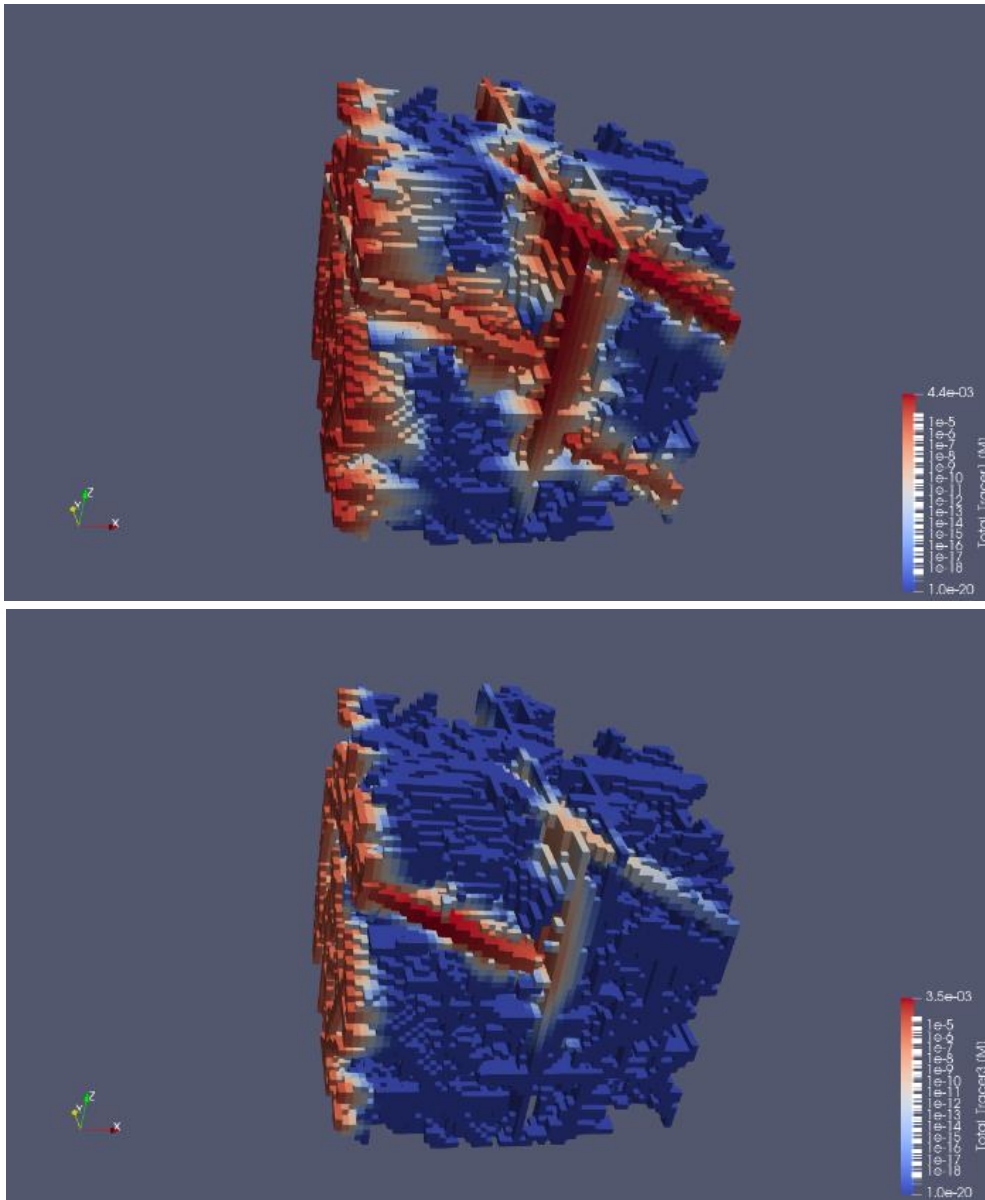
Fig. F-8. The conservative (top) and the sorbing (bottom) tracer after one year.
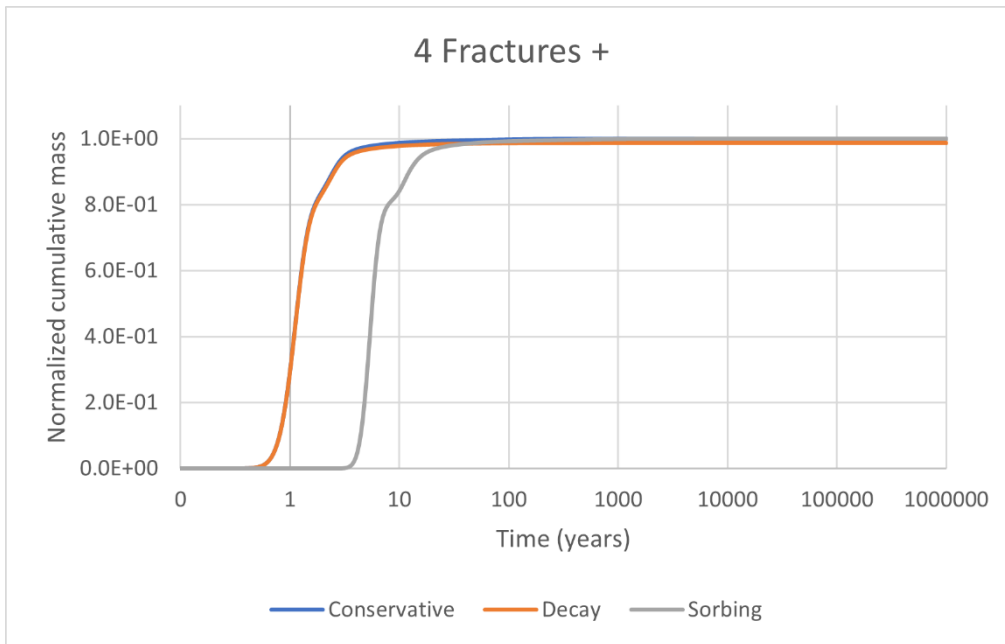
Fig. F-9. Normalized cumulative breakthrough curves of the 4-Fracture Plus model conservative, decaying and sorbing tracers.

F.3.5 Continuous Point Source

The same model setup as for 4-Fracture Plus was applied for the Point Source model. The only difference concerned the implementation of the boundary condition. The tracers were introduced as a one-day long constant concentration pulse of 1 mol/L in one cell for the Point Source model, with coordinates of -500, 7 and 248.5.
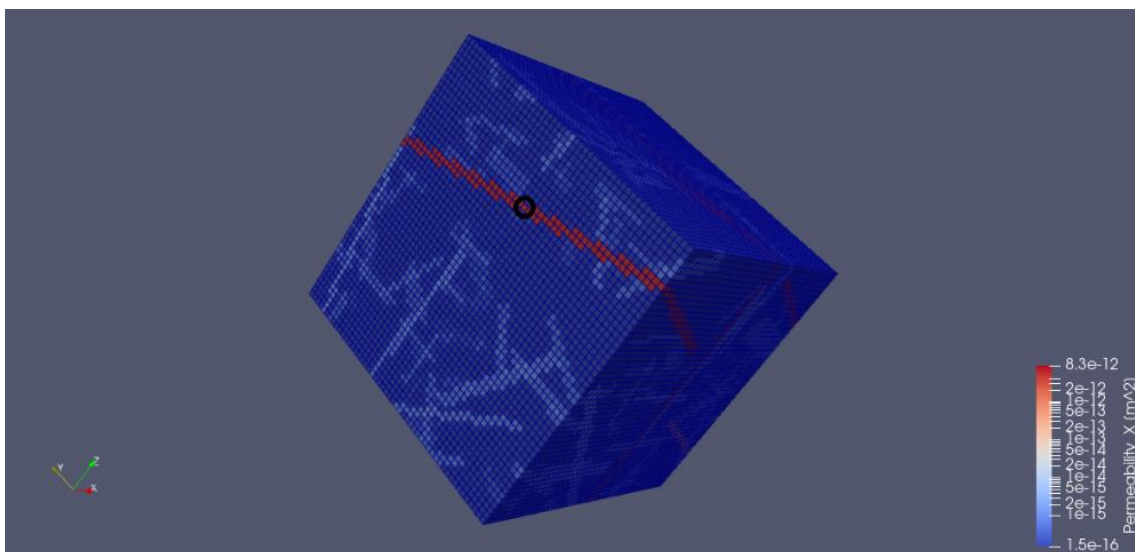
Fig. F-10. The location of the tracer point source.

The results in the form of breakthrough curves are shown in Fig. F-11. The first moment analysis results were 0.8 for the conservative, 0.74 for the decaying and 4.01 for the sorbing tracers. The first moment of the sorbing tracer reflects the retardation factor of 5 in the fractures.
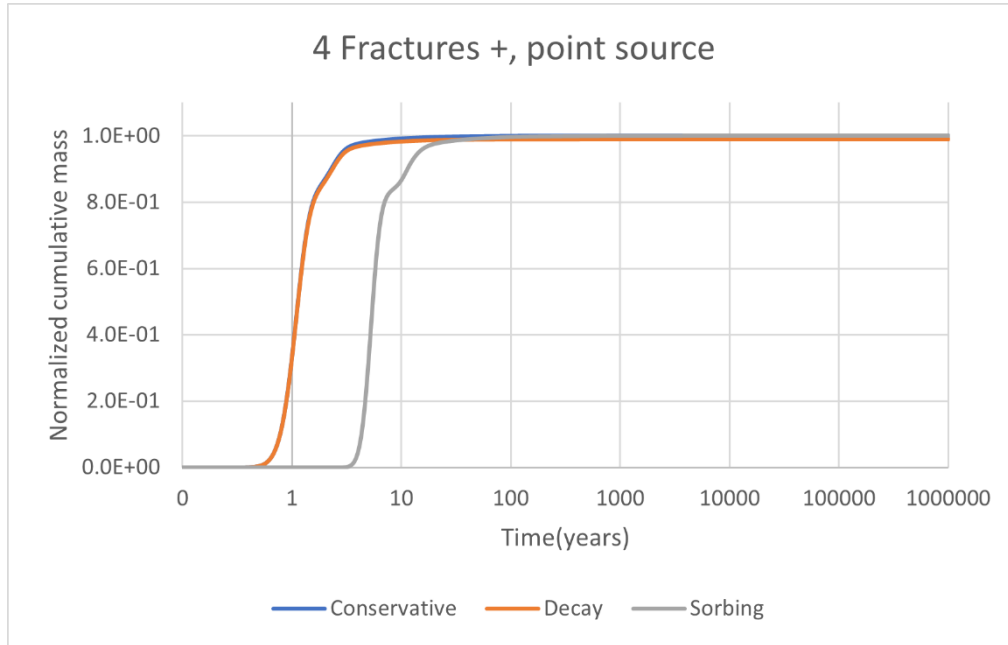
Fig. F-11. Normalized cumulative breakthrough curves of the 4-Fracture Plus Point source model.

F.4 Reference Case

F.4.1   Model domain

The model domain comprised the rock and the engineered parts of the repository. The rock was represented by the Hydraulic Conductor Domain (HCD) and the Hydraulic Rock Mass Domain (HRD). The HCD was defined by the 6 planar, deterministic fractures as set out in Table 3-3 of the Task Specification. The HRD was modelled as a stochastic fracture network divided into three depth zones in which the intensity of the open fractures and transmissivity decreased with depth. 10 independent fracture networks with the 6 deterministic fractures and stochastic fractures were generated using the pydfnworks library and upscaled into the CPM domain. None of the model parameters were changed for each of the realizations and the differences between the models were due only to the stochastic nature of the DFN parameters. The originally specified $5000 \times 2000 \times 1000$ m domain was discretized into $20 \times 30 \times 25$ m cells (the domain was 10 m wider in the Y direction than set out in the Task Specification). The background rock permeability was set at 1×10^{-18} m^2 and the background porosity value at 0.005. The background porosity

did not contribute to the calculation of the fracture porosity, and the matrix diffusion and dispersion were not considered in this reference case iteration.
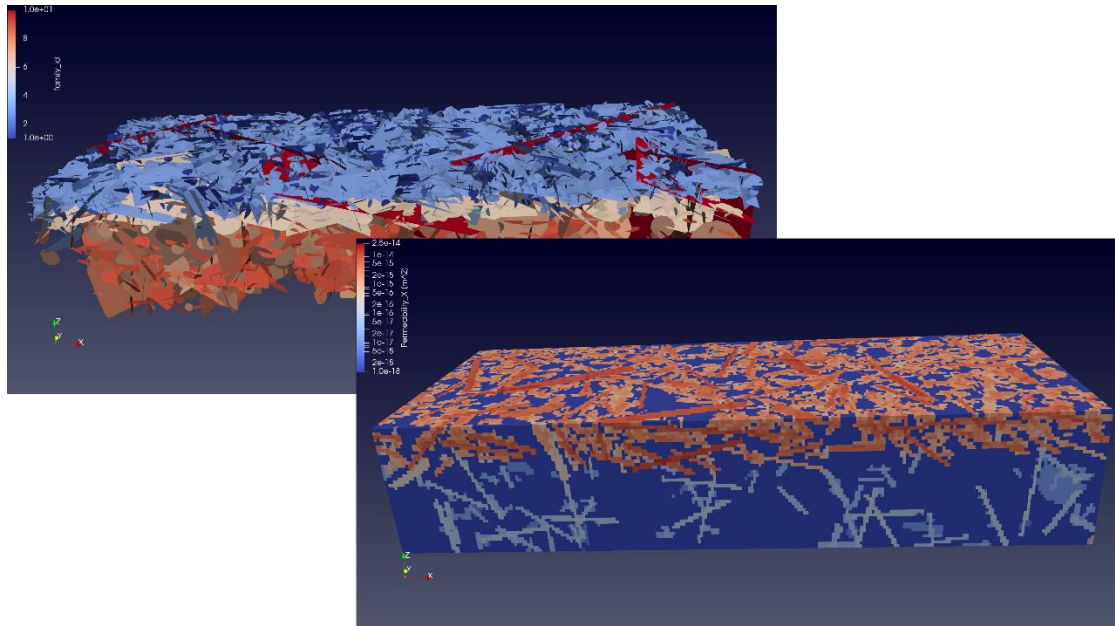

Fig. F-12. Generated fractures and the upscaled permeability field.

The repository was situated at a depth of 450 m, with the left, front corner located at the 500 m and 680 m coordinates, and comprised two central parallel access tunnels and 50 disposal drifts that branched off the tunnels, thus resulting in 1400 from east to west and 662 from north to south dimensions. The repository geometry was discretized into the original grid geometry in which each cell contained 5 waste packages (Fig. F-13). The buffer and the rock were homogenized in the same cells as the waste packages without any further grid refinement around the waste disposal holes (Fig. F-14). Homogenization was ensured via the spatial distribution of the initial source concentration and the diffusive rate as modelled by the implementation of the Reaction Sandbox DWP (see above). Concerning the near-field model and the engineered barrier system, only the buffer (as a homogenized unit) was included in the domain. The other engineered system features such as the fuel matrix, the canister shell, the access tunnels and the repository drifts were not modelled.
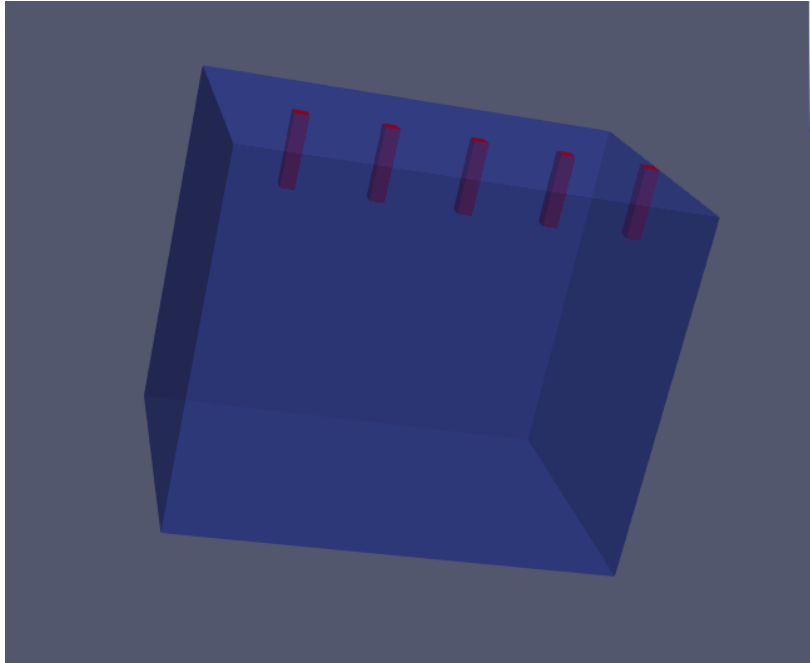
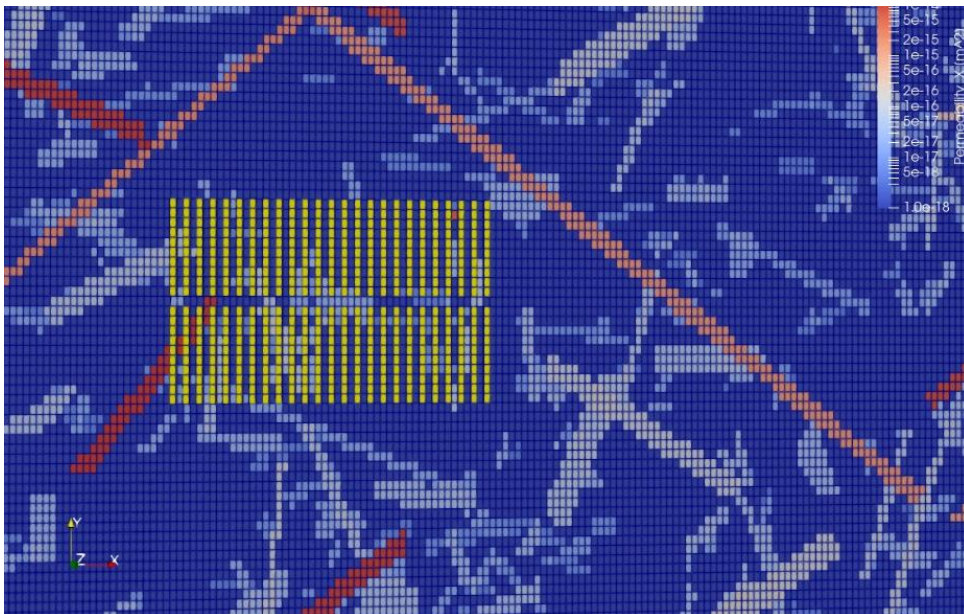**Fig. F-13. Placement of the virtual waste packages in one model cell.**

Fig. F-14. Discretization of the whole repository.

F.4.2   Flow model

The flow boundary conditions were specified as the Dirichlet hydrostatic pressure over the top of the domain. The pressure was derived internally using PFLOTRAN from the reference pressure and the elevation (the DATUM parameter). The DATUM was specified explicitly with the HDF5 file over the entirety of the top surface. The elevation of the high point area ($0 - 1700$ m) was 1200 m, the hill slope was shaped as a $10 \times \sin(r) + 1010$ curve between $1700 - 3500$ m and the low flat area between 3500

– 5000 m was set at 1000 m, all in the X direction. The elevation and pressure in the Y direction were set as constant. A reference pressure of 101 325 Pa was considered at Z = 1000 m. No other flow boundaries were set over the bottom and side domain faces. The flow field was considered as the steady state throughout the entirety of the transport simulation. The flow field was simulated with the initial flow model only, which subsequently served as input for the coupled flow-transport model.
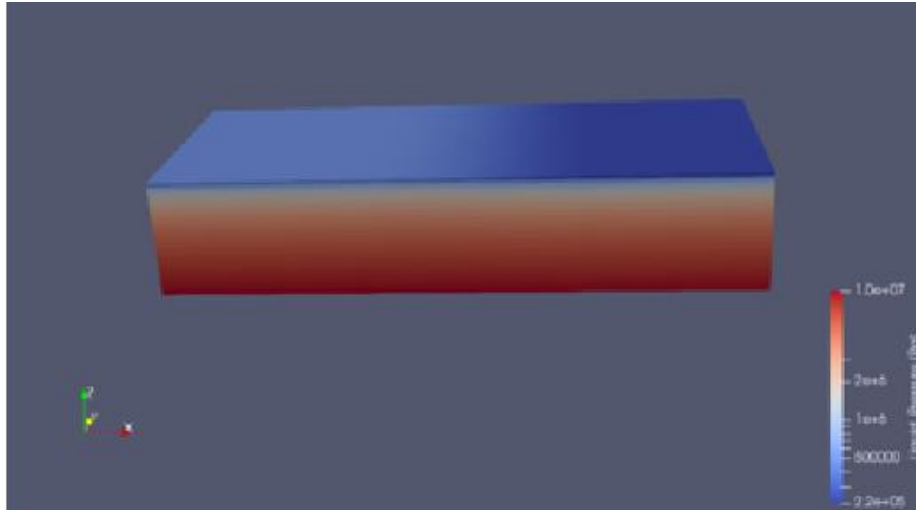

Fig. F-15. The steady state pressure field.

F.4.3   Transport Model

The conventional transport boundary condition was replaced by the DWP module as described in the Methods chapter. The tracer source and the near field model were integrated into one system. The canister shell and the backfill were not modelled. Following the implementation of the DWP module, the waste package concentration was considered to be an immobile zone and the above equation was used to simulate the release from the immobile to the mobile zone, which represented the transport in the surrounding rock. This approach was used for the instant release fraction; there was no increase in the immobile concentration due to the fractional dissolution rate. The fractional dissolution rate was simulated via the introduction of a new reactive mineral to the Reaction Sandbox module, which contributed to the immobile concentration via its volume fraction multiplied by the kinetic rate specified by the user. Moreover, the kinetic state update was implemented so as to update the mass of the remaining fuel matrix. Each of the DWP module inputs was specified by the HDF5 file generated by the modified mapdfn.py script, thus rendering it possible to spatially distribute the near field and the source term parameters.

The initial immobile concentration in one cell was set at 1.41×10^{-6} g/m^3 for Tracer 1, which was considered to have been released instantly; its initial value in the source

decreased only via its release into the rock. The release process was modelled applying the diffusion rate implemented in the DWP module. The diffusion rate in each cell with the waste packages was 9.3×10^{-12}. Tracer 2 simulated the inventory fraction, which was modelled via two release mechanisms: 1) the release from the initial concentration as scaled by the virtual mineral (the waste matrix) into the immobile phase (the waste package) and 2) the release from the immobile phase into the rock. The initial concentration of Tracer 2 was set at 1.27×10^{-5} g/m^3. Tracer 2 was released into the immobile phase at a fractional rate of 10^{-7} per year throughout the whole of the simulation, which was run up to 100,000 years. The diffusion rate at which Tracer 2 was released from the immobile phase into the rock was the same as that of Tracer 1.

F.4.4   Results

The steady state water flows for the high point area, the hillslope and the low point are shown in Fig. F-16. The most significant variations between the model realizations of the steady state water flow across the three surface regions can be observed in the hillslope region. The variations are related to the changes from the recharge area of the model (the high point region) to the discharge region (the low point region). Both regimes refer to the hillslope region and, depending on each of the fracture model realizations and the positions of the fractures crossing the hillslope, either inflow or outflow from the model prevail in this region.
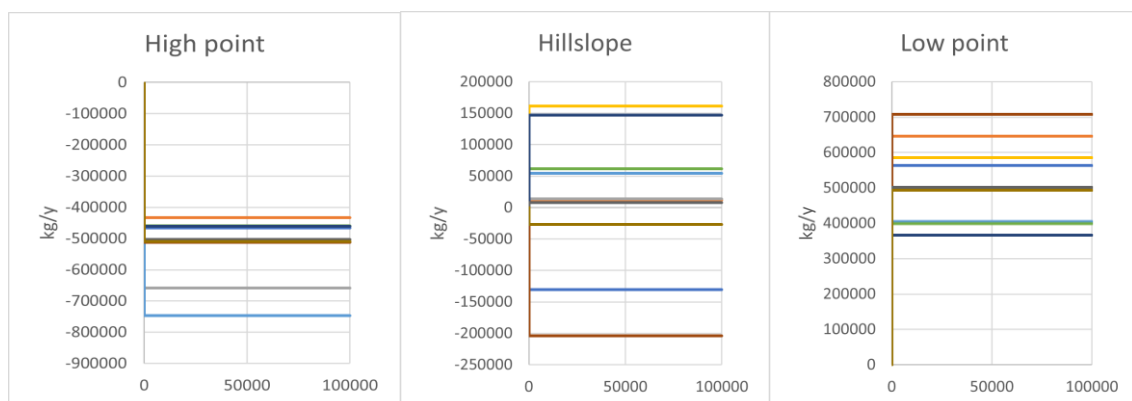

Fig. F-16. Steady state fluxes across highpoint, hillslope, and low point surface regions.

Only the Tracer 1 and Tracer 2 transport were modelled in the SÚRAO transport simulations. The two simulated tracers represent the instantly released mass and the mass released via a fractional dissolution rate of 1×10^{-7} per year. Most of the metrics from the Task Specification were processed for both tracers as output metrics for model comparison purposes:

- Tracer hill slope cumulative mass flow(Fig. F-17).

- Tracer hill slope mass flow (Fig. F-18).
- Tracer low point cumulative mass flow (Fig. F-19).
- Tracer low point mass flow (Fig. F-20).
- Tracer maximum mass flow across the hillslope (Fig. F-22).
- Tracer maximum cumulative mass flow across the hillslope (Fig. F-23).
- Tracer maximum mass flow across the low point (Fig. F-24).
- Tracer maximum cumulative mass flow across the low point (Fig. F-25).
- Tracer concentration at the 3500, 831, 1000 coordinates (Fig. F-26)
- Tracer concentration at the 4337, 609, 1000 coordinates (Fig. F-27)
- Tracer inventory remaining in the repository (Fig. F-28).

The propagation of the tracers through the domain after 100 000 years is shown in Fig. F-30, Fig. F-31 and Fig. F-32.
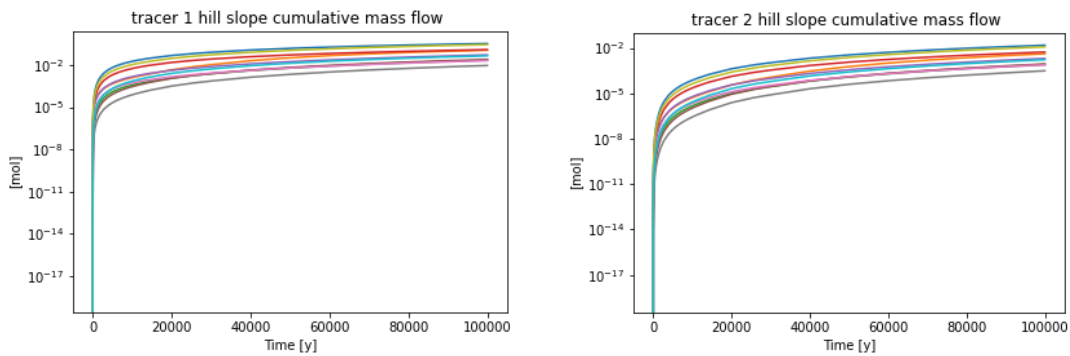
Fig. F-17. Tracer 1 and Tracer 2 hillslope cumulative mass flows.
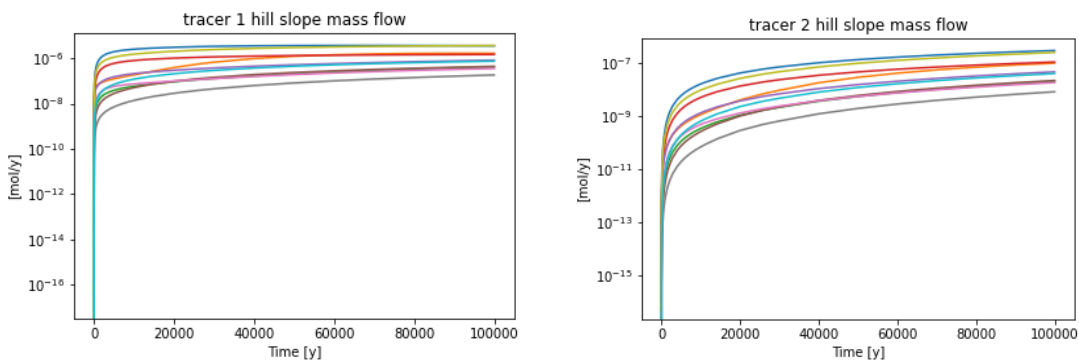
Fig. F-18. Tracer 1 and Tracer 2 hillslope mass flows.
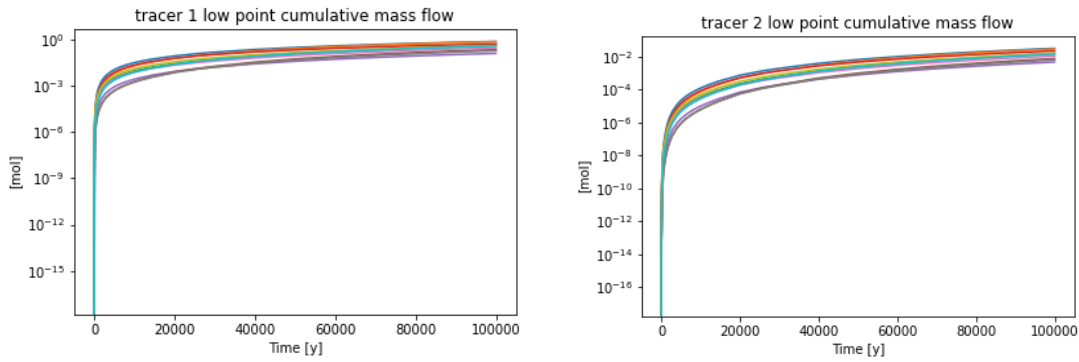
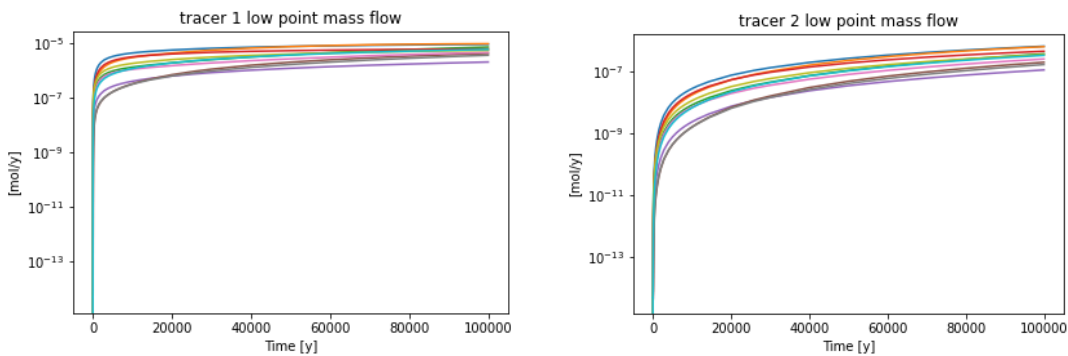**Fig. F-19. Tracer 1 and Tracer 2 low point area cumulative mass flows.**

Fig. F-20. Tracer 1 and Tracer 2 low point area mass flows.

The maximum mass flow results for both tracers are shown in Fig. F-22 - Fig. F-25. All the maximum concentration points on the hillslope were located at the bottom of the hillslope, where the hillslope water discharge rate is highest. The low point area maximum mass flow points are clustered around the 4472, 639, 1000 coordinates (Fig. F-21). Due to the differences between the discretization schemes considered by the teams, the maximum mass fluxes were normalized to the specific flux by dividing the calculated flux by the top face cell area of 600 m^2.
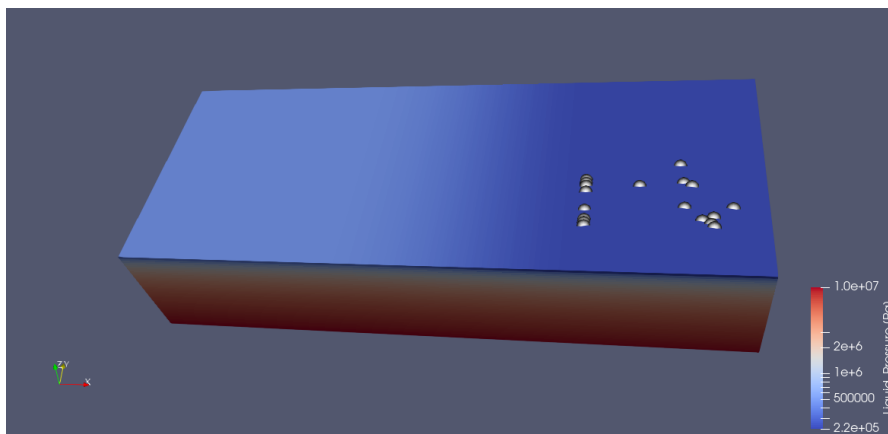
Fig. F-21. Location of the maximum mass flow points for the hillslope and the low point area.
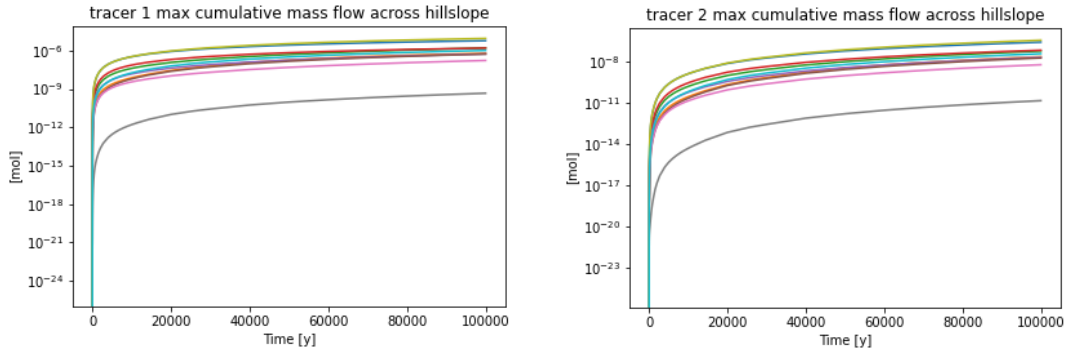
Fig. F-22. Tracer 1 and Tracer 2 maximum cumulative mass flows across the hillslope.
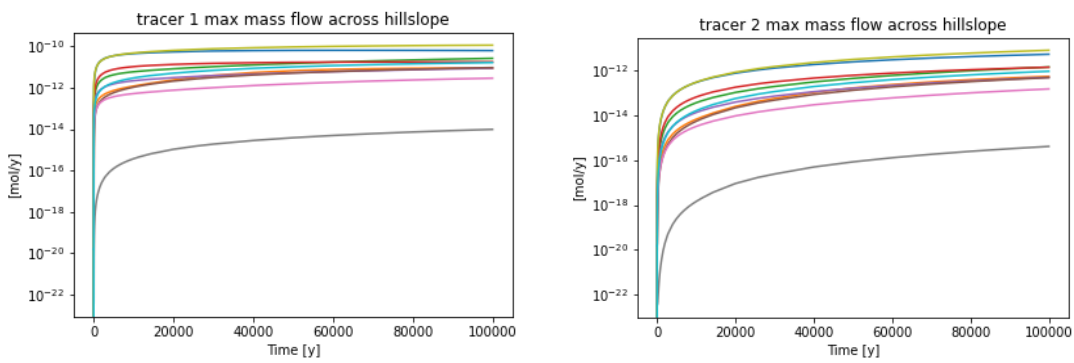

Fig. F-23. Tracer 1 and Tracer 2 maximum mass flows across the hillslope.
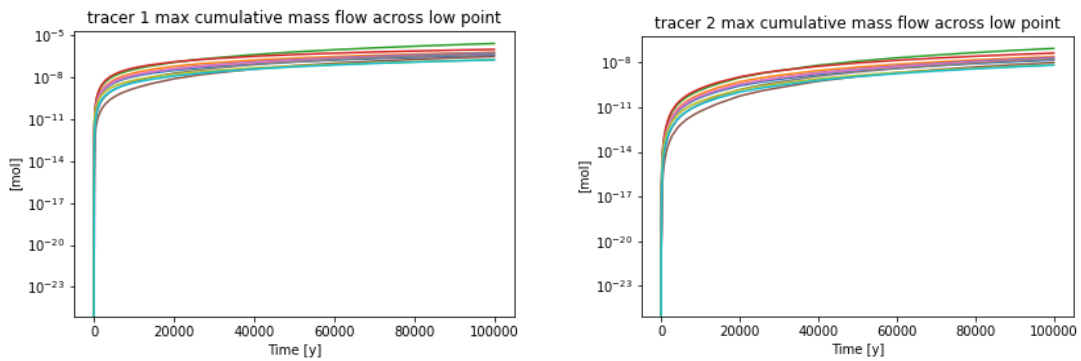

Fig. F-24. Tracer 1 and Tracer 2 maximum cumulative mass flows across the low point area.
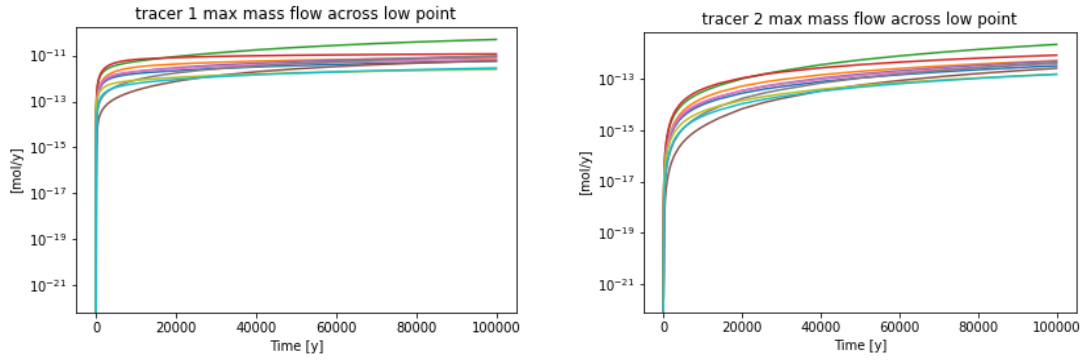
Fig. F-25. Tracer 1 and Tracer 2 maximum mass flows across the low point area.
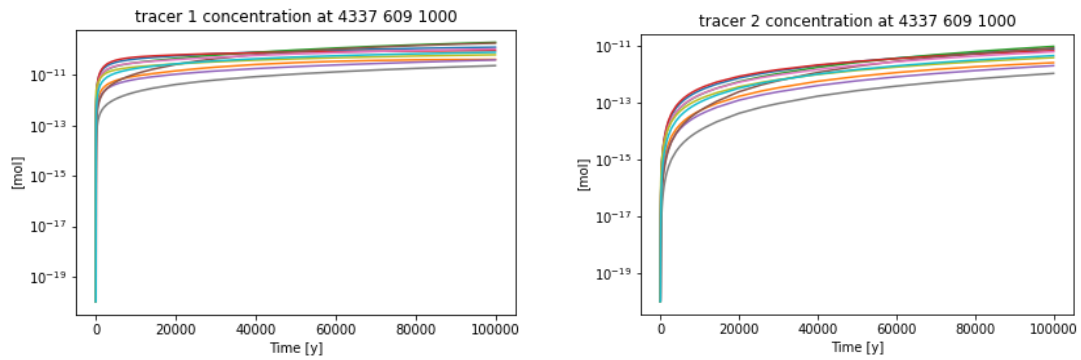

Fig. F-26. Tracer 1 and Tracer 2 mass flows at the 4337, 609, 1000 coordinates.
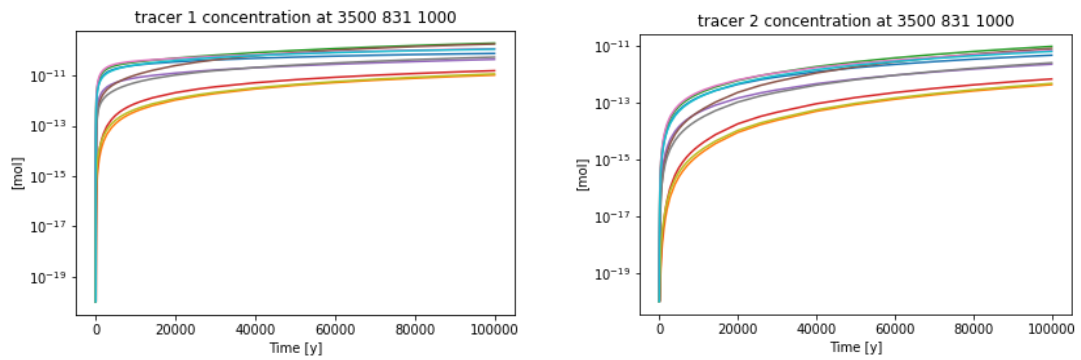

Fig. F-27. Tracer 1 and Tracer 2 mass flows at the 3500, 831, 1000 coordinates.

The mass remaining in the repository concerning Tracer 1 was interpreted as the immobile phase. In the case of Tracer 2, the remaining mass was calculated as a non-dissolved waste matrix that was added to the immobile phase. The immobile phase increased by the fractional dissolution rate of Tracer 2 and decreased via its release into the rock. Note that the results presented do not include the mass dispersed in the surrounding rock, which is also considered to be a part of the repository in the Task Specification.
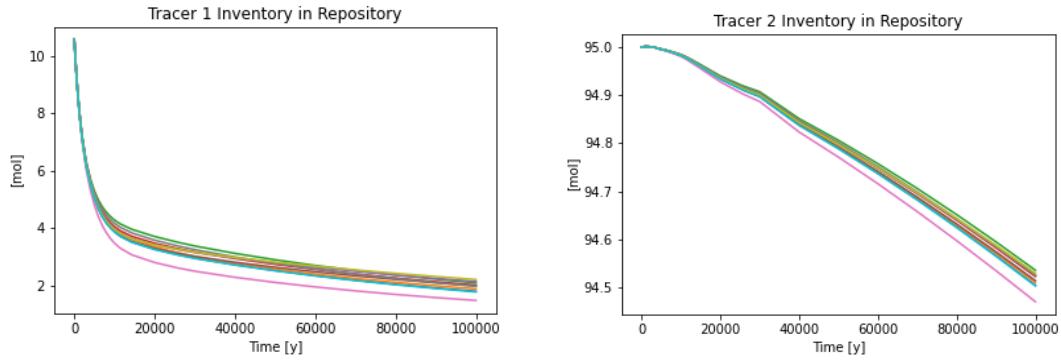
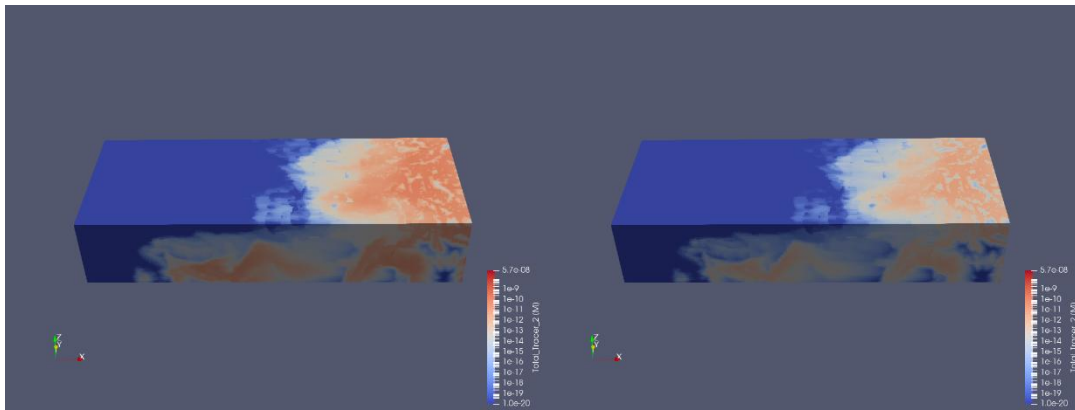**Fig. F-28. Tracer 1 and Tracer 2 remaining in the repository.**

Fig. F-29. Tracer 1 (left) and Tracer 2 (right) at the end of the simulation (realization no. 6).
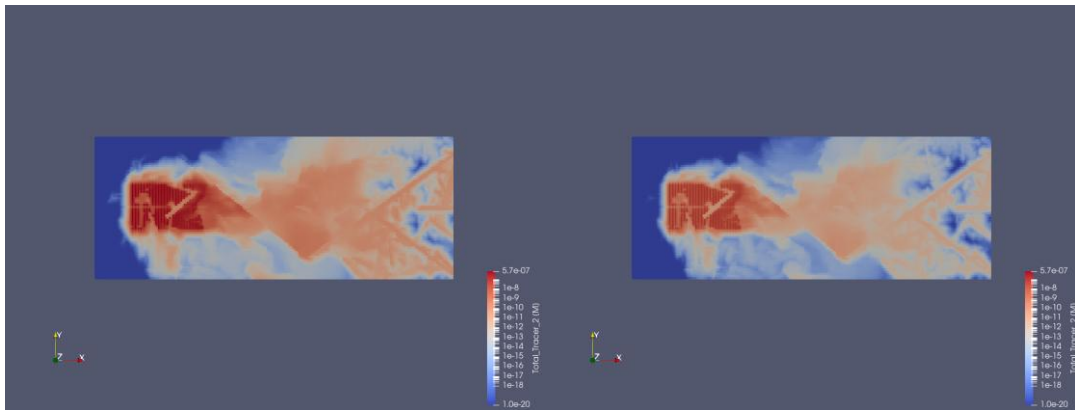

Fig. F-30. Horizontal cross-section at repository level depth for Tracer 1 (left) and Tracer 2 (right) at the end of the simulation (realization no. 6).
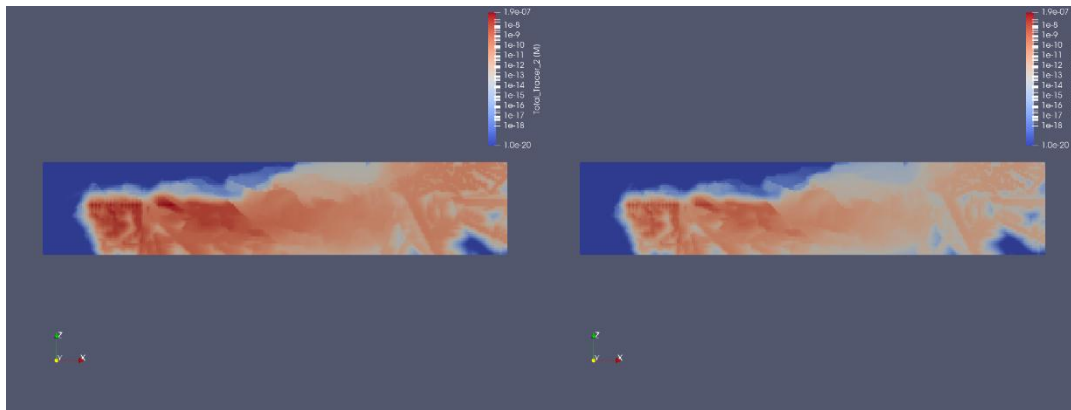
Fig. F-31. Vertical cross-section at repository level depth for Tracer 1 (left) and Tracer 2 (right) at the end of the simulation (realization no. 6).

F.4.5 Discussion

The output metric concerning which the SÚRAO results differ significantly from those of most of the other Task teams concerns the mass remaining in the repository throughout the simulation. The main source of the discrepancy results from the method according to which the repository is considered in the simulation. The source term is homogenized with the buffer and the rock, included in the repository cells and simulated as an immobile phase that diffuses into the rock according to the specified diffusive rate. The plotted remaining mass in the SÚRAO model accounts only for the mass in the immobile zone, which, in fact, represents the tracer released into the waste package from the waste matrix. However, most of the other teams adopted a different approach, which considered the repository as a hexahedral block that includes both the engineered barrier system and the surrounding rock.

Since the immobile phase was modelled applying the custom Reaction Sandbox module, and the default PFLOTRAN total mass output did not take into account the immobile phase specified by this module, adopting the second approach applied in the SÚRAO model was possible via the summation of the immobile phase with the concentration released into the rock. The concentration in the rock was calculated by subtracting the tracer diffusion rate mass, used as a scaling parameter for the spatial distribution of the waste packages and the bentonite buffer, from the total mass of the tracer (Fig. F-32). The subtraction of the scaling minerals from the total mass approach had not been tested and verified against the analytical solution by the date of the writing of the report; hence, it is currently considered to be experimental only.
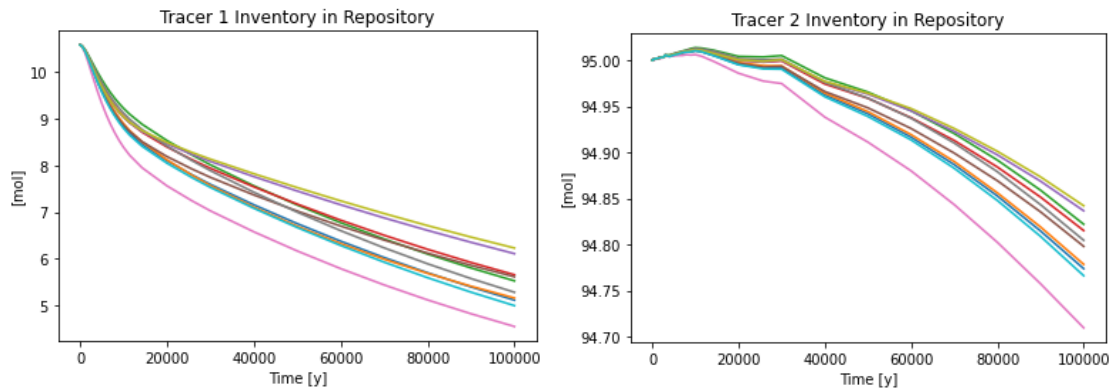
Fig. F-32. The mass remaining in the repository including the surrounding rock.

F.5 References

Březina, J. 2023. Decodfn. Computer Software.
  https://github.com/GeoMop/Decovalex2023/tree/master/decodfn.

Hammond, G. E. 2022. The PFLOTRAN Reaction Sandbox, Geosci. Model Dev., 15,
  1659–1676. https://doi.org/10.5194/gmd-15-1659-2022.

Hyman, J. D., Karra, S., Makedonska, N., Gable, C. W., Painter, S. L., Viswanathan, H. S.
  2015. dfnWorks: A discrete fracture network framework for modeling
  subsurface flow and transport, Computers & Geosciences, Volume 84, Pages
  10-19, ISSN 0098-3004. https://doi.org/10.1016/j.cageo.2015.08.001.

Stein, E., Kuhlman, K. L. 2021 Mapdfn.py. Computer Software.
  https://bitbucket.org/pflotran/mapdfn/src/master.

Lichtner, P. C., Hammond, G. E., Lu, C., Karra, S., Bisht, G., Andre, B., Mills, R., Kumar, J.
  2015. PFLOTRAN User Manual: A Massively Parallel Reactive Flow and
  Transport Model for Describing Surface and Subsurface Processes.
  https://doi.org/10.2172/1168703.

Lichtner, P.C., Hammond, G.E., Lu, C., Karra, S., Bisht, G., Andre, B., Mills, R.T., Kumar,
  J., Frederick, J.M. 2020. PFLOTRAN user manual. [online]
  https://documentation.pflotran.org/.

Tang D. H., Frind, E. O., Sudicky, E. A. 1981. Contaminant transport in fracture porous
  media: analytical solution for a single fracture. Water Resources Research,
  17(3), 555-564. https://doi.org/10:1029/WR017i003p00555.

Appendix G. The Swedish Radiation Safety Authority (SSM) and Uppsala University (UU)

G.1 Introduction

A summary of the work done by Uppsala University financed by the Swedish Radiation Safety Authority (SSM-UU) on the DECOVALEX-2023 Task F1 project is presented here. The work has been carried out by Nicholas Izuchukwu Osuji, a PhD student at Uppsala University under the supervision of Profs. Auli Niemi, Chin-Fu Tsang and Qinghua Lei. This appendix describes the strategies used for modelling the proposed task and illustrates how the computation is implemented in the software code and tools adopted for the project.

In general, task F1 benchmarks are defined from simple to complex from 1D transport, 1D transport plus matrix diffusion, to 4 fracture transport, 4 fracture plus stochastic fracture networks, point-source case (with the same realization as 4 fracture plus stochastic fracture networks), and reference case (Laforce et al., 2022). The SSM-UU team joined the project later than other groups, in January 2022. Hence, we started working directly from the 4fracture benchmark case in order to catch up with other teams. The modelling methods and computation strategies adopted for the benchmark cases are described in the following sections.

G.2 Methods

Uppsala University-SSM team is using dfnWORKS developed at Los Alamos National Laboratory (Hyman et al., 2015) for generating discrete fracture networks and COMSOL Multiphysics (subsurface module) version 6.1 (COMSOL Multiphysics, 1998), a finite element (FE) code as our modelling tool. The fracture networks generated by dfnWORKS are imported to COMSOL v 6.1 for flow and transport computations.

For the 4-fracture, 4-fracture plus stochastic fracture networks, and the point-source cases, discrete fracture networks (DFNs) are generated for flow and transport. Initially, the problem models the advection and diffusion of a conservative tracer through the DFNs within the cubic domain. The groundwater flow is modelled using 'fracture flow' physics node in COMSOL which implements Darcy's law flow in the fractures and the tracer transport is modelled using the 'transport of diluted species in fractures' physics

node which implements the advection-dispersion equation. The continuity equation as formulated and used by the fracture flow physics node is given as:

$$\frac{\partial}{\partial t}(\rho \epsilon_p) + \nabla \cdot (\rho u) = q_m$$

where, ϵ_p is the porosity, ρ represents the fluid density (kg/m³), and q_m is a source term (kg/m³·s). Since we are considering a steady-state problem, the equation reduces to:

$$\nabla \cdot (\rho u) = q_m$$

The velocity field u is defined as:

$$u = -\frac{k}{\mu}(\nabla P)$$

where, k (m²) denotes the intrinsic permeability of porous media, μ (kg/m·s) is dynamic viscosity of the fluid, and P (Pa) is pressure in the porous media. The governing equation solved for Transport of Diluted Species in Porous Media physics in COMSOL is:

$$\frac{\partial(\epsilon_p c_i)}{\partial t} + \frac{\partial(\rho c_{P,i})}{\partial t} + u \cdot \nabla c_i = \nabla \cdot [(D)\nabla c_i] + R_i + S_i$$

where, c_i represents the concentration of species i in the liquid (mol/m³) and $c_{P,i}$ represents the amount adsorbed to solid particles. The above equation is the advection-diffusion equation featuring specie reactions R_i and sources S_i. u represents the velocity field, $D = D_{D,i} + D_{e,i}$, $D_{D,i}$ (m²/s) represents the dispersion tensor, and $D_{e,i}$ (m²/s) denotes the effective diffusion. In COMSOL, the groundwater flow is usually solved first with a stationary solver, and the Darcy's velocity field obtained is implemented on the advection term for solute transport calculation using a time-dependent solver.

In the 'fracture flow' physics node, groundwater flow is simulated as steady state flow driven by a pressure gradient along the x-axis and neglecting gravity. The four-fracture case consists of deterministic fractures whose properties are explicitly defined. For the four-fracture plus stochastic fracture networks and point-source cases, the four-fracture domain is populated by statistically generated fractures. Fig. G-1 depicts the four-fracture case and the population of the domain with statistically generated fractures to obtain the four fracture plus model.
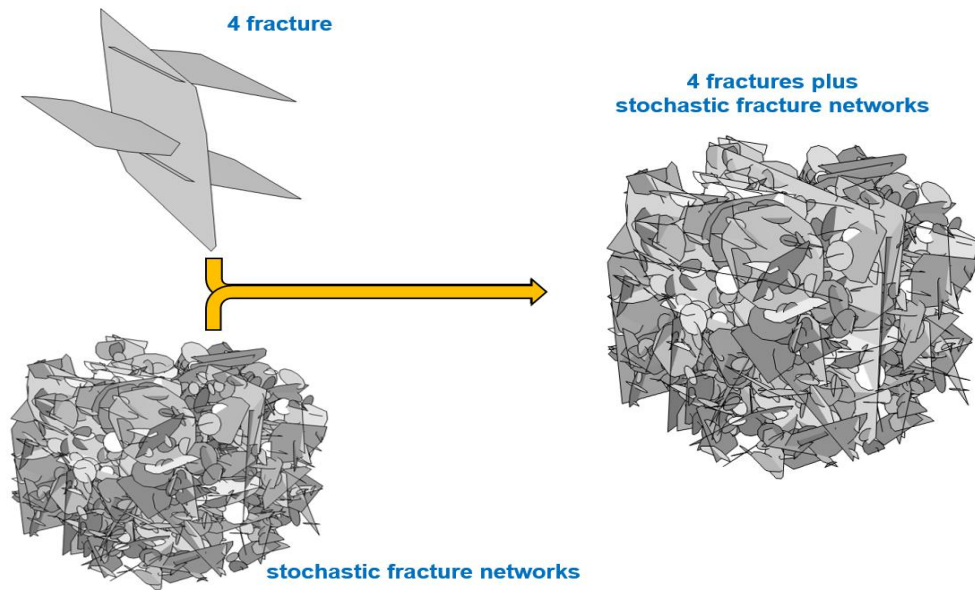
Fig. G-1. Benchmark models for 4 fracture to 4 fracture plus stochastic fracture networks.

The reference case models flow and transport in a domain of 5000m x 2000m x 1000m, and includes six deterministic fractures described as hydraulic conductor domains (HCD) and stochastically generated fracture networks described as hydraulic rock mass domains (HRD). SSM-UU explicitly defines the HCD fractures in the domain, and so far, uses equivalent porous medium approach for the statistical fracture networks (HRD). Groundwater flow is simulated as steady state flow driven by hydraulic head at the top elevation of the domain. Tracer transport is simulated as the release of two tracers with different release mechanism from the deposition holes in repository. Concise description of this case is discussed in section four.
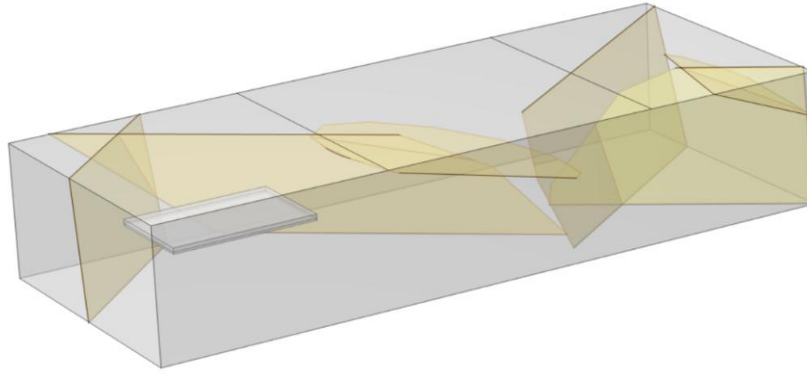
Fig. G-2. Reference case represented with six deterministic fractures and upscaled fractured rock domain.

For the four-fracture plus, point-source and reference cases, the information used to generate the stochastic fractures are provided in the Task specification report (Laforce et al., 2022). The sizes of generated fractures obey the power law size distribution:

$$f(r) = \frac{kr_0^k}{r^{k+1}}, k \geq 2, r_0 < r < \infty$$

where r is fracture radius [m], r_0 is the minimum radius [m], and k is the scaling characteristics of fractures as a function of size.

The minimum and maximum fracture radius are 30 m and 574 m, respectively, with fracture intensity (P_{32}) adjusted by:

$$P_{32}[r_{min}, r_{max}] = \frac{\pi n_0 kr_0^k}{2-k}\left(r_{max}^{2-k} - r_{min}^{2-k}\right)$$

where r_{min} is minimum fracture radius [m], r_{max} is maximum fracture radius [m], and n_0 is average number of fractures per unit volume of rock.

The fracture transmissivity which is a function of fracture size is computed using a fully-correlated power law model defined by (Follin et al., 2007):

$$\log T = \log ar^b$$

Where r is radius [m] and the coefficients a and b are dimensionless constants. Fracture aperture is calculated from the transmissivity using the cubic law (Bear et al. 1993):

$$\text{aperture} = \left(12T\frac{\mu}{\rho g}\right)^{\frac{1}{3}}$$

Where μ is viscosity of water [Pa s], ρ is density of water [kg/m³], and g is the acceleration due to gravity [m/s²].

G.3 Benchmarks

For the 4 fracture, 4 fracture plus stochastic fracture networks and point-source cases, a constant pressure boundary conditions are imposed on the inflow (1.001 MPa) and outflow (1.0 MPa) faces, with no-flow condition on all other faces (Laforce et al., 2022). Since it is assumed that flow and transport only occur in the fractures, matrix diffusion is ignored. In the 'transport of diluted species in fracture' physics node of COMSOL, an initial tracer pulse is injected uniformly for 1 day along the fracture on the west which then exits the domain through the fractures on the east face (Laforce et al., 2022). Subsequently, transport of a decaying and sorbing tracers is modelled using the same boundary and initial conditions described above under reactions and adsorption sub-nodes. The decaying tracer has a half-life of 100 years, and the sorbing tracer has a retardation coefficient of 5 in the fractures (Laforce et al., 2022). To implement sorption in COMSOL, we adopt the equation for retardation factor of solute in fractures for Freundlich Isotherm given by Suresh Kumar, (2008)

$$R = 1 + \frac{K_f * n * c_f^{n-1}}{b_f}$$

where, b_f is half aperture, K_f is the Freundlich's constant, c_f is the dissolved concentration, and n is a constant. Since we require a linear distribution coefficient, we set the constant 'n' to a value that reduces the equation to a linear form adaptable in COMSOL. To implement the decay reaction in COMSOL, we define the reaction term using this equation suitable for COMSOL.

$$R = -\delta * \frac{\ln(2)}{t_{1/2}} * c_0$$

where δ is the fracture porosity, $t_{1/2}$ is the tracer half-life, and c_0 is the initial concentration of the tracer.

G.3.1   1D Transport

We are not presenting results for this case, due to our late participation to the project.

G.3.2   1D Fracture Plus Matrix Diffusion

We are not presenting results for this case, due to our late participation to the project.

G.3.3   Four-Fracture Transport

This benchmark case features four deterministic fractures with size, orientation and locations provided in the Task specification (Laforce et al., 2022). Properties of the fractures like permeability, aperture, and transmissivity are explicitly defined. These fracture planes are discretized with unstructured triangular elements of maximum size 20m. A steady state flow is simulated by imposing a pressure boundary on the east and west faces of the domain, no flow boundary is prescribed on other faces. Then, conservative transport is simulated by introducing a one-day pulse tracer in the fracture at the west end of the domain. Fig. G-3 shows the pressure profile and conservative tracer transport at 0.75 years. Breakthrough curves for conservative, sorbing and decaying tracers are given in Fig. G-4.
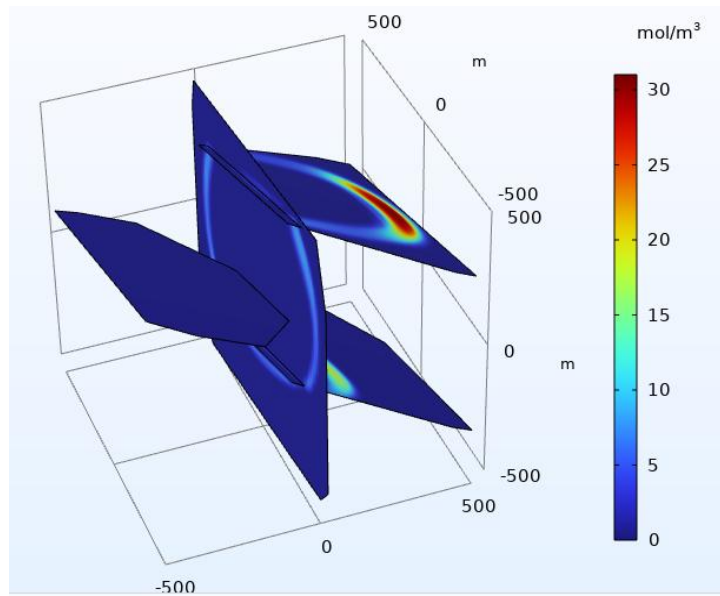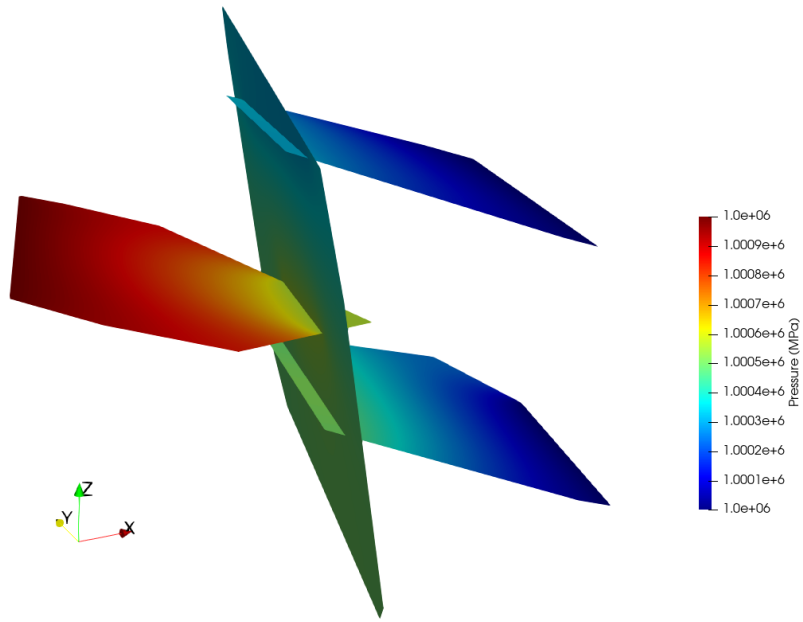
Fig. G-3. (top) Pressure profile (flow) and (bottom) tracer transport in 4 fractures at 0.75 y.
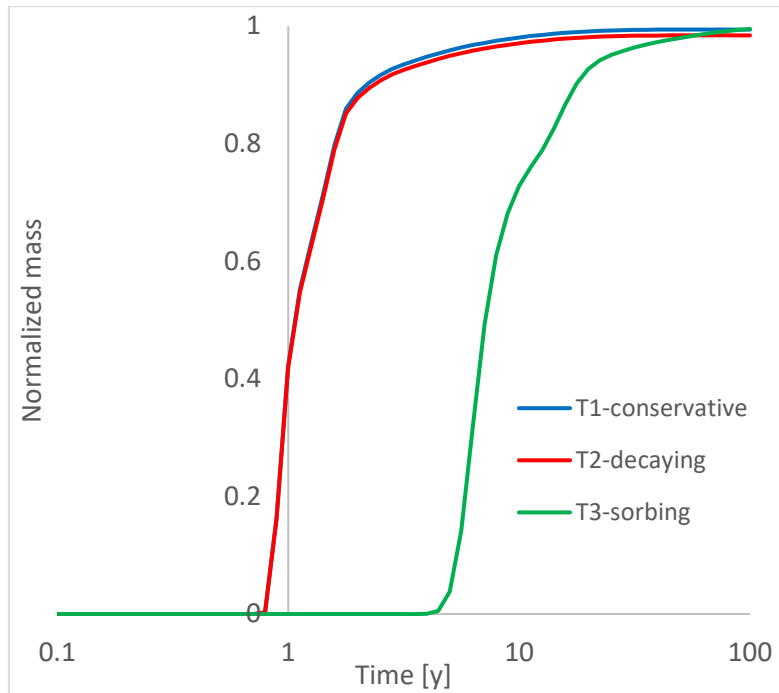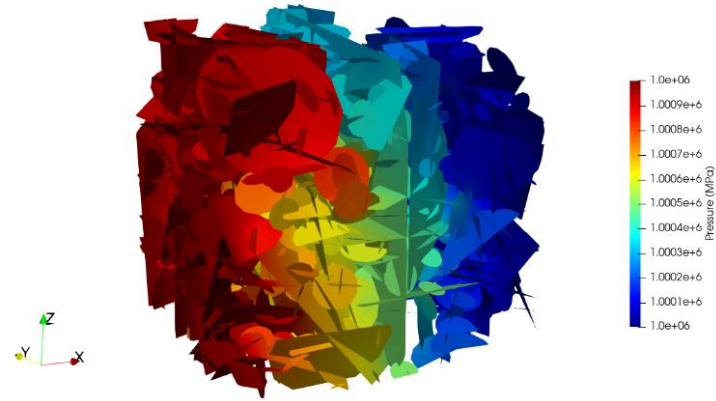
Fig. G-4. Normalized breakthrough curves for conservative, decaying and adsorbing tracers in 4 fractures.

## G.3.4   Four-Fracture Plus Stochastic Fractures

The 4-fracture plus stochastic fracture case is modelled by adding stochastic fracture networks to the 4-fracture domain as shown in Figure G-1. Stochastic fracture network realization is consistent with that provided by Sandia National Laboratories in the Task Specification (Stein et al., 2021). This problem also simulates advection and diffusion of conservative, decaying, and adsorbing tracers.

Both the deterministic and stochastic fractures are discretized with same triangular mesh of maximum and minimum element size of 20m and 5m respectively, giving a total of 329,687 elements. Then, a steady state boundary condition is imposed on the east and west ends of the domain, by defining pressure gradient that drives the flow. A conservative tracer of one day pulse is injected using a rectangular function in COMSOL through the fractures at the west end of the domain. The tracer travels through the domain to exit at east face, and the simulation runs for 1000 years. In addition, tracer transport is also simulated for a decaying and adsorbing tracer. Fig. G-5a shows the pressure profile for the steady state flow and Fig. G-5b shows the tracer transport at 0.01 years. Although tracer is injected through all the fractures at the west face of the domain, it can be seen that at 0.01 years, the major path for the tracer travel is in the deterministic fractures. Even at a later time 0.75 years as seen in Fig. G-5c, the tracer
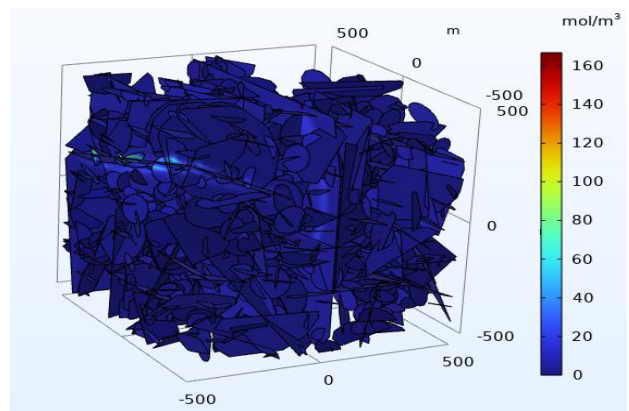
mainly migrates through the deterministic fractures. Fig. G-6 shows the breakthrough curves for conservative, decaying and adsorbing tracers.

(a)
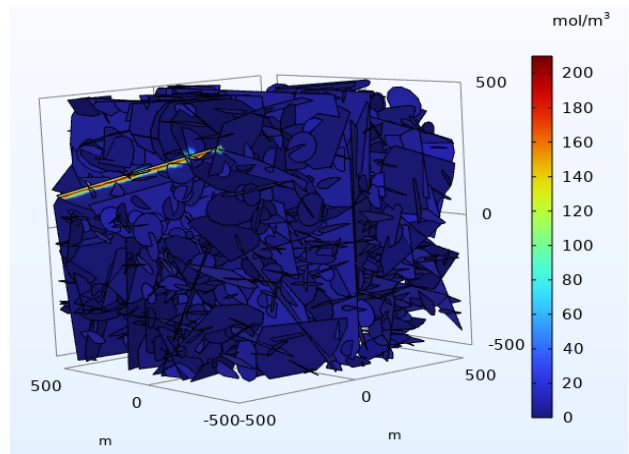
(b)

(c)

Fig. G-5. (a) Pressure profile and tracer transport at (b) 0.01 years (c) 0.75 years for 4 fracture plus case.
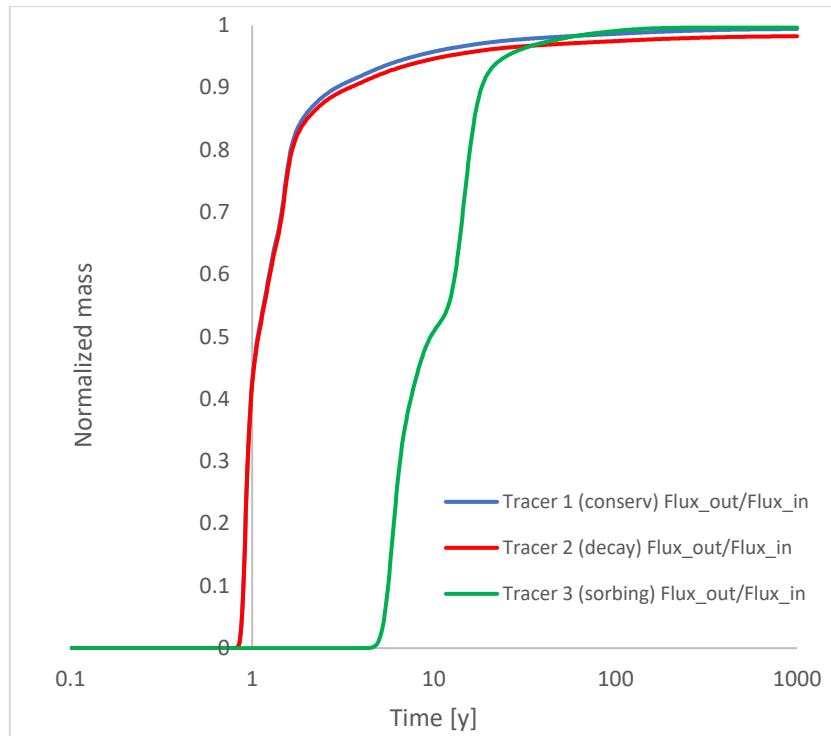
Fig. G-6. Breakthrough curves for conservative, decaying and adsorbing tracers for four fracture transport case.

From the plot in Fig. G-6, tracer 1 (conservative) initially arrives at the exit at about 0.748 years, while tracer 3 (sorbing) arrives at about 3.738 years. This gives a retardation factor of 5 as defined in the task specification. As for tracer 2, there is evidence of mass loss due to the decay reaction.

G.3.5 Continuous Point Source

The point source case uses the same DFN realization of the four fracture plus stochastic fracture networks. It simulates continuous tracer injection at a constant rate through a point located at coordinates on the west of the domain (-500,7.0, 248.25). We represent the source as a 5m line with centre at the specified coordinate. The size of the source is assumed to be the size of the cell that features the defined point. Fig. G-7 below depicts the fracture domain with the point source as indicated.
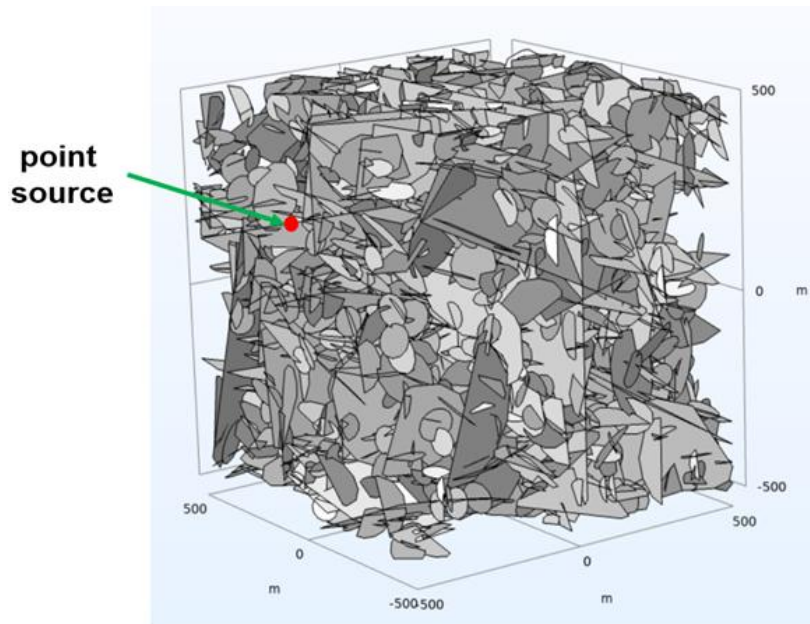
Fig. G-7. Fracture network and location of the source for point-source benchmark case.

The 4 deterministic fractures are discretized with coarse mesh of maximum element size of 50m while the stochastic fractures are discretized with finer mesh of maximum element size of 15m. Since the source size is 5m, and has an element size of 5 m, the element size is set to grow from 5m to the maximum on the deterministic fracture. In total, 439,977 elements are generated. The same flow conditions in the four fractures with stochastic fractures is imposed on the east and west boundaries. Then, a conservative tracer transport is introduced from the source through the DFNs to the exit (east face) of the domain. Further simulation is performed for the sorbing and decaying tracers, by activating the adsorption and reaction sub-nodes in COMOSL respectively. Fig. G-8 shows transport of conservative tracer from the point source at 100 years.
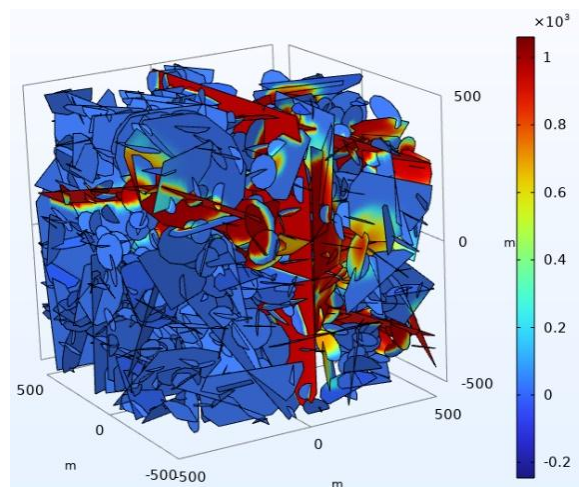

Fig. G-8. Conservative tracer transport for the point source case at 100 years.

Comparison of normalized breakthrough curves for the different cases are plotted in Fig. G-9. Mass loss is evident in the decaying tracer curve, and later arrival is observed for the adsorbing tracer due to the retardation coefficient of 5 defined in the task specification. Interestingly, it was discovered that the results are strongly dependent on mesh sizes. Detailed study was conducted on the dependence of mesh size, and the element size adopted for this computation are adequate to get reasonable results with adequate computation times.
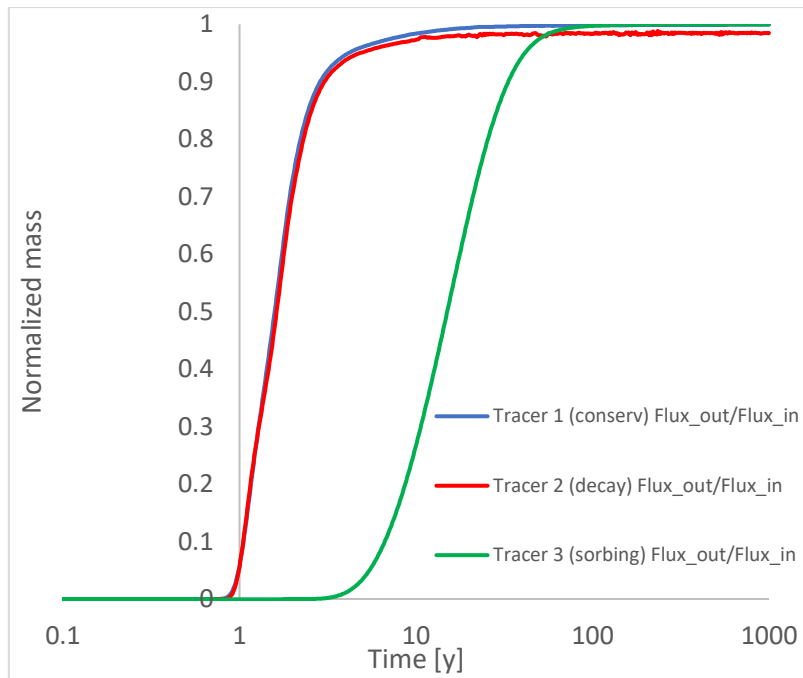
Fig. G-9. Breakthrough curves for conservative, decaying and adsorbing tracers for the point source case.

G.4 Reference Case

This section provides information on our reference case simulations and the related results. This is a preliminary effort with work continuing both to confirm these results and to study additional scenarios. The reference case domain is composed of Hydraulic Conductor Domain (HCD) which is represented by 6 deterministic fractures embedded within a fractured porous media called the hydraulic rock domain (HRD) and represented by a 3D rectangular domain. The spacing and orientations of the hydraulic conductors in HCD is obtained from observations of Brittle Fracture Zones (BFZ) at Olkiluoto site (Hartley et al., 2018), while the HRD in our model is modelled as an equivalent porous medium.

G.4.1   Model Domain

According to the task definition, the model domain covers a region of 5000m x 2000m x 1000m with six deterministic fractures (HCD) and the background rock (HRD) consisting of statistically generated fractures. In our case, we present this HRD as an equivalent porous medium. The top elevation of the domain is divided into 3 parts: hill-top, hill-slope and area of lowest elevation. The repository consists 2500 deposition holes with 50 deposition (drift) tunnels connected to the two access tunnels as defined in Task specification report (Laforce et al., 2022).

The repository volume is modelled as two rectangular boxes (tunnel box and deposition hole box) with tunnel-box superposed on deposition-holes box. Fig. G-10 below gives a schematic cross-section of this configuration. The dimensions of the tunnel box (box 1) are 1050m*660m*30m to represent the length and height of the access and drift tunnels. Also, the dimension of the deposition holes box (box 2) is 1050m*660m*15m to represent the height and distribution of the deposition holes in the repository, from which tracers are released.
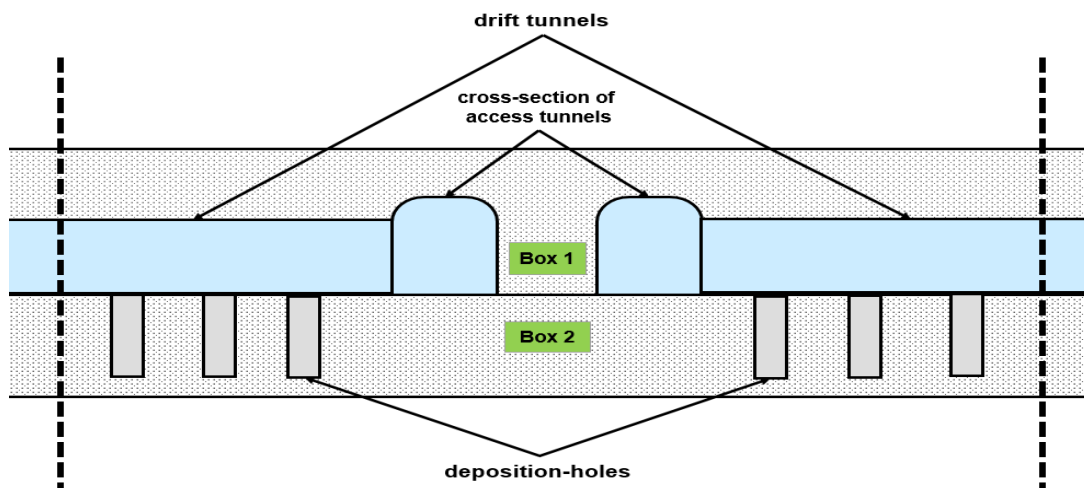

Fig. G-10. Schematic representation for the cross-section of repository boxes from the west end.

The dimensions of the tunnels and deposition holes are concurrent with the repository layout dimensions as given in section 3.4 of the Task Specification report Revision 9. These features, as imbedded to the rock mass, are schematically shown in Fig. G-11 below.
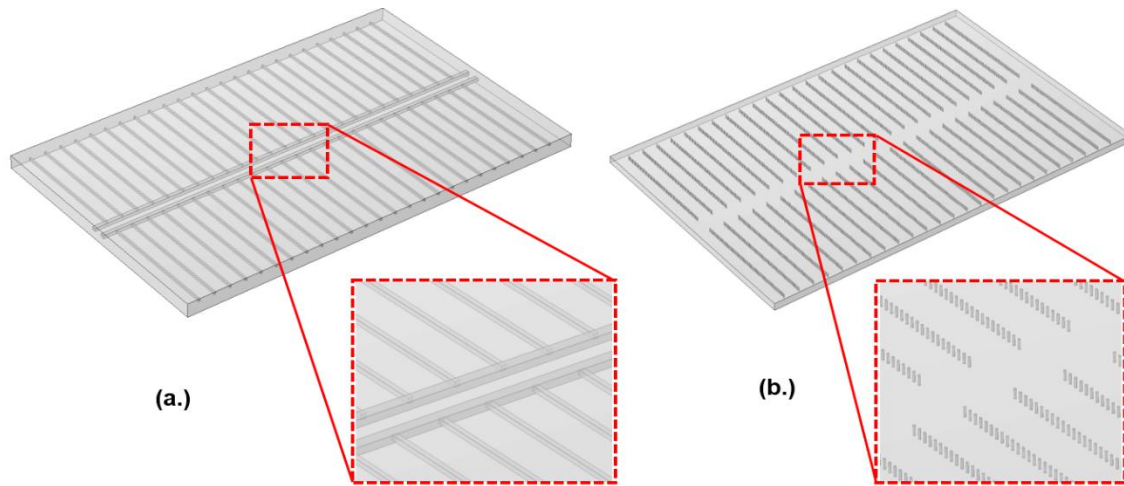
Fig. G-11. Layout configuration of (a.) tunnels and (b.) deposition-holes of the repository boxes.

The equivalent permeability of the repository boxes is obtained by a steady state flow simulation of groundwater flow across the boxes with pressure gradient imposed across two opposite faces, and no flow boundary on the other four faces. For this, the deposition holes are assigned the hydraulic properties of the buffer while the tunnels are assigned properties of the backfill as specified in Table 3.1 and 3.2 respectively, in the task specification report. In addition, the surrounding rock is assigned the property of fractured rock matrix as given in Table 3.5 of task specification report. Consequently, the equivalent permeability of the boxes representing the tunnels and deposition-holes becomes $9.79e-19m^2$ and $9.95e-19m^2$, respectively. In other words, both values are very close to the permeability of the background rock matrix, which is $1.0\ e-18\ m^2$.

G.4.2   Hydraulic Conductor Domain (HCD) and Hydraulic Rock Domain (HRD)

The Hydraulic Conductor Domain (HCD), which are the deterministic fractures and the Hydraulic Rock Domain (HRD), the stochastically distributed fractures, are the main pathways for flow and transport. In our study, the HCD is explicitly represented by 6 deterministic fractures with properties as assigned in the task definition report. The HRD in turn is represented as equivalent porous medium. The latter is assigned an equivalent permeability of $1e-18\ m^2$ and a porosity of 0.0018, as specified in the task definition. It should be pointed out that we do not account for any decreasing trend in permeability with depth for the HRD, which will be a case for our continuing studies currently underway. Fig. G-12 shows the equivalent fractured porous medium as a box domain with the embedded HCD fractures, as well as the repository boxes.

The 6 deterministic fractures are discretized with triangular element of maximum size of 25m, with a total of 50,480 elements. The HRD in turn is represented by means of tetrahedral elements of maximum size of 50m. The repository boxes are also meshed with tetrahedral elements with a maximum size of 5m. In total, there are 1,894,534 tetrahedral elements in the model domain.
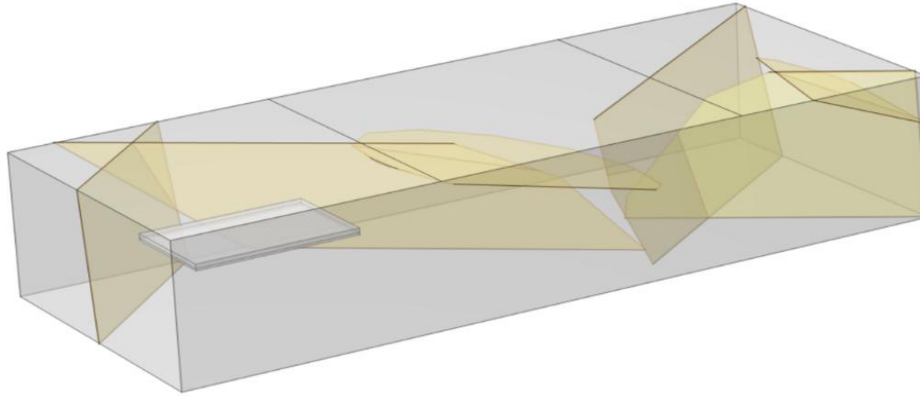

Fig. G-12. Reference case model domain (5km·2km·1km) depicting deterministic fractures, equivalent fractured rock matrix, repository and deposition holes (box).

G.4.3   Flow Model

The flow and transport occur throughout the domain according to the specified boundary conditions. Steady state flow is simulated with Darcy's Law physics node in COMSOL. A no-flow boundary condition is applied to all external boundary surfaces except for the top surface of the domain. A constant hydraulic head boundary is established at the top surface of the domain, using the surface elevation provided in the Task specification which is a function of distance as given below:

- Top of hill: z = 1,020 m   when 0 m < x < 1,700 m
- Hillslope: z = 10 * sin (π/2 + π/2000 · (x − 1,700 m)) + 1,010 m   when 1,700 m < x < 3,700 m
- Lowest elevation: z = 1,000 m   when 3,700 m < x < 5,000 m

To implement the hydraulic head at the top surface of the domain as a function of distance in x-direction, a piecewise function is used in COMSOL. This is illustrated in the Fig. G-13 below.
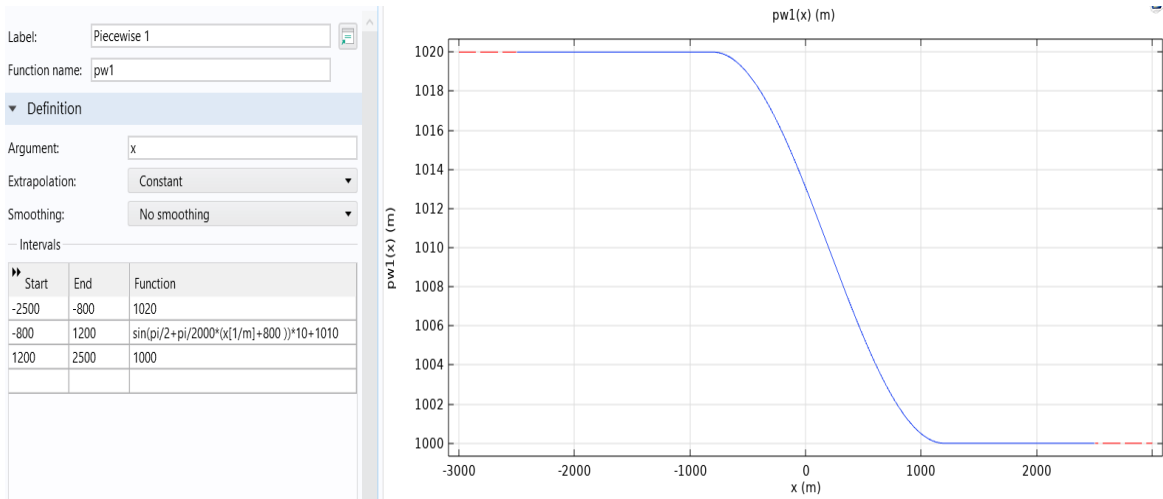
Fig. G-13. The function of hydraulic head at the top surface of domain.

Fig. G-14 shows a 3D contour plot of hydraulic pressure resulting from the imposed gradient on the top surface, and Fig. G-15 shows the streamlines of groundwater flowing from the top-hill to the lowest elevation and passing through the repository. From Fig. G-15, it is evident that most of the groundwater flow occurs through the deterministic fractures (HCD).
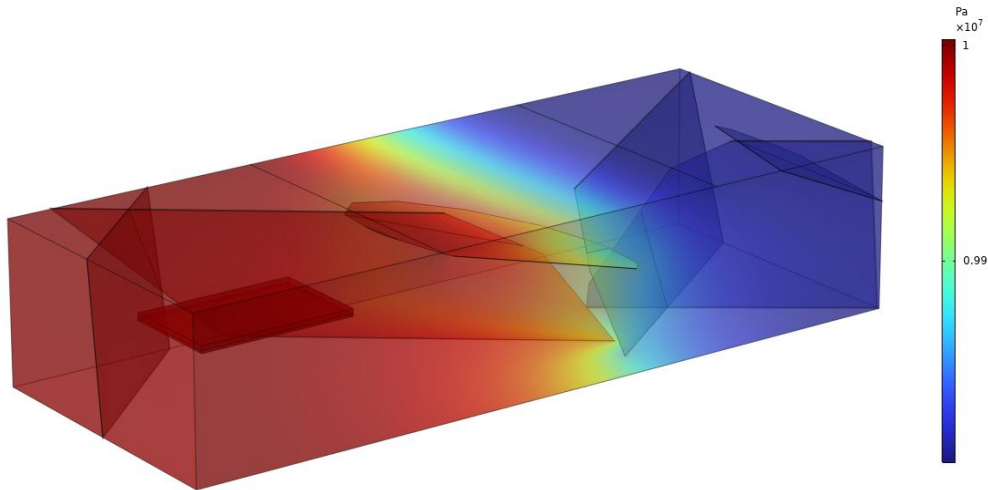
Fig. G-14. 3D contour plot of hydraulic pressure from impose gradient.

Fig. G-15. Streamlines of groundwater flow from hill-top to lowest elevation.

G.4.4   Tracer Release and Transport

The tracer transport is simulated using the time-dependent Transport of Diluted Species in Porous Media physics node of COMSOL, that implements advection-dispersion equation. Two tracers with different masses and release mechanisms are defined, and the tracers are released from the surface of the repository box representing deposition-holes. According to section 3.8 of Task Specification revision 9 (Laforce et al., 2022), the inventory of Trace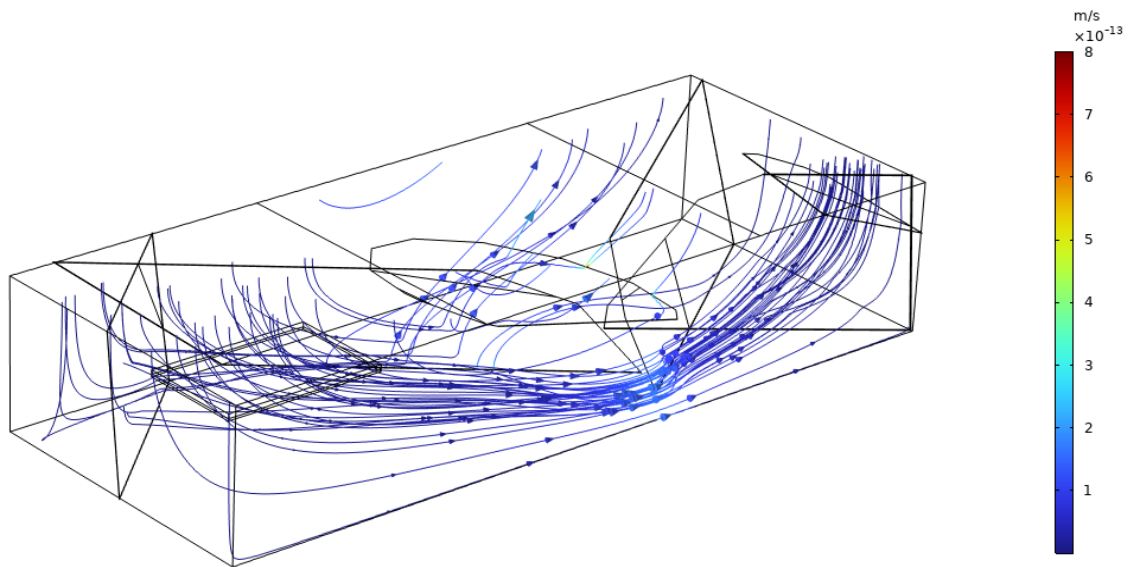r 1 is 0.545 g (0.00423 moles), or 10% of the total, which is instantly released at the start of the transport simulation. The inventory of Tracer 2 is 4.90 g (0.38 moles), or 90% of the total, which is released at a fractional rate of 10^{-7}/year throughout the transport during of 10^5 years. This is implemented in COMSOL as follows.

Tracer 1, which is considered to be released as an instant release, is assumed to be all released within 1 year. The release is distributed by means of a rectangular pulse (COMSOL feature) with a release rate given for Tracer 1 per unit area [mol/(m²s)] and at time t is expressed as follows:

$$T_1 = \frac{0.545 \text{ g}}{128.9 \text{ g/mol}} * \frac{1}{A_n t_R} * \text{rect1(t}/t_R)$$

where, A_n is the surface area of the canister [m2] and t_R is the duration of the release (1 yr).

Tracer 2 is released with constant fractional rate of 10-7/y and is expressed as

$$T_2 = \frac{4.9 \text{ g}}{128.9 \text{ g/mol}} * \frac{1}{A_n} * 10^{-7}/year$$

Since we do not account for the waste package cannisters and buffer sorption, the tracers are released directly from the surface of the box representing the deposition holes with area averaged to the area of all the 2500 deposition holes.

The tracer transport is simulated by implementing the segregated solver attribute of COMSOL which makes it possible to split the solution process into sub-steps. Each sub-step uses a damped version of Newton's method and are solved sequentially within a single iteration, and thus less memory is required. The segregated attribute approach minimizes convergence problems encountered with the fully coupled solver, but does not resolve the mass balance problem. To resolve the mass balance convergence problem, the maximum mesh size and time step should be decreased to get a Peclet number less than 1. However, this approach is computationally expensive, and prompts us to adopt an alternative approach by introducing an isotropic diffusion parameter.

The isotropic diffusion parameter is an inconsistent stabilization technique in COMSOL used to add a certain amount of diffusion (d_{art}) to the physical diffusion coefficient, d. This gives an overall diffusion coefficient of $D = d + d_{art}$. It is referred to as inconsistent, because it adds a certain amount of diffusion independently of how close the numerical solution is to the exact solution.

$$d_{art} = \delta \cdot h \cdot \|\beta\|$$

The parameter δ whose value ranges from 0 to 1 is a tuning parameter, by which the amount of artificial diffusion can be adjusted, h is the mesh element size [m], and β is the convective velocity vector. It has been proven that numerical instabilities occur when element Peclet number exceeds 1. Therefore, the implementation of isotropic diffusion approach reduces the Peclet number to a value below 1 with certain degree of coarse element size.

$$Pe = \frac{h\|\beta\|}{2(d + d_{art})}$$

Hence, the general advection-diffusion transport equation becomes

$$\frac{\partial(\epsilon_p c_i)}{\partial t} + \beta \cdot \nabla c_i = \nabla \cdot [(D)\nabla c_i] + S$$

In our study, a sensitivity analysis was performed to determine the effect of isotropic diffusion coefficient on the overall calculation result and the achieved mass balance by varying the δ value. It was observed that changing the tuning parameter δ greatly affects the mass flux and resulting mass balance in the domain.

G.4.5   Results

In this study, transport of tracers 1 and 2 are solved independently by activating two distinct transport nodes in COMSOL. This implies that the inconsistent stabilization techniques for the tracers are independent of one. To achieve the mass balance of the tracers, tuning parameter values of 0.0098 and 0.0053 are used for tracers 1 and tracer 2 respectively. Tab. G-1 below gives the amount of tracer released and tracer in the domain at 100,000 years. Here, the domain includes all features excluding the tracer source. That is: fractures, box 1 representing tunnels and surrounding rock, and the equivalent fractured porous rock including the top surfaces (hilltop, hillslope, and low elevation).

Tab. G-1. Amount of tracers for different tuning parameters.

Tracers	Tuning parameter δ	Total mass released from the repository box [mols]	Total mass in the fractured porous domain plus mass output at 10^5 years [mols]
Tracer 1	0.0098	10.0008	9.99E-01
Tracer 2	0.0053	9.5E-01	9.42E-01

In Tab. G-2, we show the average mass flux and the cumulative mass for tracer 1 and tracer 2 at hillslope and low elevation. To obtain the average mass-flux of the specified surfaces (hillslope and lowest-elevation), mass-flux is integrated across the specified surfaces of the domain.

The plot shown in Fig. G-16(a.) gives the mass fluxes of tracers 1 at hillslope (blue) and low elevation (red) while Fig. G-16(b.) gives flux of tracer 2 at the hillslope (dashed-blue) and the low elevation (dashed-red) of the top surface of the domain. In addition, Fig. G-16(c.) compares the mass-flux of Tracer 1 and Tracer 2 at hillslope and low elevation with the vertical axis in log scale.

Tab. G-2. Mass-flux per year from the hillslope and lowest elevation surfaces of the domain.

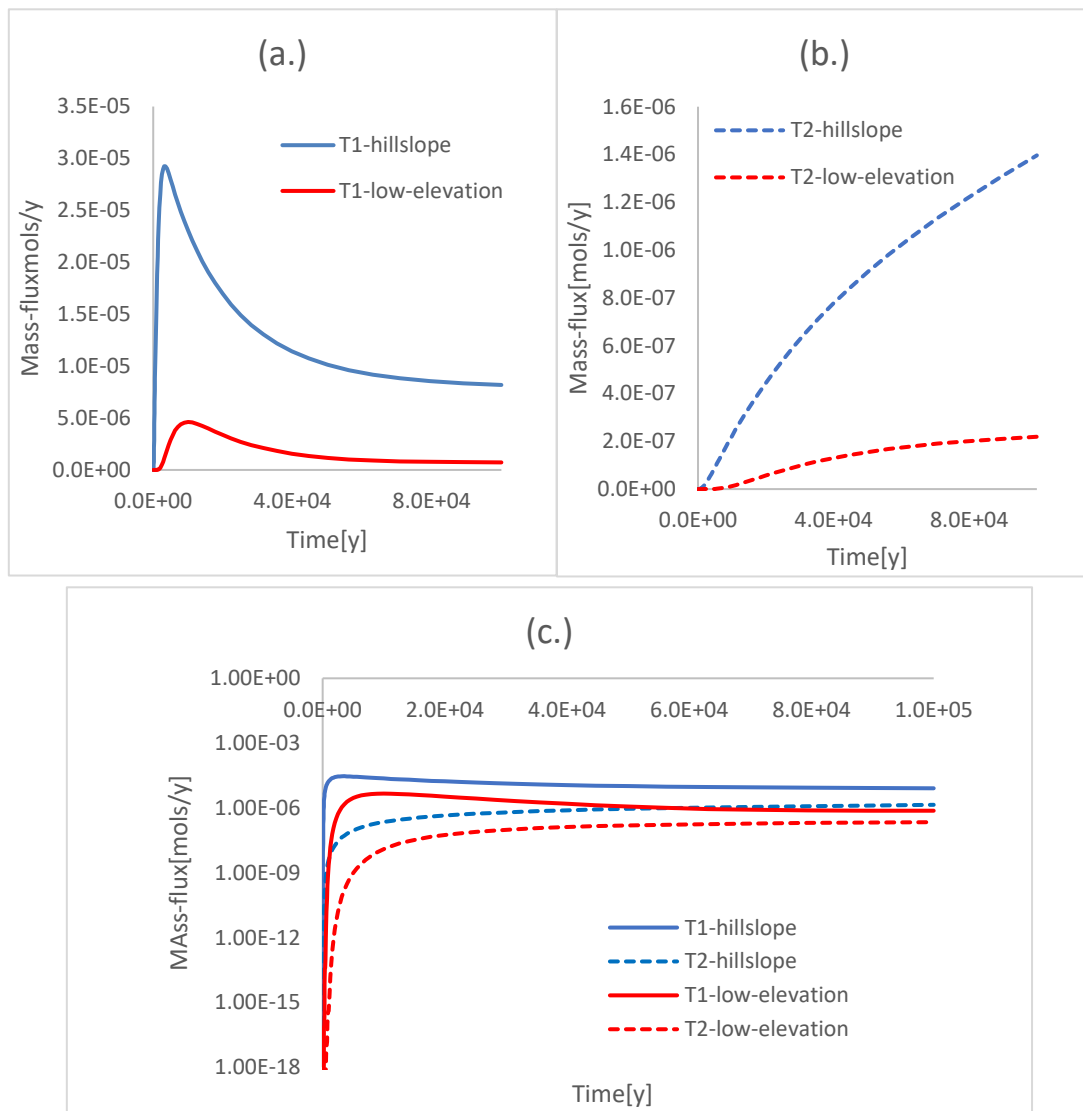|	Average mass-flux [mol/year]	Cumulative mass at 10^5 years [moles]
T1 -Hillslope	3.52E-06	1.24E+00
T1-Low Elevation	3.15E-07	1.62E-01
T2-Hillslope	6.17E-08	8.62E-02
T2-Low Elevation	8.79E-09	1.38E-02

Fig. G-16. Mass flux of (a) tracer 1 and (b) tracer 2 at hillslope and lowest elevation of the top surface of the domain and (c) combined plot in log-log scale.

Furthermore, Fig. G-17(a.) gives the cumulative mass versus time plot of Tracers 1 at hillslope(blue) and low elevation(red) while Fig. G-17(b.) gives the cumulative mass versus time for Tracer 2 at hillslope(dashed-blue) and low elevation(dashed-red) at the top surface. And Fig. G-17(c.) compares the cumulative mass of Tracer 1 and Tracer 2 at hillslope and low elevation with vertical axis in log scale.
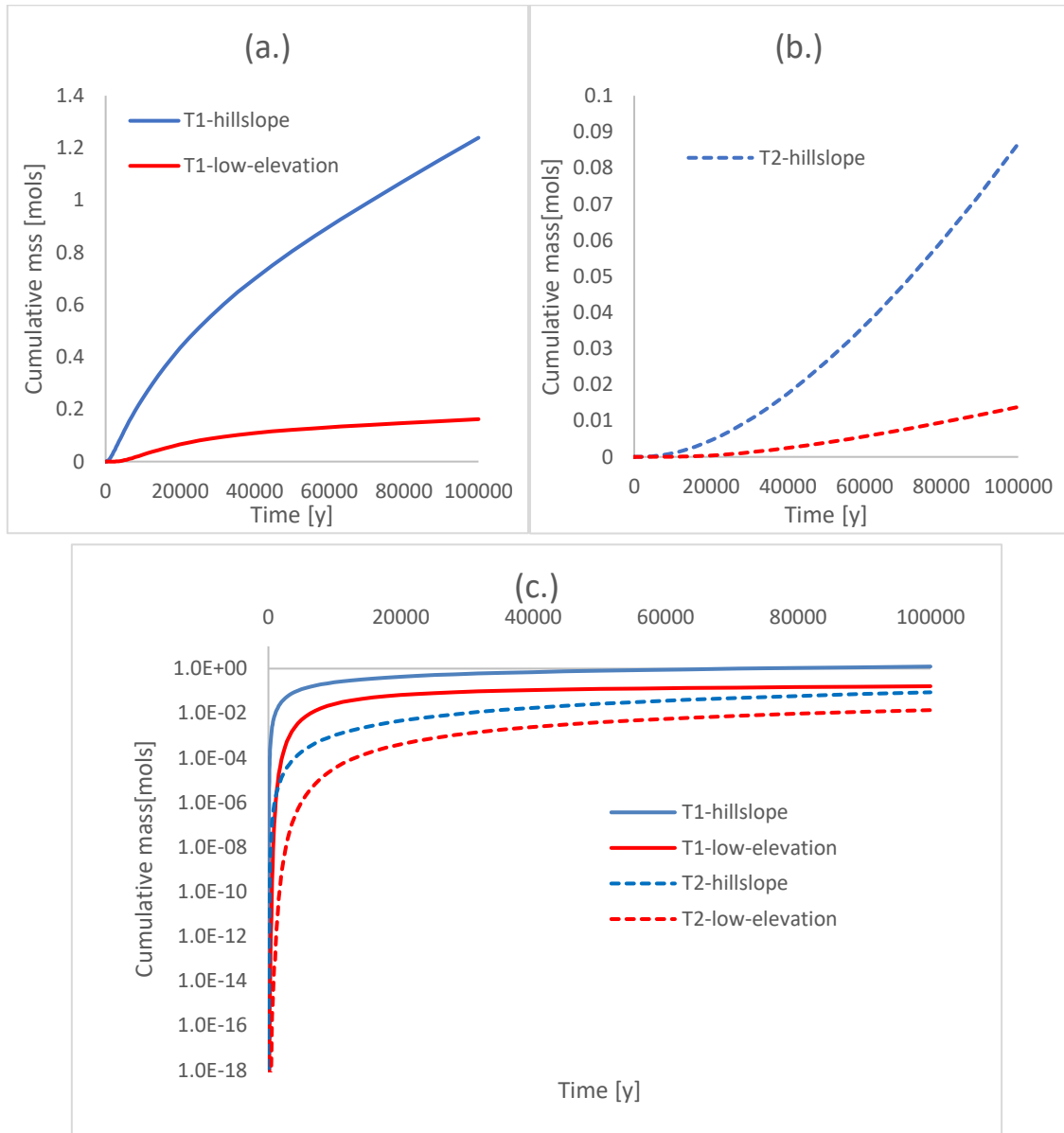

Fig. G-17. Cumulative mass of (a) tracer 1 and (b) tracer 2 at hillslope and lowest elevation of the top surface of the domain and (c) combined plot for 'a' and 'b' in log-log scale.

G.4.6   Further Sensitivity Study of Isotropic Diffusion (Tuning Parameter)

To show the influence of inconsistent stabilization introduced by isotropic diffusion, a sensitivity study is performed by varying the value of δ. Initially, tracer 1 and 2 are solved explicitly with two transport of diluted species in porous media nodes of COMSOL. This permits the use of different tuning parameters for tracer 1 and tracer 2.

Tab. G-3. Mass of tracers released for δ=0.0095.

Cases	Tracers	Tuning parameters Δ	Total mass released from the repository box [mols]	Total mass in the fractured porous domain plus mass output at 10^5 years [mols]
Case 1	Tracer 1	0.0092	10.0008	1.03E-01
	Tracer 2	0.0035	9.5E-01	1.07E+00
Case 2	Tracer 1	0.0095	10.0008	1.01E+01
	Tracer 2	0.004	9.5E-01	1.04E+00
Case 3	Tracer 1	0.0097	10.0008	9.89E+00
	Tracer 2	0.0043	9.5E-01	1.02E+00

Comparing the results in the last column for the three cases, it is evident that as the value of the tuning parameters increases, the mass in the domain decreases. Hence, it converges to the expected mass released.

We extended this study by including both tracer 1 and 2 under the same transport node and assigning one tuning parameter of 0.0095. Tab. G-4 gives the result of the mass released and mass in the domain.

It can be noticed that this approach gives the most accurate mass balance for Tracer 1, while tracer 2 shows an error of about 30%. This mass balance is not good enough, thus further investigating is being explored for case of one transport node and corresponding tuning parameter. The mass flux and cumulative mass of this case is also explored in Tab. G-5 to see how it compares with those in Tab. G-2. The results for the average mass

flux and cumulative mass for Tracers 1 and 2 at the hillslope and lowest elevation surfaces of the domain are listed.

Tab. G-4. Mass of tracers released for δ=0.0095.

Tracers	Total mass released from the repository box [mols]	Total mass in the fractured porous domain plus mass output at 10^5 years [mols]
Tracer 1	10.0008	9.89E-01
Tracer 2	9.5E-01	6.62E-01

Tab. G-5. Preliminary result of Tracer 1 and 2 Mass-flux per year from the hillslope and lowest elevation surfaces of the domain.

	Average mass-flux [mol/year]	Cumulative mass at 10^5 years [moles]
T1 -Hillslope	3.75E-06	1.28E+00
T1-Low Elevation	3.20E-07	1.69E-01
T2-Hillslope	5.36E-8	7.17E-02
T2-Low Elevation	7.16E-09	1.01E-02

Further study is underway with mesh design, time steps and the δ parameter to improve calculational accuracy in this case. Furthermore, for the HRD we have represented it as an equivalent porous medium with constant values of equivalent permeability and porosity for the whole domain. A better representation will have these values decreasing with depth, as implied by the different properties with depth of the stochastic fractures in the task specification.

For our continuing work, we shall study the upscaling of the stochastic fractures in the HRD to arrive at equivalent porous medium properties as a function of depth. Further checks will be made of all the results obtained so far to ensure calculational accuracy, mass balance, and sensitivity evaluation of various computational and physical parameter. In addition, alternative scenarios will also be investigated.

G.5 References

COMSOL Multiphysics. (1998). Subsurface Flow Module User's Guide. www.comsol.com/blogs

Follin, S., Levén, J., Lee, H., Jackson, P., Joyce, S., Roberts, D., & Swift, B. (2007). Hydrogeological characterisation and modelling of deformation zones and fracture domains, Forsmark modelling stage 2.2 Sven Follin, SF GeoLogic AB. In CM Gruppen AB. www.skb.se.

Hartley, L., Appleyard, P., Baxter, S., Hoek, J., Joyce, S., Mosley, K., Williams, T., Fox, A., Cottrell, M., La Pointe, P., Gehör, S., Caroline, D., Le Goc, R., Aaltonen, I., Vanhanarkaus, O., Jari, L., & Antti, P. (2018). Discrete Fracture Network Modelling (Version 3) in Support of Olkiluoto Site Description 2018.

Hartley, L., Hoek, J., Swan, D., Appleyard, P., Baxter, S., Roberts, D., & Simpson, T. (2013). Hydrogeological Modelling for Assessment of Radionuclide Release Scenarios for the Repository System 2012.

Hyman, J. D., Karra, S., Makedonska, N., Gable, C. W., Painter, S. L., & Viswanathan, H. S. (2015). DfnWorks: A discrete fracture network framework for modeling subsurface flow and transport. Computers and Geosciences, 84, 10–19. https://doi.org/10.1016/j.cageo.2015.08.001

Laforce, T., Jayne, R., Leone, R., Mariner, P., & Stein, E. (2022). Spent Fuel and Waste Disposition DECOVALEX-2023 Task F Specification Revision 9 DRAFT Prepared for US Department of Energy Spent Fuel and Waste Science and Technology.

Stein, E., Leone, R., Portone, T., & Jayne, R. (2021). Spent Fuel and Waste Science and Technology (SFWST)).

Suresh Kumar, G. (2008). Effect of sorption intensities on dispersivity and macro-dispersion coefficient in a single fracture with matrix diffusion. Hydrogeology Journal, 16(2), 235–249. https://doi.org/10.1007/s10040-007-0234-5.